Applications of Digitized 3-D Position-Sensitive CdZnTe Spectrometers for National Security and Nuclear Nonproliferation

by

Michael W. Streicher

A dissertation submitted in partial fulfillment
of the requirements for the degree of
Doctor of Philosophy
(Nuclear Engineering and Radiological Sciences)
in The University of Michigan
2017

Doctoral Committee:

Professor Zhong He, Chair
Professor Jionghua Judy Jin
Professor Sara A. Pozzi
Assistant Research Scientist Yuefeng Zhu

Michael W. Streicher

streichm@umich.edu

ORCID iD: 0000-0003-4842-7807

To all those striving to make the world a safer, healthier, and more educated place.

ACKNOWLEDGEMENTS

topics early in my studies. Dr. Steven Brown inspired me with his work and collaborated on much of the special nuclear material characterization. David Goodman always provided ideas and thought of potential experiments to garner a deeper understanding of CdZnTe performance and neutron interactions in CdZnTe. Sean O'Neal was a great roommate on conference travel and contributed to my understanding of detector physics (especially helping study for the qualifying exam!). Jiawei Xia was an excellent office-mate, and I appreciate the insightful intellectual (and non-intellectual) conversations we've had over the years. Jim Berry provided excellent electrical engineering assistance with this work and was always available for an insightful conversation. Thank you also to Charles Leak, Daniel Shy, and Bennett Williams who helped edit portions of this thesis work.

I would not be writing this thesis if not for the guidance of Dr. Scott Kiff at Sandia National Laboratories. He gave me an introduction to radiation detection through two summer internships and was instrumental in guiding me to the University of Michigan for my graduate studies. While at Sandia, my interactions with Dr. Patricia Schuster, Dr. Erik Brubaker, and Dr. Peter Marleau contributed to my desire to earn a doctoral degree in radiation detection.

In a healthy life, work and leisure are balanced. I appreciate the many friendships I cultivated in Ann Arbor, especially the core group of Hannah and Alex, Steven and Emily, Will and Elizabeth, and Jeff and Miranda. Dinner parties, trips to Kelly's Island, and floats down the Huron River were a welcome break from research. Sean O'Neal, Hao Yang, and Tommy Saller also provided valuable friendship during my time in Ann Arbor.

Many people supported me from a distance throughout my graduate studies. My parents instilled a love of learning in me at a young age which I really appreciate. My mom's weekly phone calls, which always included a brief update on my research, shows how much she cares about me and my work. Jesse, Adam, and Laura have

been incredible siblings and I appreciate their support from afar, and I applaud all of their academic and non-academic accomplishments.

I have tremendous friends from around the country who supported me throughout my graduate studies made in Cedar Falls and at Purdue - too many to list here. But their love was felt and appreciated throughout my studies.

Finally, most importantly, thank you to my beautiful wife, Bailey Streicher. Thank you for being my best friend, moving with me to Ann Arbor, and loving me unconditionally throughout it all. And to our child who will be joining us soon, I love you and dedicate much of this work to you and your future.

TABLE OF CONTENTS

LIST OF FIGURES

xiii

LIST OF TABLES

LIST OF ABBREVIATIONS

CdZnTe Cadmium Zinc Tellurium Semiconductor Detectors

CZT See CdZnTe

ASIC Application Specific Integrated Circuit

SNM Special Nuclear Material

NPT Non-Proliferation Treaty

FWHM Full Width at Half Maximum

PMT Photomultiplier Tube

SiPM Silicon Photomultiplier

APD Avalanche Photodiode

HPGe High-Purity Germanium Semiconductor Detector

IDEAS Integrated Detector Electronics AS, Inc.

BNL Brookhaven National Laboratory

VAS Voltage ASIC with Stretcher

TAT Trigger ASIC with Timing

THM Traveling Heater Method

VAD Voltage ASIC Digital

UM University of Michigan

FPGA Field-Programmable Gate Array

ADC Analog-to-Digital Converter

SNR Signal-to-Noise Ratio

CAR Cathode-to-Anode Ratio

WPCT Weighting Potential Crosstalk

ONR Opposing-Neighbor Ratio

SRF System Response Function

FWTM Full Width at Tenth Maximum

HVDB High Voltage Distribution Board

OGB Optimal Grid Bias

PET Positron Emission Tomography

SPECT Single-Photon Emission Tomography

CT Computed Tomography

CMOS Complementary Metal-Oxide-Semiconductor

JFET Junction Gate Field-Effect Transistor

ROI Region of Interest

IAEA International Atomic Energy Agency

DU Depleted Uranium

HEU Highly-Enriched Uranium

LEU Low-Enriched Uranium

WGPu Weapons-Grade Plutonium

DAF Device Assembly Facility

PDF Probability Density Function

MLEM Maximum Likelihood Estimation Maximization

NNSS Nevada National Security Site

PVC Polyvinyl Chloride

BeRP Beryllium Reflected Plutonium

DD Deuterium-Deuterium Neutron Generator

NRF Nuclear Resonance Fluorescence

DR Dynamic Range

ABSTRACT

A nuclear weapon detonation remains one of the gravest threats to the global community. Although the likelihood of a nuclear event remains small, the economic and political ramifications of an event are vast. The surest way to reduce the probability of an incident is to account for the special nuclear materials (SNM) which can be used to produce a nuclear weapon. Materials which can be used to manufacture a radiological dispersion device ("dirty bomb") must also be monitored.

Rapidly-deployable, commercially-available, room-temperature imaging gamma-ray spectrometers are improving the ability of authorities to intelligently and quickly respond to threats. New electronics which digitally-sample the radiation-induced signals in CdZnTe detectors have expanded the capabilities of these sensors. This thesis will explore national security applications where digital readout of CdZnTe detectors significantly enhances capabilities.

Radioactive sources can be detected more quickly using digitally-sampled CdZnTe detector due to the improved energy resolution. The excellent energy resolution also improves the accuracy of measurements of uranium enrichment and allows users to measure plutonium grade. Small differences in the recorded gamma-ray spectrum can be used to estimate the effective atomic number and mass thickness of materials shielding SNM sources. Improved position resolution of gamma-ray interactions through digital readout allows high resolution gamma-ray images of SNM revealing information about the source configuration.

CdZnTe sensors can detect the presence of neutrons, indirectly, through measure-

ment of gamma rays released during capture of thermal neutrons by ^{113}Cd or inelastic scattering with any constituent nuclei. Fast neutrons, such as those released following fission, can be directly detected through elastic scattering interactions in the detector. Neutrons are a strong indicator of fissile material, and the background neutron rate is much lower than the gamma-ray background rate. Neutrons can more easily penetrate shielding materials as well which can greatly aid in the detection of shielded SNM.

Digital CdZnTe readout enables the sensors to maintain excellent energy resolution at high count rates. Pulse pile-up and preamplifier decay can be monitored and corrected for on an event-by-event basis limiting energy resolution degradation in dose rates higher than 100 mR/hr. Finally, new iterations of the digital electronics have enhanced gamma-ray detection capabilities at high photon energies. Currently, gamma rays with energy up to 4.4 MeV have been detected. High-energy photon detection is critical for many proposed active interrogation systems.

CHAPTER I

Introduction

In physics, radiation is simply the emission or transmission of energy through space via waves or particles. Detecting the emission or transmission of radiation allows one to characterize the source or the transmission medium. Visible light is a form of electromagnetic radiation which can be detected by human eyes by focusing photons on the retina after refraction in the lens. Measurement of the incident direction and energy (color) of light allows sighted human beings to discern the world spatially.

Nature has engineered solutions for humans to detect light, acoustic waves, and heat via our innate senses. However, with the discovery of the expanse of the electromagnetic spectrum, including ionizing radiation (radiation which can ionize an atom, generally requiring an energy of greater than 10 eV), in the late 1800s, the means to detect radiation humans cannot innately sense become of great importance [1, 2].

Most terrestrial ionizing radiation comes in the form of x-rays, α particles, β particles, γ-rays, and neutrons [3]. α and β radiation are simpler to detect, since they consist of charged particles, and thus gaseous detectors or thin semiconductors can be used to detect their presence and energy. Since charged particles readily interact via Coloumbic forces, minimal stopping power (detector density) is required to fully halt the incident radiation.

Neutrons, gamma rays, and x-rays are not charged and thus typically must non-

Coulombically interact with electrons (in the case of γ-rays and x-rays) or nuclei (primarily in the case of neutrons). These interactions give rise to charged reaction products which can be detected electrically and information about the incident radiation can be discerned.

Ionizing radiation detection has applications in many fields. Radiation detectors are included on satellites for astronomy and astrophysics research as stellar phenomena produce ionizing radiation. Detectors are used in medical imaging equipment to diagnose and treat disease. Every nuclear facility such as nuclear power plants or nuclear fuel processing facilities requires radiation detectors to ensure workers do not receive too much harmful radiation dose.

Government agencies also use radiation detectors in order to provide security from radioactive dispersion devices (commonly known as dirty bombs) or nuclear weapons by detecting the clandestine movement of nuclear materials across borders. These detectors for national security may be used to enforce treaties such as the Non-Proliferation Treaty (NPT) by safeguarding nuclear material and verifying the material accounting of each country privy to the agreement terms. Finally, in the worst case scenario, governments maintain radiation detection equipment to analyze fallout to determine the source of the detonated weapon to inform response and identify the culprit. Photon and neutron signatures from nuclear material provide information about the isotopic composition of the source and data to characterize and localize the source spatially.

1.1 Gamma and X-ray Radiation Detection

Gamma rays and x-rays are high frequency ($> 10^{17}$ Hz) electromagnetic radiation (photons) produced by nuclear de-excitation (gamma rays) or atomic de-excitation (x-rays). These high-energy photons can be produced from a number of different sources. Gamma-ray sources used in the laboratory are primarily radioisotopes which

emit photons following beta decay (such as ^{137}Cs or ^{60}Co). Many sources encountered in the real world are of this variety as well, including uranium and plutonium. High-energy photons can also be generated via positron annihilation, nuclear reactions, bremsstrahlung, or emission of characteristic x-rays.

1.1.1 Photon Interactions with Matter

The primary interaction mechanism for photons with matter depends on the photon energy and the atomic number (Z number) of the target. At lower photon energies, especially for targets of high atomic number, photoelectric absorption is the primary interaction mechanism. In this process, the energy of the photon is absorbed by the atom, and an electron is expelled from its shell (statistically, the inner-most shells are likeliest) with energy of E_γ, the incident photon energy, minus the binding energy of the electron [4]. The probability of photoelectric absorption in a material with atomic number Z for a photon of energy E_γ is given in Eq. 1.1 [3].

$$P(\text{photoelectric}) \propto \frac{Z^n}{E_\gamma^m} \tag{1.1}$$

In Eq. 1.1, the exponents, n and m, are empirically determined: $m \approx 3.5$ and $n \approx 4.5$.

At photon energies between 500 keV and 5 MeV, Compton scattering becomes the dominant interaction mechanism in most materials. In this process, a photon interacts with the outer shell electrons. An electron is given some kinetic energy and the photon continues on its path at a deflected angle with lower energy. The scattering kinematics are given in Eq. 1.2

$$E'_\gamma = \frac{E_\gamma}{1 + (E_\gamma/m_0 c^2)(1 - \cos\theta)} \tag{1.2}$$

where E_γ is the incident energy of the photon, E'_γ is the scattered photon energy, $m_0 c^2$ is the rest mass energy of an electron, and θ is the scattering angle of the photon in the

lab frame of reference. The probability of Compton scattering increases proportionally to the Z number of the target material.

At high gamma-ray energies (above 1.02 MeV), pair production becomes energetically possible. In this process, in the vicinity of the nucleus, it is possible for the photon energy to be transfered to an electron-positron pair. The positron and electron will slow down via Coulombic reactions with the electrons in the target material. When the positron reaches low enough energies, it will annihilate with an electron in the target producing two 511 keV photons. These photons can escape the detector or be simultaneously captured via photoelectric absorption, perhaps following Compton scattering. The likelihood of pair production scales proportionally to Z^2.

1.1.2   Gamma-ray Detection using Inorganic Scintillators

In all three primary photon interaction mechanisms with matter, charged carriers are produced in the target material. This charge must be measured in order to relate the charge produced in the material to the energy deposited by the incident radiation. One of the first methods to detect radiation was to view the scintillation light produced when alpha particles were incident on ZnS screens. In fact, this detection mechanism was used to discover the atomic nucleus, informing the Rutherford model of the atom. The scintillation light produced was optically visible for experimentalists to count the number of interactions by noting flashes of light on the screen.

In 1948, Hofstadter investigated salts which would scintillate upon gamma-ray irradiation [5]. Cesium iodide doped with thallium (CsI:Tl) and most notably sodium iodide doped with thallium (NaI:Tl) produced large numbers of optical photons per MeV of gamma-ray energy deposited. This allowed them to achieve acceptable energy resolution performance, defined as the full width at half maximum (FWHM) of the photopeak in a histogram of pulse amplitudes for many gamma-ray interactions.

NaI:Tl and CsI:Tl scintillators, often noted simply as NaI and CsI, can achieve

photopeak FWHMs on the order of 45 keV for 662 keV gamma-ray energy depositions. Often, the FWHM is divided by the peak centroid to quote the energy resolution as a percentage. Thus, the resolution of NaI detectors is 7% FWHM at 662 keV. Recent advances have improved the energy resolution of small detectors to less than 5% FWHM at 662 keV by changing the dopant materials to enhance optical photon emission [6]. NaI detectors are commercially available and fairly inexpensive and thus find wide use in many applications [7].

In scintillators, the primary electron generated from a photon interaction slows down via Coulombic scattering which excites the constituent atoms of the scintillator. They de-excite via the emission of optical photons [8]. The photons can then be collected and turned into a voltage signal in a photomultiplier tube (PMT), a silicon photomultiplier (SiPM), or avalanche photodiode (APD).

In the early 2000s, new scintillating materials such as lanthanum bromide doped with cerium ($LaBr_3$:Ce) [9] and strontium iodide doped with europium (SrI_2:Eu) [10] became commercially available and provided energy resolution on the order of 3% FWHM at 662 keV. However, these detectors were more expensive than the previous generation of scintillators due to their exotic constituent materials.

Scintillating detectors are commonly used for national and homeland security applications because they have high densities, are composed of high-Z materials, and can be grown to large sizes, resulting in efficient detectors. Non-spectroscopic scintillators such as polyvinyltoluene [11] are used in radiation portal monitors and for some search applications by noting an increased count rate in the presence of a radiation source. Spectroscopic scintillators are used for quantifying the enrichment of uranium and in the search for and identification of radioactive materials. However, the energy resolution of scintillators will always be limited by inefficiencies in optical photon generation and collection, higher energy requirements to free charge carriers, and Fano factors greater than one [12]. This led to the development of semiconductor

detectors with better energy resolution.

1.1.3   Semiconductors for Gamma-ray Spectroscopy

Semiconductors are materials with loosely held outer-shell electrons, meaning it does not take much energy to excite an electron to the conduction band where it can freely migrate. Yet, the conductivity of semiconductors is orders of magnitude lower than metals. These characteristics makes semiconductors useful as radiation detectors. Particles deposit energy in the sensor, promoting a large number of electrons to the conduction band, minimizing the influence of Poisson statistics so the detectors exhibit excellent energy resolution. This is further characterized by the W value, or the amount of deposited energy required to produce one electron-ion pair in the material. Scintillators such as NaI have a W value of about 100 eV per electron, whereas semiconductors have a W value between 3 and 6 eV per generated electron.

Silicon and germanium are the most widely used semiconductor or solid-state detector materials. [13]. The use of silicon detectors has been limited to charged particles and x-ray spectroscopy due to the difficulty in growing wafers thicker than 2 cm, low atomic number of 14, and low density of 2.3 g/cm^3, leading to inefficient detectors for gamma rays.

Germanium has been successfully used as a gamma-ray spectrometer, first by drifting the germanium with lithium in the 1970s to compensate the material to reduce the impact of impurities, and later, by purifying the material to the parts per trillion magnitude to create an intrinsic semiconductor in the 1980s. The lithium drifted germanium, Ge(Li), detectors had to be maintained at 70 K at all times or else the detector would permanently fail. However, intrinsically pure germanium detectors, known as high-purity germanium, HPGe, do not need to remain at 70 K at all times. They do need to be maintained at 70 K during operation as the small germanium bandgap allows a large number of charge carriers to be thermally generated at higher

temperature, ruining the spectroscopic performance. The probability of thermally exciting an electron to the conduction band is given in Eq. 1.3.

$$P(T) = CT^{3/2} \exp\left(\frac{-E_g}{2kT}\right) \tag{1.3}$$

T is the absolute temperature of the detector, E_g is the bandgap of the semiconductor, k is the Boltzmann constant, and C is a proportionality constant. Substitution of the bandgaps for silicon (1.1 eV) and germanium (0.7 eV) into Eq. 1.3 demonstrates why germanium requires cryogenic cooling whereas silicon may be operated at room temperature.

While HPGe detectors have remained the gold-standard for energy resolution and have been deployed for national security applications, the need remained for a high-resolution spectrometer that operated at room temperature with greater efficiency than HPGe, which has a Z number of 32 and a density of 5.3 g/cm^3. Of the room temperature materials investigated, CdZnTe appears most poised to replace HPGe in many applications, particularly in the area of national security.

1.1.4 Room Temperature Semiconductor Materials

The existence of compound semiconductors such as CdTe may be postulated by simply looking at the periodic table and combining elements so that the average electron structure resembles silicon or germanium. Room-temperature semiconductors such as GaAs, CdTe, HgI$_2$, and TlBr can all be envisioned simply by considering electron structure.

CdTe was first grown in the 1970s and attracted interest as a competing technology to Ge(Li) and HPGe [14]. Adding 10 wt% zinc to the CdTe melt, creating CdZnTe, resulted in more homogeneous ingots, higher resistivity, lower leakage current, and most importantly, no observed detector polarization which was a major problem in

CdTe [15, 16]. Polarization remains a problem for HgI_2 [17, 18] and TlBr [19, 20] spectrometers. However, the mobility of holes in CdZnTe was found to be even lower than the hole mobility in CdTe [21]. For both CdZnTe and CdTe, the electron mobility is approximately two orders of magnitude greater than the hole mobility. For planar devices, electrons and holes must be fully collected for the induced signal amplitude to be proportional to the energy deposited in the device. Until Shockley-Ramo Theorem implications were fully grasped, the use of CdZnTe and CdTe was limited to x-ray spectroscopy.

1.2 History of CdZnTe Detector Development

1.2.1 Shockly-Ramo Theorem

In order to design circuitry to readout semiconductor detectors, one needs to understand how charge is induced on each electrode. The Shockley-Ramo Theorem allows one to do this in a straightforward way [22, 23, 24]. The theorem states that the induced charge on an electrode is equal to the generated charge multiplied by the change in weighting potential the charge migrates through for the electrode of interest.

The weighting potential, ϕ_0 is a *virtual* field. It is calculated by solving the Poisson Equation, given in Eq. 1.4, using the following boundary conditions:

1. The potential at the electrode of interest is 1 V

2. The potential at all other electrodes is 0 V

$$\nabla^2 \phi_0 = 0 \tag{1.4}$$

Once the weighting potential is calculated for all points in space, the total charge

induced on an electrode at any point along its drift is given by Eq. 1.5.

$$\Delta Q = -q \left[\phi_0(\vec{x_f}) - \phi_0(\vec{x_i}) \right] \qquad (1.5)$$

where ΔQ is the total induced charge, $\vec{x_f}$ is the final position of the moving charge, and $\vec{x_i}$ is the initial position of the charge (i.e. where the radiation interaction occurred). To predict the pulse waveform as it would appear on an oscilloscope, one must know the electric field profile in the detector. The electric field determines how the charge moves in the device as a function of time, whereas the weighting potential provides the relative amplitude as a function of position. The convolution of the weighting potential and true charge motion provides the induced charge as a function of time.

The Shockley-Ramo theorem demonstrates that by changing the geometry of the electrodes, the signal induction will be different. It was this insight that allowed CdZnTe spectrometers to truly develop.

1.2.2 Electrode Designs for CdZnTe Detectors

Ionization chambers have long employed "Frisch-grids" to account for mobility differences between electrons and ions. A metallic grid is placed near the anode side of the gas chamber to block the signal induction from the bulk of the detector. Only when electrons reach the region between the anode and Frisch grid is signal induced on the anode electrode. This design is impossible in solid-state detectors, so researchers looked for different methods to obtain similar results.

Luke first developed a co-planar grid electrode [25]. In this design, strips of electrodes are placed in an interlocking scheme as shown in Fig. 1.1 [26, 27]. Both electrodes are read out for each event. The difference in signal amplitude between the electrode which collects the charge and the non-collecting electrode is independent of depth and proportional to the energy deposited.
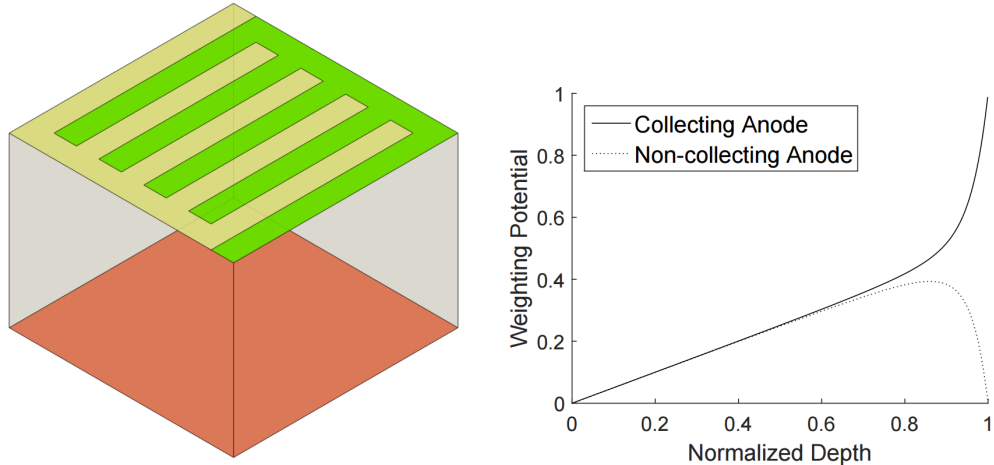
Figure 1.1: Sketch of coplanar grid electrode design. A planar cathode electrode is shown in orange, whereas the coplanar anode electrodes are shown in yellow and green (left). The weighting potential for the collecting and non-collecting anodes in the coplanar grid geometry (right).

Very soon after, Barber, Barrett, and Eskin discovered that one could generate depth-independent signals from pixel arrays through what become known as the "small-pixel effect" [28, 29]. In pixelated detectors, the induced charge is shared by many pixels for much of the charge drift. Only when electrons reach the anode vicinity is a significant amount of charge induced.

In the 1990s, He discovered that by having one electrode insensitive to depth and one electrode sensitive to the energy deposited and the depth of interaction, one could correct for material nonuniformity [30]. By having a pixelated anode and planar cathode, one can calculate the three-dimensional interaction position of the gamma ray in the device and correct differences in signal amplitude due to electron path length and material non-uniformities [31]. Pixelated detectors may also be used to reconstruct multiple pixel events allowing Compton imaging in a single-volume CdZnTe detector.

Alternatively, McGregor devised an electrode geometry known as a "virtual Frisch Grid" to obtain depth-independent signals [32]. This design has been used by researchers at Brookhaven National Laboratory to improve CdZnTe material by reduc-

ing Te inclusions and grain boundaries [33, 34, 35, 36].

1.2.3   Pixelated CdZnTe Detectors and Readout

Pixelated detectors are the electrode configuration with the brightest future for the following reasons:

1. Leakage current through the detector is distributed across many pixels reducing the effective electronic noise.

2. Likewise the detector capacitance is distributed resulting in lower electronic noise.

3. Multi-interaction site events can be reconstructed

4. The three-dimensional interaction position of each event can be determined, so the signal amplitude can be corrected for electron trapping, weighting potential effects, or CdZnTe material non-uniformities.

The downside of pixelated detectors is that many independent channels must be read out simultaneously, but this task is possible by employing application specific integrated circuits (ASICs).

The first ASIC readout system for CdZnTe was completed in 1998 [37]. The VA1 chip was capable of reading out 128 anode channels, but discrete circuitry had to be constructed to read out the cathode signal. The energy resolution using this ASIC and a good CdZnTe detector was 1.75% FWHM at 662 keV. In 2004, another ASIC generation designed by the University of Michigan and Integrated Detector Electronics AS (IDEAS) in Oslo, Norway [38] was fabricated. This ASIC included a timing detection circuit so that the depth of interaction for multi-site interactions could be calculated. Eventually, an energy resolution of 0.93 % FWHM at 662 keV for single-pixel events for an entire $1.5{\times}1.5{\times}1$ cm^3 detector was achieved [39]. A
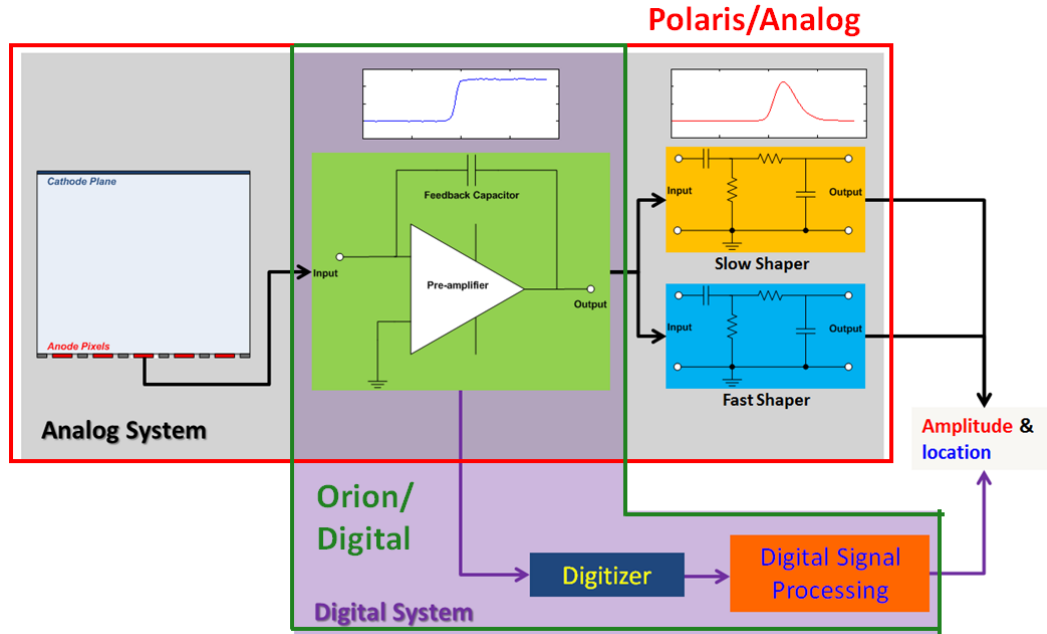
Figure 1.2: Illustration of the difference between an analog ASIC framework and digital ASIC design for reading out pixelated CdZnTe detectors.

third generation ASIC was delivered shortly thereafter in 2005 with lower electronic noise which was able to achieve an energy resolution of 0.76 % FWHM at 662 keV for single-pixel events for the entire detector volume [40].

Simultaneously, ASIC collaborations began with IDEAS to design a digital read-out system and with Brookhaven National Laboratory (BNL) to design an analog ASIC, with lower electronic noise than systems previously delivered by IDEAS. The difference between the analog and digital ASIC circuitry is illustrated in Fig. 1.2.

In both ASIC frameworks, a charge sensitive preamplifier is used to read out the charge induced on the anode pixels, planar cathode, and guard ring. In the analog framework, the preamplifier signal is sent to a slow shaper with a long shaping time which is used to determine the amplitude of the pulse waveform and a fast shaper with a short shaping time to determine the time at which the pulse waveform began to rise. In the IDEAS design, the slow shaping time leg is known as the VAS (Voltage ASIC with Stretcher) and the timing pickoff circuitry is known as the TAT (Trigger ASIC

with Timing). In a digital ASIC framework, the charge sensitive preamplifier signal is directly sampled, so that the entire pulse waveform may be analyzed. In many instances, this can provide richer information. Systems originating at the University of Michigan which use the analog ASIC framework are known as "Polaris" detection systems whereas products which use the digital framework are known as "Orion" systems.

The collaboration with BNL was very fruitful, creating a CdZnTe readout system which achieved a resolution of 0.48% FWHM at 662 keV for single-pixel events [41, 42]. The collaboration with IDEAS to design a digital ASIC known as VAD (Voltage ASIC Digital) began in 2007. To date, four VAD generations have been delivered. The VAD_UMv1.0 ASIC, delivered in 2010, had excess electronic noise and several design flaws which limited its application. However, the redesigned VAD_UMv1.2 ASIC, delivered in 2011, exhibited much better performance. This capable system demonstrated comparable performance to the BNL ASIC with an energy resolution of 0.41% FWHM at 662 keV [43]. A fully populated system was reported in 2014 with a recorded energy resolution of 0.63% FWHM for all events [44].

The VAD_UMv1.2 ASIC was modularized beginning in 2013. The VAD_UMv1.2 ASIC also required a positive and negative bias supply for operation. The next generation, VAD_UMv2.0, delivered in 2015, required only positive bias supply. Furthermore, the VAD_UMv2.0 ASIC had several dynamic range settings so that the energy resolution and acceptable energy range could be selected based on the users' needs. However, the VAD_UMv2.0 ASIC had significant crosstalk between channels, rendering some pixels unusable. Furthermore, the preamplifier design resulted in a "ringing" oscillation after charge collection. The VAD_UMv2.2 ASIC, delivered in 2016, addressed these problems and reduced electronic noise.

CdZnTe detection systems have improved due to improvements in electronics, reconstruction algorithms, and CdZnTe material. High-quality CdZnTe crystals were

thought to only be grown using the high-pressure Bridgman technique [45]. However, Redlen Technologies (Saanichton, British Columbia) has shown high quality CdZnTe grown using the traveling heater method (THM) [46]. This lowers the cost of CdZnTe detectors and improves the charge transport properties. As the quality of CdZnTe has improved, larger monolithic crystals have been used. $1 \times 1 \times 1$ cm^3 were used in the 1990s. In the early 2000s, $1.5 \times 1.5 \times 1.5$ cm^3 CdZnTe crystals were studied. In the late 2000s, the detector size was standardized to $2 \times 2 \times 1.5$ cm^3 although $2 \times 2 \times 0.5$ cm^3 were used to study different fabrication techniques [27, 47]. Over 300 of the standard $2 \times 2 \times 1.5$ cm^3 detectors were delivered by Redlen Technologies to UM between 2009 and 2016. As shown in Fig 1.3, the single-pixel energy resolution at 662 keV improved and became less variable between 2009 and 2016, showing that Redlen's process improved considerably. Other detector parameters such as the electron mobility-lifetime product, $(\mu\tau)_e$, also showed improvement over time [48].

1.2.4 Anode Pixel Configuration

Two anode pixel geometries have been studied extensively, one with a common steering grid as shown in Fig. 1.4 and one without as illustrated in Fig. 1.5. The models were created in ANSYS Maxwell software which was used to calculate the weighting potential for different detector geometries [49]. Both detectors include a 500 μm guard ring around the peripheral pixels. The pitch between pixels in both designs is 1.72 mm. The common steering grid detectors have a 100 μm thick electrode between each pixel which is biased slightly to steer electron clouds toward the pixel pad which is 1.22 mm wide. In the simple pixel design, there is no electrode between pixels, so the gap between pixel pads can be decreased to 60 μm.

For many years, common steering grid detectors were thought to be required to accurately reconstruct multiple pixel events. However, with the development of digital readout of detectors, the common grid became less important as the reconstruction
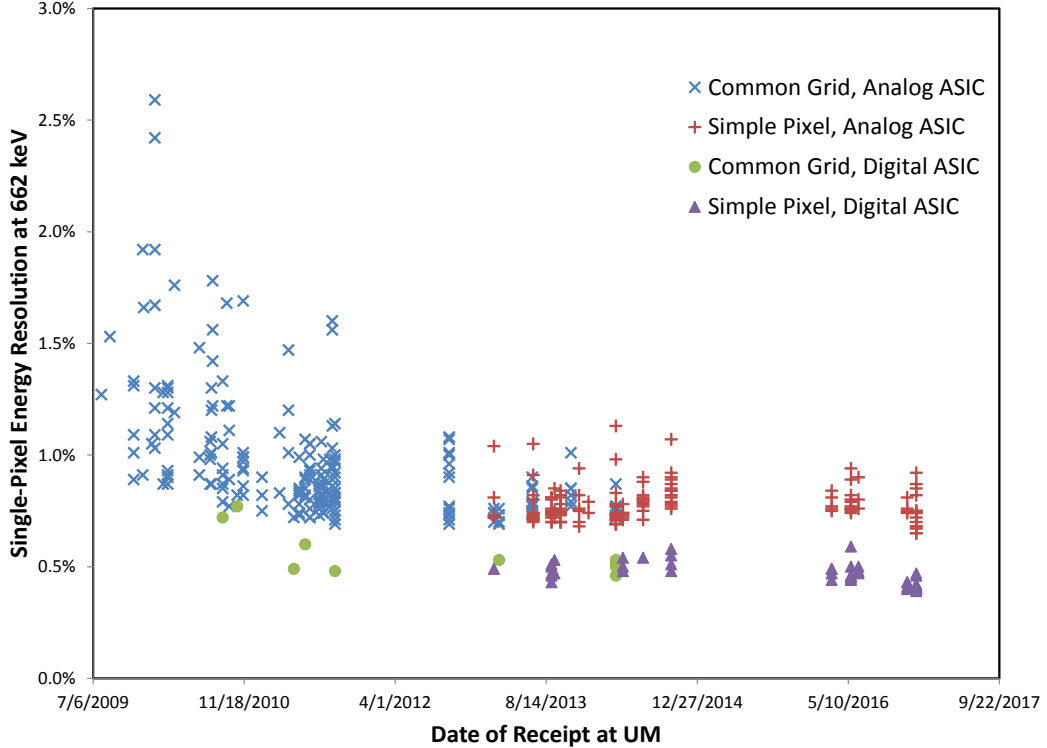
Figure 1.3: Energy resolution for each $2\times2\times1.5$ cm^3 detector received from Redlen Technologies over time. The markers indicate the anode electrode configuration and the readout system used to test the detector.

could be accomplished algorithmically. Furthermore, the steering grid is difficult to fabricate and contributes electronic noise in the form of leakage current. Equivalent energy resolution and better sub-pixel position resolution was achieved using simple pixel detectors [50]. All the results shown in this thesis were recorded with simple pixel detectors read out by a VAD digital ASIC.

1.3 Neutron Detection

In this thesis, CdZnTe as a neutron detector is discussed. While the material was developed for photon detection, CdZnTe has some unique properties that may make it attractive as a thermal neutron and fast neutron detector. In national security applications, a sensor which can provide high-resolution gamma-ray spectroscopy and imaging while simultaneously detecting both fast and thermal neutrons in a rapidly-
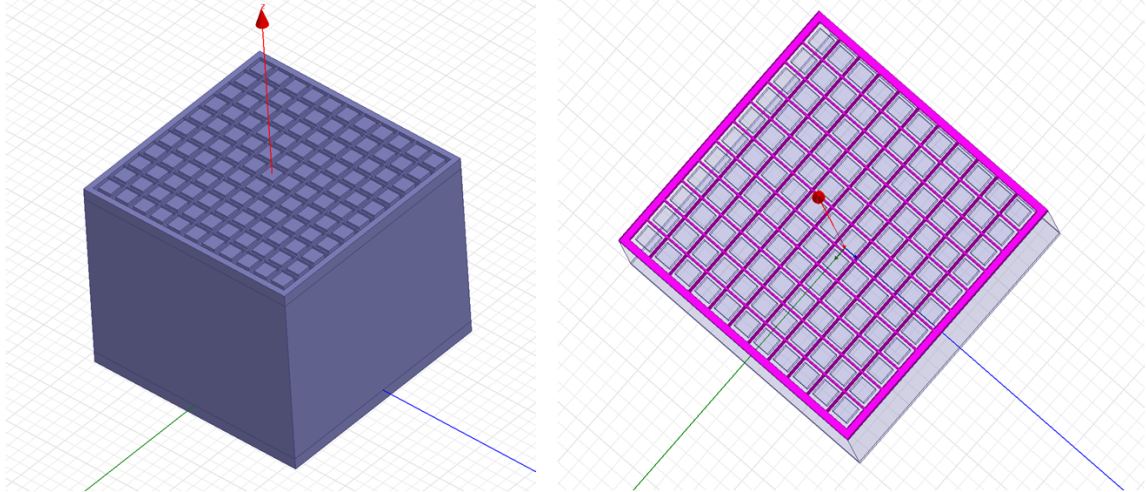
Figure 1.4: Illustration of a CdZnTe detector with a common steering grid. The grid is highlighted in the right pane in pink.
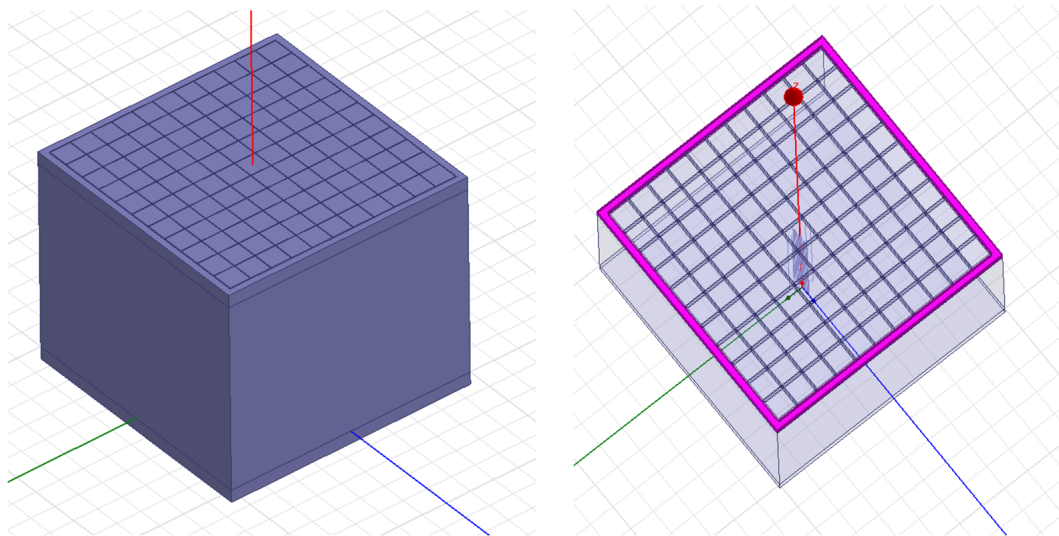
Figure 1.5: Illustration of a simple pixel CdZnTe detector. The guard ring is highlighted in pink in the right pane. Several possible electron paths are shown near the center pixel.

deployable package could be quite valuable.

SNM emits high-energy neutrons after spontaneous fission or fission following active interrogation with a neutron or high-energy photon source [51]. Neutrons produced by fission will have energies following a Watt distribution. The most probable neutron energy is about 1 MeV while the mean neutron energy is about 2 MeV. Fast neutrons can be produced via thermonuclear reactions (such as deuterium-deuterium

and deuterium-tritium fusion) or other nuclear reactions such as (α,n) or (p,n).

Fast neutrons generally interact with matter via elastic or inelastic scattering reactions. Momentum and energy are conserved by a recoil nucleus and the neutron in elastic scattering reactions, whereas a photon is emitted to conserve energy in inelastic scattering. The typical microscopic cross sections for these reactions are several barns for MeV neutrons.

Fast neutrons are rare in the natural background with a flux of only 1.8 ± 0.2 $\times 10^{-3}$ cm^{-2}s^{-1} at sea level [52] (although some have measured higher rates [53]). For comparison, the background gamma-ray flux (> 100 keV) is around 10 cm^{-2}s^{-1}, but varies greatly depending on location. Also, unlike gamma rays, fission-energy neutrons are not easily shielded and can escape high atomic number shielding materials without significant attenuation. Therefore, fast neutrons provide a complementary signal to gamma rays for detecting shielded SNM.

After many scattering reactions, fast neutrons slow to thermal energies [54]. Thermal neutrons are easier to detect than fast neutrons because interaction cross sections are significantly higher at thermal energies (thermal neutron reaction cross sections can be several thousand barns). Many thermal neutron detectors have been developed based on ^{10}B, ^{7}Li, and most notably, ^{3}He reactions. The production of a charged particle from a high-Q value reaction within the detector makes detection straightforward. (n, γ) reactions have also been used to detect thermal neutrons, even using CdTe [55] or CdZnTe as the conversion layer [56, 57].

Often, fast neutrons are detected by thermalizing fast neutrons through scattering interactions in a moderator, and then, detecting the initially fast neutrons via thermal neutron interactions. However, by thermalizing neutrons, information about the incident neutron energy spectrum is lost. A neutron energy spectrum can be useful to discriminate different neutron sources. Also, by estimating the energies of individual neutron scatters, one can image neutron sources using scattering kinematics

[58]. Low-Z scintillating materials with good neutron-gamma pulse shape discrimination have been employed to estimate incident neutron energy spectra after unfolding [59, 60].

Semiconductor detectors such as high-purity germanium (HPGe) have been used to study elastically and inelastically scattered neutrons in semiconductor materials [61, 62]. A similar approach is taken using CdZnTe spectrometers in this thesis.

1.4   Contributions to the Field in this Dissertation

This work demonstrates areas where digital readout of CdZnTe enhances capabilities, especially for national security applications. Chapter II introduces the electronics used for reading out CdZnTe detectors and the algorithms applied to calculate the energy and position of individual gamma-ray interactions. Chapter II also presents some cases where digital readout enhances detector physics understanding. Chapter III describes how algorithms can be applied to the pulse waveforms in high count rate environments to recover energy resolution degradation and estimate the dose rate.

The energy resolution of CdZnTe is improved by using digital readout techniques. Resolution improvements matter when attempting to measure the isotopic composition or other characteristics of SNM. Chapter IV compares the resolution of CdZnTe with HPGe to characterize special nuclear materials and introduces a method to calculate intervening shielding between the detector and source by noting small differences in the recorded gamma-ray energy spectrum only discernible with a high-resolution spectrometer.

Digitally-sampled CdZnTe spectrometers have achieved very low energy thresholds. With these low-energy thresholds, it is possible to measure elastic scattering of fast neutrons within CdZnTe. Chapter V describes the process of tuning the low-energy threshold and provides proof that elastic scattering neutron interactions are detectable in CdZnTe.

Multi-MeV gamma-rays are prominently produced from fission sources and neutron captures. These photon sources are important for active interrogation applications. The performance of CdZnTe detectors at high photon energies is presented in Chapter VI.

CHAPTER II

Energy and Interaction Position Reconstruction in Digitized CdZnTe Spectrometers

One of the main benefits of pixelated CdZnTe is that the three-dimensional interaction position of photon interactions can be determined. The signal amplitude can then be adjusted based on the interaction position. Longer electron drift distances lead to more trapped charge, but interactions closer to the anode go through less weighting potential change, resulting in smaller induced charge. Anode pixels may have different electronic gain due to anode fabrication imperfections or slight differences in the ASIC preamplifier circuit. Furthermore, the CdZnTe material may be nonuniform which can lead to electron trapping which varies as a function of interaction position.

Multiple-pixel interactions require drift-time measurements to reconstruct the depth-of-interaction to correct for weighting potential and electron trapping. Additionally, when two charges move simultaneously in a detector, the signal induced by one charge affects the measured amplitude of another and vice versa; this phenomenon is known as weighting potential crosstalk (WPCT). The ASIC response may also vary as a function of gamma-ray energy deposited. The energy resolution of the sensor degrades unless these effects are accounted for and corrected. Several dissertations have been dedicated to discovering and implementing various correction
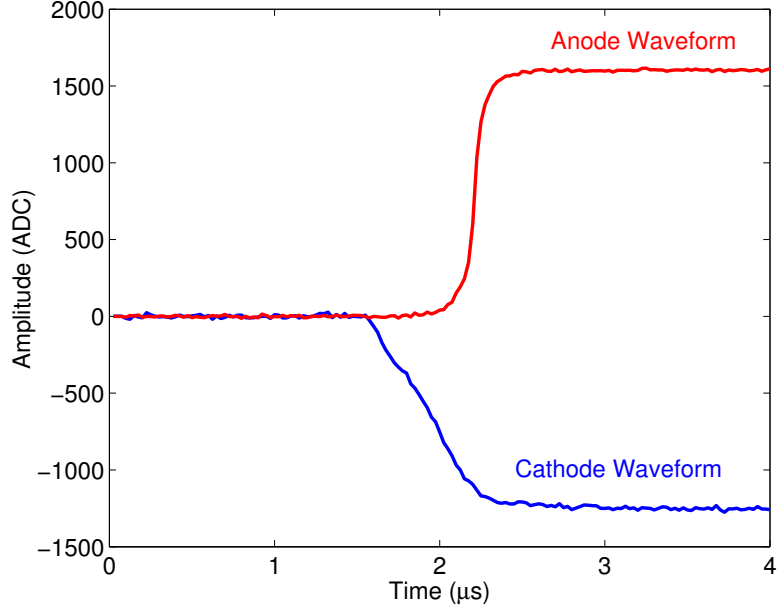
Figure 2.1: Example anode and cathode pulse waveforms for a 662 keV photopeak event near the cathode-side of the detector read out by the VAD_UMv1.2 ASIC.

algorithms [63, 64, 65, 66].

This chapter will explore energy correction methods for analog and digital readout systems, sub-pixel position sensing with digital readout systems, and situations where pulse waveforms can provide additional information about the CdZnTe detector.

2.1   Digital Readout Systems

The measured amplitude of the cathode and anode signals and the collecting pixel location are required to calculate the energy deposited by a gamma ray. In analog readout, the filter which shapes and measures the signal amplitude is configured in the ASIC. However, digital readout systems output the preamplifier signal directly. Fig. 2.1 shows example pulse waveforms for a single-pixel 662 keV photopeak event read out by the VAD_UMv1.2 ASIC.

A photograph of the VAD_UMv1.2 ASIC system, also known as the prototype Orion system or the digital array system, is shown in Fig. 2.2. The Orion prototype system has four ASIC modules in a 2×2 array bonded to a printed circuit board. The

21
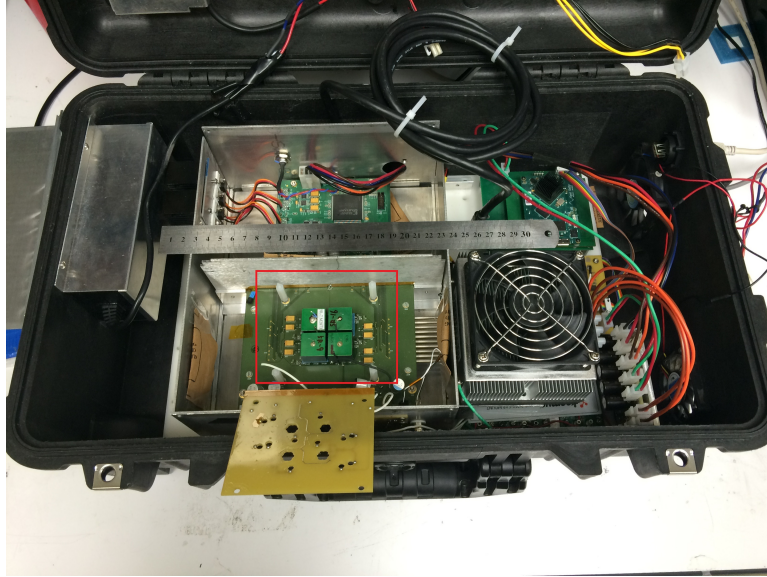
Figure 2.2: Photograph of the prototype Orion VAD_UMv1.2 digital ASIC array system. The locations of the CdZnTe detectors are highlighted by the red rectangle.

ASIC itself is a 124 channel pipeline circuit with charge sensitive preamplifiers. One channel is dedicated to each anode pixel, with additional channels for the cathode, guard ring, and a reference channel for baseline monitoring. Each channel has a charge sensitive preamplifier, triggering logic, and 160 sample cells to store the signal amplitude. The electrode signal is sampled constantly in a round-robin fashion at 10, 20, 40, or 80 MHz. The sample cells always have the signal amplitude stored, but they are read out only when a readout sequence is initiated. The readout sequence is initiated from a field-programmable gate array (FPGA). A readout frequency can be configured by the user in a mode known as "forced readout" mode, so the ASIC is read out periodically independent of radiation interactions. In "triggered readout" mode, the ASIC sends a trigger signal telling the FPGA to initiate readout. Forced readout is useful to perform ASIC calibrations and estimate the electronic noise of the system whereas triggered readout is required to perform gamma-ray spectroscopy.

In the triggered readout mode, the signal induced on the anode pixels is shaped by a short shaping-time filter on-board the ASIC. If the shaped signal surpasses a threshold, set by the user and trimmed on a channel-by-channel basis, an internal

trigger is generated. The ASIC continues to sample the preamplifiers after the internal trigger for a time known as the "sample-hold delay time". After the sample-hold delay time has passed, the ASIC signals the FPGA that a trigger has been recorded. The FPGA then initiates the readout sequence.

Depending on the system settings, the FPGA can instruct the ASIC to read out all 124 channels in what is known as "full-readout mode". This is useful for calculating noise and correcting common-mode noise. Alternatively, the FPGA can instruct the ASIC to read out only the triggered pixel or the triggered pixel plus the neighboring pixels. This limited data readout mode is known as "sparse readout mode". Sparse readout reduces readout time, increasing the maximum event rate. Reading out neighboring pixels preserves the ability to perform sub-pixel position sensing which is discussed later in this Chapter.

During the readout sequence, the sampled value in each cell is passed in an analog fashion to a receiver and then to an analog-to-digital converter (ADC). Multiple ASICs can be read out using the same receiver and ADC chain. Another circuit board handles data buffering and communication between the user's personal computer and the radiation detection system.

The pulse waveform amplitude is roughly calculated after a trigger to ensure charge is collected by the triggered pixel. Transient signals, which are discussed at length later, may cause the system to unnecessarily trigger. This amplitude requirement is known as the "software threshold". If this threshold is exceeded, the trigger is valid. If the software threshold is not exceeded, the event is reclassified.

The prototype Orion system, shown in Fig. 2.2, can convert 120 V AC power to DC and deliver power to ASICs, circuit boards, and a Peltier thermoelectric cooler to dissipate heat. The system provides -3 kV bias to the cathodes of each detector to generate an electric field so that radiation-generated charges move. The system is contained in a case for portability. A battery provides system power for 30 minutes.
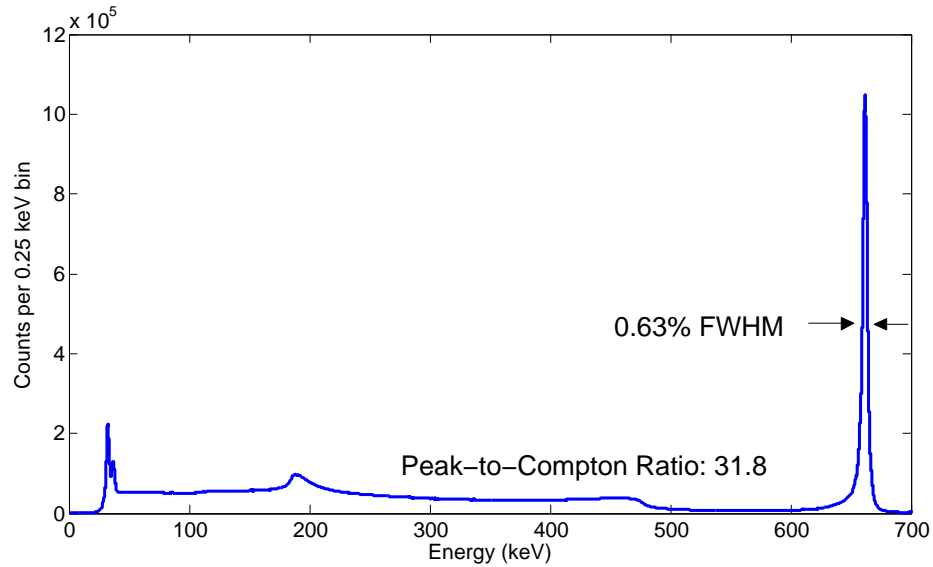
Figure 2.3: All-events ^{137}Cs gamma-ray energy spectrum measured using the 2×2 CdZnTe detector array read out by VAD_UMv1.2 ASICs.
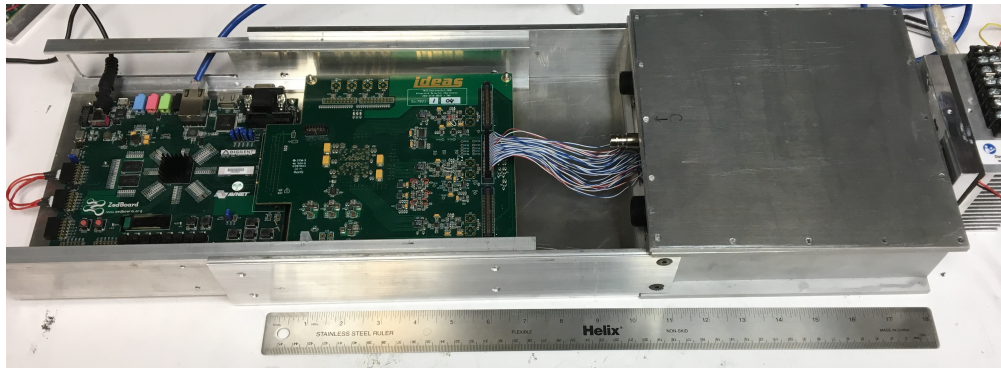
Figure 2.4: Photograph of the VAD_UMv2.2 readout system.

The system consumes about 20 W during operation.

The prototype Orion system was a very important instrument to demonstrate applications of digitally-sampled CdZnTe detectors. The energy resolution of the system for single-pixel events was 0.43% FWHM at 662 keV. For all events from four detectors, the energy resolution was 0.63% FWHM at 662 keV at a count rate of 2500 counts per second as shown in Fig. 2.3. The barium x-rays at 31 and 35 keV are clearly resolved.

While, the VAD_UMv1.2 ASIC was very useful, it had some flaws which were

addressed in the design of the next generation, VAD_UMv2.2 ASIC. First of all, the ASIC was modularized. The VAD_UMv1.2 ASIC was implanted on a circuit board. If one ASIC module sustained damage, that module could not be replaced, reducing the efficiency of the system and limiting its application for coded aperture imaging. Modular ASICs can be swapped if one is damaged and can more easily be directly attached to a CdZnTe detector to reduce electronic noise. The VAD_UMv1.2 ASIC required biases of $+1.5$ V and -2.0 V. It is marginally more difficult to design a power board to supply two polarities, so the VAD_UMv2.2 ASIC only required positive bias supplies of $+1.8$ V and $+3.3$ V. Additionally, the system was made to accommodate nine detectors in a $3{\times}3$ array compared to four detectors in the VAD_UMv1.2 system. Finally, the ASIC was designed with four different dynamic range settings to detect the following maximum gamma-ray energies: 700 keV, 3 MeV, 7 MeV, and 9 MeV. This should allow CdZnTe detectors to more easily detect high-energy photons using the 9 MeV dynamic range setting and improve the energy resolution at 662 keV using the 700 keV dynamic range setting.

Fig. 2.4 shows a photograph of the assembled system. As indicated with the ruler in the photograph, the system is quite large. The receiver/ADC board and the data buffering board were redesigned for a smaller physical footprint in future design iterations. However, the system has demonstrated improved energy resolution of 0.34% FWHM at 662 keV using a detector directly coupled to an ASIC and the 700 keV dynamic range setting as discussed in Sect. 2.5.

Regardless which readout system is used, digital pulse processing methods are required to determine the energy and location of each photon interaction. The first step is to determine the amplitude of the recorded anode and cathode pulse waveforms.

2.1.1 Basic Depth-of-Interaction Correction for Single Pixel Events

Correcting single-pixel events using a digital readout system is fairly straightforward. First, the amplitude of the cathode and anode waveforms must be measured. The simplest method to determine the amplitude is known as simple-subtraction. The mean value in the tail portion of the waveform (the segment after the charge has been fully collected) minus the mean value in the baseline portion of the waveform (before the radiation interaction) is used to estimate the amplitude. In Fig. 2.1, the tail region is between 2.5 and 4 μs whereas the baseline region is between 0 and 1.5 μs.

To improve the single-pixel events energy resolution at 662 keV, digital filters may be applied in post-processing to measure the pulse waveform amplitude. Through trial and error, the best performing filter is a trapezoidal filter with 1.8 μs rising time and 400 ns flat-top time for anode pixels and 1.2 μs rising time and 1.5 μs flat-top time for the cathode waveform. The effect of this filter on the recorded pulse waveform is shown in Fig. 2.5. To process the waveforms quickly, the convolution between the filter and pulse waveform is done in the frequency domain.

In order to calibrate a CdZnTe detector, the anode and cathode waveform amplitude for several hundred thousand single-pixel photopeak events from a ^{137}Cs source must be binned into a histogram on a channel-by-channel basis. Fig. 2.6 shows an example of the raw (i.e. not depth-corrected) anode and cathode pulse height spectra for a calibration measurement. Cutoffs for the anode and cathode spectra are calculated. The cathode cutoff is a measurement of the cathode signal amplitude for a 662 keV single-pixel energy deposition very near the cathode surface (i.e. the largest possible cathode amplitude from a 662 keV energy deposition). The cathode cutoff is shown with the vertical green line in Fig. 2.6. Since the anode spectrum has a photopeak, a photopeak region is determined. The high-side anode cutoff is shown with a vertical black line in Fig. 2.6.
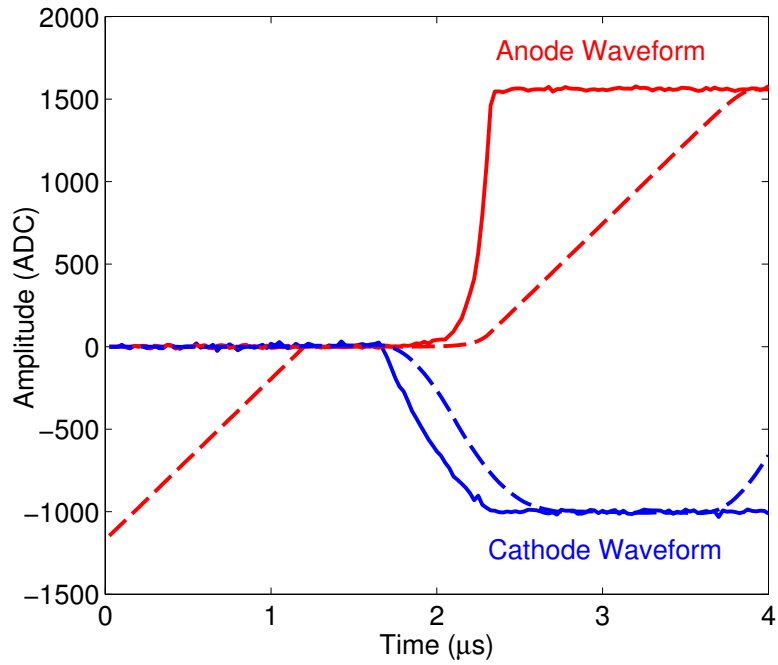
Figure 2.5: Example anode and cathode pulse waveforms for a 662 keV energy deposition in the center of the detector read out by the VAD_UMv1.2 ASIC shaped with the best performing filter in the dashed lines.
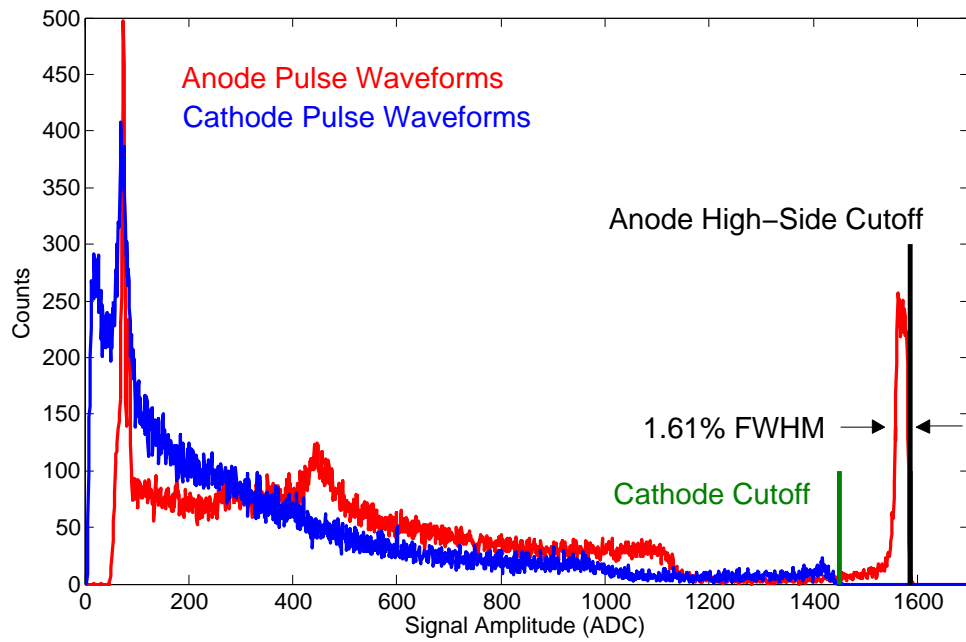
Figure 2.6: Example anode and cathode pulse height spectrum for ^{137}Cs calibration measurement. The anode and cathode cutoffs are shown with the vertical lines.
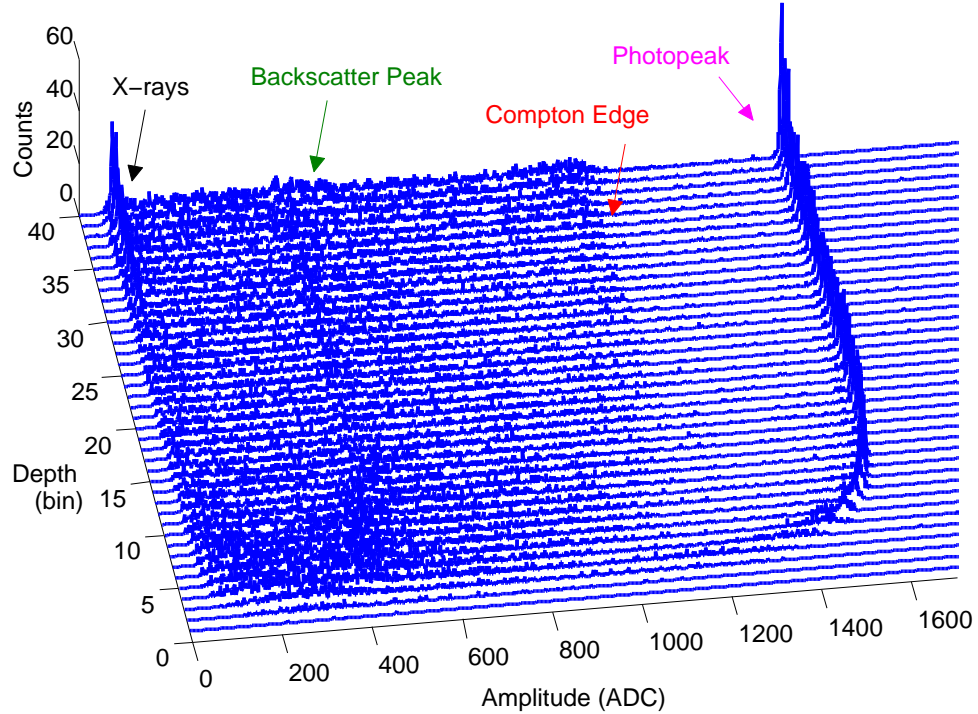
Figure 2.7: Pulse height spectrum as a function of energy and interaction depth for single-pixel events in one anode channel. Note that the pulse height decreases near the anode due to weighting potential effects and decreases near the cathode due to electron trapping.

Next, the spectrum is broken into three-dimensional pixels (or "voxels") to determine the applicable gain for each 3-D interaction position to align the photopeaks. The depth is determined by the cathode-to-anode ratio (CAR) which is calculated using the cutoffs and pulse waveform signal amplitudes as shown in Eq. 2.1 [67].

$$Depth\,(\text{bin}) = N_{bins}\left(\frac{A_{cathode}}{A_{anode}}\right)\left(\frac{C_{anode}}{C_{cathode}}\right) \tag{2.1}$$

The number of depth bins, N_{bins}, is determined by the user, but forty is usually sufficient, based on an electron cloud size of 300 μm at 662 keV [66]. The signal amplitude ratio of of the cathode, $A_{cathode}$, to the anode, A_{anode}, is multiplied by the cutoffs, C_{anode} for the high amplitude anode cutoff and $C_{cathode}$ for the cathode cutoff, to limit the ratio between zero and the number of depth bins selected.

The anode photopeak amplitude centroid is calculated for the spectra in each

28

voxel of the detector to determine the gain as illustrated in Fig. 2.7. In the energy domain, the centroid should be at 661.7 keV regardless of the interaction position. This can greatly improve the energy resolution. For instance, the energy resolution of the anode channel shown in Fig. 2.6 improves from 1.61% FWHM to 0.45% FWHM at 662 keV after the depth correction.

This particular detector has a fairly low electron mobility-lifetime product, $(\mu\tau)_e$, of about 1.5×10^{-2} cm^2/V. Small mobility-lifetime product values increase the importance of the depth correction as the photopeak amplitude considerably changes as a function of interaction depth due to electron trapping.

The measured energy resolution using a VAD_UMv1.2 ASIC for single-pixel events at 662 keV is generally 0.25% FWHM lower than the energy resolution of the same CdZnTe detector measured using a VAS_UMv2.3/TAT4 ASIC. The resolution is better because the amplitude is sampled multiple times, reducing measurement uncertainty. Also, filters that are less sensitive to the rising edge of the anode pulse waveform may be used to determine the signal amplitude, improving the energy resolution.

2.1.2 Multiple-Pixel Events Reconstruction

Multiple anode channels can be triggered due to the interaction of a single photon. If a photon is photoelectrically absorbed near a pixel boundary, but the electron cloud formed from the initial photoelectron extends beyond the pixel boundary so that two pixels collect charge, both channels will trigger. These are known as charge-sharing events. An incident photon can Compton scatter under one anode pixel and then, be photoelectrically absorbed under another anode pixel. These are true multiple-interaction-site events. Alternatively, a photon could undergo pair production and the resulting annihilation photons could be captured underneath another anode pixel.

Fig. 2.8 shows pulse waveforms for a multiple-interaction-site two-pixel event. To calculate the depth-corrected total energy deposited in this event, the depth of
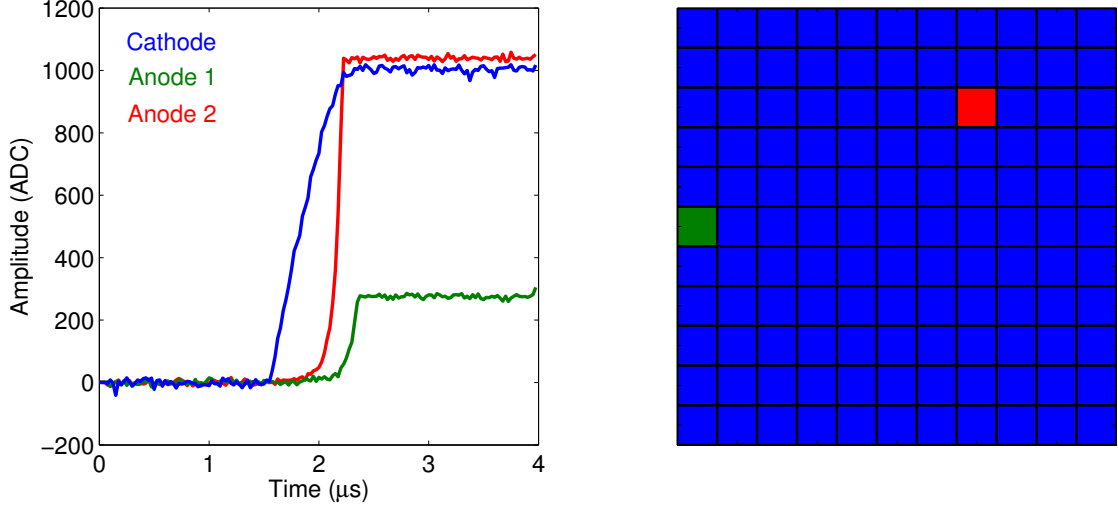
Figure 2.8: Pulse waveforms for a two-pixel, non-side-neighbor event (left). The corresponding collecting pixels for the event are shown on the pixelated anode (right).

each interaction must be determined. For multiple-pixel events, the timing differ-
ence between the initial cathode signal induction and anode waveform rise is used
to calculate depth. A CR-$(RC)^4$ filter with a short shaping time (100 ns for anode
channels and 250 ns for the cathode) is applied to the waveforms to calculate the
depth-from-timing. The point where the filtered signal exceeds 50% of the maximum
is set as the start time. Fig. 2.9 shows how the timing is calculated for single-pixel
events occurring at different depths.

The CAR is linear with true interaction depth [63, 64], so by relating the depth-
from-timing to the CAR using single-pixel events, the uncertainty in depth-from-
timing can also approach 300 μm. Once the depth-of-interaction for each interaction
site is calculated, the energy can be corrected based on the single-pixel correction
photopeak calibration factor.

Multiple-pixel events require another set of calibrations and corrections due to
weighting potential crosstalk (WPCT). WPCT results when multiple charge clouds
move simultaneously in the device. Fig. 2.10 shows the weighting potential curves
to illustrate WPCT. One curve shows the collecting pixel weighting potential for a
charge drifting in the center of the detector whereas the other shows the weighting
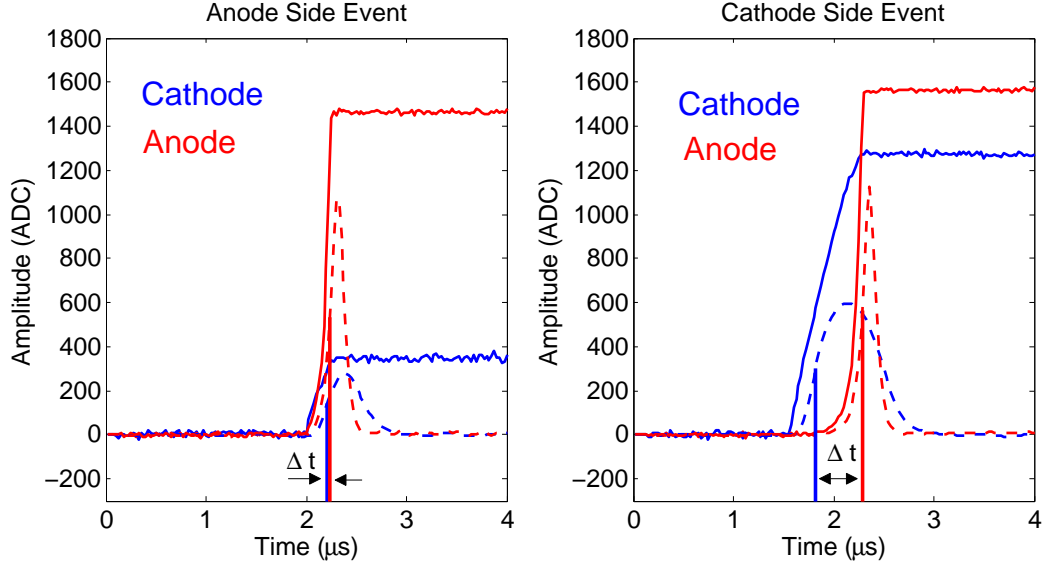
Figure 2.9: Pulse waveforms (solid lines) and filtered waveforms for timing calculation (dashed lines). The resulting timing information is shown for an anode-side event (left) and cathode-side event (right) by the vertical lines.

potential for the same event induced on the side-neighbor pixel.

Consider a -2 fC charge generated 5 mm from the anode which, under an electric field, drifts towards the collecting anode pixel. Using the Shockley-Ramo Theorem (see Sect. 1.2.1), this moving charge will induce a charge of $-q[1 - \phi_0(5 \text{ mm})]$ on the electrode after being fully collected if there is no electron trapping. For the detector geometry used in this thesis, this results in an induced charge of 1.97 fC. By knowing the interaction depth, the induced charge can be corrected to the full 2 fC.

Now consider that -2 fC charge is distributed in two charges. One -1 fC charge is located at (10,10,5) mm and another -1 fC charge is at (8.75,10,5) mm. Both charges drift to the anode due to the electric field. If the response was proportional, one would expect the charge at (10,10,5) mm to induce 0.987 fC, half the charge induced from the -2 fC initial charge. However, one has to consider the effect of the second moving charge. Eq. 2.2 gives the entire statement for the charge induced on the
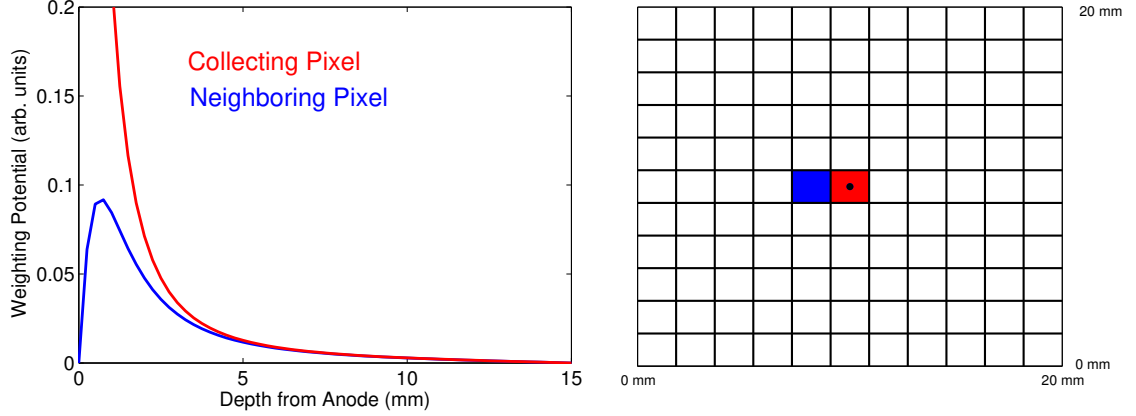
Figure 2.10: Weighting potential for the center pixel in the anode pixel array and a side-neighbor pixel for the straight-line path from the cathode to the anode pixel at an (x,y) interaction position of (10,10) mm. For the collecting pixel, the weighting potential continues to rise to a value of one at 0 mm. The right pane illustrates the pixels read out in red and blue and the photon interaction location as a black circle.

center pixel for the two moving charges using the notation from Eq. 1.5.

$$\Delta Q = -q_1[\phi_{0\,\text{collecting}}(\vec{x_f}) - \phi_{0\,\text{collecting}}(\vec{x_i})] + -q_2[\phi_{0\,\text{non-coll}}(\vec{x_f}) - \phi_{0\,\text{non-coll}}(\vec{x_i})] \quad (2.2)$$

$$\Delta Q = (1\text{ fC})[1 - \phi_{0\,\text{collecting}}(5\text{ mm})] + (1\text{ fC})[0 - \phi_{0\,\text{non-coll}}(5\text{ mm})] \quad (2.3)$$

Using the non-collecting pixel and the collecting pixel weighting potential, Eq. 2.3 results in an induced charge of 0.976 fC, lower than expected, due to the movement of the charge collected by the neighboring pixel. This whole effect is known as WPCT. It is corrected by creating a look-up table based on the centroid depth of the two interactions and the distance between the triggered pixels for a large ^{137}Cs calibration data set. The centroid depth is the energy-weighted average depth of the two interactions. The photopeak centroid for each triggered pixel separation and depth-centroid is used to correct the centroid back to the known gamma-ray energy of 661.7 keV. This can improve the energy resolution of two-pixel events by up to 0.5% FWHM at 662 keV.

Transient signals (an example of which is shown in Fig. 2.11) can disturb the
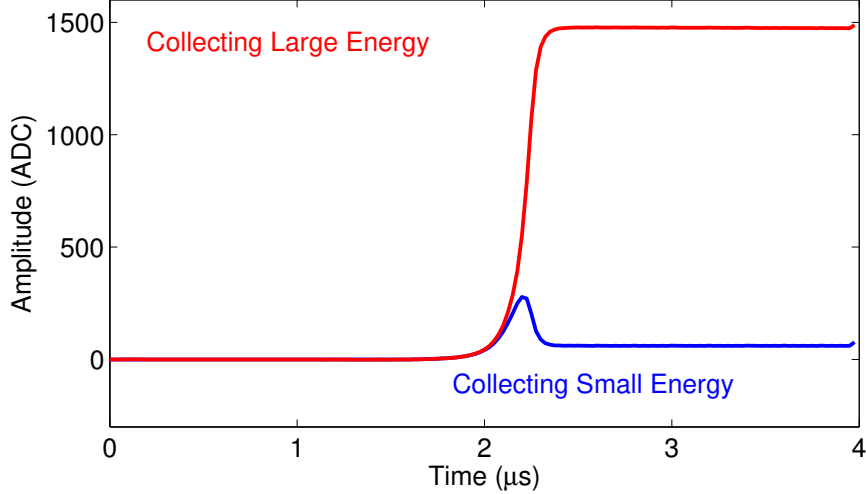
Figure 2.11: Example two-pixel side-neighbor event with high energy ratio and significant transient signal. The waveform which collects the "small" amount of charge does collect about 25 keV equivalent charge.

calculation of signal amplitude and timing using the implemented digital filters. As the energy ratio, a description of how the charge is shared for side-neighbor events expressed in Eq. 2.4, and the calculated depth-difference between the interaction sites change, the effect of transient signal induction varies. The energy ratio is the difference between the larger energy deposition, E_{large}, and the smaller energy deposition, E_{small}, divided by their sum. Events which share charge equally will have an energy ratio near zero whereas interactions with unequally shared charge will have an energy ratio which approaches one.

$$E_{ratio} = \frac{E_{large} - E_{small}}{E_{large} + E_{small}} \tag{2.4}$$

Another look-up table is formed by noting the photopeak centroid location for depth-corrected and WPCT-corrected 662 keV photopeak data as a function of the depth-difference between interaction sites and the energy ratio. Small differences between the expected photopeak centroid and recorded photopeak centroid can be corrected using the look-up table. This is known as the energy ratio correction. The resolution for two-pixel side-neighbor events may improve by 0.1% at 662 keV

using this correction. The energy ratio correction is applied to only side-neighbor events whereas the WPCT correction is used for non-neighboring and neighboring interactions.

For events which trigger more than two pixels, the same look-up tables are used to correct the WPCT and transient signal effect for each event pair after determining depth from drift time and correcting for the interaction depth. The energy resolution improvement for three-pixel and four-pixel events with these corrections can be quite substantial, as much as 0.8% FWHM at 662 keV for four-pixel events.

2.2 Sub-pixel Position Sensing

Thus far, non-collecting pixel effects have been discussed somewhat negatively. Weighting potential interference from non-collecting pixels have required corrections to reduce the influence of WPCT and transient signals. However, non-collecting pixels contain information about the sub-pixel interaction position of the photon. Fig. 2.12 shows the weighting potential for the non-collecting anode pixel (shown as the solid black pixel) for five interaction positions. The pixel collecting the charge is the pixel immediately to the left of the solid black pixel. The closer the interaction is to the neighbor pixel, the higher the transient signal induced on the non-collecting pixel.

In order to calculate the sub-pixel interaction position of the gamma ray for the inner 9×9 anode pixels, the opposing-neighbor ratio is calculated. The amplitude of the transient signal in each of the eight neighbors is calculated as the maximum value of the shaped signal using a CR-RC shaper with 100 ns shaping time. Fig. 2.13 provides an example of the signal induced on neighbor pixels for a single-pixel 662 keV photopeak energy deposition near the cathode in same collecting pixel shown in Fig. 2.12. To estimate the x sub-pixel position, the maximum shaped amplitude in each neighbor pixel is used to calculate the opposing-neighbor ratio given in Eq. 2.5
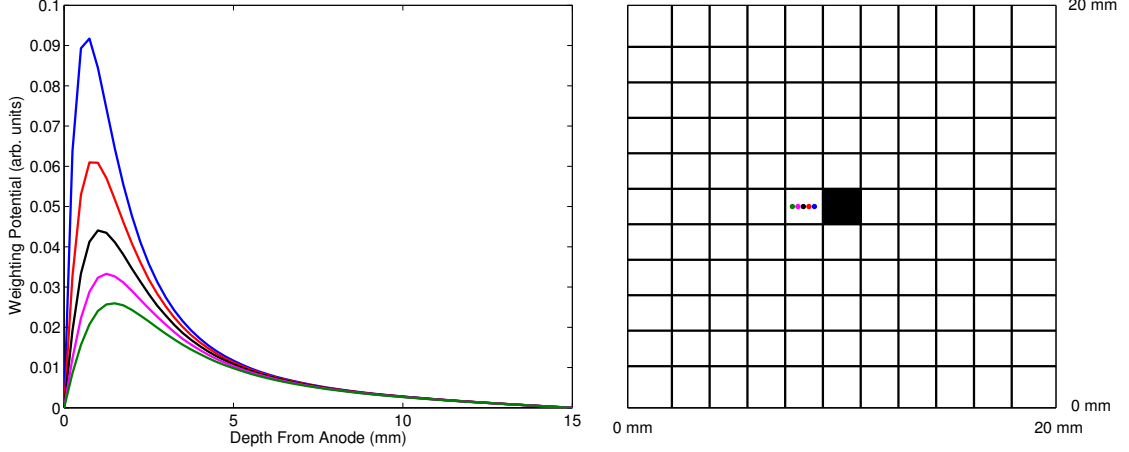
Figure 2.12: Weighting potential for straight-line paths from the cathode to the anode for the non-collecting pixel (shown as the black square on the right) for five (x,y) interaction positions illustrated in the pixel map on the right.

$$R_{ONR}(x) = \frac{S_R - S_L}{S_R + S_L} = \frac{(S_{13} + S_{23} + S_{33}) - (S_{11} + S_{21} + S_{31})}{(S_{13} + S_{23} + S_{33}) + (S_{11} + S_{21} + S_{31})} \qquad (2.5)$$

S is the shaped signal amplitude in the pixel location indicated in Fig. 2.13. S_R is the sum shaped amplitude of neighbor pixels in the right column of Fig. 2.13 whereas S_L is the left column sum. The opposing-neighbor ratio is a linear function of sub-pixel interaction position [66]. The maximum and minimum ratio is calculated for each detector at 662 keV in order to calibrate the ratio to interaction position. The maximum and minimum ratios correspond to the pixel pad edges. The same procedure is used to calculate the y sub-pixel location only using the shaped neighbor amplitude sum of the top and bottom rows as given in Eq. 2.6.

$$R_{ONR}(y) = \frac{S_T - S_B}{S_T + S_B} = \frac{(S_{11} + S_{12} + S_{13}) - (S_{31} + S_{32} + S_{33})}{(S_{11} + S_{12} + S_{13}) + (S_{31} + S_{32} + S_{33})} \qquad (2.6)$$

Fig. 2.14 shows the neighbor pulse waveforms and the reconstructed sub-pixel interaction position using the opposing-neighbor ratio for a single-pixel 662 keV photopeak event. The amplitude induced on the right neighbors is significantly greater than the signal on the left neighbor pixels. Thus, the x interaction position is on
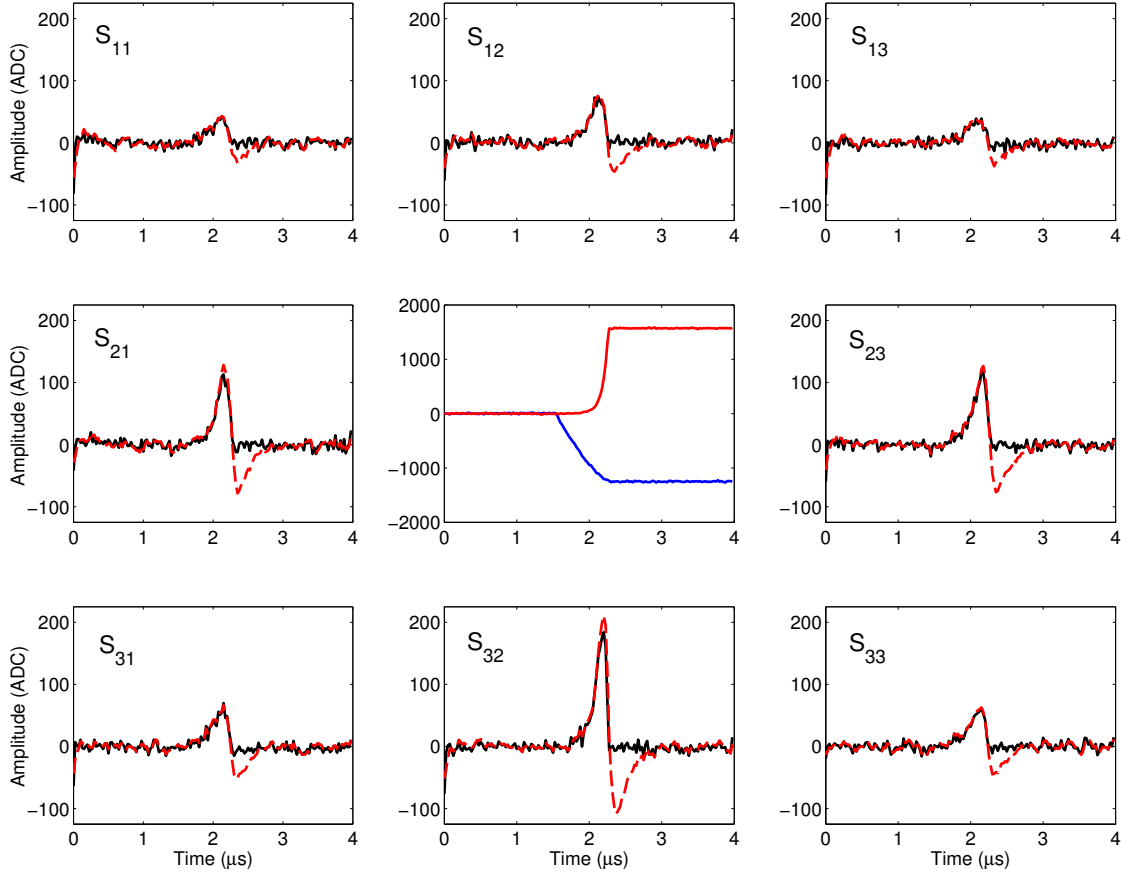
Figure 2.13: Neighbor waveforms for a 662 keV photopeak energy deposition near the cathode side in the same collecting pixel as shown in Fig. 2.12. The eight neighbor locations are labeled (S_{11}, etc.). The shaped signal is shown in red whereas the recorded waveform is in black. The center pane shows the collecting anode (red) and cathode (blue) pulse waveforms.

the right boundary of the pixel. Since the neighbor amplitude induced on the top and bottom rows are similar, the y interaction location is in the center portion of the pixel. The color surrounding the reconstructed location represents the position uncertainty which is about 300 μm for 662 keV energy depositions and 700 μm for 122 keV depositions measured using a slit collimator. The position resolution degrades at lower photon energies due to smaller induced signals on neighboring pixels, hindering the ability to accurately measure the amplitude in the presence of electronic noise. At higher photon energies, above 700 keV, the position resolution degrades due to the larger electron cloud.
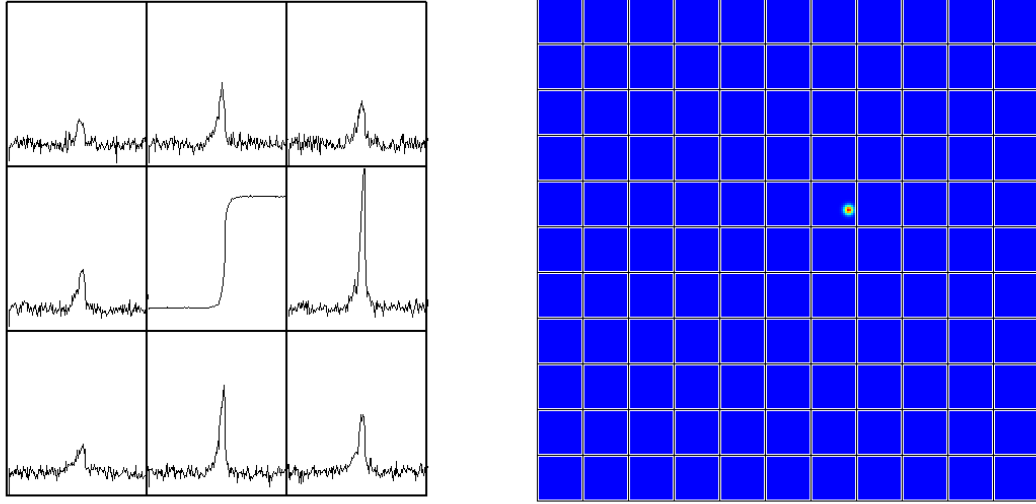
Figure 2.14: Sub-pixel position reconstruction for a single-pixel event 662 keV photo-peak event. The triggered pixel and eight neighbors (left) and reconstructed position in the 11×11 pixel array (right) are shown.

Determining the sub-pixel interaction position for edge-pixel events is more challenging because there is not an opposing neighbor to compare. The neighbor-to-center ratio compares the side-neighbor pixel amplitude to the collecting pixel amplitude to estimate the sub-pixel interaction position [66]. This achieves adequate performance, but the ratio as a function of sub-pixel position varies from the corner pixel to the center edge pixel. Furthermore, the relationship is not linear resulting in additional position uncertainty for events near the guard ring.

To solve this issue, the guard ring-to-neighbor ratio was developed. The guard ring signal read out by VAD_UMv1.2 ASICs is not overly distorted by electronic noise so its amplitude can be measured with high fidelity. The guard ring-to-neighbor ratio is calculated in Eq. 2.7 where the locations of S are given in Fig. 2.15 and G is the signal induced on the guard ring. The ratio is linear with respect to sub-pixel interaction location for edge pixels excluding the corner pixel as shown in Fig. 2.15.

$$R(x) = \frac{G - (S_1 + S_2 + S_3)}{G + (S_1 + S_2 + S_3)} \tag{2.7}$$

37
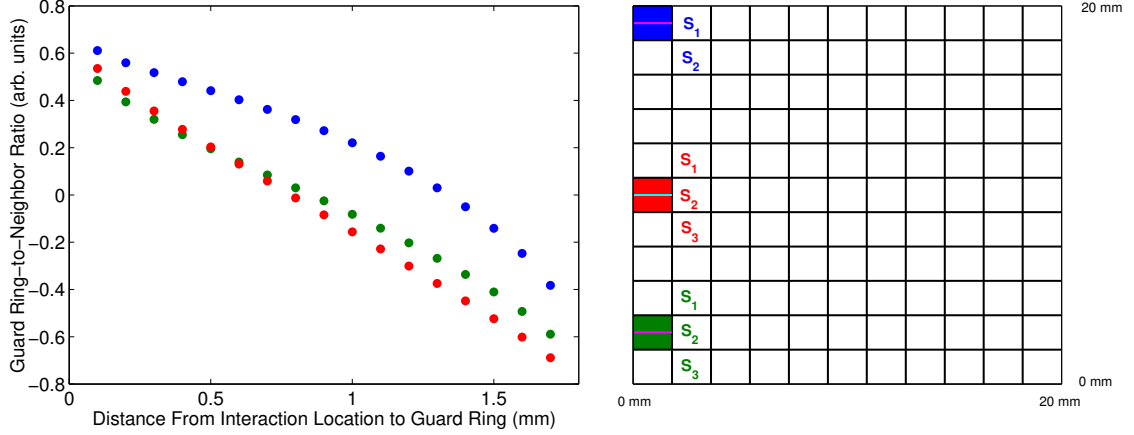
Figure 2.15: Sub-pixel position reconstruction technique for edge pixel events occurring near the cathode side. The edge pixel location is shown in the right window using different colors for different collecting pixels (solid squares). The read out pixels used to calculate the ratio are labeled S_1, S_2, S_3 with color corresponding to the collecting pixel. The magenta or cyan lines in each collecting pixel show the simulated interaction locations used to generate the left plot.
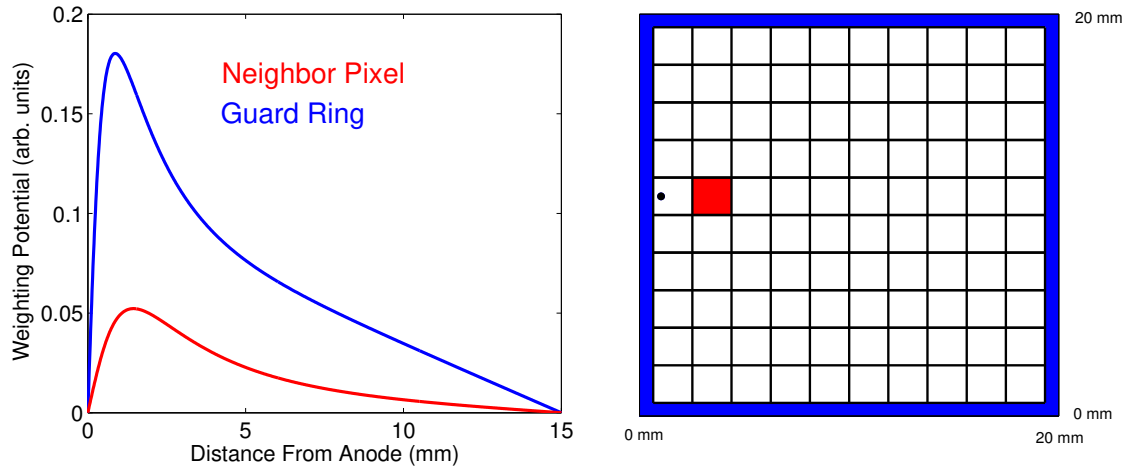
Figure 2.16: Weighting potential as a function of depth for the side-neighbor pixel and guard ring for a charge collected by an edge pixel 0.5 mm from the guard ring (left). Illustration of the electrodes read out and photon interaction position in black (right).

The guard ring signal is more sensitive to depth than neighbor pixel signals as the guard ring weighting potential increases linearly throughout the bulk as shown in Fig. 2.16. However, the depth-of-interaction can be calculated using the CAR or timing to correct the bulk guard ring rise.

A coded aperture mask with element pitch smaller than the pixel pitch, can
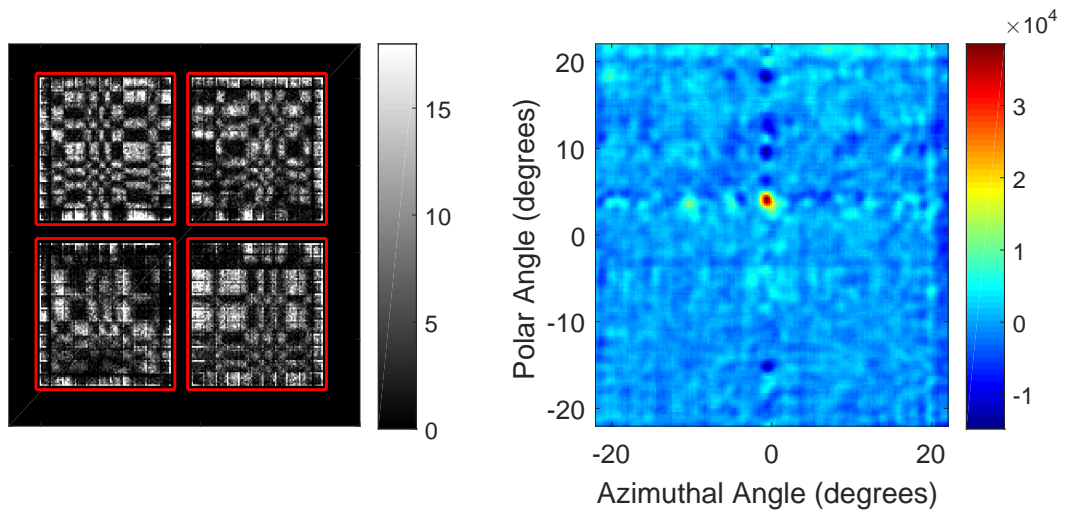
Figure 2.17: The recorded interaction location of 122 keV photons from a 80 μCi ^{57}Co point source in the far field using a 2×2 prototype digital ASIC array (right). Reconstructed image of the measurement (left). The spacing between elements in the coded aperture mask was 0.86 mm. The measurement duration was 30 minutes.

demonstrate the position resolution of sub-pixel reconstruction techniques. Coded aperture imaging, like pinhole imaging, requires knowledge of photon interaction locations and a modulating mask [68, 69, 70]. High-resolution sub-pixel position sensing is required to reconstruct images from small-element masks.

The opposing-neighbor ratio for inner 9×9 pixels and the neighbor-to-center ratio for edge pixels were used to estimate the sub-pixel photon interaction position with a coded aperture mask present. A tungsten mask with 0.86 mm between mask elements was designed for the 2×2 prototype digital ASIC array system. As shown in Fig. 2.17, a ^{57}Co source was imaged clearly. The resolution of the image was 1.3° FWHM in the polar and azimuthal directions. The signal-to-noise ratio (SNR) was 18.2 measured using the measurement method proposed by Joshi [69]. The average intensity in the active detector area was placed in the gap between detectors during reconstruction to reduce artifacts. The remaining artifacts in the image are from improperly corrected gaps between detectors, small gaps between pixels, and poorer sub-pixel position resolution for edge pixels which results in high intensity in the last position bin

near the detector edge in the interaction map. A size mismatch between the mask dimension and magnified pattern on the detector may also cause artifacts in the image.

Coded aperture imaging resolution depends on the mask element pitch, so sub-pixel position sensing results in improved coded aperture angular resolution. Also, Compton-imaging angular resolution is improved due to reduced position uncertainty [71]. Processing neighbor waveforms also improves understanding of detector physics as explored in Sect. 2.4.2.

2.3 System Response Function Fitting

All of the corrections discussed thus far (depth-of-interaction, WPCT, minimum energy, depth-from-timing, and sub-pixel position sensing, albeit with poorer performance) can be applied to analog ASIC systems. The only difference thus far is that the initial information is calculated using digital filters. However, Zhu developed a method to use the entire pulse waveform to estimate the interaction position and energy [66]. Using the aggregate information contained in pulse waveforms from the cathode, collecting pixels, and non-collecting pixels allows additional corrections for multiple-pixel events as well.

The system response function (SRF) is calculated empirically. The goal is to calculate the average pulse waveform for an energy deposition in each detector voxel. A ^{137}Cs measurement with more than a million single-pixel 662 keV photopeak events is used to generate the SRF. First, a simple subtraction is used to determine the cathode and anode cutoffs, like the first calibration step discussed in Sect. 2.1.1. Then, the average photopeak waveform in each channel and depth bin (calculated using the CAR from Eq. 2.1) is determined. Fig. 2.18 shows some example SRF waveforms at various depths for the center pixel and a corner pixel. The corner pixel SRF waveforms appear considerably different than those of the center pixel because
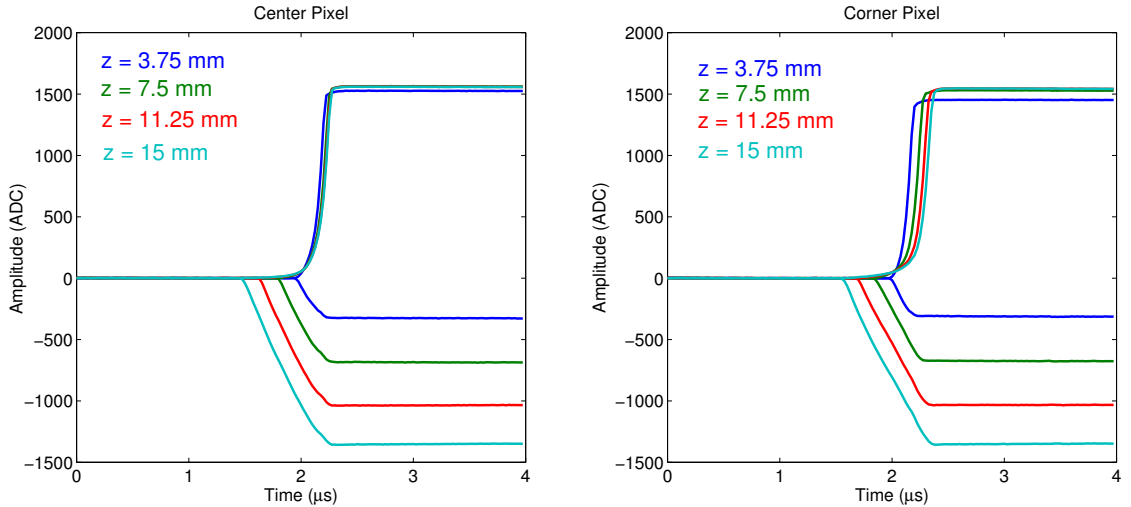
Figure 2.18: Example system response function waveforms for 662 keV single-pixel photopeak events at various depths from the anode pixel array for the center pixel (left) and a corner pixel (right).

the weighting potential is affected by its proximity to the guard ring.

Once the SRF is calculated for each voxel, individual waveforms can be fit to the SRF to estimate the energy and depth of each gamma-ray interaction. A Levenberg-Marquardt iterative algorithm is used to fit the anode and cathode waveforms to the SRF. Three fitting parameters are updated iteratively: the energy deposited (basically the scaled SRF amplitude), the depth-of-interaction, and a time-shift parameter to align the waveforms. For multiple-pixel events, the energy deposited, depth-of-interaction, and time-shift are calculated for every triggered pixel. Fig. 2.19 shows an example two-pixel non-side-neighbor event fit using the system response function. The interaction shown in the red edge pixel is reconstructed to have occurred at a depth of 10.1 mm from the anode and deposited 179 keV whereas the interaction in the green pixel deposited 403 keV, 4.7 mm from the anode.

In general, the single-pixel energy resolution performance using the SRF matches the resolution achieved using digital filters. However, multiple-pixel events tend to demonstrate energy resolution improvement as shown in Table 2.1. This is due to better depth reconstruction and less sensitivity to transient signals. The depth re-
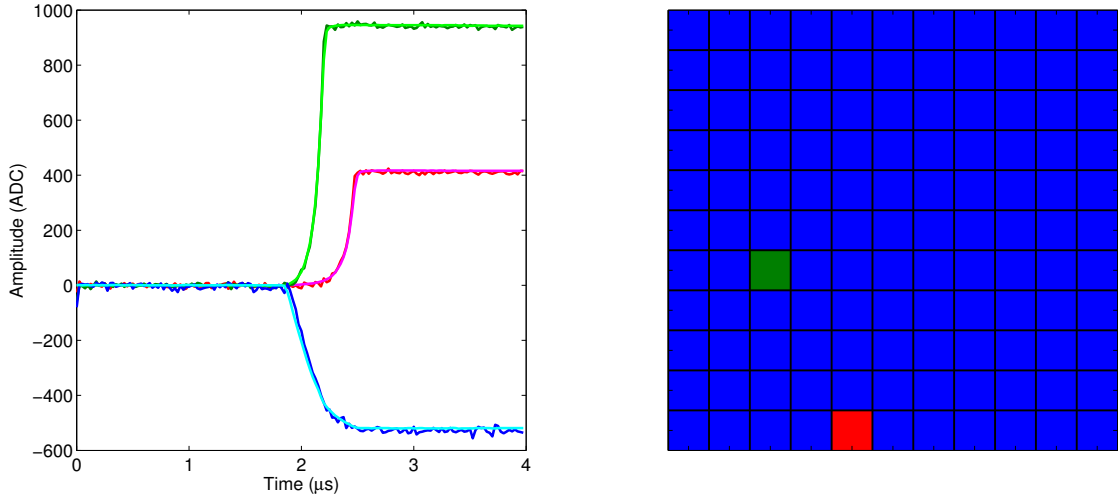
Figure 2.19: Example two-pixel non-side-neighbor event fit using the system response function (left). The light green, cyan, and magenta lines fit the recorded pulse waveforms. The cathode pulse waveform is shown in blue. The pixel map shows the collecting pixel locations (right).

construction is improved by ensuring the estimated energies and depths match the anode and cathode pulse waveform amplitudes in addition to matching the timing characteristics.

A system response function can be generated for neighbor waveforms as well. The sub-pixel interaction position is estimated using the described filter-based techniques. The average neighbor waveform at each interaction depth and sub-pixel location is then calculated. These average waveforms can be used to fit recorded data to estimate the sub-pixel interaction location. This has not significantly improved the sub-pixel position resolution, however, and requires more processing time, so filters are still generally used to reconstruct the sub-pixel position.

Several algorithms have been developed which use the pulse waveforms to correct some specific challenging events including charge leak and transient signal interference.

Table 2.1: Measured energy resolution at 662 keV for detector 5R-64 by number of pixels triggered and reconstruction method.

N Pixels Triggered	Trapezoidal Filter Reconstruction Resolution (%FWHM)	SRF Reconstruction Resolution (%FWHM)
1	0.45	0.45
2	0.86	0.76
3	1.27	1.07
4	1.77	1.34

2.3.1 Charge Leak Corrections

Charge leak is a phenomenon where the entire electron cloud is not collected by the collecting pixel. Some charge "leaks" to the gap between pixels or the neighbor pixel. These events do not significantly degrade the FWHM energy resolution, but do add to a low-energy photopeak tail. To correct these events, the mean tail amplitude of the neighbor waveforms is calculated. If the measured amplitude of one neighbor pixel exceeds a user determined threshold, the additional charge collected by the neighbor pixel is added to the triggered pixel's amplitude.

Fig. 2.20 shows an example event corrected using this method. Note that the tail amplitude of the left-side-neighbor pixel significantly exceeds the average tail amplitude. The amplitude difference between the mean neighbor waveform and the pixel collecting a small amount of charge is added to the triggered pixel's signal amplitude. In this example, the estimated energy of the interaction increases by 10.5 keV when the leaked charge is included.

Charge leak is related to the software threshold. If the software trigger threshold is too low, charge leak events may be promoted to multiple-pixel events. The charge leak threshold and software trigger threshold must be optimized for the user's application.
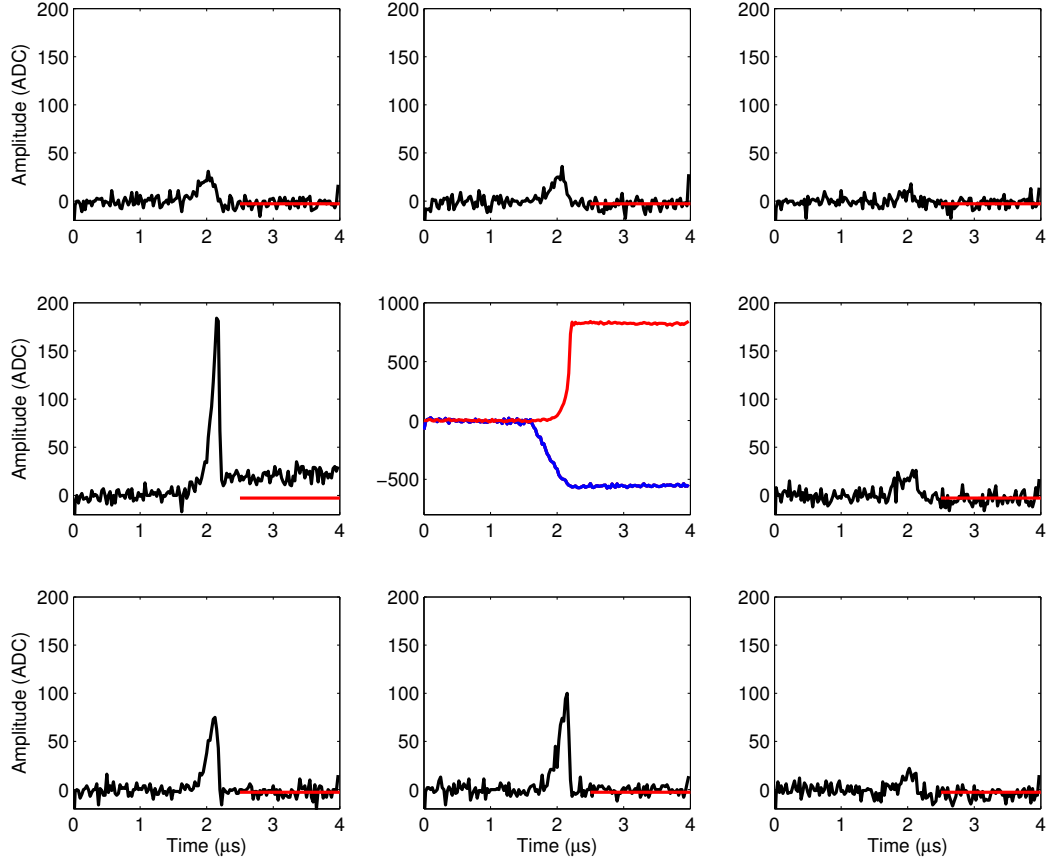
Figure 2.20: Pulse waveforms for triggered pixel (center) and eight neighbors for an event exhibiting charge leak. The mean tail amplitude of the neighbor signals is shown with a horizontal red line.

Fig. 2.21 shows the photopeak shape improvement with the charge leak correction for a system with a low-energy threshold of 15 keV. The low-energy tail to the left of the photopeak is less intense, and the photopeak shape is more Gaussian.

2.3.2 Crosstalk Suppression

Two-pixel side-neighbor events are most affected by weighting-potential crosstalk and transient signal induction on the pixel collecting the smaller amount of charge. Fig. 2.22 shows a two-pixel side-neighbor event with crosstalk and the algorithm to try to remove the influence of the transient signal.

The signals induced on the non-collecting side-neighboring pixels of the pixel that collects the majority of the charge are used to estimate the transient signal amplitude.
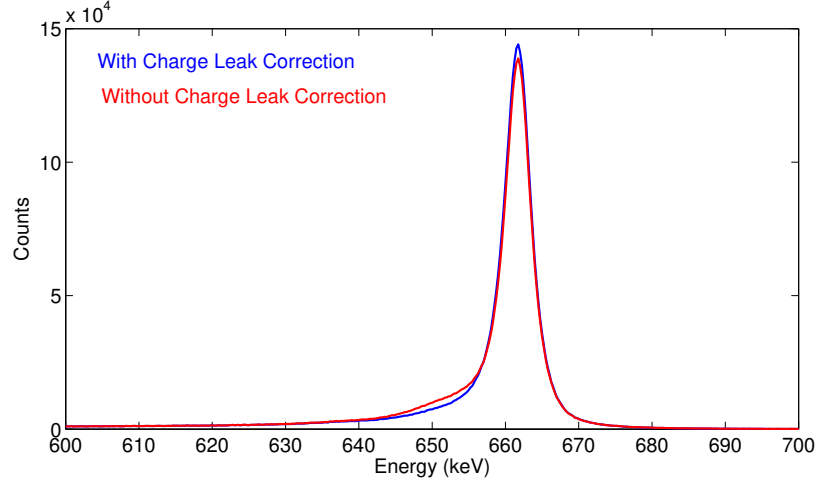
Figure 2.21: Measured all-events ^{137}Cs spectrum with and without charge leak correction. With the charge leak correction, the full width at tenth maximum (FWTM) of the 662 keV photopeak improves from 1.99% to 1.75%.
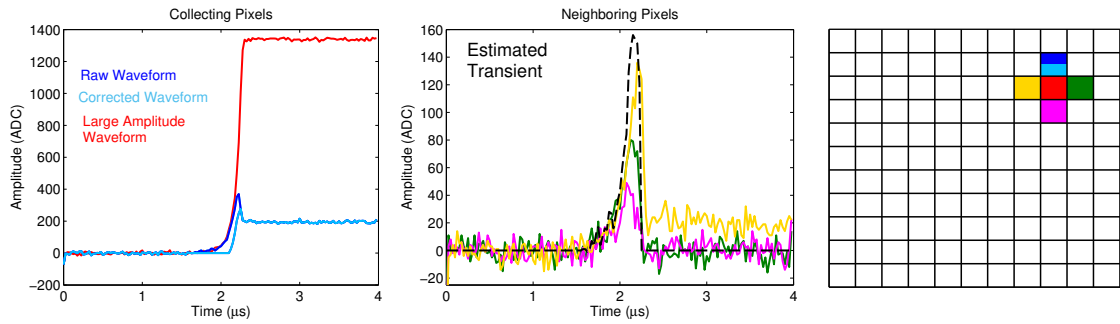
Figure 2.22: Pulse waveforms induced on collecting pixels illustrating crosstalk suppression algorithm (left). Neighbor waveforms used to estimate transient signal (center). Locations of the collecting and neighboring pixels (right).

These pixels are shown in Fig. 2.22 as the yellow, green, and magenta pixels and waveforms. Interestingly, in this event, it appears some charge has leaked to the yellow pixel as well, but the threshold to apply the charge leak correction was not surpassed. The farthest pixel from the side-neighbor interaction location (shown in magenta in Fig. 2.22) is subtracted from the sum of the other side neighbors (shown in green and yellow) to estimate the transient signal pulse waveform for the triggered pixel collecting less charge. A moving average filter is applied to smooth the estimated transient which is multiplied by the energy ratio from Eq. 2.4 and subtracted from the waveform of the pixel collecting less charge. The difference between the blue and

cyan pulse waveforms in the left pane of Fig. 2.22 shows how this correction influences the pulse waveform to be fit using the SRF.

This process makes detecting the signal amplitude using the SRF simpler, but investigation into the accuracy of depth reconstruction using this correction is ongoing. In the future, more study should be dedicated to this topic to see if the neighbor SRF can be used to predict the transient accurately, especially for charge clouds separated in depth.

2.4 Improved Understanding of CdZnTe Detector Physics Using Digital Pulse Processing

Pulse waveforms provide the maximum amount of information about charge drift and radiation interactions in a detector. In addition to using the pulse waveforms to develop correction algorithms, detector physics problems in two areas were studied: space charge which can cause "pixel-jumping", where the charge carriers generated from a photon interaction are not collected by the pixel they were generated under, and non-uniform electric fields.

2.4.1 Pixel-Jumping Effects

While CdZnTe manufacturers have solved this problem for the most part, historically, some detectors were delivered with significant areas of space charge. This sometimes led to pixel-jumping [69]. One such detector, 4R-208 was delivered by Redlen Technologies in 2014. Fig. 2.23 shows the number of photopeak count as a function of depth for each anode pixel. Note that in the lower left-hand corner, there is an area (highlighted in red) which showed fewer photopeak counts near the cathode side. Several of the nearby pixels appeared to show an increase in photopeak counts in the center of the detector. One hypothesis to explain this observation was that
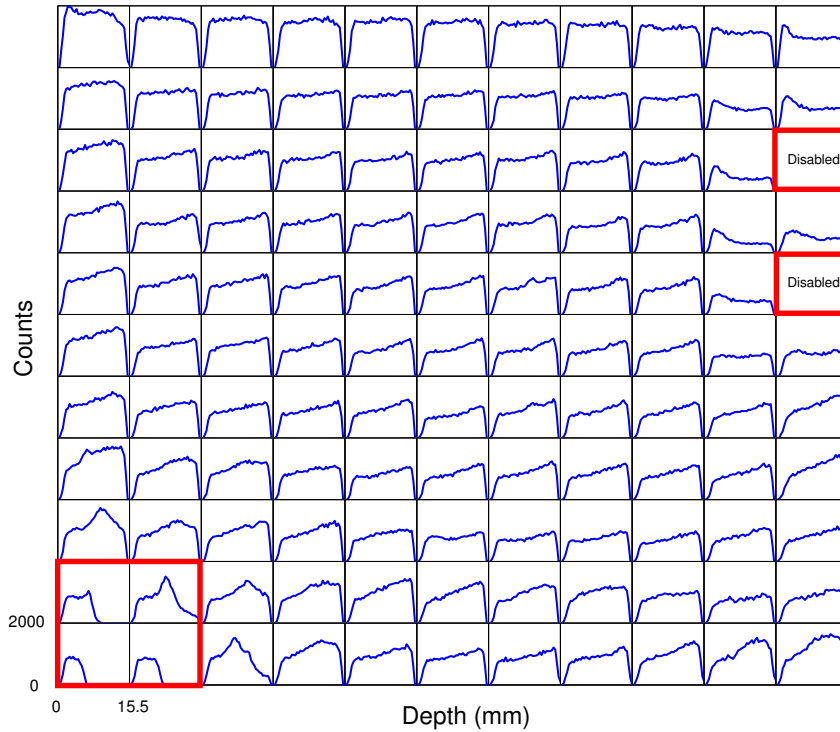
Figure 2.23: Single-pixel photopeak counts as a function of depth for detector 4R-208. Two pixels on the right side were disabled. The unusual performance area is highlighted with a red square in the bottom left-hand corner.

space charge alters the electrons' trajectory so that a neighboring pixel collects the charge, rather than collection by the pixel underneath the interaction.

Fig. 2.24 shows the results of an experiment used to validate this hypothesis. A ^{137}Cs source was collimated to a thin slit and the interaction locations of single-pixel 662 keV photopeak depositions were recorded. The collimator was set up to maintain a straight line across a column of pixels. Near the top of the detector, the interaction locations are tightly packed along a line. Near the bottom however, the location distribution fans out. These interactions must have occurred along the line, but space charge deflected the electron trajectory so that they are not collected below the interaction location.

The number of pulse waveforms collected by the guard ring in this portion of the detector is also unusual. As shown in Fig. 2.25, the unbiased guard ring rarely collects charge in the upper left-hand corner of the detector. Only 5% of events occurring in
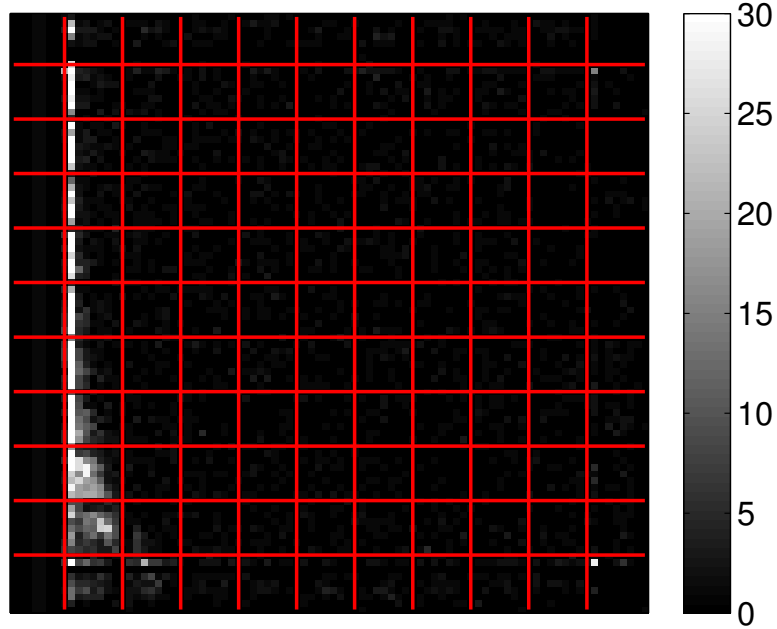
Figure 2.24: Single-pixel 662 keV photopeak interaction locations of a collimated ^{137}Cs measurement across detector 4R-208 using sub-pixel position sensing. Note that the line of high intensity is strong at the top of the detector but weakens and spreads near the bottom of the detector indicating pixel-jumping from space charge.
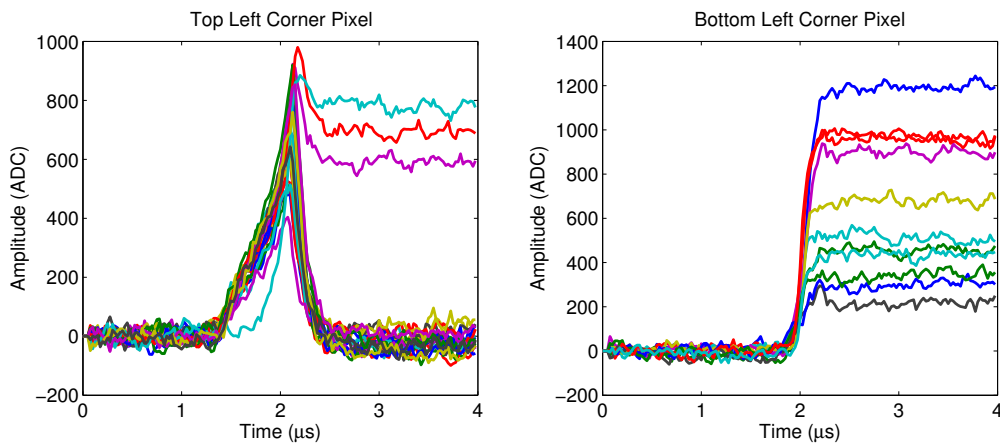
Figure 2.25: Pulse waveforms induced on the guard ring in detector 4R-208 for the top left corner pixel (left) and bottom left corner pixel (right). Note that the bottom left corner pixel has many more events collected by the unbiased guard ring. A ^{137}Cs source was used to generate the gamma-ray interactions.

the upper left-hand corner pixel result in charge collected by the guard ring. Yet in the lower left-hand corner, the guard ring collects some charge in more than 95% of interactions. The entirety of the evidence suggests that some material in this region

deflects charge and inhibits its direct, full collection by the pixel under the radiation interaction. This is an instance where pulse waveforms and sub-pixel sensing can provide a deeper understanding of charge drift and collection in CdZnTe detectors.

2.4.2 Non-Uniform Electric Fields

Koehler suggests that impurity space charge may also contribute to non-uniform electric fields in room-temperature semiconductor detectors [72]. Regardless of their cause, non-uniform electric fields exist in CdZnTe detectors. Koehler and Streicher showed that non-uniform electric fields affect $(\mu\tau)_e$ measurements [73]. Non-uniform electric fields may be observed as non-linear cathode pulse waveforms during electron drift. The electric field profile can be estimated by taking the derivative of the cathode pulse waveform which is proportional to the electron velocity. Assuming the electric field and electron mobility are proportional to electron velocity as given in Eq. 2.8, and the electron mobility is roughly constant, the electric field profile may be estimated by the cathode waveform derivative [3]. In Eq. 2.8, v is the electron drift velocity at any three-dimensional point in space, $\vec{x}$. Eq. 2.8 allows the electric field, $\vec{E}$, to vary spatially whereas the electron mobility, μ_e, is a constant scalar material parameter.

$$v(\vec{x}) = \mu_e \cdot \vec{E}(\vec{x}) \tag{2.8}$$

The SRF for seven simple-pixel $2 \times 2 \times 1.5$ cm^3 detectors delivered by Redlen Technologies, were generated and compared as shown in Fig. 2.26. The left pane in Fig. 2.26 shows the mean anode and cathode pulse waveforms for a 662 keV energy deposition near the cathode surface for the seven detectors tested. The cathode pulse waveform for detector 5R-27 is noticeably non-linear. This likely means the electric field is non-uniform. The mean anode waveforms also provide a wealth of information. Note that 5R-48, 5R-27, and 5R-62 turn much more slowly as the electrons are
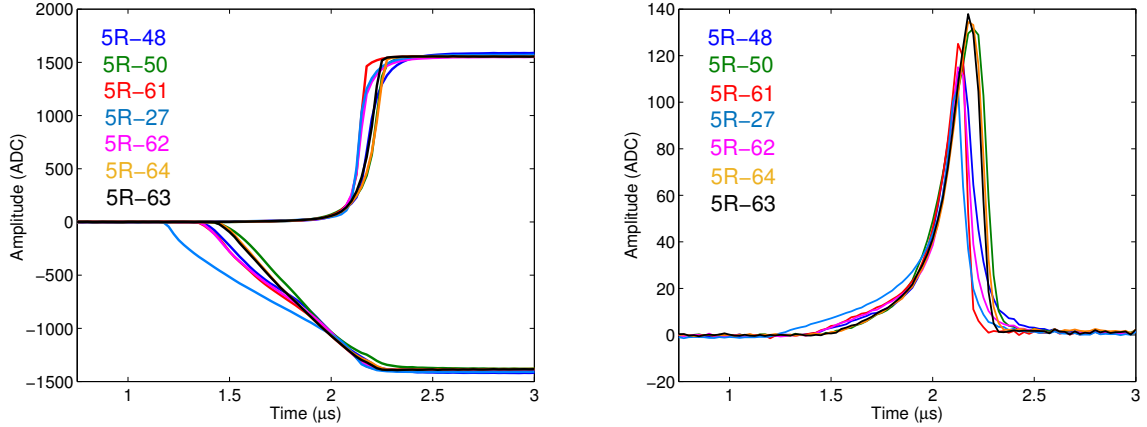
Figure 2.26: Average anode and cathode waveforms for a single-pixel 662 keV photo-peak interaction near the cathode in the center pixel of the array for seven detectors (left). The corresponding mean neighbor waveform for a side-neighbor pixel for a single-pixel 662 keV photopeak event in the center sub-pixel position bin near the cathode (right).

collected compared to the other detectors. This can indicate electrons are trapped and then de-trapped as they drift, effectively elongating the electron cloud.

The right pane of Fig. 2.26 shows the photopeak amplitude-adjusted pulse wave-forms induced on a side-neighbor pixel for an interaction in the center of an inner 7×7 pixel. The neighbor waveforms do not have the same amplitude nor the same shape. The amplitude of neighbor waveforms should be maximized to improve sub-pixel posi-tion resolution. Therefore, it is critical to understand what material properties affect the neighbor signal amplitude.

To determine what factors affect neighbor pulse waveform amplitude, correlations of three parameters were studied. First was the average drift time, the time between the start of cathode signal induction and when the collecting anode reaches 50% of its final amplitude. Second, was the amount of electron trapping/de-trapping, estimated by the time required for the anode pulse waveform to go from 50% of its amplitude to 98%, known as the "half-to-full" collection time. Finally, the maximum ampli-tude of the mean neighbor waveform was compared with the other parameters. Fig. 2.27 shows the results of these correlations for 662 keV photopeak interactions near
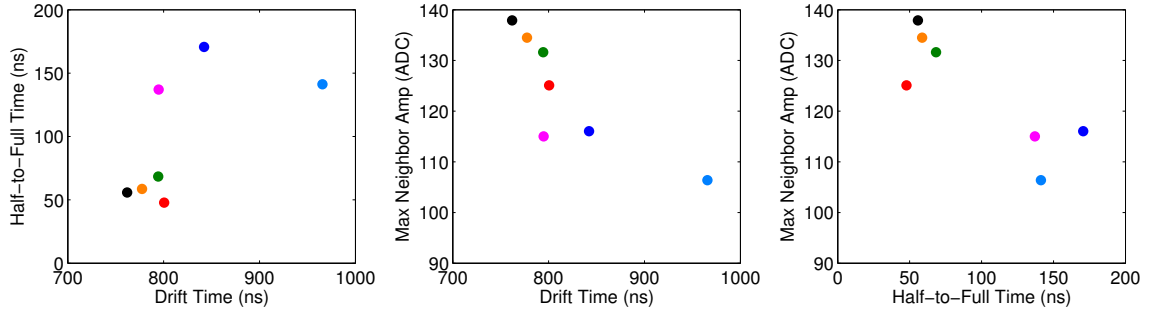
Figure 2.27: Correlations between waveform parameters for seven detectors for 662 keV single-pixel photopeak events close to the cathode surface. The color coordination is maintained from Fig. 2.26. The correlations presented are drift time versus the half-to-full collection time (left), the maximum neighbor amplitude versus the drift time (center), and the neighbor amplitude versus the half-to-full collection time (right).

the cathode. The strongest correlation is between the drift time and the maximum neighbor amplitude.

From the Shockley-Ramo Theorem, the drift time should not affect the neighbor amplitude. However, electron trapping/de-trapping may reduce the neighbor waveform amplitude as the weighting potential is traversed by different portions of the elongated electron cloud at different times. The amount of electron trapping/de-trapping will depend on the interaction location of the gamma ray assuming the trapping centers are uniformly distributed in depth. This appears to be the case as shown in Fig. 2.28 which shows the SRF waveforms for the same seven detectors for single-pixel 662 keV photopeak interactions 4.5 mm from the anode. Detectors which formerly showed slow turning during collection, such as 5R-27, 5R-48, and 5R-62, turn much faster, albeit still slower than the other detectors. The neighbor waveform amplitudes and shapes are much more similar for the seven detectors than they were for interactions near the cathode.

Fig. 2.29 shows that CdZnTe detectors with smaller neighbor waveform amplitudes for cathode-side events have reduced half-to-full collection times for events occurring near the anode. The vertical distance between the black line and the point demonstrates the relative reduction in trapping/de-trapping from shorter electron
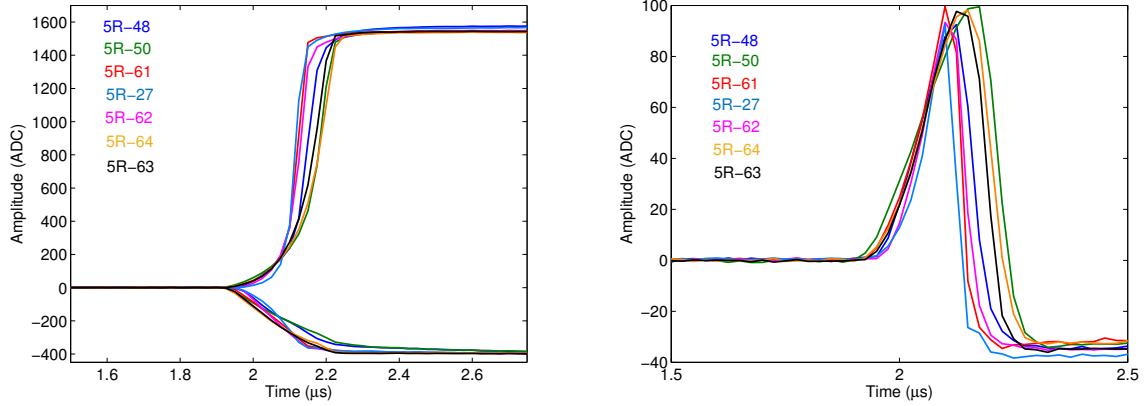
Figure 2.28: Average anode and cathode waveforms for a single-pixel 662 keV photopeak interaction 4.5 mm from the anode in the center pixel of the array for seven detectors (left). The corresponding mean neighbor waveform for a side-neighbor pixel for a 662 keV photopeak single-pixel interaction in the center sub-pixel position bin 4.5 mm from the anode surface (right).
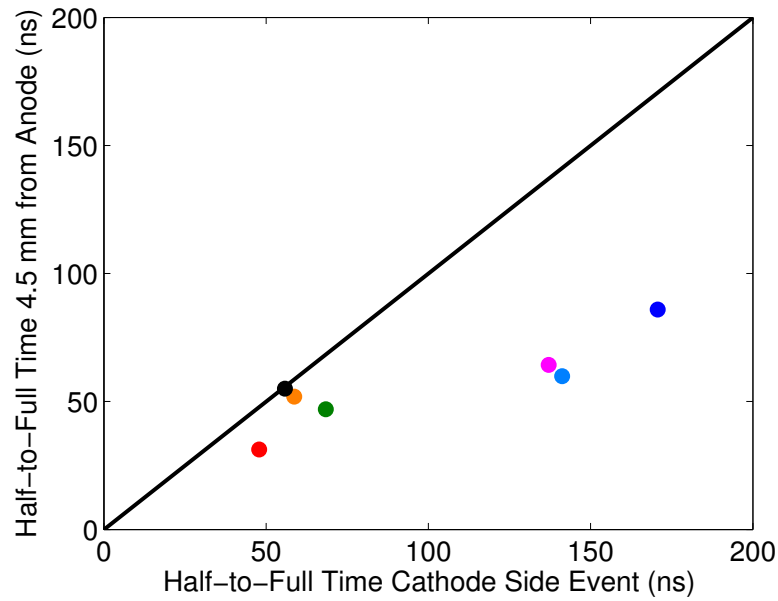
Figure 2.29: Comparison of half-to-full collection time for seven detectors for single-pixel 662 keV photopeak interactions near the cathode and 4.5 mm from the anode surface.

drift distance. This indicates trapping/de-trapping in the material influences neighbor pixel pulse waveform signal amplitude.

Fig. 2.30 shows the same correlations from Fig. 2.27 with the same scale when feasible, but for 662 keV photopeak events 4.5 mm from the anode pixel array. The
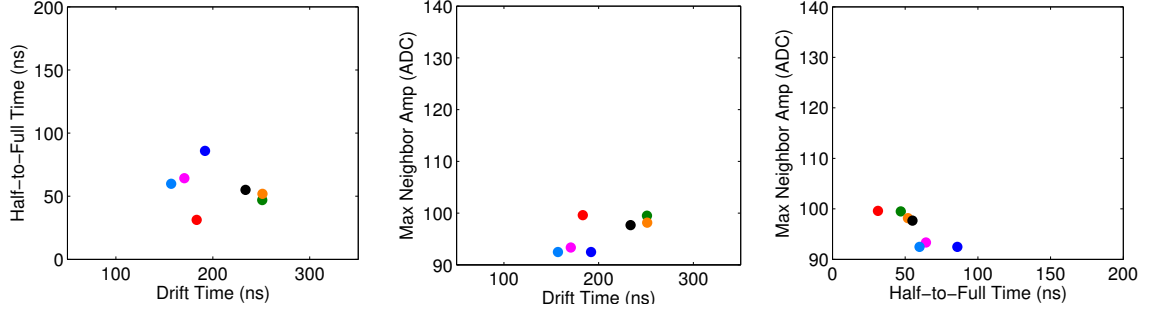
Figure 2.30: Same correlations between waveform parameters for seven detectors as shown in Fig. 2.27, but for single-pixel 662 keV photopeak events 4.5 mm from the anode.

results are bunched closer together, demonstrating electron drift plays an important role in the neighbor waveform amplitude and shape. Now the strongest correlation is between trapping/de-trapping (half-to-full collection time) and neighbor amplitude.

Another interesting observation is that detectors with the longest drift times from Fig. 2.27 (5R-27, 5R-48, 5R-61, and 5R-62) now have the shortest drift times. This is because the electric field is non-uniform in these detectors. Generally, the electric field is weak in the center of the detector and strong near the cathode and anode. Detectors that require a long drift time for cathode-side events have slow electron drift in the bulk and correspondingly fast drift near the anode leading to this phenomenon.

A non-uniform electric field can actually artificially elongate an electron cloud as the electrons nearer to the anode will travel faster than those farther from the anode, exacerbating trapping/de-trapping. A simulation was developed to validate this hypothesis. As shown in Fig. 2.31, the simulation allows the user to enter different electric field profiles, so long as the integral area is equal to 3000 V (the bias applied). The initial electron cloud profile is also entered by the user. For the results shown, the electron cloud was initially uniformly distributed over 600 μm with a centroid 9 mm from the anode for all four electric field profiles. The mobility was set to be 750 cm^2/Vs. As illustrated in the middle pane of Fig. 2.31, the collected electron cloud is elongated to more than 1 mm if the electric field is non-uniform.
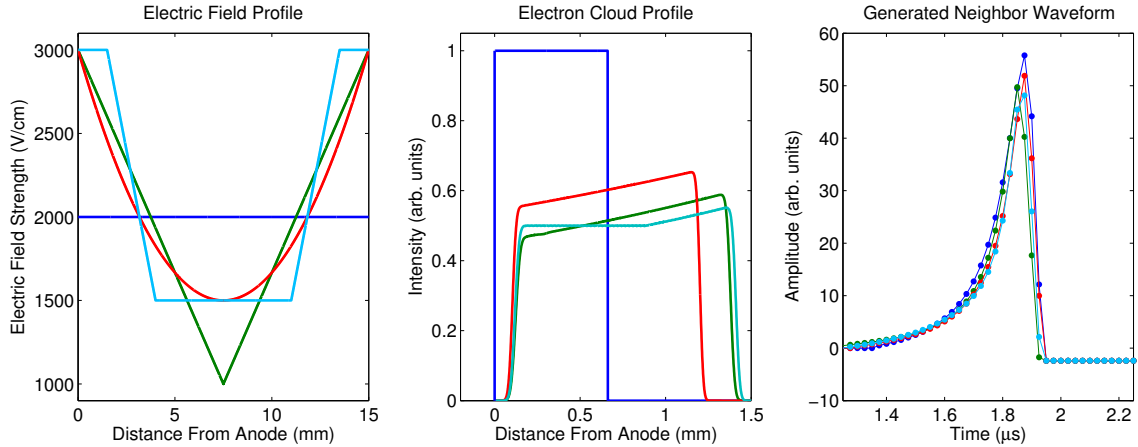
Figure 2.31: Simulated electric field profiles (left) and resulting electron cloud distribution at collection by anode (center). Generated neighbor waveforms for different electric field profiles with same initial electron distribution (right).

The corresponding neighbor waveform amplitude is reduced due to the elongated electron cloud from non-uniform fields. The amplitude deficit can be as large as 15%. Furthermore, since the charge is drifting much faster near the anode in detectors with non-uniform electric fields, the induced neighbor pulse waveform may be under-sampled increasing the uncertainty in the measured neighbor amplitude. In fact, the standard deviation of simulated sampled neighbor pulse waveform amplitudes in detectors with non-uniform electric fields is double the standard deviation of detectors with uniform fields due to under-sampling.

2.5   Recent Developments with Directly-coupled ASICs and CdZnTe Detectors

The best CdZnTe detectors are limited by electronic noise in terms of the energy resolution they can achieve. If the electronic noise is reduced, the energy resolution improves. The electronic noise of a bare (no detector attached) VAD_UMv1.2 ASIC is 1.4 keV. The noise is calculated by recording pulse waveforms in forced readout mode and calculating the amplitude using a simple subtraction filter that would
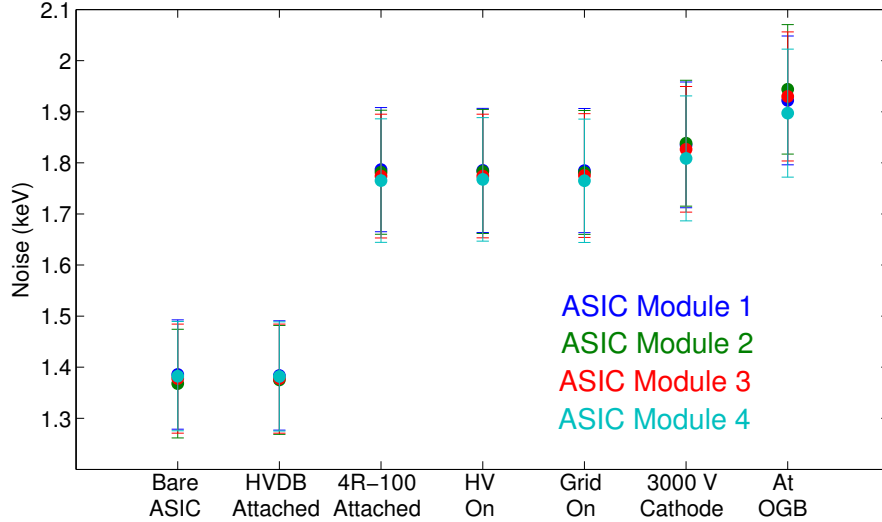
Figure 2.32: Measured electronic noise as a function of system configuration for the ASIC modules in the prototype digital CdZnTe array system. The noise was measured using a simple subtraction of the pulse waveforms in forced readout mode.

accurately measure the amplitude of a gamma-ray energy deposition. The filter should not include the cells which capture the anode rise, electron drift in the bulk, nor waveform turning from trapping/de-trapping following collection. The FWHM of the resulting amplitude distribution is used to calculate the noise in ADC. By measuring the photopeak centroid of a known gamma-ray line, one can convert from ADC to energy.

Fig. 2.32 shows the measured electronic noise for a number of detector system configurations. No electronic noise increase occurred when the high voltage distribution board (HVDB) was connected to the ASIC as expected. The largest increase in electronic noise occurred when a CdZnTe detector (detector #4R-100 was used for the test in Fig. 2.32) was plugged into the ASIC module socket. Biasing the detector, which increased the leakage current, had a small effect on the measured electronic noise. 4R-100 is a common grid detector (see Sect. 1.2.4) so the grid was biased to its optimal level (OGB). The grid-to-pixel leakage current increased the electronic noise by only 0.1 keV.

The increase in electronic noise when a detector was plugged-in must be due

to either the CdZnTe material capacitance or the pin connector capacitance. A direct-attachment carrier board was designed by IDEAS which a CdZnTe detector is bump-bonded to, resulting in very short traces to the preamplifier. Several CdZnTe detectors were connected to ASICs in this fashion in a configuration known as "direct-attachment". Fig. 2.33 compares a direct-attachment CdZnTe detector to a standard-attachment detector and ASIC module.

By using the 700 keV dynamic range setting in the VAD_UMv2.2 system, the measured electronic noise from a directly-attached detector is 1.5 keV at -3 kV cathode bias. The reduced electronic noise corresponds to an improvement in measured energy resolution. Fig. 2.34 shows that the single-pixel energy resolution of a directly-attached detector can reach 0.34% FWHM at 662 keV. These results indicate that the additional noise from the standard-attachment is mostly due to the length of input traces to the preamplifier.
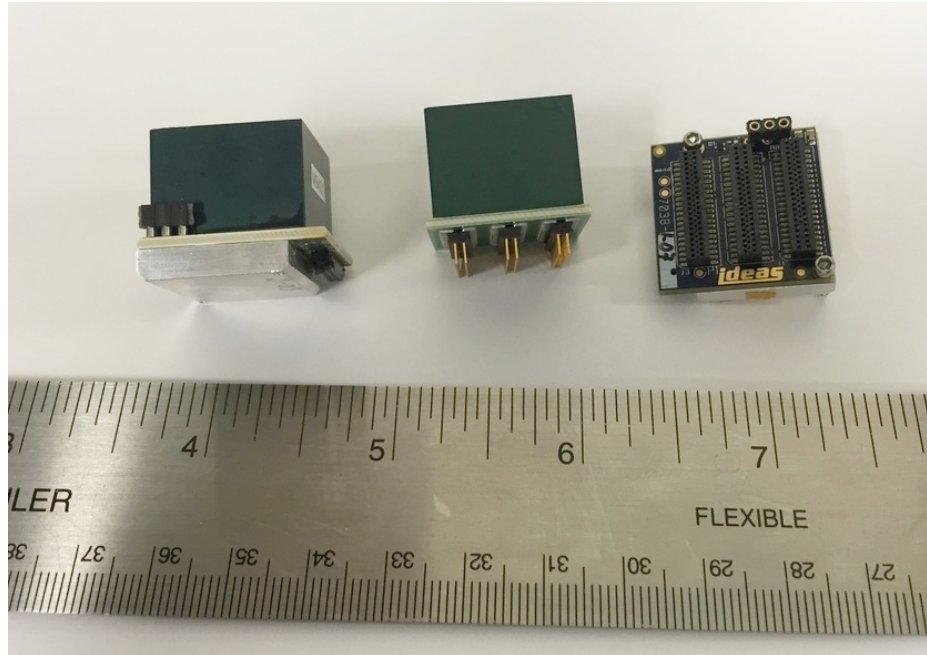
Figure 2.33: Photograph of a VAD_UMv2.2 ASIC directly-attached to a standard $2\times2\times1.5$ cm^3 detector (left). Photographs of a standard detector with pin connectors to an ASIC module (center) and a VAD_UMv2.2 ASIC module (right).
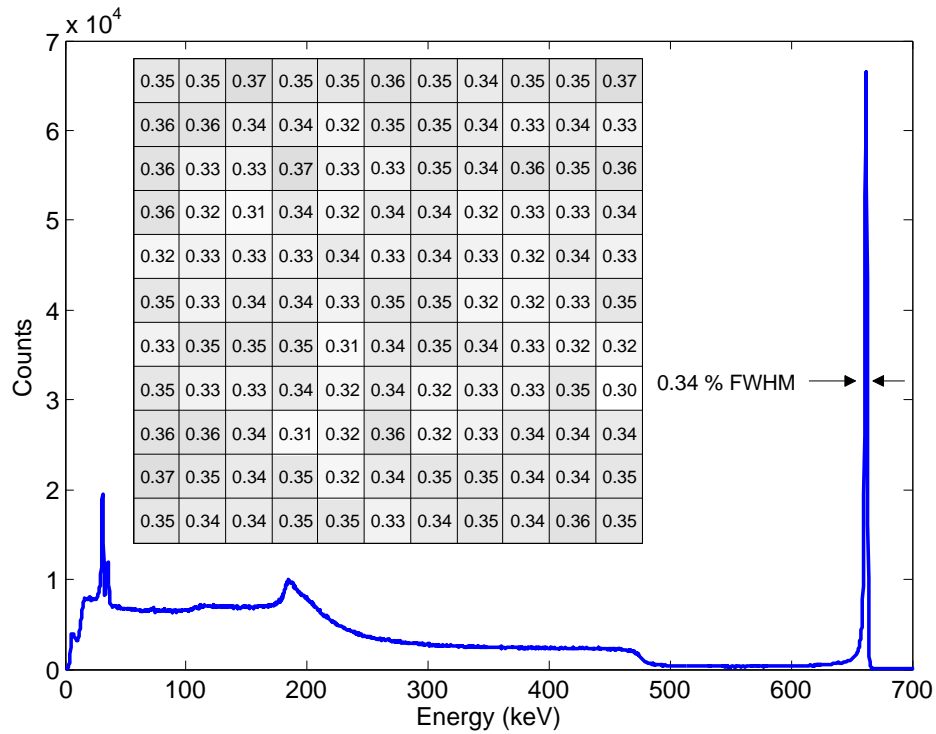
Figure 2.34: Measured ^{137}Cs gamma-ray energy spectrum using 6RID-29, a $2\times2\times1.5$ cm^3 CdZnTe detector directly-attached to a VAD_UMv2.2 ASIC. The inset map shows the measured energy resolution at 662 keV in each anode pixel.

CHAPTER III

Performance of Digitally-Sampled CdZnTe Arrays in High Count Rate Environments

While most of the focus for CdZnTe detector development has been to detect the presence of small amounts of radioactive materials, the excellent imaging and spectroscopic performance of CdZnTe has encouraged its use in high count rate environments as well. CdZnTe has been explored to replace traditional detectors at nuclear power plants and nuclear processing facilities. Many large medical imaging vendors have investigated using CdZnTe for applications such as positron emission tomography (PET), single-photon emission tomography (SPECT), or computed tomography (CT). However, at high dose rates, the operation of CdZnTe systems becomes more difficult due to preamplifier decay and reset time, accumulation of space charge in the device, and limited bandwidth for data communication.

Detector systems which utilize the VAS_UMv2.3/TAT4 ASIC show significant energy resolution degradation at high count rates as shown in Fig. 3.1. A system using digital readout should be able to correct some of the energy resolution degradation by identifying defects in the pulse waveforms.

In order to test the performance of a digital CdZnTe array system in a high count rate environment, an 80 mCi ^{137}Cs source was held stationary while the digital ASIC array system was moved through a series of distances to alter the dose rate at the
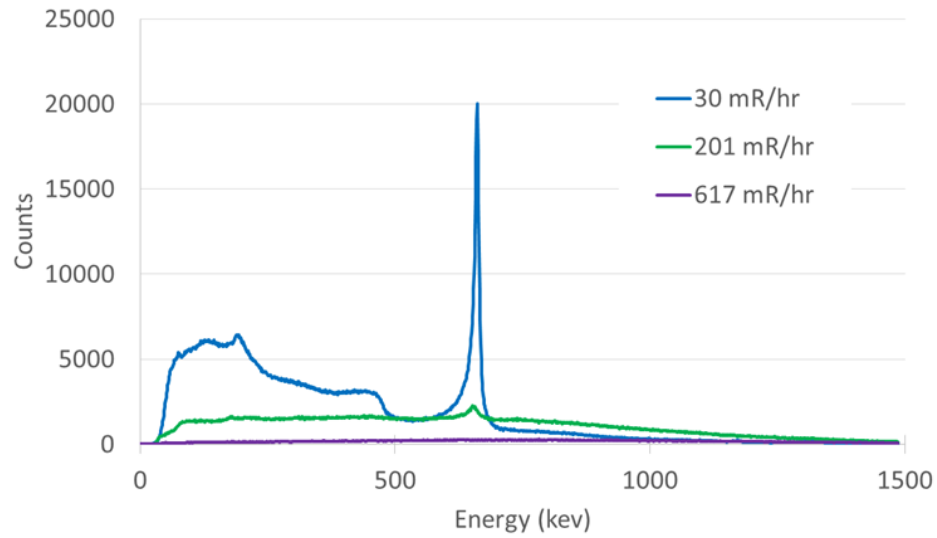
Figure 3.1: ^{137}Cs spectra at different dose rates recorded using a CdZnTe detector read out by the VAS_UMv2.3/TAT4 ASIC. The resolution of the 662 keV photopeak degrades considerably at higher doses. This figure courtesy of H3D Inc.
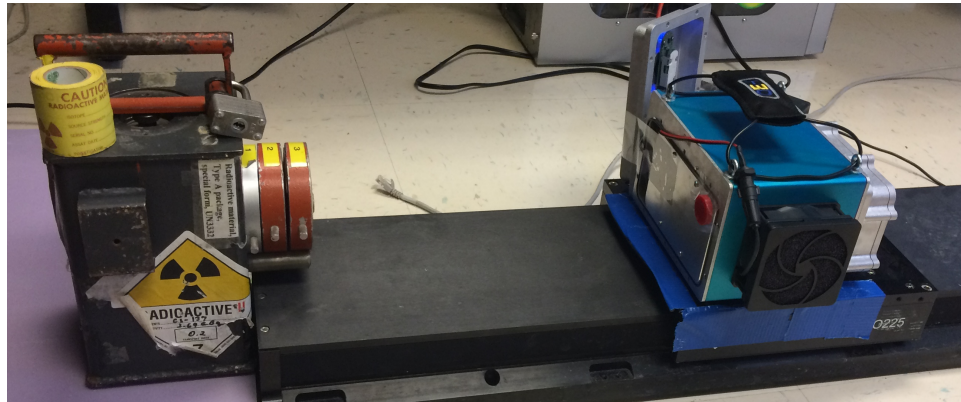
Figure 3.2: A beam of 662 keV photons from an 80 mCi ^{137}Cs source impinging on a Polaris-H CdZnTe system. A 60 μCi ^{60}Co source is held stationary on the detector housing (red button source). This work uses the same experiment design but with a prototype digital ASIC readout system.

detectors as shown in Fig. 3.2 using a Polaris-H CdZnTe system [74]. A 60 μCi ^{60}Co source was attached to the detector housing in an attempt to resolve the relatively weaker source in the presence of a very strong ^{137}Cs source.

59
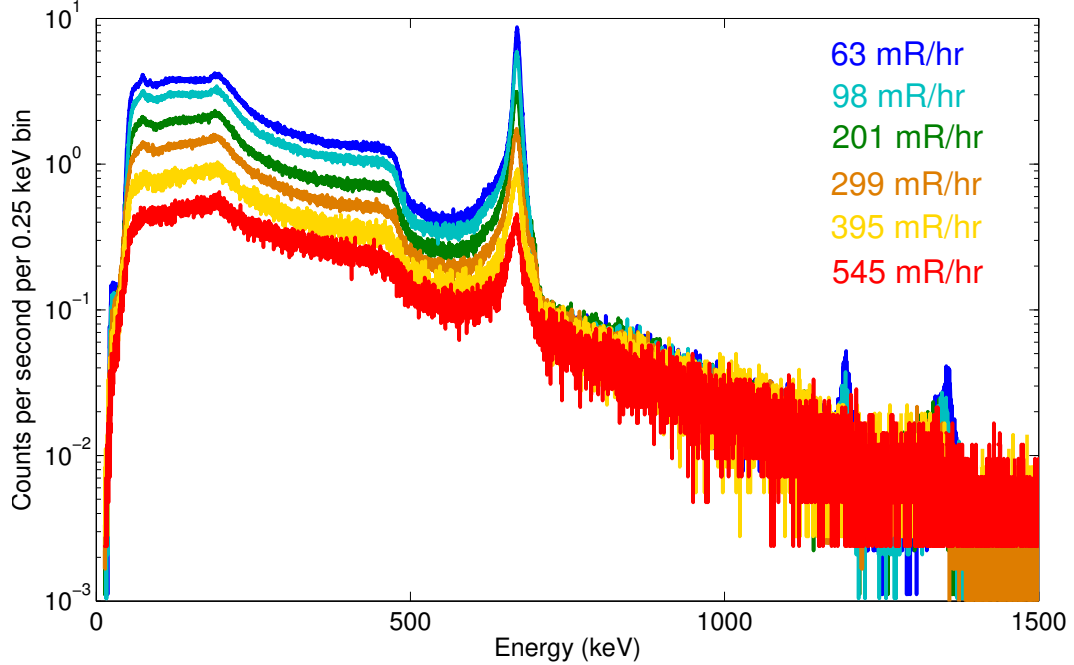
Figure 3.3: All-events spectra for the experiment shown in Fig. 3.2. The different colors represent different dose rates which were generated by moving the detector array closer to the ^{137}Cs source. The 60 μCi ^{60}Co source was present for these measurements to monitor energy resolution degradation. Each measurement lasted one hour.

3.1 Initial Results at High Dose Rates

The measured ^{137}Cs spectra as a function of dose rate are given in Fig. 3.3. The spectra in Fig. 3.3 were generated by using a trapezoidal filter to determine the pulse waveform amplitude and a CR-$(RC)^4$ filter to calculate the relative timing between each anode waveform and the cathode pulse waveform. The standard corrections discussed in Chapter II were applied to produce the spectra.

The count rate appears to decrease as the dose rate increases. At higher dose rates, more waveforms are rejected as "false triggers" for reasons which will be discussed in later sections. Also, the rate of chance coincidence increases, so the expected number of triggers per event increases. Multiple-pixel events take longer to read out, so the effective number of events read out per unit time decreases at higher dose rates.

The resolution of the 662 keV photopeak degrades at higher dose rates. However,
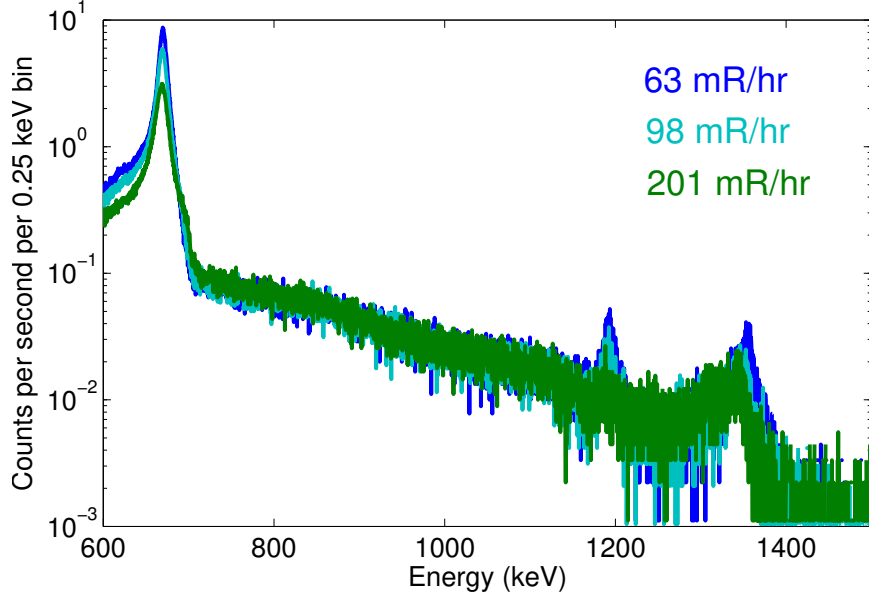
Figure 3.4: All-events spectra for the experiment shown in Fig. 3.2, highlighting the photopeaks from the 60 μCi ^{60}Co source.

the photopeak is still clearly resolved at a dose rate of 545 mR/hr, unlike when the VAS_UMv2.3/TAT4 ASIC is used. The 1173 keV photopeak from the 60 μCi ^{60}Co source is resolvable up to 98 mR/hr as shown more clearly in Fig. 3.4. It is difficult to resolve the 1333 keV photopeak from the sum coincidence peak of two 662 keV interactions.

The following sections will demonstrate defects in the pulse waveforms at high dose rates and present algorithms to correct the flaws. Improved energy resolution results from properly correcting the waveforms.

3.2 Trigger Interference in VAD_UM ASICs

The VAD_UMv1.2 ASIC digitizes the signals induced on the anode pixels which trigger the system as well as the cathode and guard ring. To initiate a readout sequence, a digital impulse signal, indicating a radiation event triggered the system, is sent from the ASIC to the FPGA. However, at high count rates, the interference of these digital signals can affect the digitized waveforms by adding spikes to the
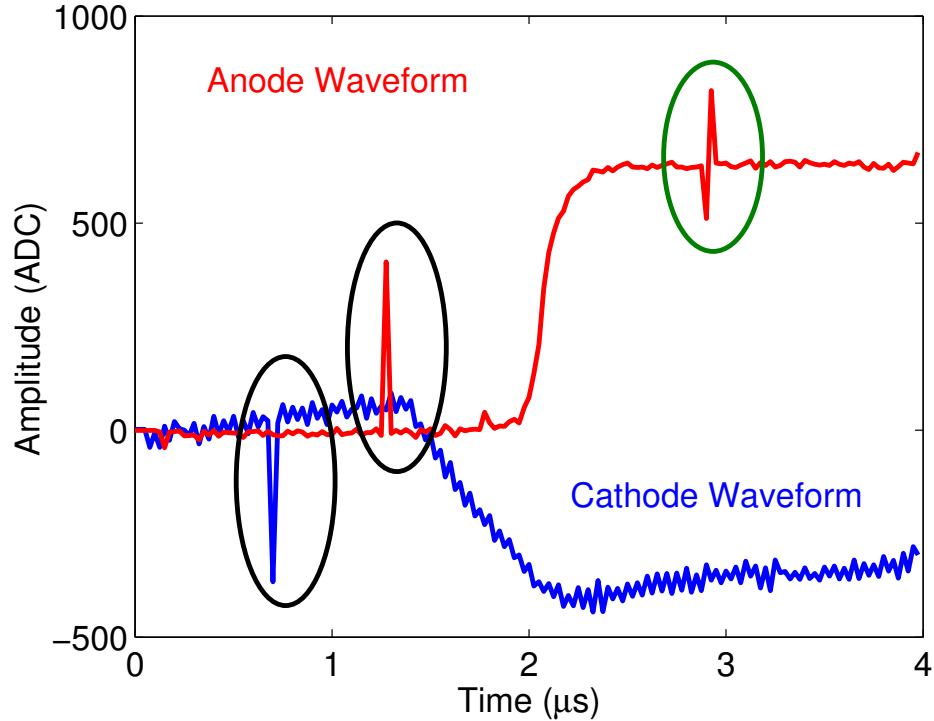
Figure 3.5: Anode and cathode pulse waveforms with spikes from digital trigger interference. Notice that the first two interferences (circled in black) are the same amplitude and demonstrate one interference phase. The other interference (circled in green) is a different interference pattern.

signals as shown in Fig. 3.5. The observed spikes have one of four specific spike characteristics which are thought to be from various phase interferences of the trigger signal. The spikes can be removed by disabling channels from triggering the system or by identifying the type of interference and removing its influence from the waveforms. Fig. 3.6 shows the four interference patterns. The interferences can be identified by applying a moving average filter to the waveforms and identifying abrupt negative changes in the signal amplitude.

In an array of VAD_UMv1.2 ASICs, each ASIC can be individually disabled so it is unable to trigger. Alternatively, the motherboard can be configured to ignore triggers from certain ASICs. If the motherboard is configured to ignore triggers, interference from the trigger signal can still manifest itself as a spike in the waveforms. This is the case shown with the blue points in Fig. 3.7. At higher dose rates, the spike
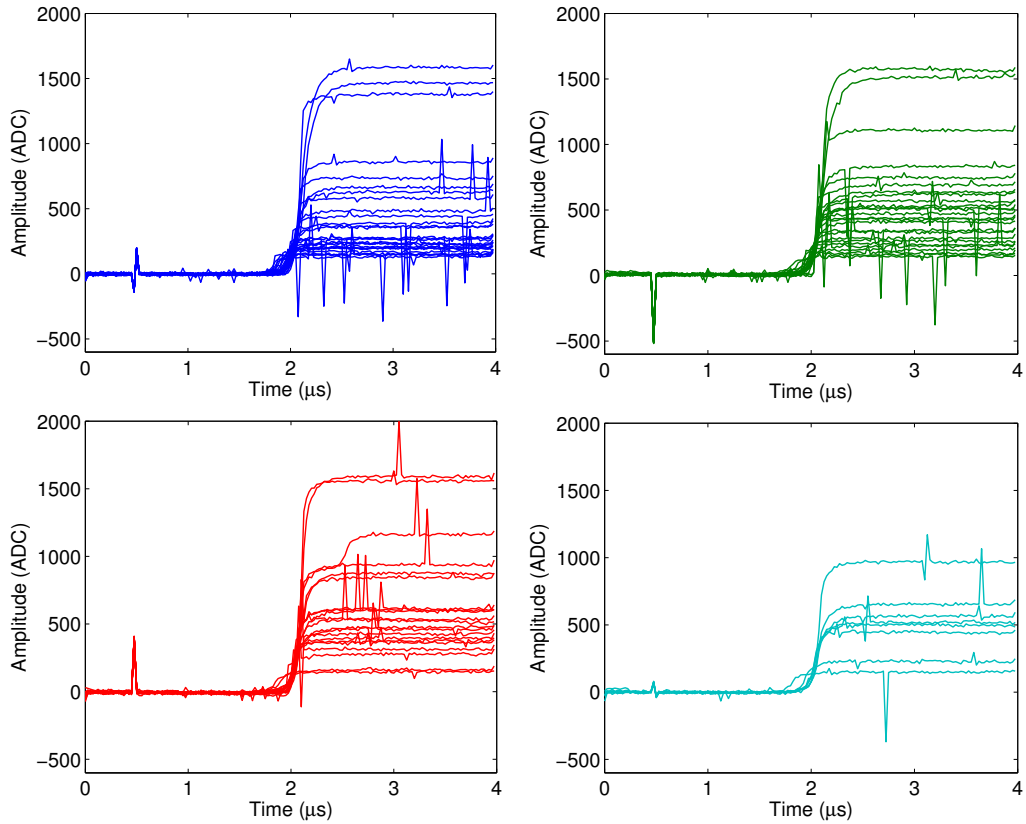
Figure 3.6: Four different interference patterns occurring in anode waveforms at high count rates in cell number 20. Note that the interference can be classified, and, since it is the same amplitude at all times, removed via subtraction.

frequency increases rapidly so that almost all waveforms have at least one spike in them. However, if the ASICs are disabled from triggering as shown in red in Fig. 3.7, the interference frequency is reduced.

The position of the ASIC module in the readout chain matters in terms of spike frequency. Module_12 and Module_22 have spikes in the waveforms at high count rates. However, Module_11 and Module_21 do not. Therefore, the trigger signals in Module_11 and must influence Module_12 based on its position in the readout sequence, but the trigger interference cannot be passed backwards through the chain.
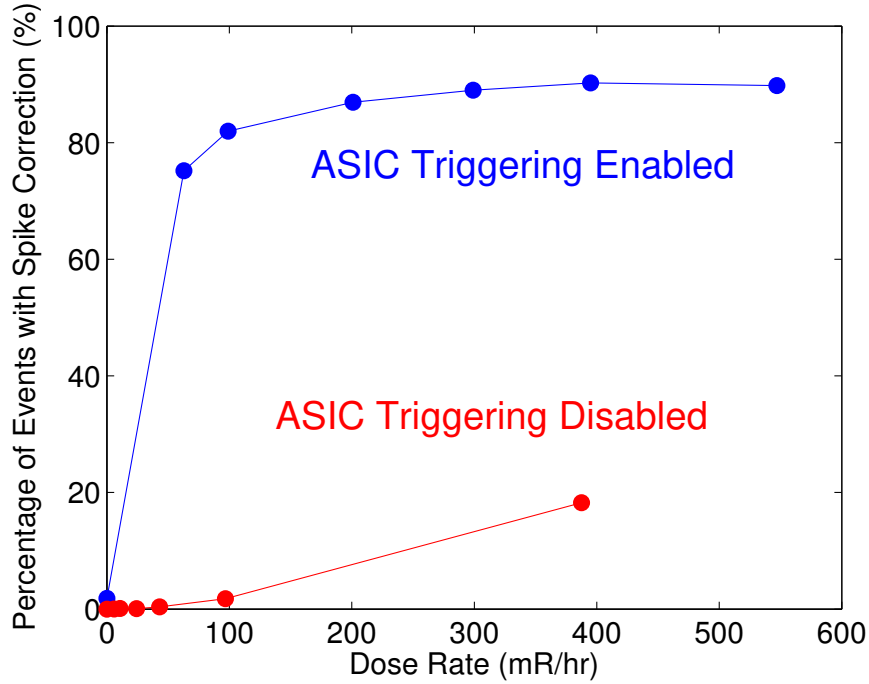
Figure 3.7: Frequency of interference patterns in Module_12 as a function of dose rate when Module_11 is disabled from readout on the motherboard (enabled) or the ASIC is disabled from triggering internally (disabled).

3.3   Cathode Waveform Baseline and Tail Slopes

When the event rate is high, the cathode preamplifier does not have time to decay to the baseline before the next event. Charge is induced on the cathode preamplifier in almost all radiation interactions, so it is more affected than anode pixels. Therefore, there is some permanent slope in the waveform which must be subtracted in order to obtain meaningful amplitude information from the cathode signals. Fig. 3.8 shows the average cathode waveforms for 662 keV photopeak events at different dose rates showing the permanent slope in the baseline and tail of the waveforms. Furthermore, the slope increases at higher dose rates. As shown in Fig. 3.9, the slope of the cathode waveform is very similar whether one looks at the slope in the tail or the baseline of the waveform. Also, the slope in the tail and the baseline becomes more variable at higher dose rates (lower portion of Fig. 3.9). Therefore, any correction for the slope in the cathode waveform must be completed on an event-by-event basis as the slope
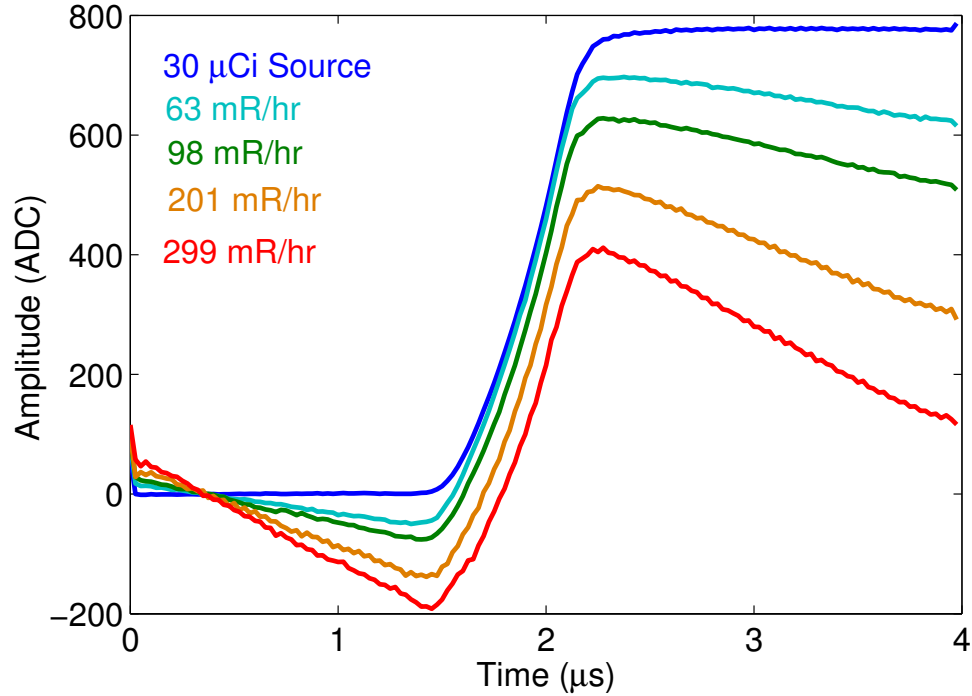
Figure 3.8: Average cathode waveforms for photopeak events at different dose rates demonstrating slope in the baseline and tail which increases with dose rate.

can vary substantially from one event to the next.

One can plot the average slope in the cathode baseline as a function of dose rate as shown in Fig. 3.10. The slope changes monotonically with dose rate meaning that the cathode slope can be used to estimate the dose rate during a measurement if a functional relationship is determined *a priori*. A knowledge of the dose rate is useful in many health physics applications.

3.4 Waveform Corrections

The final problem encountered during high count rate measurements is that the cathode becomes saturated, so the ASIC has to reset. The reset signal can create an interference pattern on the read out cathode waveform. An example cathode waveform with a reset interference is demonstrated early in the waveform shown in Fig. 3.11. These events can be identified by applying a moving average filter to
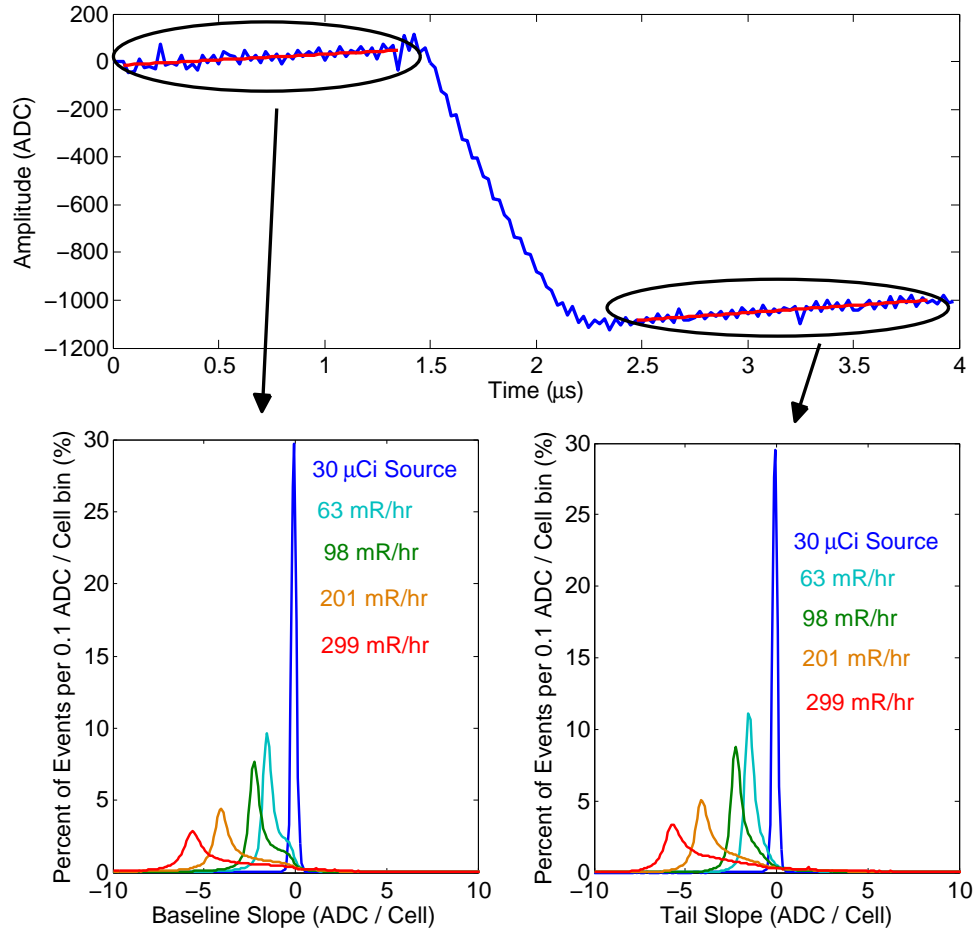
Figure 3.9: Example of cathode slope determination in the tail and baseline (top). The histograms show how the distribution of slopes in the cathode waveforms change as a function of dose rate (bottom).

identify waveforms where a rapid negative change in signal amplitude occurs that does not correspond to one of the trigger interference patterns described in Sect. 3.2. These waveforms are very difficult to correct because the slope before, during and after the reset are all different. It is challenging to fit all three regions accurately so instead, events with resets in the pulse waveforms are removed from the final spectrum.

On the other hand, the cathode slope and trigger interferences can be identified and removed for each event. Fig. 3.12 gives an example of a recorded waveform with trigger interferences and cathode slopes which are corrected by identifying and removing the defects.
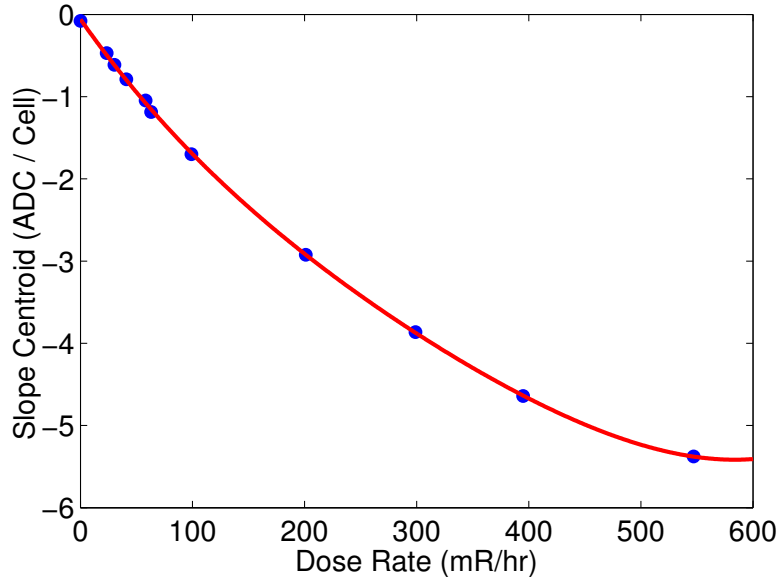
Figure 3.10: Average cathode slope in the baseline from the histogram in Fig. 3.9. Note that the slope is a monotonic function of dose rate.

The waveform corrections considerably improve the energy resolution as shown in Fig. 3.13. At higher dose rates, more waveforms are affected by defects, so the waveform corrections improve the resolution more.

3.5 Improved Resolution at High Dose Rates by Reducing Preamplifier Feedback Resistance

Reducing the feedback resistance of the preamplifier will force the induced signal to decay more quickly so the system is ready for the next trigger and reduces the probability that the preamplifier will saturate. This is a well known approach that has been used in other sensors [75, 76].

The Johnson noise associated with a resistor is inversely related to the resistance. Therefore, for the lowest Johnson noise, the resistance should be as high as possible. However, in response to leakage current and radiation-induced pulse waveforms, the resistance should be reduced in order to accurately measure the signal amplitude. Therefore, in a high count rate environment, a trade-off must be made between
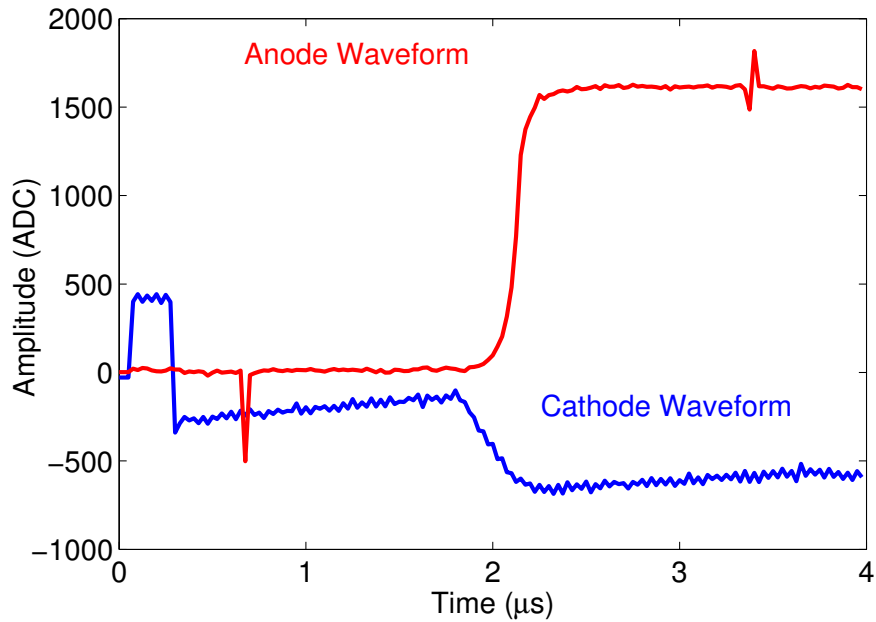
Figure 3.11: Example of a cathode waveform with an ASIC reset interference pattern.
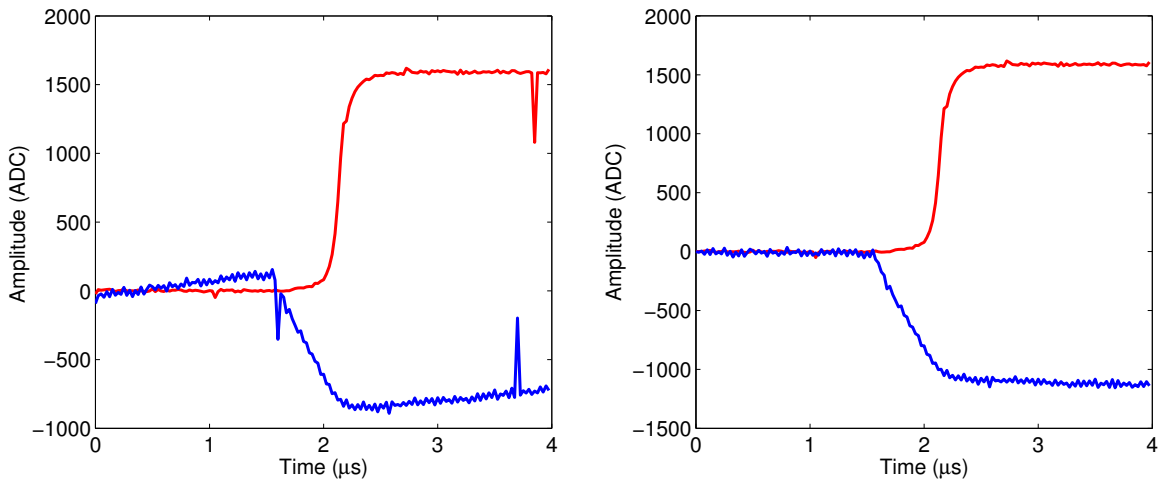
Figure 3.12: Recorded event at 100 mR/hr with clearly visible slopes in the baseline and tail of the cathode waveform and trigger interference patterns (left). The same waveform is corrected using the algorithms described (right).

Johnson noise and the time required to reset the system before the next radiation interaction.

In most CMOS (Compound Metal-Oxide-Semiconductor) front-end circuits (including the VAD_UMv1.2 ASIC), a JFET (Junction Gate Field-Effect Transistor) is actually used to control the equivalent feedback resistance of the circuit. A bias
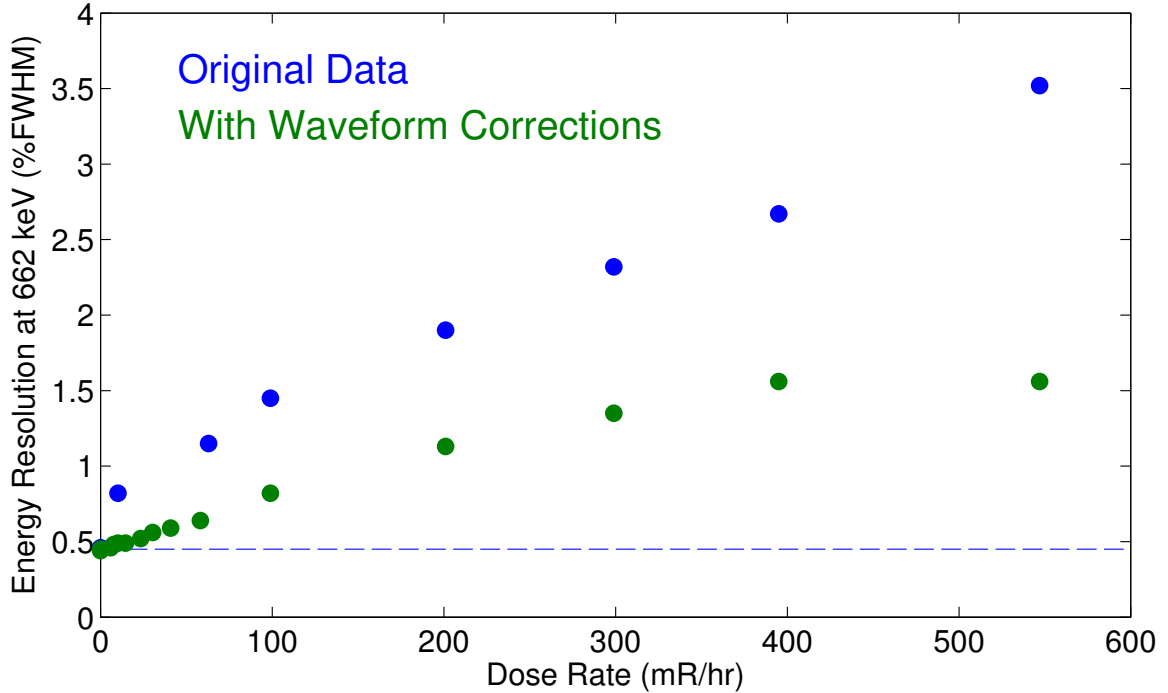
Figure 3.13: Single-pixel events energy resolution of the 662 keV photopeak versus dose rates with and without the described waveform corrections. The dashed blue line shows the energy resolution at low dose rates to compare the degradation at high dose rates.

voltage controls the relative speed of the preamplifier decay. In the VAD_UM suite of ASICs, this is known as the Vfp setting. Fig. 3.14 demonstrates how different Vfp settings change the average anode waveform for a single-pixel 662 keV photopeak event. A smaller Vfp corresponds to a smaller equivalent feedback resistance, so the preamplifier decay is faster.

Normally, the digital CdZnTe array system is operated with a Vfp setting of 70 ADC. However, at high count rates, the setting should be lowered so that the ASIC recovers quickly and is ready for the next event. The left pane of Fig. 3.15 shows the relative energy resolution of the 662 keV photopeak at a ^{137}Cs dose rate of 100 mR/hr as a function of the Vfp setting. At 100 mR/hr, a Vfp setting of 62 ADC provides the best performance - a 20% improvement from leaving the Vfp setting at 70 ADC.
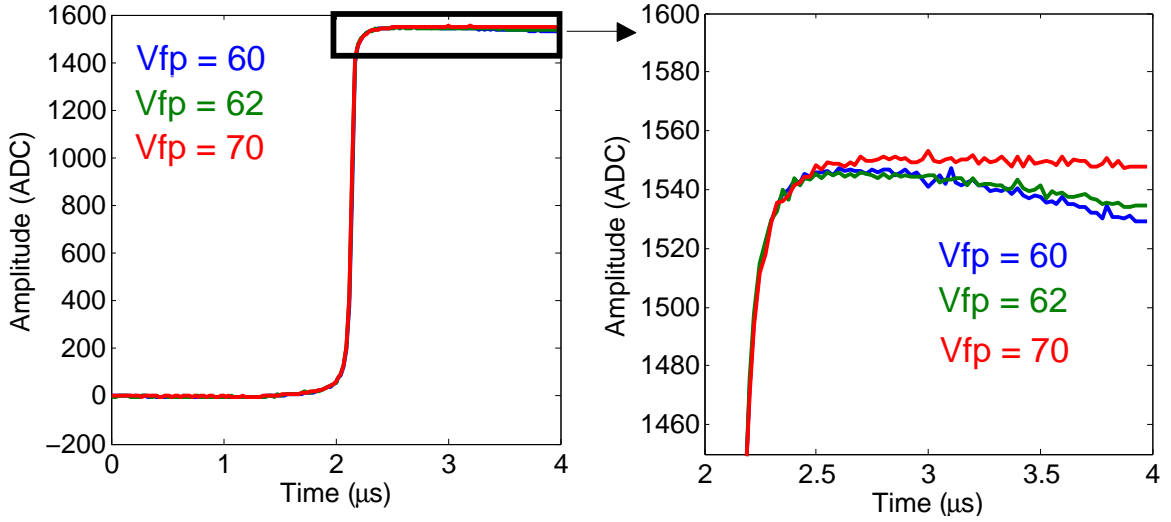
Figure 3.14: Average anode pulse waveform from a single-pixel 662 keV photopeak energy deposition near the cathode surface in a CdZnTe detector recorded using different Vfp settings.
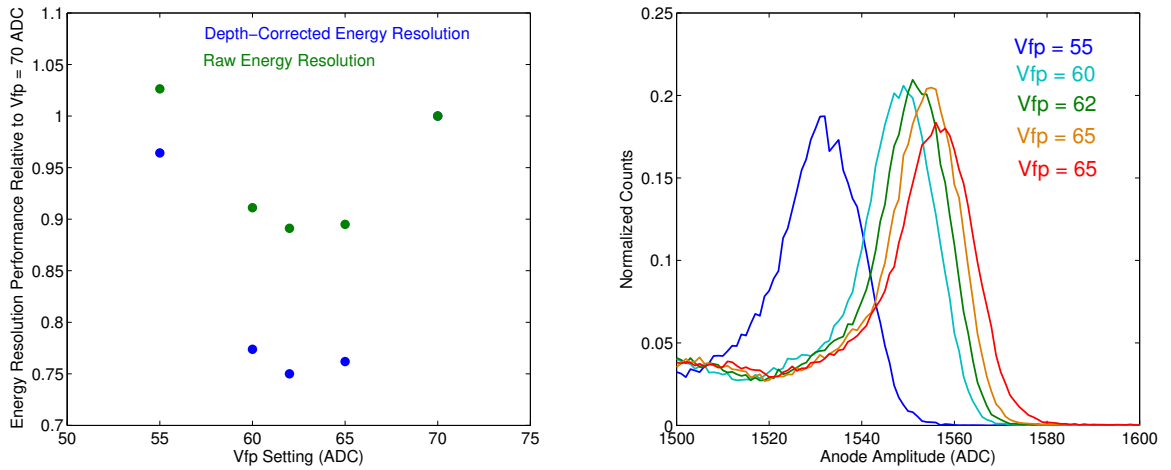
Figure 3.15: Raw and depth corrected single-pixel energy resolution compared to the value recorded with a Vfp setting of 70 ADC at 100 mR/hr for the 662 keV photopeak from ^{137}Cs (left). The recorded raw single-pixel energy resolution spectra for different Vfp settings at a dose rate of 100 mR/hr (right).

Overall, the combination of waveform corrections and applying the optimal feedback resistance allows a digital CdZnTe array to maintain an energy resolution of less than 0.8% FWHM at 662 keV up to 100 mR/hr when all events are included. Without this suite of corrections, the all events energy resolution at 100 mR/hr is 2.5% FWHM at 662 keV. An energy resolution of less than 1% FWHM at 662 keV
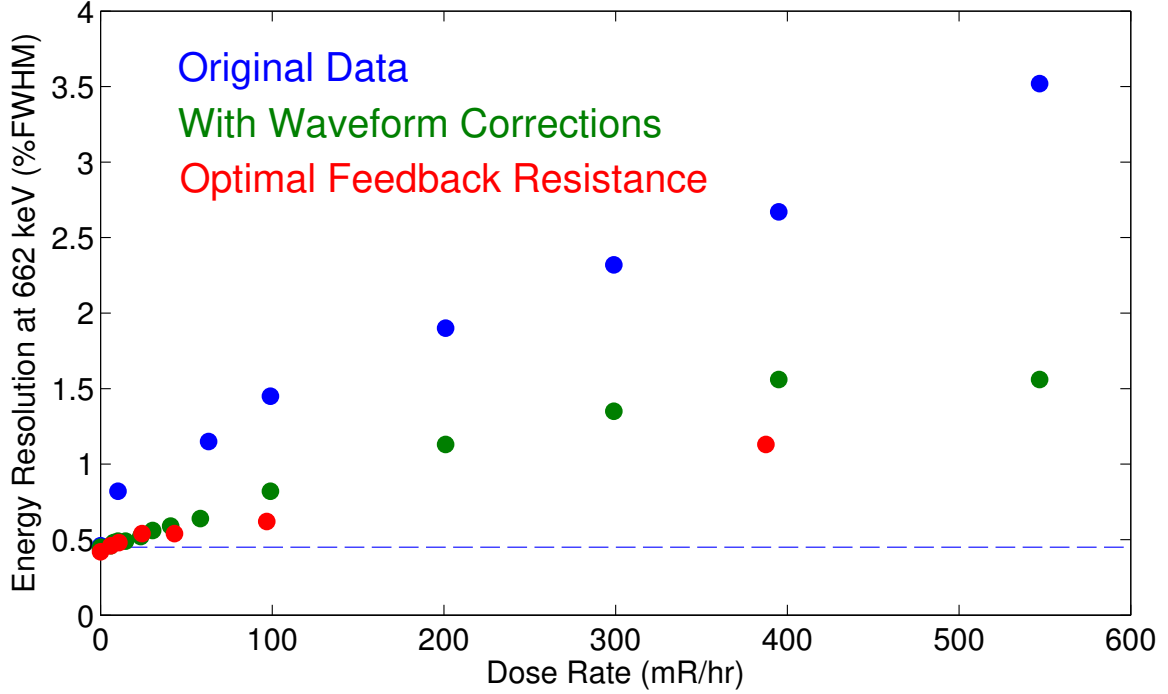
Figure 3.16: Single-pixel events energy resolution of the 662 keV photopeak as a function of dose rate, demonstrating the effectiveness of the described correction procedures. The blue dashed line shows the energy resolution at low dose rates to compare the degradation to at higher dose rates.

can be maintained for single-pixel events at dose rates up to 400 mR/hr. Without these corrections, the resolution is about 2.8% FWHM, indicating these corrections can improve resolution by at least 1.7% FWHM at 662 keV in high count rate environments.

3.6   Remaining Degradation and Future Work

A portion of the remaining degradation comes from polarization in the detector. This form of polarization refers to space charge which builds up in the detector, distorting the electric field. This is especially problematic in CdZnTe because holes move very slowly in the device. At high dose rates, there is a lot of positive charge migrating slowly through the detector. Fig. 3.17 shows that at high dose rates, the electrons are moving measurably slower through the device. The cathode waveform
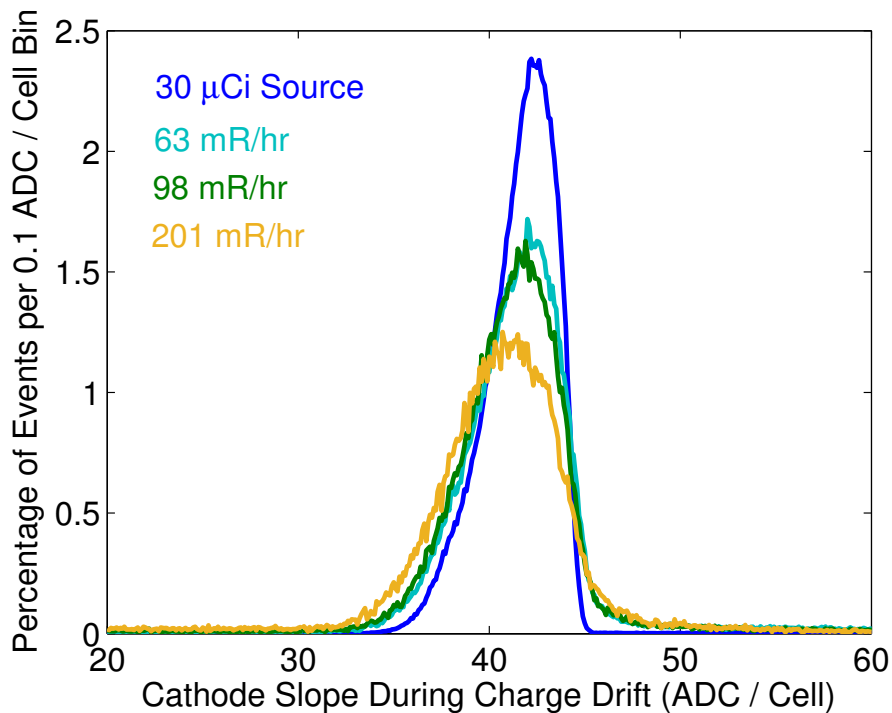
Figure 3.17: Histogram of the cathode slope during charge drift for single-pixel 662 keV photopeak events near the cathode side. The charge drift time domain is between 1.5 and 2.2 μs for the example waveform shown in Fig. 3.9. In this time regime, radiation-generated electrons are moving, inducing signal on the cathode. At higher count rates, the average slope is lower and more variable indicating instabilities in the electric field.

slope is more variable and, on average, shallower at higher dose rates. This variability in the electric field may lead to additional variance in electron trapping which may degrade the energy resolution.

Future ASIC designs should consider high count rate applications to reduce the frequency of spikes in waveforms from trigger interference and digital reset interferences. Furthermore, the readout electronics in future systems should be designed to read out events at a higher frequency. In the "triggered pixel only" readout mode, only 6,000 events per second can be processed using the VAD_UMv1.2 system. Switching to Ethernet-based data communication should improve the readout speed.

CHAPTER IV

Detection and Characterization of Shielded Special Nuclear Material

4.1 Rapid Detection of Radioactive Material with Improved Energy Resolution

In the field, users want to determine the identity of a radioactive source as quickly as possible. The time required to detect a source depends on the source strength, the background radiation intensity, the detector efficiency, and the energy resolution of the detector [77]. In order to detect a specific isotope, the photopeak area of interest must exceed the expected background fluctuations. Therefore, it is simply a matter of maximizing the signal-to-noise ratio in the photopeak region of interest (ROI).

The signal depends only on how efficiently the system detects photons. The photopeak detection rate, $\dot{P}$, is given in Eq. 4.1.

$$\dot{P} = \dot{S} f_\gamma \left(\frac{\Omega}{4\pi} \right) \varepsilon_{ip} \tag{4.1}$$

$\dot{S}$ is the source disintegration rate, and f_γ is the branching ratio of the photopeak line of interest. Ω is the solid angle subtended by the detector, and ε_{ip} is the intrinsic photopeak efficiency of the detector for the photon energy of interest.

The noise in the detection rate, $\sigma_{\dot{P}}$, is comprised of the Poisson statistical variation in the photopeak count rate and the background count rate as shown in Eq. 4.2.

$$\sigma_{\dot{P}} = \sqrt{\left(\dot{P} + \bar{\dot{C}}R_W\right)t} \tag{4.2}$$

In Eq. 4.2, t is the measurement duration and $\bar{\dot{C}}$ is the background continuum count rate per unit of energy in the region of interest, R_W. In other words, if $\dot{c}(E)$ is the continuum count rate at energy E, $\bar{\dot{C}}R_W$ is equal to the integral in Eq. 4.3.

$$\left(\bar{\dot{C}}R_W\right) = \int_{R_W} \dot{c}(E)dE \tag{4.3}$$

By improving the energy resolution, the width of R_W decreases, lowering the noise term, therefore increasing the SNR for detection. To declare detection, the ratio of $\dot{P}t$ to $\sigma_{\dot{P}}$ must exceed some threshold, T. The theoretical time required for the SNR to exceed the threshold is given in Eq. 4.4.

$$t = \frac{T^2}{(\dot{S}f_\gamma(\frac{\Omega}{4\pi})\varepsilon_{ip})^2}\left(\dot{S}f_\gamma\left(\frac{\Omega}{4\pi}\right)\varepsilon_{ip} + \bar{\dot{C}}R_W\right) \tag{4.4}$$

Eq. 4.4 can provide valuable insight about the relative time required to detect an isotope for different detectors and source-to-background intensity ratios. One of the most common radioisotope identifiers in the field uses a $\oslash$ 5.08 $\times$ 5.08 cm^2 NaI cylinder to perform identification spectroscopy. Eq. 4.4 was used to compare the relative time to detect an isotope using a common NaI detector and a 2$\times$2 array of 2$\times$2$\times$1.5 cm^3 CdZnTe detectors. For a very strong source (high source-to-background ratio), the NaI detector can detect the source in half the time the CdZnTe array requires because the improved resolution to reject background counts matters less for very strong sources. However, in the much more useful case, the CdZnTe array can detect a source up to five times faster than the NaI detector for weak sources in a high background environment.
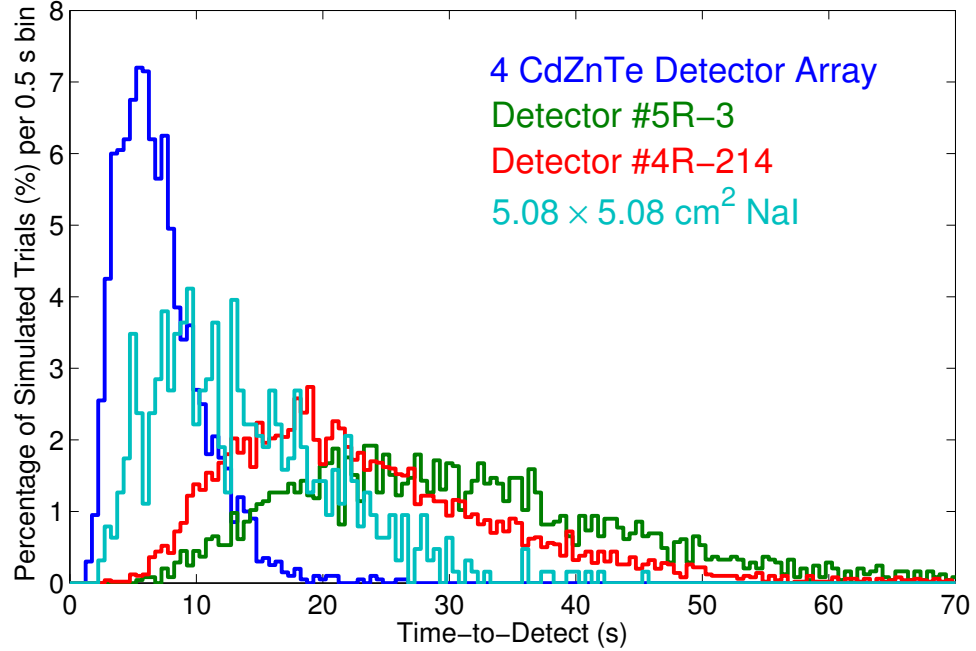
Figure 4.1: Histogram of the time required to detect a 10 μCi ^{137}Cs source from 1 m away from different detectors using a bootstrap sampling procedure on the recorded spectra. 5R-3 and 4R-214 are individual CdZnTe detectors in the array.

To verify this prediction, a 10 μCi ^{137}Cs source was placed 1 m away from the 2×2 CdZnTe array and the $\oslash$ 5.08 × 5.08 cm^2 NaI cylinder. Identical detection algorithms were used for the two systems (albeit with slightly different ROI widths to account for the different energy resolutions). The CdZnTe array detected the presence of the source in 4.8 ± 1.6 seconds over the course of ten trials whereas the NaI detector required 7.7 ± 2.1 seconds. Because there was large variance in the time required to detect a source, a long measurement was recorded using both detectors. The resulting spectra were bootstrapped in order to simulate a large number of measurements [78]. A histogram of the time required to detect the source by the CdZnTe array, two individual detectors in the array (5R-3 and 4R-214), and the NaI cylinder is shown in Fig. 4.1. For this particular measurement scenario, the mean detection time for the CdZnTe array is roughly half the time required by the NaI detector.

A commercially available GR-135 radioisotope identifier [79], was also compared against the CdZnTe array for the same measurement scenario (a 10 μCi ^{137}Cs source
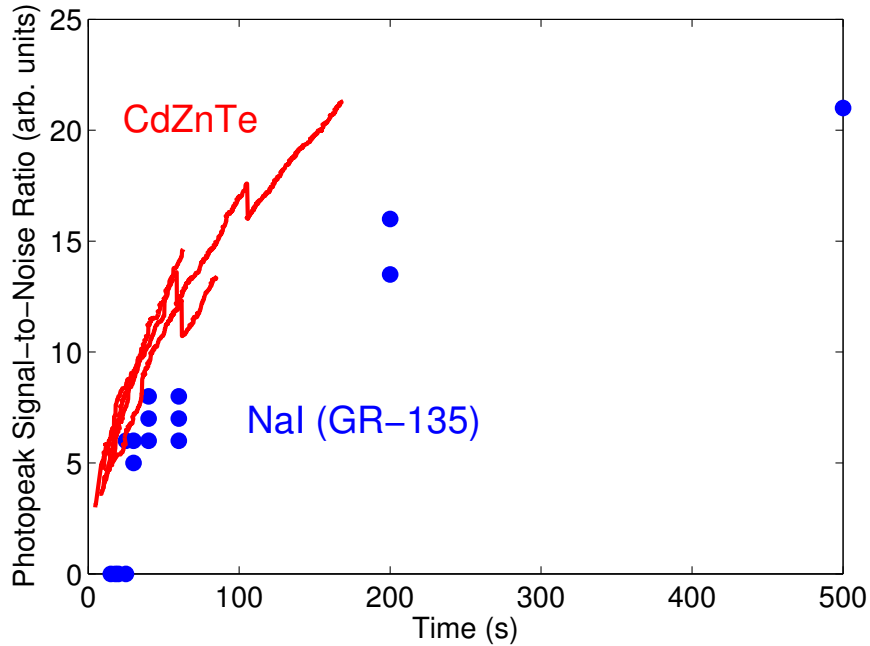
Figure 4.2: SNR of 662 keV photopeak as a function of time for the GR-135 NaI detector and digital CdZnTe array. The 10 μCi ^{137}Cs source was placed 1 m away from both detectors.

measured with 1 m standoff). The GR-135 provides a list of the detected isotopes and the photopeak SNR for each isotope detected. Fig. 4.2 shows how the SNR of the detected peak changes as a function of time for the CdZnTe detector array and the GR-135 . Points in the upper left portion of the plot indicate more certainty in the detection at an earlier time so the source is detected more quickly. From Fig. 4.2, the CdZnTe array outperforms the NaI detector for this particular measurement. The SNR decreases rapidly in the CdZnTe measurement when an interaction occurs in the continuum region used to estimate the background variation (i.e. noise).

4.2   Uranium Enrichment

Spectrometers using $2\times2\times1.5$ cm^3 CdZnTe semiconductor detectors are excellent candidates to be used for rapid SNM characterization, especially in scenarios where material cannot be easily removed from a location for mass spectroscopy or active in-

terrogation analysis. These conditions may exist during International Atomic Energy Agency (IAEA) inspections or international treaty verification.

4.2.1   Efficiency and Resolution for Uranium Gamma-ray Lines

CdZnTe has demonstrated energy resolution below 0.5% FWHM for single-pixel events at 662 keV. The energy resolution at 185.7 keV has been measured in this thesis work to be 1.55% FWHM. The intrinsic photopeak efficiency for 59.5 keV gamma rays for a cathode side irradiation is 99% and 11.2% at 662 keV [41]. For 185.7 keV gamma-rays, the intrinsic photopeak efficiency is 93% for a single detector. The photopeak efficiency can be improved by building larger tiled systems with multiple rows of detectors to capture the full energy from Compton scattering events. The capabilities of these sensors are significantly better than the previous generation of portable CdZnTe spectrometers [80, 81].

Verifying uranium enrichment is critical in international safeguards for material accountancy. Knowledge of uranium enrichment can provide valuable insight into both the provenance and the likely end uses of recovered materials [51, 82]. However, due to weakly penetrating radiation and often unknown geometries, the enrichment is challenging to measure in realistic scenarios using gamma-ray spectroscopy [83].

Site 2 at the Y-12 Nuclear Detection and Sensor Testing Center provided eleven uranium metal samples with various enrichments. Each sample was a disk approximately 3 cm in diameter and 3 mm thick. The sample enrichment varied from 0.2 to 93.2 wt% ^{235}U [84]. Fig. 4.3 shows the measured spectra for samples of uranium with various enrichments measured using the prototype digital CdZnTe array system. The 3 wt% ^{235}U sample had substantially more thorium than other samples which is characterized by the prominent 238 keV line.

The strongest emission from ^{235}U is the 185.7 keV gamma ray with an intensity of 4.32 x 10^4 photons per second per gram of ^{235}U [51]. When the dimensions of the
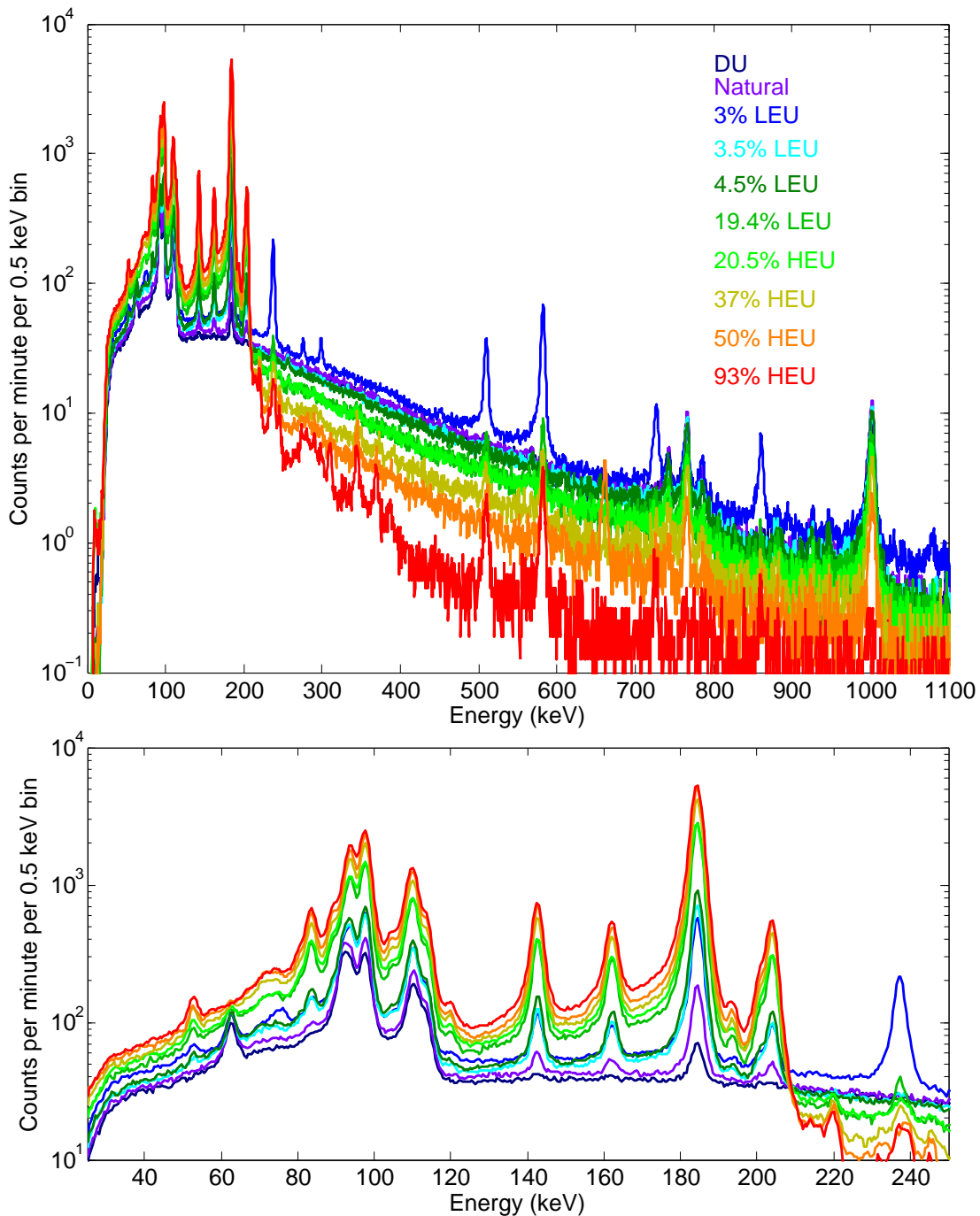
Figure 4.3: Recorded all-events gamma-ray energy spectra from uranium metal disk samples of various enrichments. The sources were 3 cm in diameter and 3 mm thick. No background subtraction was carried out for the spectra presented. Each measurement lasted about an hour.
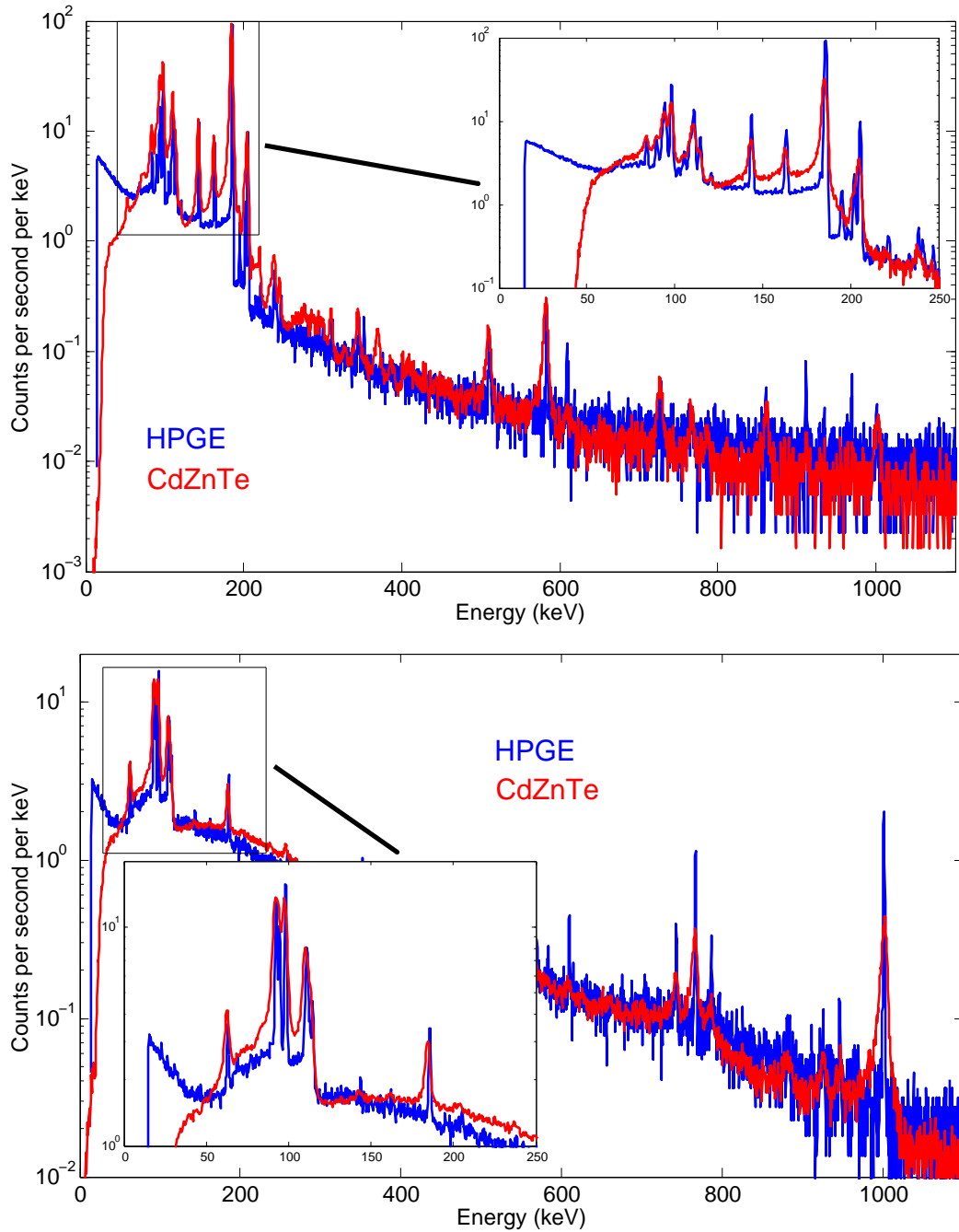
Figure 4.4: Gamma-ray spectra from a 93 wt% ^{235}U HEU disk sample from 25 cm away recorded using prototype digital CdZnTe array system and a commercially available mechanically cooled HPGe detector (top) and spectra from a 0.2 wt% ^{235}U DU sample (bottom). The insets compare the recorded spectra between 0 and 250 keV. Many prominent ^{235}U gamma-ray lines are emitted in this energy range.

sample under investigation are known, dead-time corrected counting measurements of the 185.7 keV line are used to determine the enrichment of a sample [51, 85, 86, 87, 88]. The calculated net photopeak area is affected by the photopeak efficiency of the detector as well as the energy resolution.

A depleted uranium (DU) sample and a 93 wt% ^{235}U highly-enriched uranium (HEU) sample were measured using the Orion prototype digital CdZnTe array. An ORTEC (Oak Ridge, TN) micro-detective hand-held radioisotope identifier [89] was used to simultaneously measure the samples to compare the energy resolution and efficiency of the commercial detector with the CdZnTe prototype. The p-type germanium detector was in a coaxial geometry, 50 mm in diameter and 33 mm in height. Fig. 4.4 shows the spectra recorded using both detectors. The energy resolution of CdZnTe, while inferior to HPGe is sufficient to resolve almost all of the gamma-ray lines of interest. The net photopeak counts in each region of interest was used to compare the efficiency of HPGe and CdZnTe. Geant4 was used to simulate the intrinsic photopeak efficiency of the two detectors [90]. As shown in Fig. 4.5, the efficiency of CdZnTe is better at low gamma-ray energies. However, at higher energies, as multiple interaction Compton scattering becomes the dominant interaction mechanism, the larger HPGe detector has improved efficiency to capture the full energy from multiple scatters. The measured relative count rate roughly matches what is predicted from simulation as shown in Fig. 4.6. The energy resolution of the various uranium signatures are shown for both detectors in Fig. 4.7.

The relative errors in the net count rate of the 186 keV photopeak are 0.28% and 0.39% respectively for the HPGe detector and CdZnTe array for the 93 wt% ^{235}U HEU sample. The uncertainty is greater for the CdZnTe array because the energy resolution is worse, so a larger background contribution must be subtracted. Likewise, the standard errors in the net count rate of the 186 keV photopeak from the 0.2 wt% ^{235}U DU sample are 1.3% and 3.6% for HPGe and CdZnTe respectively.
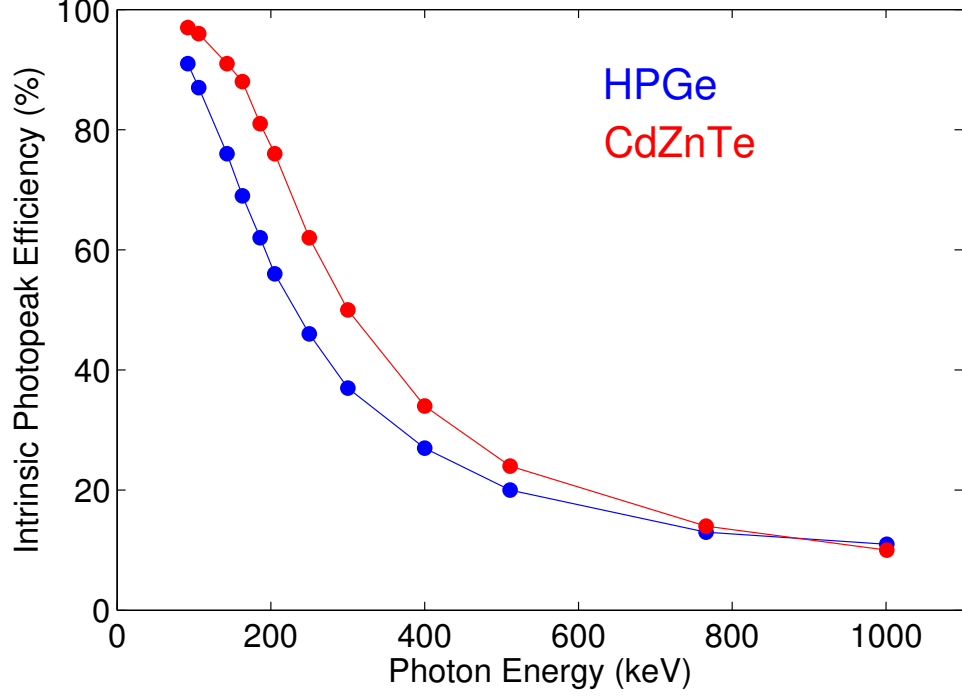
Figure 4.5: Intrinsic photopeak efficiency for gamma-ray lines of interest for uranium measurements using the ORTEC HPGe detector and CdZnTe array from a Geant4 simulation.

4.2.2 Uranium Enrichment Measurements

The strongest emission from ^{238}U daughters is at 1001 keV with an intensity of 73.4 photons per second per gram of ^{238}U [51]. The ratio of the 186 keV line to the 1001 keV line provides an estimate of the sample enrichment, if one can estimate the source extent. The ratio of measured counts in the two lines is given in Eq. 4.5.

$$\frac{\dot{m}_{186 \text{ keV}}}{\dot{m}_{1001 \text{ keV}}} = \left(\frac{E}{1-E} \right) \left(\frac{\dot{S}_{186 \text{ keV}}}{\dot{S}_{1001 \text{ keV}}} \right) \left(\frac{\epsilon_{\text{pp } 186 \text{ keV}}}{\epsilon_{\text{pp } 1001 \text{ keV}}} \right) \left(\frac{\varepsilon_{\text{escape } 186 \text{ keV}}}{\varepsilon_{\text{escape } 1001 \text{ keV}}} \right) \qquad (4.5)$$

In Eq. 4.5, $\dot{m}$ is the measured count rate of the indicated gamma-ray line and E is the enrichment of the sample. $\dot{S}$ is the source term for the gamma-ray line of interest (73.4 photons per second per gram for the 1001 keV line and 4.32 x 10^4 photons per second per gram for the 186 keV line). ϵ_{pp} is the absolute photopeak efficiency of the
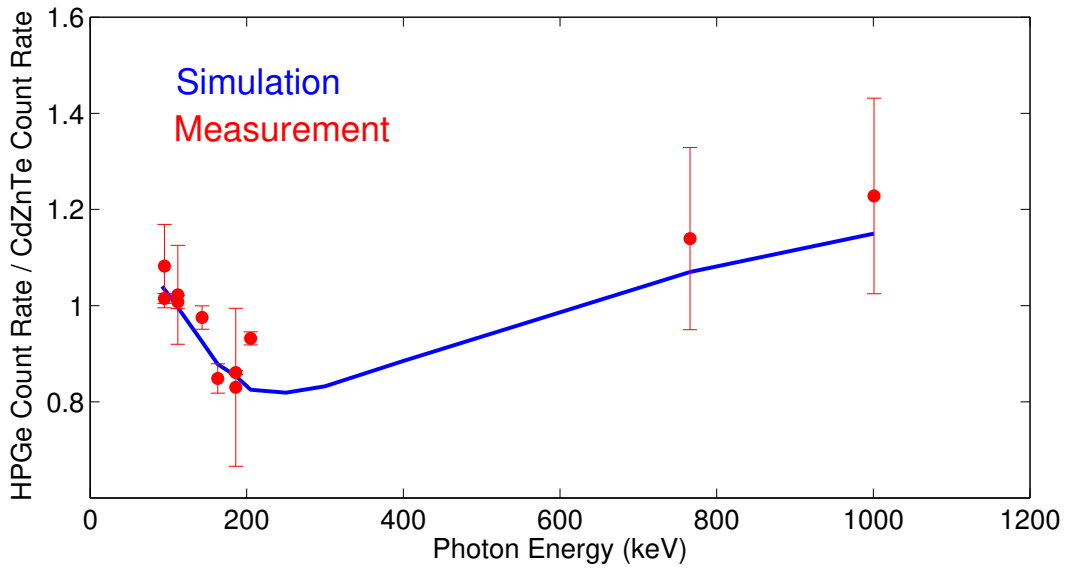
Figure 4.6: Measured net count rate ratios for various uranium gamma-ray lines compared with the expected ratio from Geant4 simulation. The measured net photopeak count rates were calculated using the two spectra shown in Fig. 4.4 from a 0.2 wt% ^{235}U DU sample and a 93 wt% ^{235}U HEU samples.
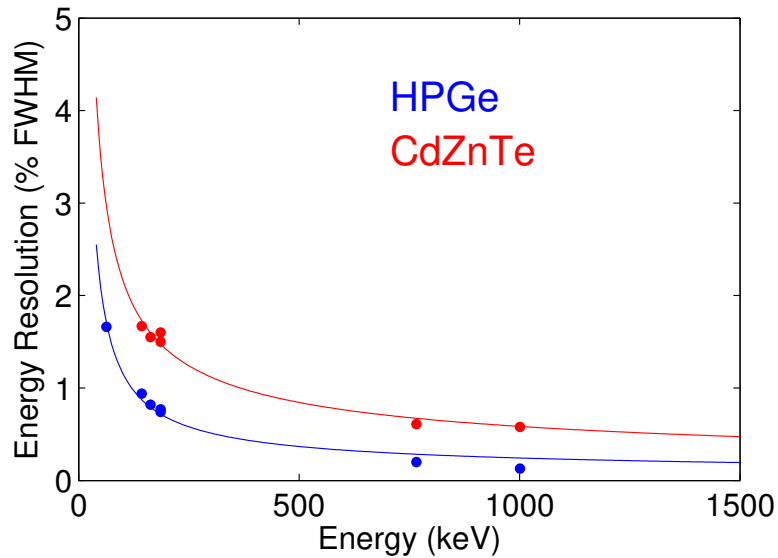
Figure 4.7: Measured energy resolution of HPGe detector and CdZnTe array for characteristic uranium gamma-ray lines. The measured energy resolutions were calculated using the two spectra shown in Fig. 4.4 from a 0.2 wt% ^{235}U DU sample and a 93 wt% ^{235}U HEU sample.
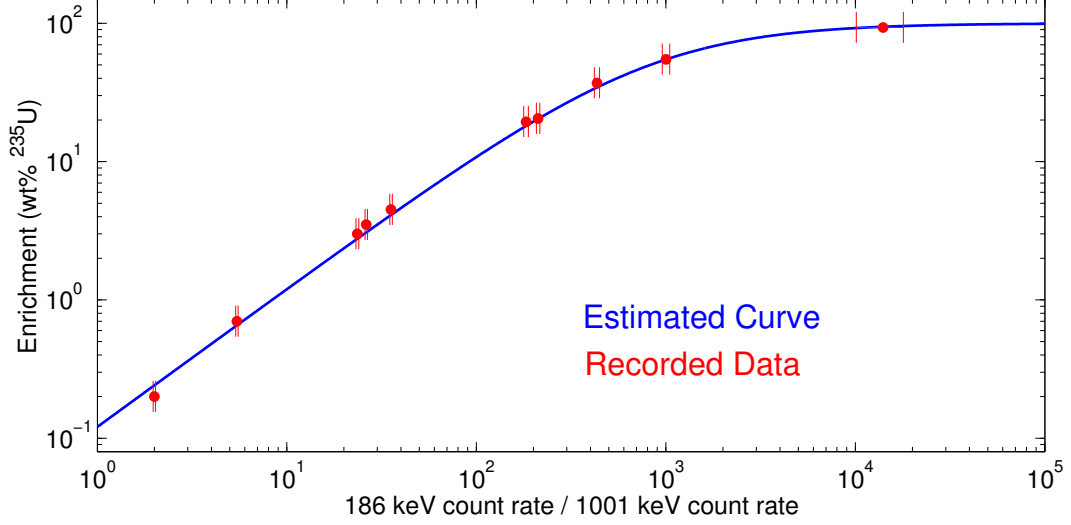
Figure 4.8: Estimated enrichment curve for the source geometry used at the Y-12 National Security Complex. The measured results match the estimated values quite well. This demonstrates that the count rate ratio can be used to predict the enrichment of an unknown sample if the source geometry is known.

CdZnTe detector for the indicated gamma-ray line. $\varepsilon_{\text{escape}}$ is the probability that a source photon of the indicated energy escapes from the source (avoids self-shielding). The detection efficiency ratio can be measured or simulated. For a four detector CdZnTe system, $(\epsilon_{pp186}/\epsilon_{pp1001}) = 9.4$ for photons incident from the cathode side. For the HPGe detector, $(\epsilon_{pp186}/\epsilon_{pp1001}) = 5.9$. Contrastingly, escape probabilities requires *a priori* knowledge about the source or use of information about the source thickness from radiation images. The extent of the source, the source material (uranium metal, UO_2, etc.), and shielding around the source can change this ratio. For the samples measured at Y-12 with a thickness of 3 mm, $(\varepsilon_{\text{escape 186 keV}}/\varepsilon_{\text{esccape 1001 keV}}) = 0.15$. This can be calculated in simple cases, by evaluating Eq. 4.6.

$$\left(\frac{\varepsilon_{\text{escape 186 keV}}}{\varepsilon_{\text{escape 1001 keV}}} \right) \approx \frac{\int_0^D e^{-\mu_1 x} dx}{\int_0^D e^{-\mu_2 x} dx} \tag{4.6}$$

In Eq. 4.6, D is the thickness of the source material, μ_1 is the total attenuation coefficient of the 186 keV gamma-ray line and μ_2 is the total attenuation coefficient of the 1001 keV gamma-ray line. In realistic measurement scenarios, the sample

83
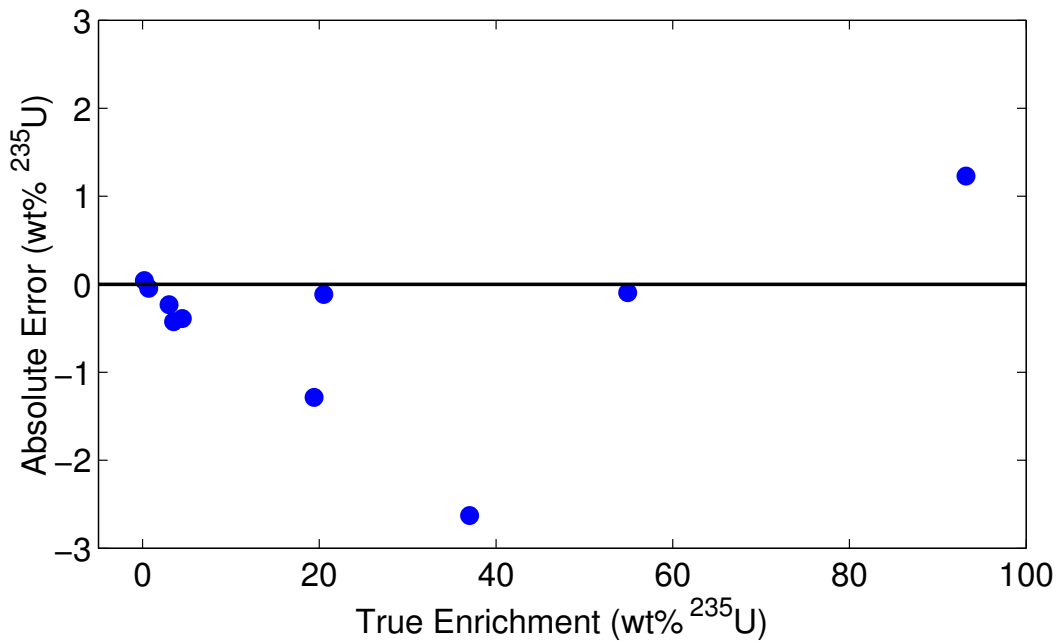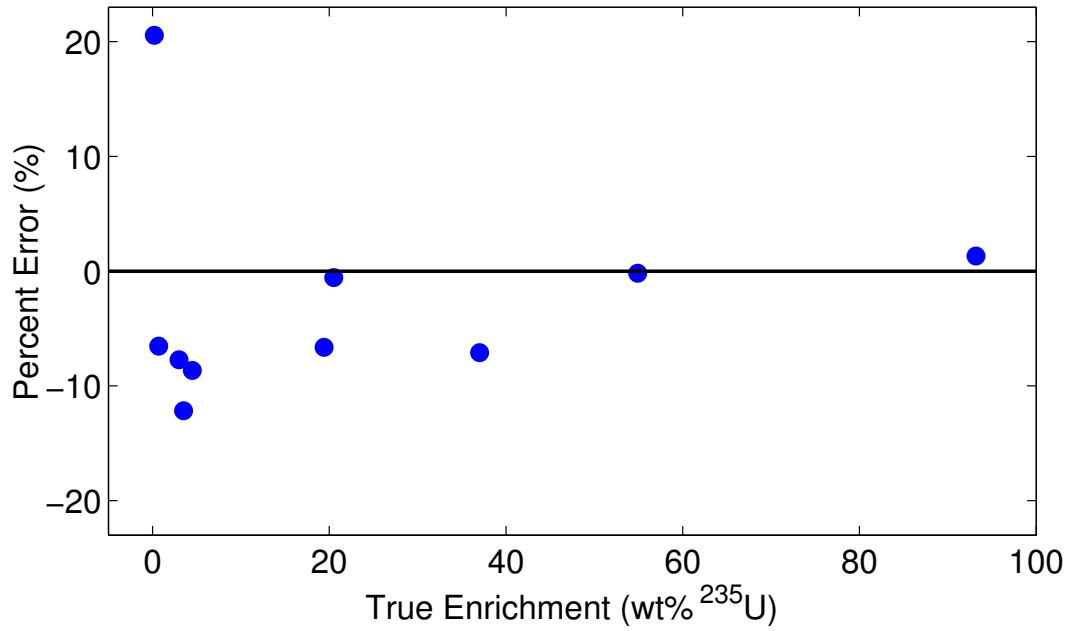
Figure 4.9: Relative error between calculated enrichment using the peak ratio technique and the declared enrichment (top). The absolute error in wt% ^{235}U between the calculated enrichment and the declared enrichment (bottom).

thickness could be estimated using multiple views of the sample from coded aperture gamma-ray imaging [69]. The attenuation coefficient could be estimated by measuring the relative attenuation of the higher energy lines from ^{238}U daughters using photopeak ratios. Eq. 4.5 can be manipulated to calculate the enrichment of the source given the net photopeak count ratio of the two gamma-ray lines. The measured data and the expected distribution of the enrichment as a function of the peak ratio is given in Fig. 4.8. Fig. 4.9 shows the percent error and the absolute error between the calculated enrichment using the described peak ratio technique and the declared enrichment of the sample. Using this method, the enrichment is correctly estimated to within 7% error on average. The largest discrepancy in this model is for the 0.2 wt% ^{235}U sample where the measurement result is incorrect by 20% due to uncertainty in the background-subtraction for the 186 keV photopeak region.

Using this method, the enrichment of the 0.2 wt% ^{235}U DU sample was estimated to be 0.19 ± 0.01 wt% ^{235}U using the spectrum recorded by the HPGe detector. The enrichment was estimated to be 0.24 ± 0.02 wt% ^{235}U using the spectrum recorded by the prototype digital CdZnTe array. The enrichment of the 93 wt% ^{235}U HEU sample was measured to be 91.3 ± 2.5 wt% ^{235}U using the HPGe detector. Using the CdZnTe array, the enrichment was estimated to be 94.4 ± 10.1 wt% ^{235}U. The resolution of the HPGe detector is significantly better for the 1001 keV line leading to lower measurement uncertainties. The superior detection of the 1001 keV line at high enrichments is a significant advantage for the HPGe detector.

4.2.3   Enrichment Estimate from Uranium X-rays

Between 90 and 100 keV, signatures of both ^{238}U and ^{235}U are present [91]. The energies and sources of the various lines are shown in Table 4.1. The gamma-ray energy spectra in the x-ray region recorded using the prototype digital CdZnTe array from various uranium samples are shown in Fig. 4.10. The energy resolution of
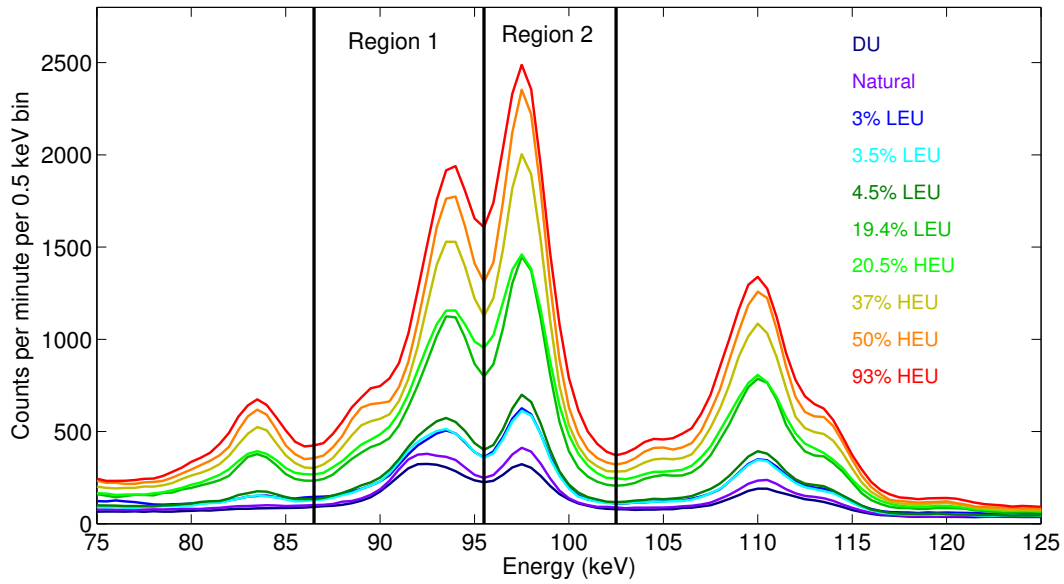
Figure 4.10: Gamma-ray spectra recorded from uranium samples of various enrichments using the digital CdZnTe array system to illustrate the enrichment measurement method using the uranium x-ray region. The two ROIs in the spectra are indicated.
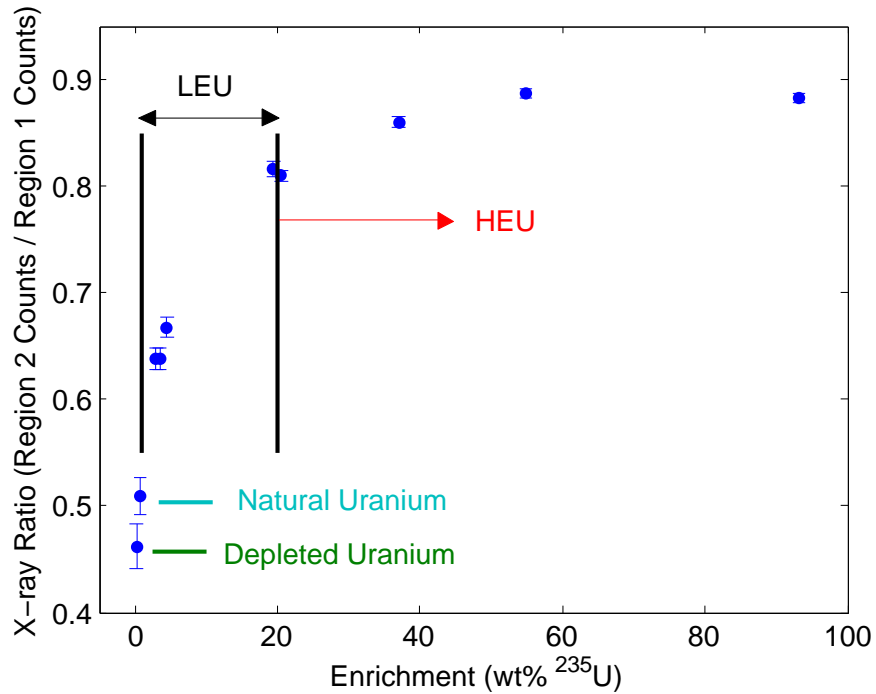
Figure 4.11: Enrichment measurement using uranium x-ray emissions. Various regions of the x-ray ratio indicate different levels of uranium enrichment.
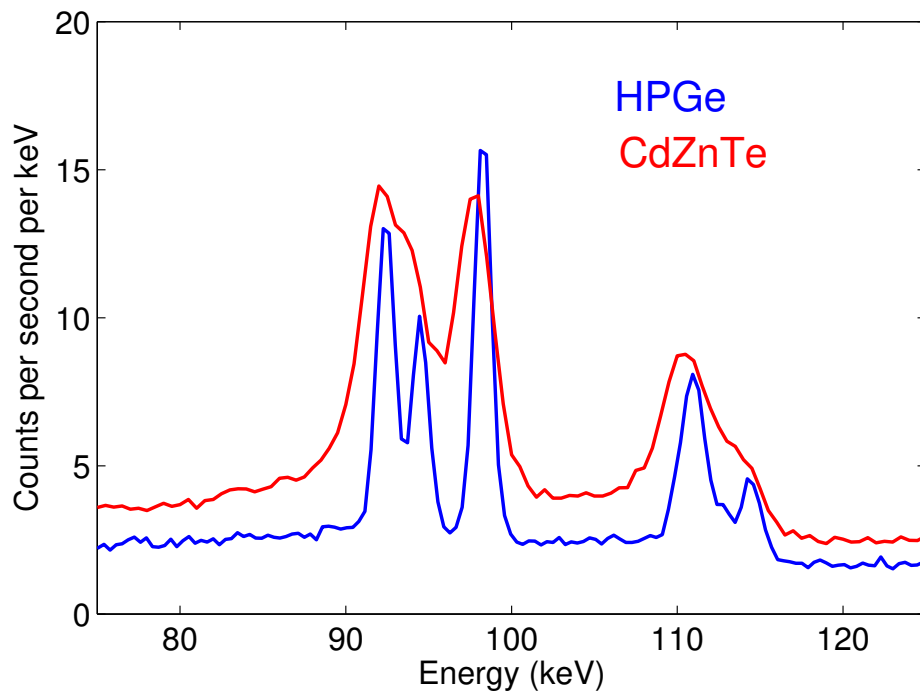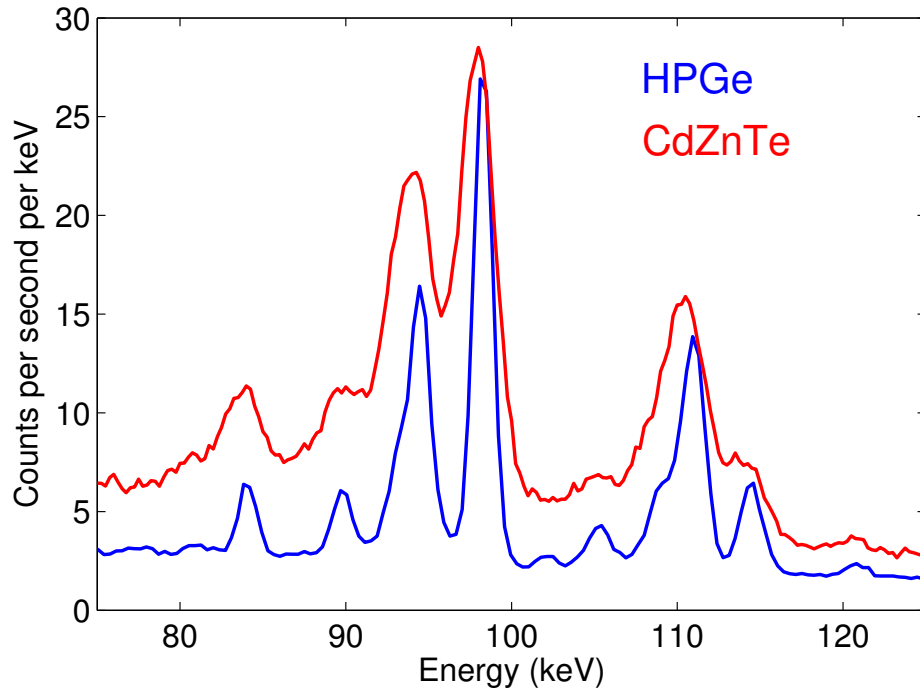
Figure 4.12: Gamma-ray spectra from a 93 wt% ^{235}U HEU disk sample from 25 cm away recorded using prototype digital CdZnTe array system and a commercially available mechanically cooled HPGe detector (top) and spectra from a 0.2 wt% ^{235}U DU sample (bottom) focused on the x-ray region (75-125 keV).

Table 4.1: Energies and branching ratios of photons in the x-ray energy region from uranium samples.

Photon Energy (keV)	Photon Source	Branching Ratio (%)
81.23	^{231}Th γ-ray (^{235}U)	0.89
82.09	^{231}Th γ-ray (^{235}U)	0.4
84.21	^{231}Th γ-ray (^{235}U)	6.6
89.95	^{231}Th γ-ray (^{235}U)	0.94
89.96	Th Kα_2 x-ray	-
92.28	Pa Kα_2 x-ray	-
92.38	^{234}Th γ-ray (^{238}U)	2.81
92.8	^{234}Th γ-ray (^{238}U)	2.77
93.35	Th Kα_1 x-ray	-
94.65	U Kα_2 x-ray	-
95.86	Pa Kα_1 x-ray	-
96.09	^{235}U γ-ray	0.086
98.43	U Kα_1 x-ray	-

CdZnTe detectors does allow one to measure the enrichment of a uranium sample by comparing the ratio of counts in the region between 95.5 keV and 106 keV (Region 2 in Fig. 4.10) and the region between 86 keV and 95.5 keV (Region 1 in Fig. 4.10) [92]. The enrichment can be determined from the ratio of counts in Region 2 to Region 1 because the impact of the ^{234}Th lines around 92 keV decrease as enrichment increases. The intensity of the Kα x-rays from uranium increases as enrichment increases, but the ratio of Kα_1 to Kα_2 does not change, so fewer events from ^{234}Th increases the ratio. At very high enrichments, the 89.95 keV gamma-ray from ^{231}Th adds to the number of counts in Region 1, degrading the results. However, as demonstrated in Fig. 4.11, this method can effectively discriminate DU, natural uranium, low-enriched uranium (LEU), and HEU. The intrinsic photopeak efficiency of 1.5 cm thick CdZnTe

detectors is more than 96% for photons at these energies, so no efficiency calibration is required for this method. Very thin samples may not produce enough x-rays to use this simple uranium enrichment measurement method.

Contrastingly, the energy resolution of HPGe allows one to separate the characteristic gamma-ray lines in order to more accurately quantify the enrichment. As shown in Fig. 4.12, the germanium detector is able to resolve the gamma-ray lines around 92 keV which are characteristic of ^{238}U. Then, photopeak count ratios may be used to estimate the uranium enrichment by comparing the relative intensity of the gamma-ray lines characteristic of ^{238}U with the gamma-ray lines characteristic of ^{235}U (84 and 90 keV) [93].

4.3 Determination of Plutonium Isotopic Composition

Plutonium grade, much like uranium enrichment, determines whether the material can be used in a nuclear weapon. The plutonium grade can be measured using photopeak ratios [51]. Most often, users are interested in the ratio between ^{239}Pu and ^{240}Pu because the spontaneous fission rate of ^{240}Pu limits the capability of the material to be weaponized. While many methods for measuring plutonium grade use ratios of lines below 200 keV [94], this work focuses on using the gamma-ray emissions between 630 and 670 keV to measure plutonium grade because these lines are significantly more penetrating through intervening material. However, excellent energy resolution is required to discriminate the gamma-ray lines caused from the decay of three isotopes: ^{239}Pu, ^{240}Pu, and ^{241}Am [95]. Table 4.2 provides a list of gamma rays in this energy region and the radioisotope source.

Fig. 4.13 compares the measured gamma-ray energy spectrum from a 5 kg disk of 95 wt% ^{239}Pu recorded on the prototype digital readout CdZnTe system and the energy spectrum from the same object recorded with a field-deployable high-purity germanium gamma-ray spectrometer [89]. Particularly between 300 and 450 keV,

Table 4.2: Photon sources, energies, and activities from plutonium samples in the range of 630 keV to 670 keV. The isotopic composition of the sample can be estimated using gamma-ray lines in this energy range.

Isotope	Energy (keV)	Activity (γ's / s-g)
^{241}Am	633.0	1.59×10^3
^{239}Pu	633.2	5.80×10^1
^{239}Pu	637.8	5.87×10^1
^{239}Pu	640.1	1.88×10^2
^{241}Am	641.4	8.98×10^3
^{240}Pu	642.5	1.05×10^3
^{239}Pu	646.0	3.42×10^2
^{239}Pu	649.3	1.63×10^1
^{239}Pu	650.5	6.19×10^0
^{239}Pu	652.1	1.50×10^2
^{241}Am	653.0	4.77×10^4
^{239}Pu	654.9	5.16×10^1
^{239}Pu	658.9	2.22×10^2
^{241}Am	662.4	4.61×10^5
^{239}Pu	664.6	3.80×10^1
^{239}Pu	668.2	9.02×10^{-1}

there are some distinct photopeaks in the HPGe spectrum that are unresolvable in the CdZnTe single-pixel events energy spectrum.

Other notable differences include the more prominent 511 and 558 keV photopeaks in the CdZnTe spectrum. The 558 keV peak arises from thermal neutron capture on ^{113}Cd. Approximately 75% of all thermal neutron captures on ^{113}Cd result in a 558 keV photon emission from nuclear de-excitation. The cross section for thermal neutron capture is large for ^{113}Cd (20,600 barns) so that 96% of thermal neutrons are
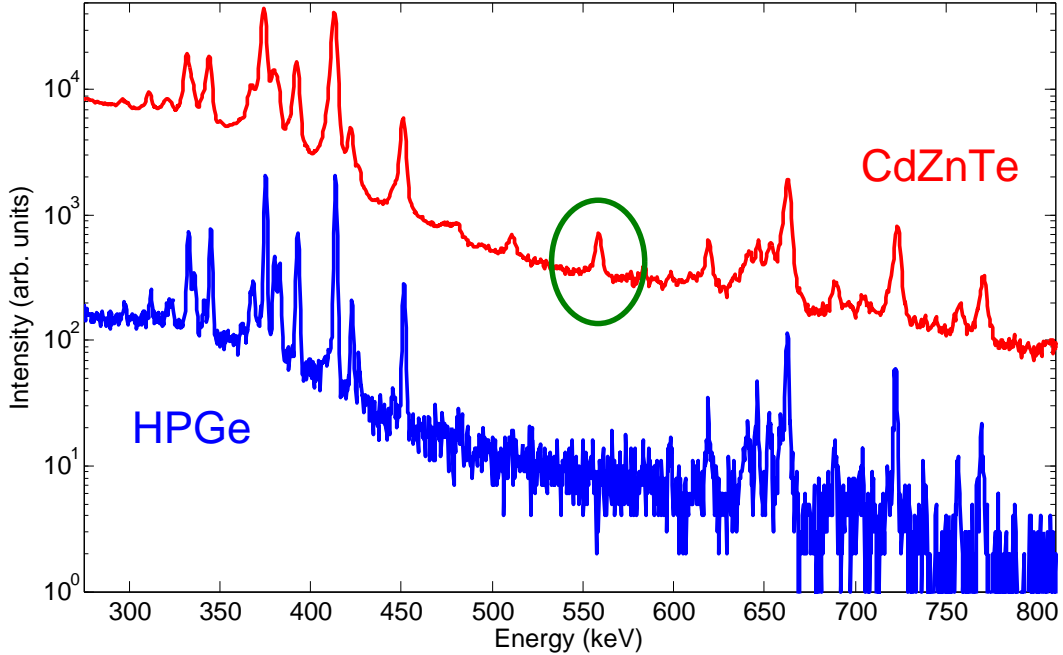
Figure 4.13: Comparison of recorded gamma-ray spectrum from plutonium source recorded with a field-deployable HPGe detector and the prototype CdZnTe system. The 558 keV peak indicative of thermal neutron capture is shown circled in green. The source was measured for ten hours.

absorbed within 1 mm of the surface of the CdZnTe detector. The 558 keV photopeak is a useful indicator that a neutron source is present because fast neutrons thermalize in the environment and are then absorbed on the CdZnTe detector surface. HPGe does not have a comparable indicator of a neutron source. The 511 keV peak is also more prominent in the CdZnTe spectrum due to thermal neutron capture on cadmium. The total energy released following a capture on cadmium is around 9 MeV. Some of the gamma rays emitted in the cascade will be of high energy (much greater than 1 MeV). These gamma rays undergo pair production in the environment which results in a higher number of annihilation photons. In addition, the plutonium source was driven with an AmBe neutron source during the CdZnTe measurement. This would have resulted in more fission-energy gamma rays which may be the source of more annihilation photons in the energy spectrum recorded with CdZnTe.

In the 600 to 700 keV region, where the isotopic composition of plutonium can
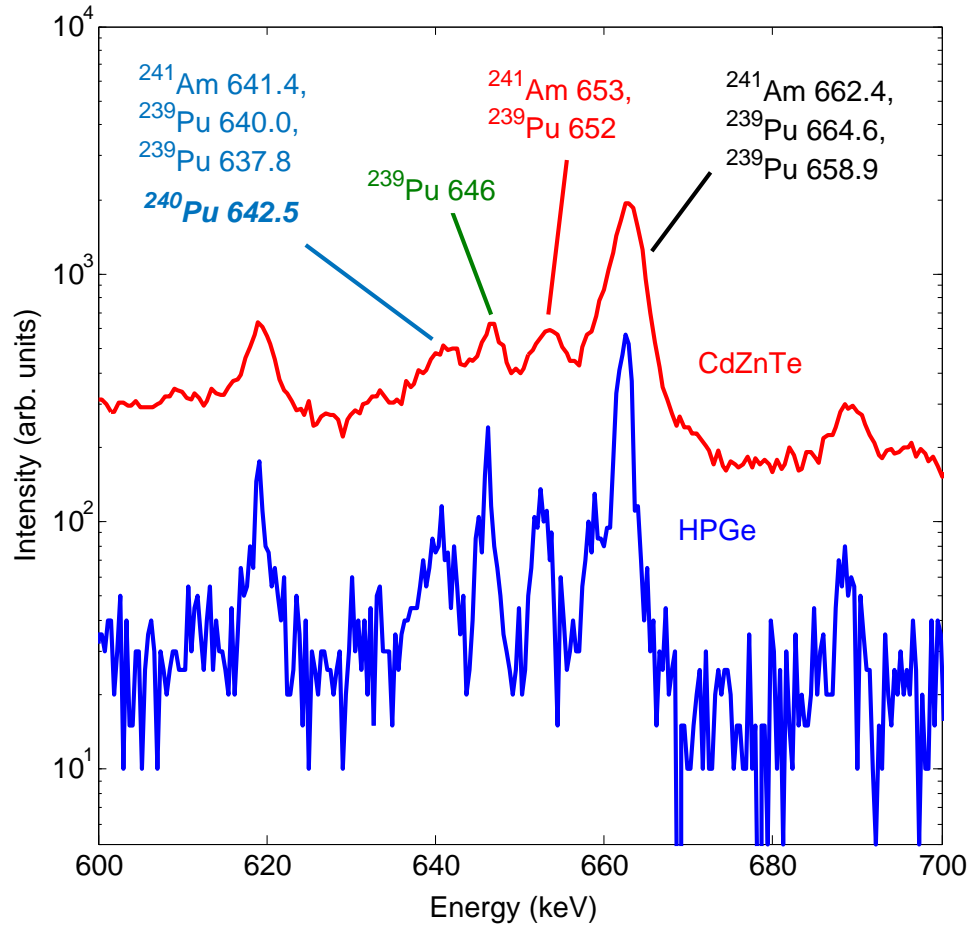
Figure 4.14: Comparison of recorded gamma-ray energy spectra from a plutonium sample recorded with a field-deployable HPGe detector and the prototype digital CdZnTe array system in the ROI where the isotopic composition of plutonium can be ascertained. The four areas of interest are indicated.

be ascertained, the energy spectrum recorded with HPGe shows more separated photopeaks than the CdZnTe spectrum as shown in Fig. 4.14. However, the peaks are similarly resolvable in both spectra. Some peaks that are not resolvable using CdZnTe are also unresolvable in the HPGe spectrum. For instance, between 648 and 655 keV, there should be two separable lines; however, only one peak is present in both spectra. The separation is slightly better for the region between 655 and 665 keV using the HPGe sensor, but it is still very challenging to obtain different peak areas for each line.

In order to measure the fraction of ^{240}Pu in the sample, the relative intensity of

^{239}Pu must first be estimated from the 646 keV peak. This is a true signature of only ^{239}Pu content, not contaminated by other lines. Then, the relative amount of ^{241}Am can be estimated from the two peak regions between 650 keV and 665 keV accounting for the amount of ^{239}Pu. Finally, the ^{240}Pu content is estimated from the region between 635 keV and 642 keV accounting for the estimated quantities of ^{241}Am and ^{239}Pu calculated from the other regions. Los Alamos National Laboratory provided analysis assistance to estimate the plutonium grade using this general method and enhanced peak fitting. The estimated ratio of ^{240}Pu to total plutonium content was 3.63 ± 1.02 wt% ^{240}Pu. The estimate was within two standard deviations of the true grade of 5.02 wt% ^{240}Pu. Further improvement of energy resolution by using lower noise ASICs and improved CdZnTe material will improve the accuracy and precision of plutonium isotopic composition measurements.

The energy resolution of CdZnTe spectrometers has improved to the point where measuring plutonium isotopic composition is now possible [96]. CdZnTe detectors also offer signatures indicative of neutrons which is important for national and homeland security applications and will be discussed thoroughly in Chapter V.

4.4 Characterization of Intervening Materials

Shielded SNM in the form of HEU or weapon-grade plutonium (WGPu) can be extremely difficult to detect, identify, and characterize [97]. This work assumes that shielded SNM has been detected and identified; now the material needs to be characterized. The characterization includes estimating the isotopic composition of the source and determining its physical configuration [68]. In order to properly estimate the isotopic composition of the sample using raw count rates or photopeak ratios of gamma-ray lines, the unshielded emission rate needs to be determined [98, 99]. Therefore, one must correct for shielding material attenuation in order to accurately estimate the isotopic composition of the sample [83, 100]. In addition to correcting

the recorded gamma-ray spectrum to obtain the true emission spectrum from the source, identifying the shielding materials can inform the response to a discovered source and provide insight regarding the configuration of the SNM containing device if it cannot be optically observed.

Many efforts to calculate the composition of shielding materials rely on template matching techniques [101]. These methods require a number of simulated or measured spectra which are fit to new data in order to estimate the true source activity or characterize intervening materials. Other solutions use cross sections and user input parameters to estimate the detector response to different photon sources and intervening materials [102]. The fit with the smallest squared residual difference between the expected spectrum and the recorded data is selected as the most likely source configuration. Others have suggested using Bayesian approaches for estimating sample configurations [103], but Ref. [103] assumed that intervening materials were known and attempted to calculate plutonium mass. These approaches are required for low-resolution spectrometers. This work uses direct spectroscopic information which is possible when a high-resolution spectrometer is employed.

4.4.1 Ratios of Gamma-ray Line Attenuation

Because uranium samples emit multiple gamma-ray lines, it is possible to estimate attributes of shielding materials based on the attenuation of different gamma-ray energies [104]. The most prominent gamma-ray lines from ^{235}U occur at 143.8 keV, 163.4 keV, 185.7 keV, 202.1, and 205.3 keV [51]. The 202.1 keV line is grouped with the 205.3 keV line to calculate photopeak ratios since the energy resolution of the detector is not sufficient to resolve it. In order to identify the shielding material and its thickness, a photopeak ratio technique was employed.

Consider the attenuation of two different gamma-ray lines through a shielding material. The intensity of the lines after passing through the shield can be calculated

94

using Eq. 4.7 and Eq. 4.8 [3].

$$I_1 = I_{01}e^{-\left(\frac{\mu}{\rho}\right)_1 \cdot \rho x} \tag{4.7}$$

$$I_2 = I_{02}e^{-\left(\frac{\mu}{\rho}\right)_2 \cdot \rho x} \tag{4.8}$$

In Eqs. 4.7 and 4.8, I is the intensity of the line after passing through the shielding material, I_0 is the initial intensity of the line at the surface of the source, μ is the linear attenuation coefficient of the shielding material which depends on the gamma-ray energy and the Z number of the shield, ρ is the mass density of the shielding material, and x is the thickness of the shield. The subscripts indicate gamma-ray lines of different energies. Eqs. 4.7 and 4.8 can be combined as shown in Eq. 4.9.

$$\frac{I_1}{I_2} = \frac{I_{01}}{I_{02}}e^{-\left[\left(\frac{\mu}{\rho}\right)_1 - \left(\frac{\mu}{\rho}\right)_2\right] \cdot \rho x} \tag{4.9}$$

The natural logarithm linearizes the expression as shown in Eq. 4.10 [71, 105].

$$\ln\left(\frac{I_1}{I_2}\right) - \ln\left(\frac{I_{01}}{I_{02}}\right) = \left[\left(\frac{\mu}{\rho}\right)_2 - \left(\frac{\mu}{\rho}\right)_1\right] \cdot \rho x \tag{4.10}$$

The mass attenuation coefficient, (μ/ρ), for a given gamma-ray energy is simply a function of the effective atomic number of the shielding material, Z_{eff}.

Using the known mass attenuation coefficient as a function of atomic number for each gamma-ray line, expected photopeak ratios are calculated as a function of the atomic number and density-thickness product of the shield (ρx). The density-thickness product is also referred to as the mass thickness or areal density of the shield [3]. The measured photopeak ratio is compared to the expected ratio for each effective Z number and mass thickness. The residual (squared difference) between the left-hand side (measured quantity) and right-hand side (expected value) of Eq. 4.10
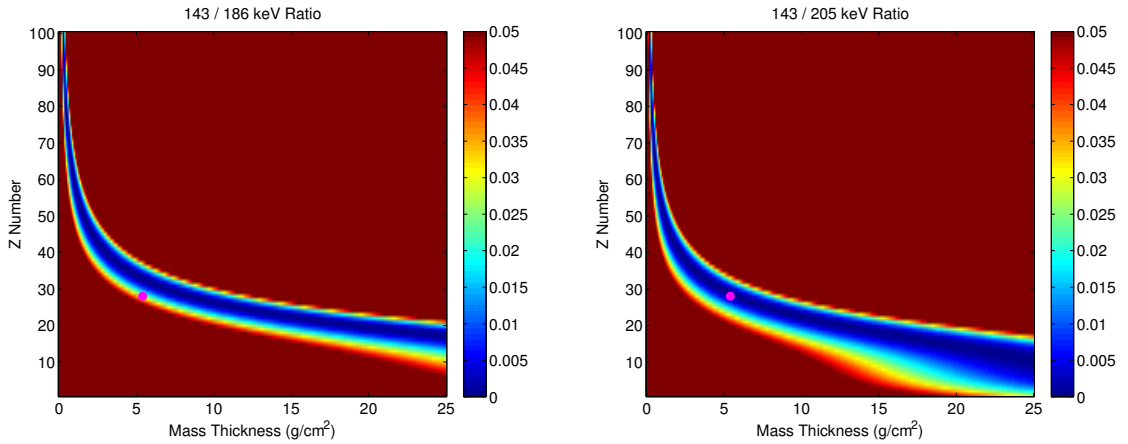
Figure 4.15: Simultaneous estimate of the effective atomic number and the thickness of the shielding material using the gamma-ray line attenuation ratio technique described. The magenta dot shows the true effective atomic number and mass-thickness, ρx, of the shield.
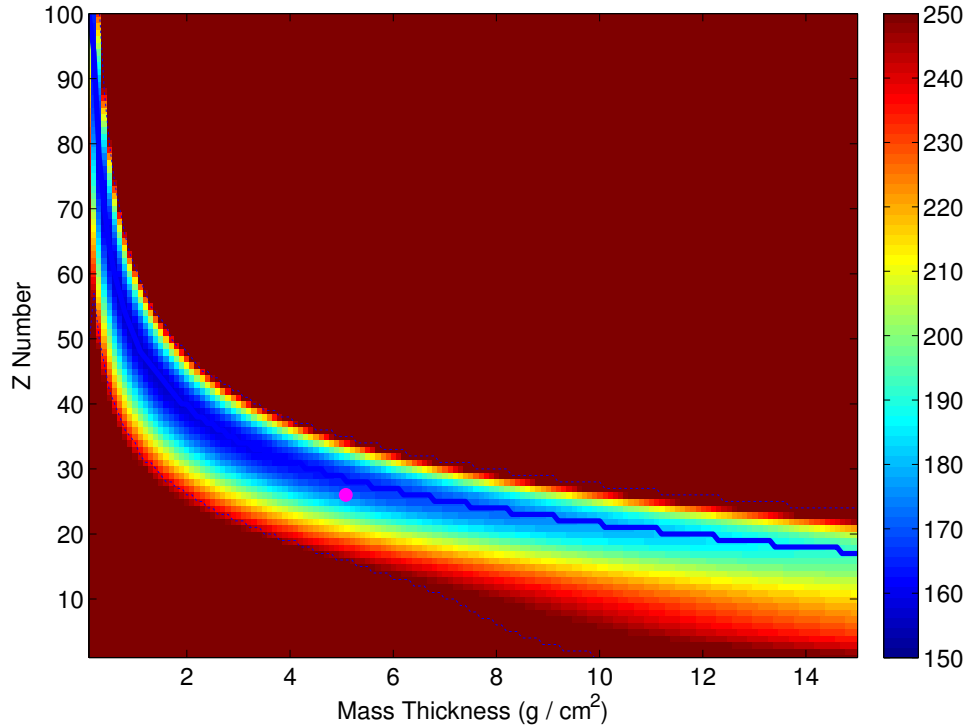
Figure 4.16: Combined residuals from all of the gamma-ray line intensity comparisons to estimate the effective atomic number and the thickness of the shield. The true combination of mass thickness and effective atomic number is shown with the magenta dot. A line representing the effective atomic number with the lowest combined residual as a function of mass-thickness is overlaid in blue. There is a small systematic overestimate of Z number using this method which is further explored in Section 4.4.4.

is used to quantify the agreement between measurement and theory for a particular combination of mass thickness and effective Z number. For some mass-thickness, $(\rho x)_i$ and effective atomic number, $Z_{\text{eff},j}$ which provides mass attenuation coefficients, $(\mu/\rho)_{2j}$ and $(\mu/\rho)_{1j}$, the residual value, r_{ij}, is calculated in Eq. 4.11.

$$r_{ij}^2 = \left[\ln\left(\frac{I_1}{I_2}\right) - \ln\left(\frac{I_{01}}{I_{02}}\right) - \left[(\frac{\mu}{\rho})_{2j} - \left(\frac{\mu}{\rho}\right)_{1j}\right] \cdot (\rho x)_i \right]^2 \tag{4.11}$$

In Eq. 4.11, (I_1/I_2) is the measured net photopeak count ratio for two characteristic gamma-ray lines and (I_{01}/I_{02}) is the expected photopeak count ratio if no shielding is present. The residual results for two line ratios from a uranium measurement are shown in Fig. 4.15. The dark blue areas in Fig. 4.15 have the lowest residuals and are the most probable combinations of shielding material parameters to produce the observed attenuation. In Fig. 4.16, the residuals from all six line ratios are combined into one metric by weighting the residuals by the propagated error as shown in Eq. 4.12. There is no definitive point where the residual is lowest.

$$R_{ij}^2 = \sum_{k=1}^{6} \left(\frac{r_{ijk}^2}{\sigma_k^2}\right) \tag{4.12}$$

In Eq. 4.12, r_{ijk} is the residual of the kth photopeak ratio for one effective atomic number and mass thickness combination, and σ_k is the propagated uncertainty in the measured net photopeak count ratio of the kth gamma-ray line combination.

For this method to work, the isotope must be identifiable. This means that the photopeaks must be visible above the continuum in order to measure the net intensity of the line. The term (I_{01}/I_{02}) is known for a given sample configuration and thickness. This term will also account for the branching ratios of the different gamma-ray lines from ^{235}U. For uranium samples, the initial intensity ratio does not vary with enrichment. It does vary slightly with the material composition and uranium thickness. Fig. 4.17 shows how the line ratios are affected by the thickness of the sample.

97
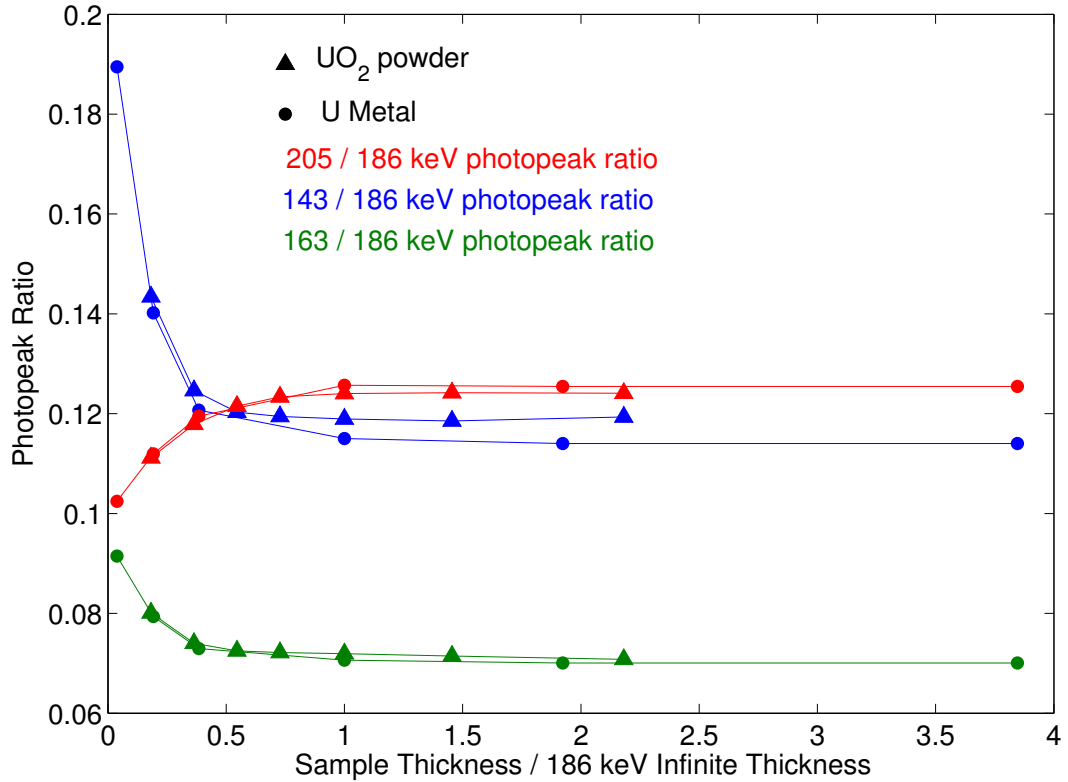
Figure 4.17: Intensity ratios for gamma-ray lines as a function of the sample thickness for uranium metal (circles) and UO_2 powder (triangles). The infinite thickness for the 186 keV emission is given in the PANDA manual for various uranium compositions. These results were simulated in Geant4.

The data for Fig. 4.17 were generated using the Geant4 simulation package [90].

The results for three different measured steel thicknesses are given in Fig. 4.18. The source was a 20 wt% ^{235}U metal disk, 3 cm in diameter and 0.3 cm thick. The steel shields were 30×30 cm^2 planar slabs. The lines in Fig. 4.18 show the possible combinations of shield thickness and atomic numbers which could account for the measured attenuation differences of the various gamma-ray lines. For shields made from large atomic number materials, characteristic x-rays could be used to identify the shielding type. This has been experimentally demonstrated with tungsten and lead shields [71].

While useful information can be extracted using the attenuation method, it cannot definitively predict the shielding thickness and effective atomic number of the shield.
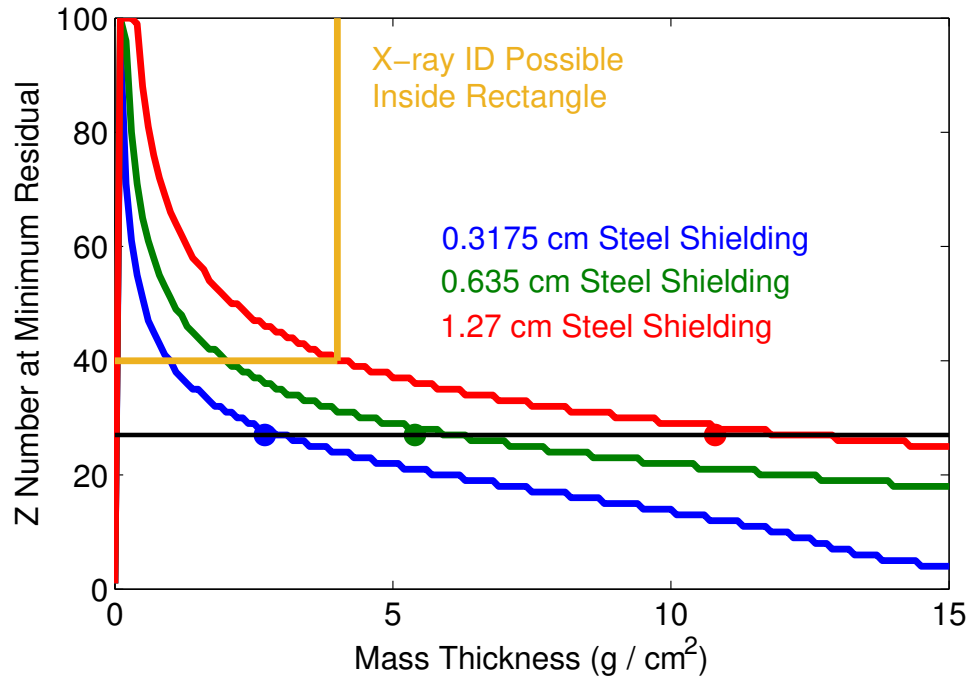
Figure 4.18: Lowest residual atomic number for each mass thickness for three different steel shielding thicknesses. The true combinations of material and mass thickness are shown using the large circles. The yellow region is the area where characteristic x-rays may be available to reveal the identity of the shielding material.

As a result the estimated unattenuated intensities of gamma-ray lines from different isotopes cannot be uniquely determined. More information is required.

4.4.2 Forward Compton Scattering

While the photoelectric absorption cross section depends considerably on the effective atomic number of the shield, the probability of Compton scattering depends on the number of electrons a photon encounters as it travels through the shield, which correlates strongly with mass thickness. Differences in recorded energy spectra due to Compton scattering in the shield are illustrated in Fig. 4.19. The spectra were taken with a 20 wt% ^{235}U sample of uranium metal through various thicknesses of shielding. Note that above 210 keV, the background gamma intensity is about the same for all of the measurements except for when 2.54 cm of steel shielding is used. Notice that the intensity of the 186 keV photopeak is reduced when 0.3175 cm of steel
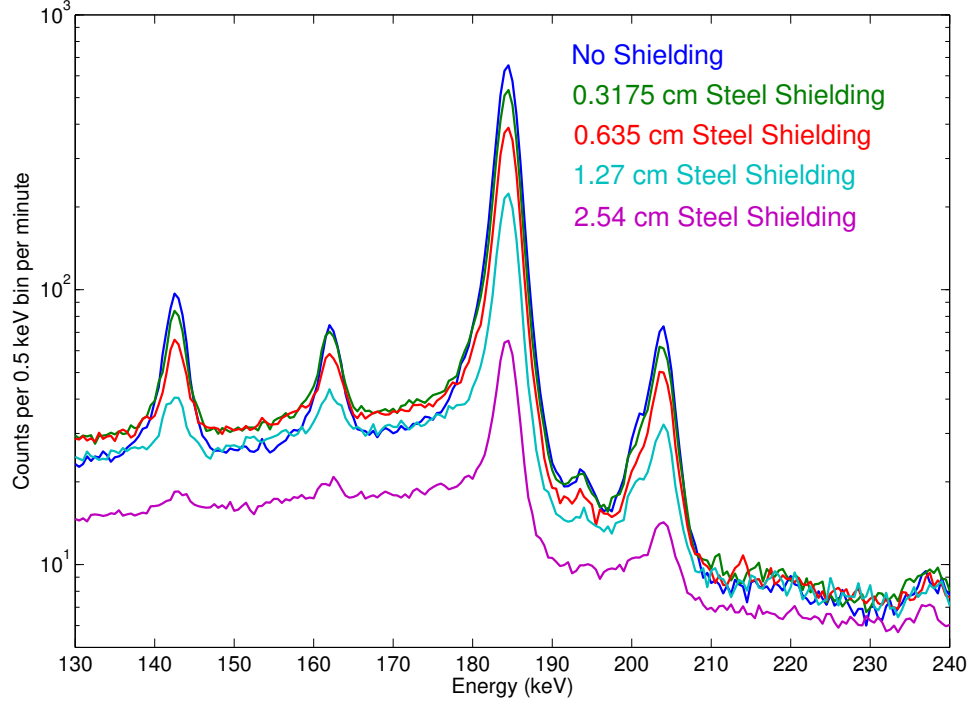
Figure 4.19: Gamma-ray energy spectra of a 20 wt% ^{235}U uranium metal sample from Y-12 with various thicknesses of steel shielding between the source and detection system. Each configuration was measured for 30 minutes.

is used to shield the source. However, the continuum to the left of the peak (166 - 176 keV) is higher when the shield is present due to forward Compton scattered 186 keV gamma rays in the steel.

Scattered photons in shielding have been explored before to assist spectral fitting techniques estimate the identity and thickness of intervening materials [106]. However, this work presents a method to directly measure shielding mass thickness using ratios of net counts in ROIs.

The probability that a photon incident on a shield scatters once in dx about x into solid angle $d\Omega$ about Ω and escapes is the product of four probabilities. First is the probability that a photon reaches some shield depth, x, without undergoing an interaction, given in Eq. 4.13 where $\mu_{t,1}$ is the total linear attenuation coefficient of the shield.

$$P(\text{unnattenuated to x}) = e^{-\mu_{t,1}x} \tag{4.13}$$

Then, the photon must interact within some depth slice, dx, of the shield, the probability of which is given in Eq. 4.14.

$$P(\text{interact in dx}) = \mu_{t,1}dx \tag{4.14}$$

Then, the interaction must result in the photon scattering into some solid angle, $d\Omega$, which is given by Eq. 4.15 where σ_t is the total interaction cross section and $\frac{d\sigma_c}{d\Omega}$ is the Klein-Nishina cross section.

$$P(\text{scatter within } d\Omega) = \frac{1}{\sigma_t}\frac{d\sigma_c}{d\Omega}d\Omega \tag{4.15}$$

Finally, the scattered photon has to escape the remainder of the shield without undergoing another interaction, the probability of which is given in Eq. 4.16

$$P(\text{scattered photon escapes shield}) = e^{-\mu_{t,2}(D-x)} \tag{4.16}$$

where D is the thickness of the shield, and $\mu_{t,2}$ is the linear attenuation coefficient for the scattered photon. In truth, the path length will be longer, but by making Ω small, one can make the assumption that the true path length, l, approximately equals $D - x$ as $d\Omega$ goes to zero. By integrating over the thickness of the shield from $x = 0$ to $x = D$ and over acceptable forward-scattering angles, from $\Omega = \Omega_i$ to $\Omega = \Omega_f$, where Ω_f is the largest acceptable scattering angle, the ratio of events which are scattered through a small angle to the incident flux can be calculated as shown in Eq. 4.17 where C is the rate of events which undergo small-angle Compton scattering in the shield and escape it without further attenuation and I_0 is the incident photon flux.

$$\frac{C}{I_0} = \int_{\Omega_i}^{\Omega_f} \int_0^D \left(e^{-\mu_{t,1}x}\right) \left(\mu_{t,1}dx\right) \left(\frac{1}{\sigma_t}\frac{d\sigma_c}{d\Omega}d\Omega\right) \left[e^{-\mu_{t,2}(D-x)}\right] \qquad (4.17)$$

The largest acceptable scattering angle for uranium samples is limited by contamination of the 163 keV photpeak. For the proof of principle in this work, $\Omega_f \approx 50°$ and $\Omega_i \approx 30°$. If one assumes that the linear attenuation coefficient does not change after scattering (i.e. $\mu_{t,1} = \mu_{t,2} = \mu_t$), Eq. 4.17 can be simplified to Eq. 4.18.

$$\frac{C}{I_0} = e^{-\mu_t D} \int_0^D \mu_t dx \int_{\Omega_i}^{\Omega_f} \frac{1}{\sigma_t}\frac{d\sigma_c}{d\Omega}d\Omega \qquad (4.18)$$

$$\frac{C}{I_0} = \mu_t D \ e^{-\mu_t D} \int_{\Omega_i}^{\Omega_f} \frac{1}{\sigma_t}\frac{d\sigma_c}{d\Omega}d\Omega \qquad (4.19)$$

Eq. 4.19 can be thought of as a product of three probabilities. The term $\mu_t D$ is the probability that the photon interacts once within the shield, $e^{-\mu_t D}$ is the probability that the photon traverses the shield without further interactions, and the integral represents the probability that the interaction was a Compton scattering event to within the specified solid angle. These equations were verified using a Geant4 simulation and with measured data. A demonstration of the agreement between the model and simulated data is shown in Fig. 4.20.

Rather than compare the rate of events Compton scattered to the incident flux, one must compare it to the unattenuated photon rate exiting the shield because that is what the spectrometer actually measures. The unattenuated photon flux exiting the shield is given by Eq. 4.20 where U is the unattenuated photon flux.

$$\frac{U}{I_0} = e^{-\mu_t D} \qquad (4.20)$$
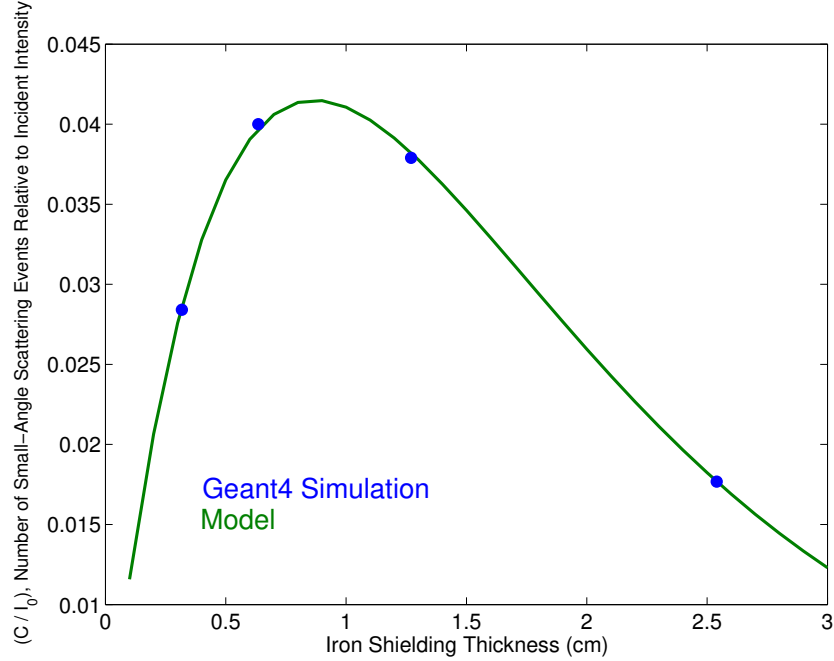
Figure 4.20: Proportion of events which undergo small-angle Compton scattering in an iron shield versus the thickness of the iron shield. Good agreement between the analytical model and simulation is observed.

Combining Eq. 4.19 and Eq. 4.20 results in Eq. 4.21

$$\frac{C}{U} = \mu_t D \, \frac{1}{\sigma_t} \int\limits_{\Omega_i}^{\Omega_f} \frac{d\sigma_c}{d\Omega} d\Omega = \rho D \, \frac{\mu_t}{\rho} \frac{1}{\sigma_t} \int\limits_{\Omega_i}^{\Omega_f} \frac{d\sigma_c}{d\Omega} d\Omega \tag{4.21}$$

where ρ is the mass density of the shield. Eq. 4.21 can be simplified because the macroscopic mass attenuation coefficient is related to the microscopic cross section by Eq. 4.22 where A is the relative atomic mass of the shield and u is the atomic mass unit.

$$\frac{\mu_t}{\rho} = \frac{\sigma_t}{uA} \tag{4.22}$$

Finally, because the Klein-Nishina cross section is proportional to the effective atomic number of the shield, the ratio of photons Compton scattered in the forward direction to the unattenuated photon flux is proportional to the mass thickness and atomic number of the shield as shown in Eq. 4.23. Note that ρD in Eq. 4.23 is the same

parameter as ρx in Eq. 4.10, the mass thickness.

$$\frac{C}{U} \propto \rho D \left(\frac{Z}{uA}\right) \tag{4.23}$$

In practice, background-subtracted counts in the 186 keV photopeak and 166-176 keV forward-scattered region are compared. This ROI was selected because it was below the low energy tail of the 186 keV photopeak and above the influence of the 163 keV photopeak. Also, the 186 keV line is the most prominent, so more source photons will be scattered in the shield from this line than others. In order to account for the photons scattered in the forward direction by the source itself and the detection apparatus, the net counts in the small-angle Compton scattering region needs to be multiplied by a factor, β. This β factor was found to be 5% experimentally by measuring the amount of scatter in the 166-176 keV region without a shield present. Eq. 4.24 describes how to calculate the measured small-angle Compton scattering ratio.

$$\frac{I_{\text{small angle Compton Scattering}}}{I_{\text{unattenuated}}} = \frac{C}{U} = \frac{(A_{CS} - B) - \beta (A_{PP} - B)}{(A_{PP} - B)} \tag{4.24}$$

The left-hand side of Eq. 4.24 is equivalent to the left-hand side of Eq. 4.23. A_{CS} is the area in the small-angle Compton scattering region, B is the estimated background, and A_{PP} is the photopeak area. Fig. 4.21 demonstrates these regions on a measured uranium spectrum.

Once again, using this model, the expected ratio of forward-scattered photons to unattenuated source photons as a function of effective Z number and mass thickness is calculated. The expected ratio of forward-scattered photons to unattenuated source photons is compared with the measured ratio in the same fashion as photopeak attenuation was in Sect. 4.4.1. The expected ratio is calculated from linear fits of nuclear data based on Eq. 4.23. A residual plot is generated as shown in Fig. 4.22 which pro-
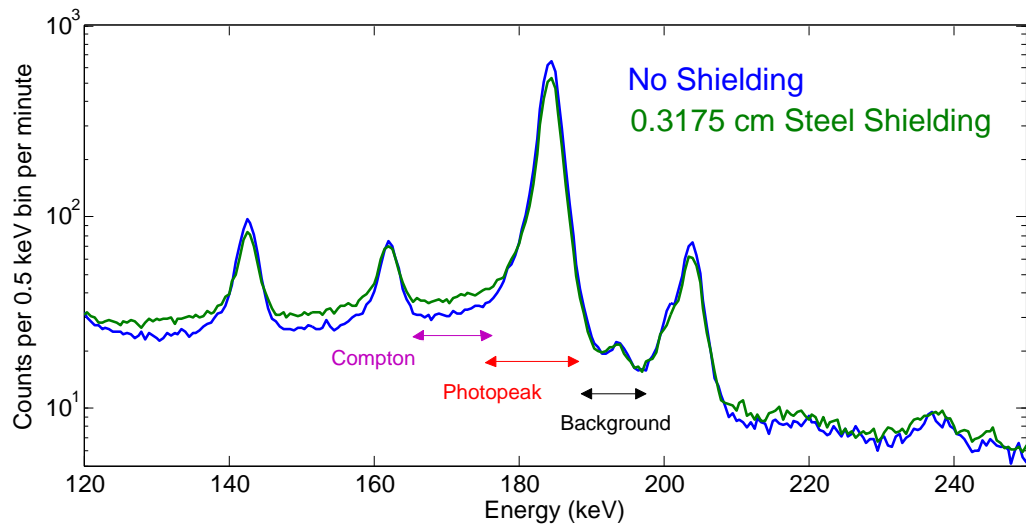
Figure 4.21: Illustration of the regions used to calculate the ratio of source 186 keV source photons that undergo small-angle Compton scattering in the intervening material to the unattenuated 186 keV intensity.
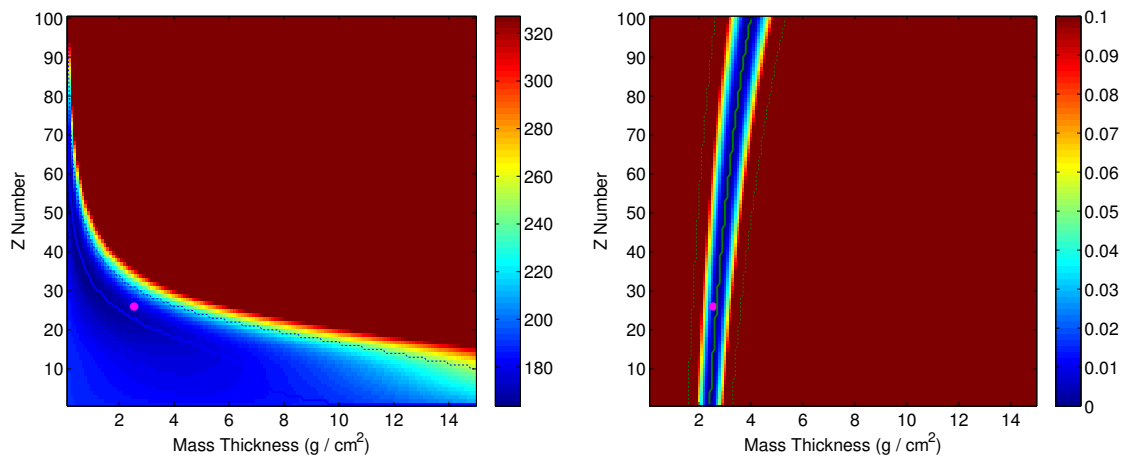
Figure 4.22: Two measurement methods to estimate the effective Z number and thickness of material shielding uranium using photopeak attenuation ratios (left) and the ratio of Compton-scattered to unattenuated photons (right). The correct combination of Z number and mass thickness is shown by the magenta dot in both panes.
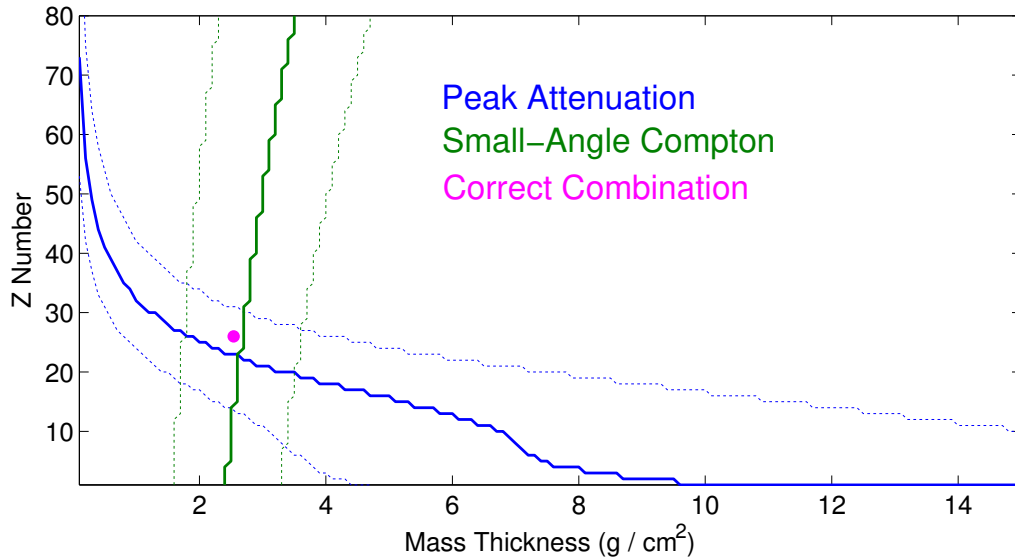
Figure 4.23: Contour plot combining photopeak attenuation and small-angle Compton scattering methods to predict the composition of shielding material. One sigma uncertainty curves are shown by dashed lines. The magenta dot shows the true mass thickness and effective atomic number of the shield.

vides a range of effective Z numbers and mass thicknesses for the intervening material which could cause the observed spectral effects. The data from peak attenuation and Compton forward-scattering is then combined to predict the effective Z number and mass thickness of the shield. The intersection point of the two characteristic lines is used to estimate the shielding material characteristics as shown in Fig. 4.23.

From measurement and simulation, the β factor used to account for self-small-angle Compton scattering remained relatively unchanged regardless of the shielding orientation or thickness. Simulation predicted the β value to be 3%, but measurements indicated 5% was a better estimate as it is difficult to simulate all scattering elements in the detector apparatus. Different source compositions and thicknesses were simulated, and the predicted β factor changed by less than 1% (in absolute terms). However, the value used can significantly alter the predicted shielding material. Fig. 4.24 shows how the β factor can effect the results. If the β factor is incorrect by 5%, the mass thickness can be incorrect by 4 g/cm^2 while the estimated atomic number of the shield can change by five.

106
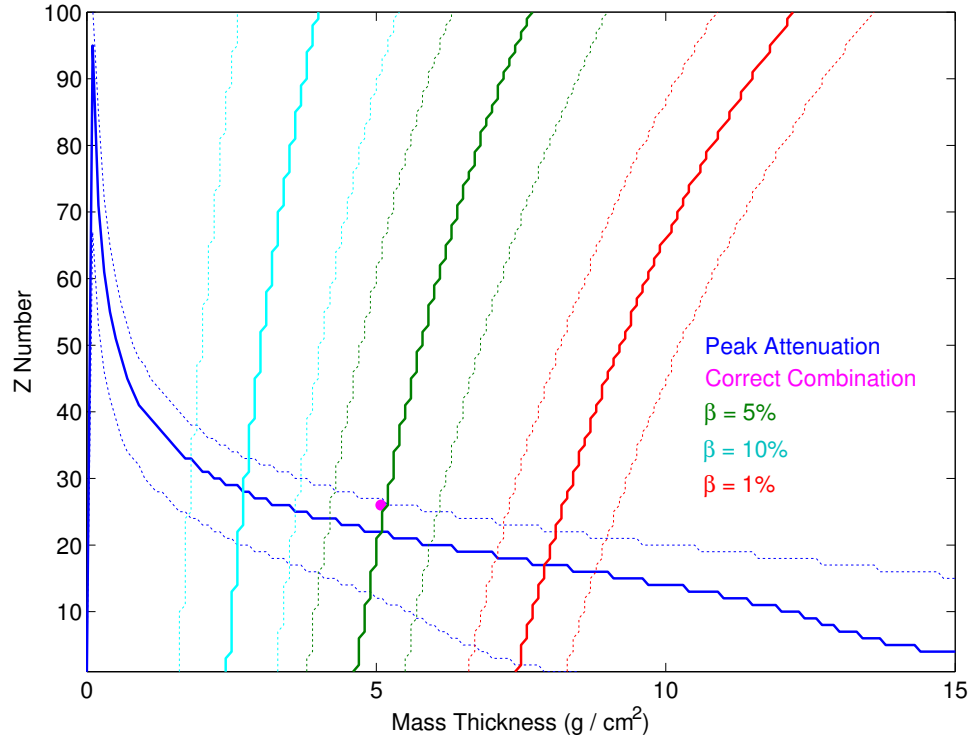
Figure 4.24: Effect of β factor on the shielding identification algorithm. In all measurements using the prototype digital CdZnTe array system, the β factor is 5% from unshielded uranium sample experimental results. One sigma uncertainty curves are shown by dashed lines. The magenta dot shows the true mass thickness and effective atomic number of the shield.

4.4.3 Accuracy for Uranium Measurements

This method correctly predicted steel thicknesses from 0.3175 cm to 2.54 cm in measurements [107]. Fig. 4.25 shows the results of the algorithm for steel shields of various thicknesses. Also, the method was accurate for planar or spherical uranium configurations. The Rocky Flats Shell at the Device Assembly Facility (DAF) at the Nevada Nuclear Security Site (NNSS) was measured with a 1.27 cm thick steel shell surrounding the highly enriched uranium [108]. The algorithm correctly estimated the mass-thickness and effective atomic number of the shield as shown in Fig. 4.26.

The method was also applied for aluminum and polyethylene shielded measurements in simulation and experiment and worked adequately for various thicknesses. As shown in Fig. 4.31, the uncertainty in the effective atomic number is larger for
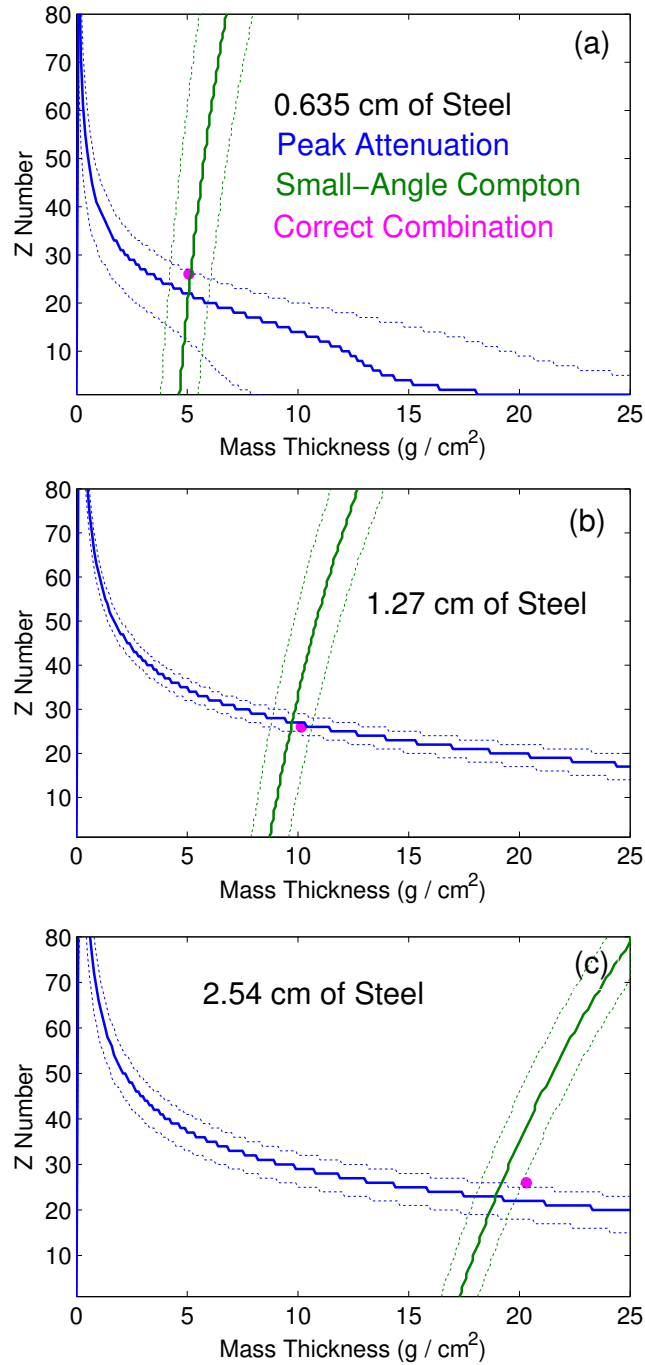
Figure 4.25: Contour plot combining peak attenuation and small-angle Compton scattering to predict the true composition of shielding material for 30×30 cm^2 planar steel shields with thicknesses of 0.635 cm (a) 1.27 cm (b) and 2.54 cm (c). One sigma uncertainty curves are shown by dashed lines. The sample was a 20 wt% ^{235}U calibration standard at the Y-12 National Security Complex with the shielding material 40 cm from the source and the detector apparatus 50 cm from the source. The magenta dot shows the expected intersection point based on the true Z number and mass thickness of the shield.
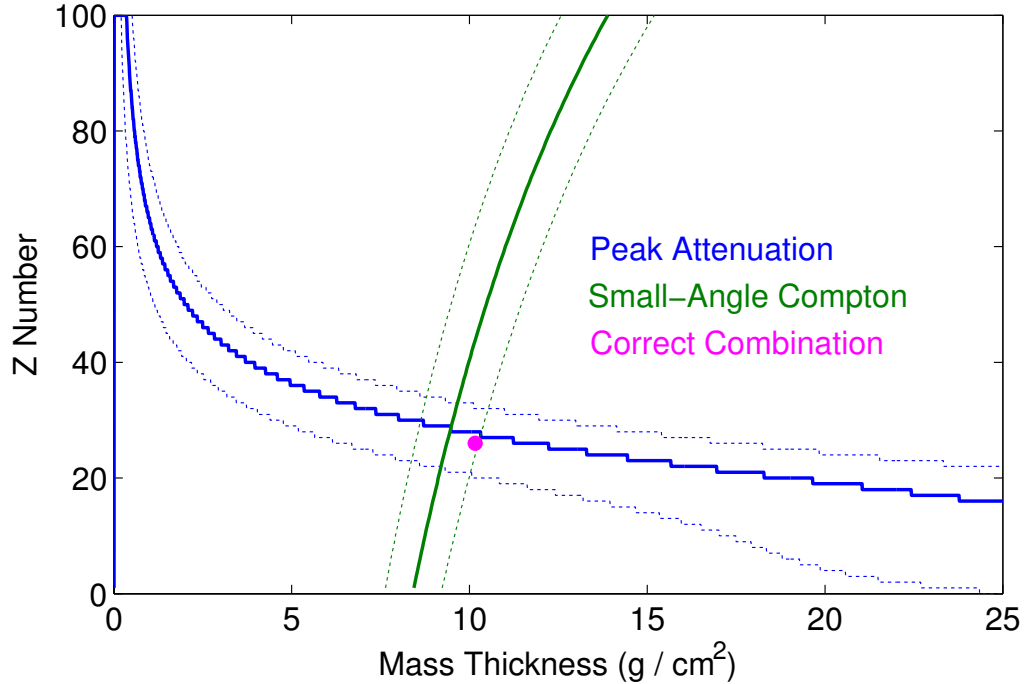
Figure 4.26: Shielding characterization method applied to the Rocky Flats HEU shell surrounded with a 1.27 cm steel shell. The shell was made of 93 wt% ^{235}U metal with an inner radius of 3 cm and an outer radius of 6 cm. A steel shell, serving as shielding material, encased the Rocky Flats Shell. The detector apparatus was 2 m from the sample. The correct combination for the effective atomic number and mass-thickness of the shield is shown with the magenta dot.

low-Z shields. This phenomenon is explored further in Section 4.4.4. In simulation, the method did not work well for thick lead shields because almost all of the source photons are photoelectrically absorbed rather than Compton scattered. However, in this case, characteristic x-rays could provide an estimate of the intervening material identity and photopeak attenuation ratios could be used to predict the mass thickness of the shield. Table 4.3 summarizes the performance of this method for identifying intervening materials during uranium measurements.

4.4.4 Uncertainty Quantification of Estimated Shielding Parameters

The uncertainty in estimated shielding parameters can be calculated using the bootstrap method [78]. The recorded gamma-ray energy spectrum is used as the initial probability density function (PDF) and that distribution is sampled many times.

Table 4.3: Summary of results using a 20 wt% ^{235}U sample at the Y-12 National Security Complex shielded with various materials. In each case, 1000 spectra with 200,000 events in the region between 0 and 250 keV are used to estimate the shielding parameters and uncertainty. The first four measurements in the table were shielded with planar steel shields. The next three measurements were shielded with various thicknesses of planar aluminum shielding. The eighth measurements included 7.62 cm of planar polyethylene shielding. The ninth test was shielded by 3.81 cm of planar aluminum shielding plus 5.08 cm of polyethylene. The final measurement was conducted with 0.635 cm of planar steel plus 2.54 cm of aluminum shielding.

Mass Thickness ρx (g/cm^2)	Estimated Mass Thickness (g/cm^2)	Effective Atomic Number (Z_{eff})	Estimated Z_{eff}
2.54	3.33 ± 0.18	26	28.0 ± 5.6
5.08	5.81 ± 0.21	26	26.8 ± 4.2
10.16	10.37 ± 0.28	26	26.7 ± 3.0
20.32	18.34 ± 0.68	26	22.6 ± 6.2
3.42	3.21 ± 0.18	13	10.2 ± 6.5
6.84	6.99 ± 0.27	13	8.8 ± 6.5
10.26	10.3 ± 0.41	13	11.3 ± 7.9
8.76	8.79 ± 0.30	≈ 4	6.95 ± 5.9
12.7	12.37 ± 0.45	≈ 10	10.0 ± 7.5
11.9	12.37 ± 0.43	≈ 17	15.2 ± 7.5

If desired, the other input parameters can be varied as well (the initial expected peak ratios when no shielding is present and the amount of forward-scattering caused by the detection apparatus). The method to estimate the thickness and identity of intervening materials is applied to each sampled spectrum. A histogram of the calculated parameters can be generated and the uncertainty quantified. Fig. 4.27 shows the distribution of probable shielding materials and areal densities for a uranium disk shielded with 1.27 cm of steel shielding. The solid red and green lines show the results of the method using the recorded data. One thousand spectra were generated, each with 200,000 events between 0 and 250 keV. This particular uncertainty evaluation
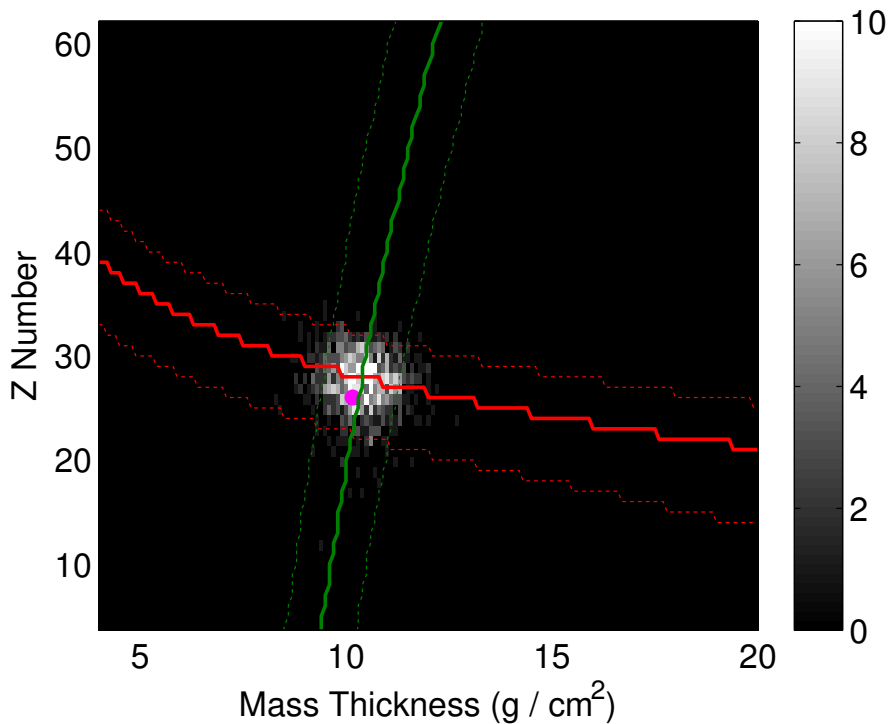
Figure 4.27: Histogram of bootstrap sampled spectra results using the shielding detection method. The solid green and red lines show the results using the recorded data. The binned results are calculated by sampling the PDF created from the recorded data and estimating the shielding parameters from each sampled spectra. The true mass thickness and atomic number of the shield is shown with the magenta dot.

allowed the β parameter to vary from a Gaussian distribution with a mean of 5% and a standard deviation of 1% to demonstrate how uncertainty in that factor propagates to the final answer.

As shown in Fig. 4.28, there is some bias in the estimate of the mass thickness and effective atomic number of the shielding material. The mass thickness is underestimated for very thick shields because the unattenuated flux is overestimated. The photopeak region is comprised of events which are truly unattenuated by the shield, events which are scattered through a very small angle in the shield, and events which are down-scattered from higher energy peaks or from the background. Because the detectors have imperfect energy resolution, some events which are forward-scattered will be counted as unattenuated counts, even when using the peak area calculation method described in Ref. [3].
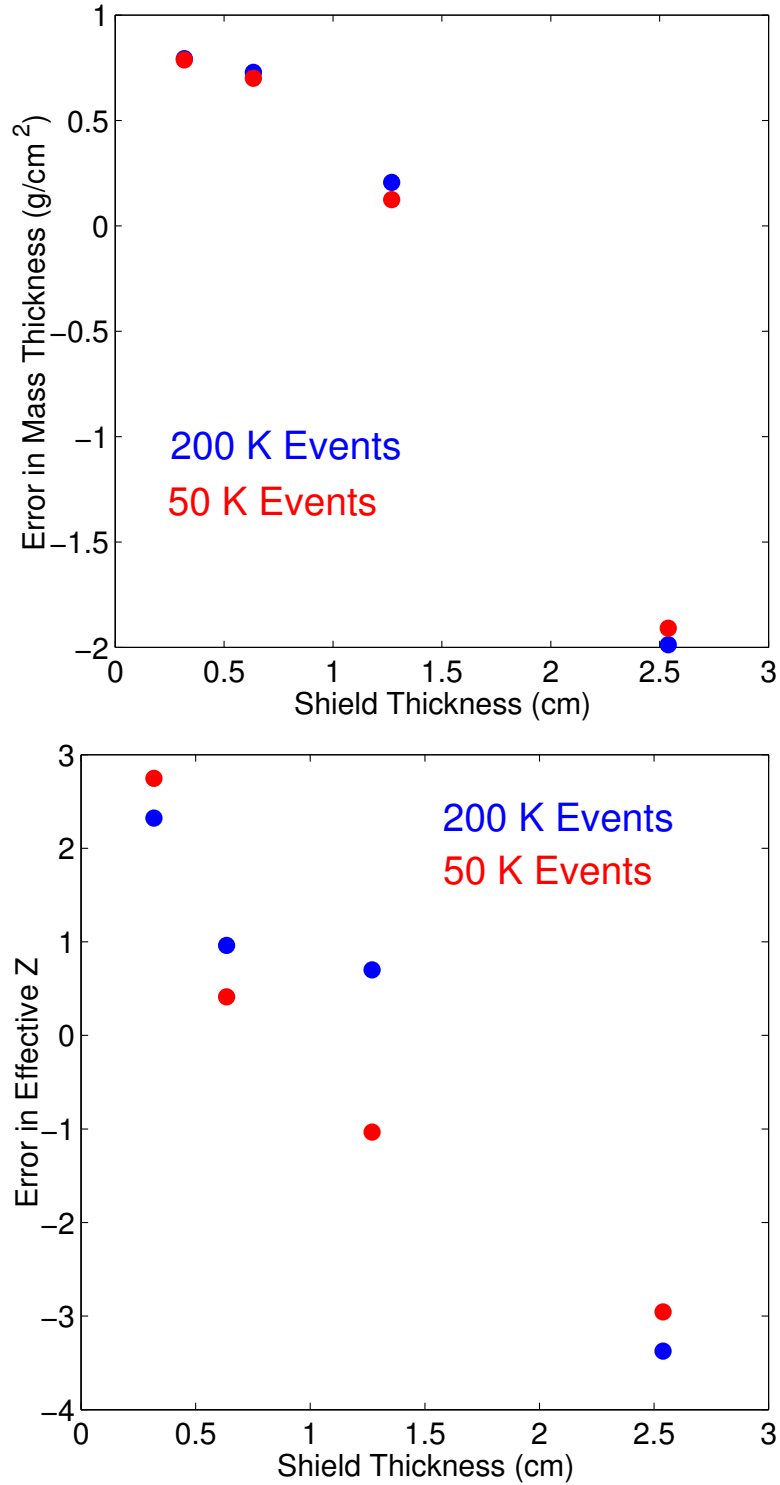
Figure 4.28: Systematic errors in the estimate of mass thickness (top) and effective atomic number (bottom) as function of iron shield thickness. The number of events indicated corresponds to the number of events in the simulated spectra between 0 and 250 keV to calculate the bootstrapped uncertainty in the estimated shielding parameters.
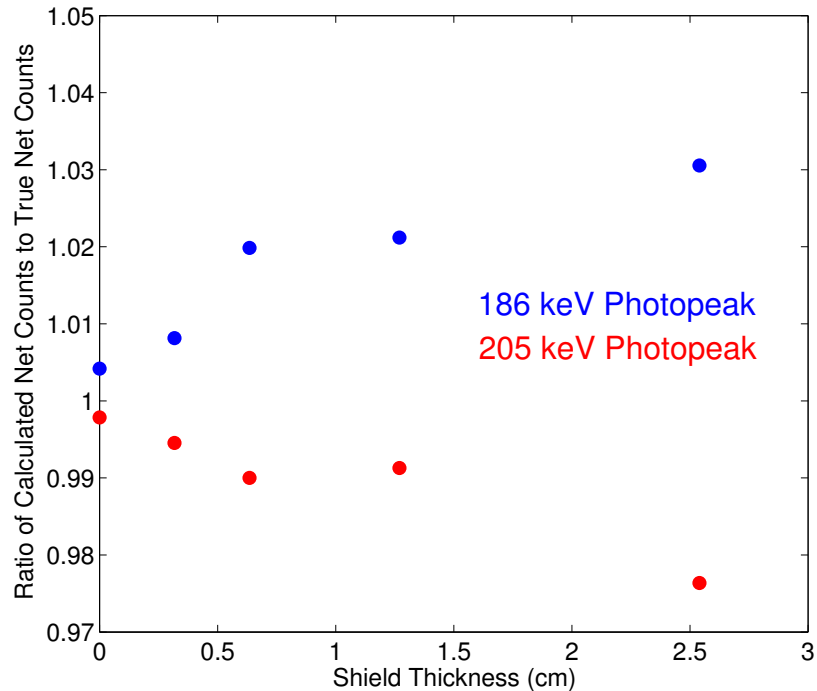
Figure 4.29: Ratio of net counts calculated from the blurred spectrum to the true number of unattenuated counts for two uranium gamma-ray lines with intervening iron shielding.

To verify this hypothesis, a simulation was conducted in Geant4 for HEU samples shielded by various thicknesses of iron. The simulated spectra were then blurred assuming the resolution of the detector was limited by 2 keV FWHM electronic noise. The net counts in each photopeak were calculated. For the un-blurred simulated spectra, the net counts can be calculated directly, whereas the peak area calculation method was applied to the blurred spectrum. As shown in Fig. 4.29, the calculated unattenuated flux for the blurred spectrum is 3% higher than the true unattenuated flux for a 2.54 cm thick shield. Since the estimated mass thickness is inversely proportional to the unattenuated flux, an overestimate in the unattenuated flux results in an underestimate of mass thickness. This explains the behavior seen in Fig. 4.28.

For thick shields, the signal from the 143 keV and 163 keV gamma-ray lines is mostly attenuated. Therefore, most of the information for the effective atomic number estimate comes from the weighted residual of the 186 keV to 205 keV photopeak
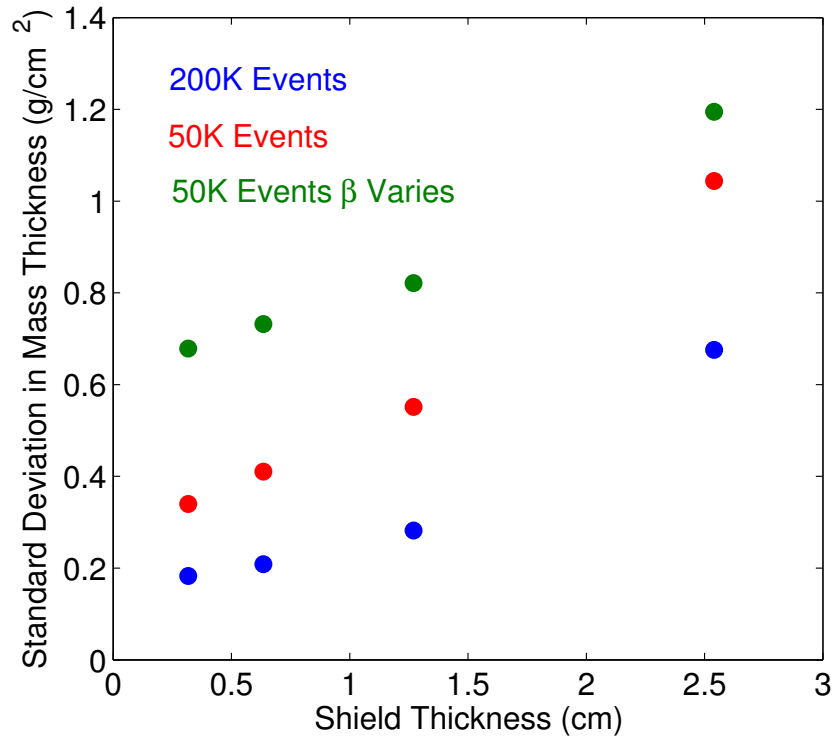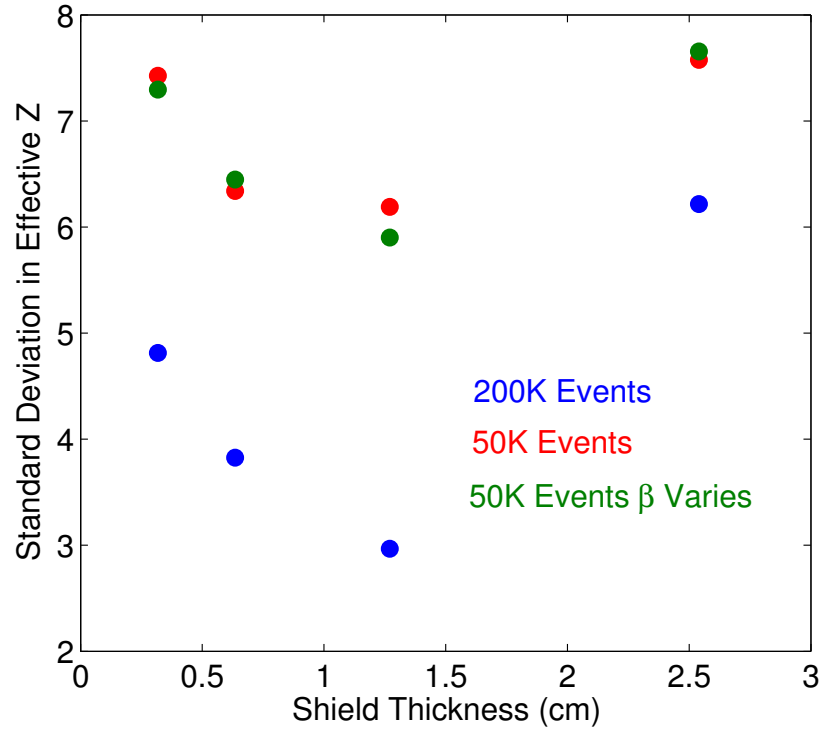
Figure 4.30: Standard deviation in calculated effective Z (top) and mass thickness (bottom) as a function of iron shield thickness from bootstrapped results. In one case, β is allowed to vary about 5% from a Gaussian distribution with a standard deviation of 1%.
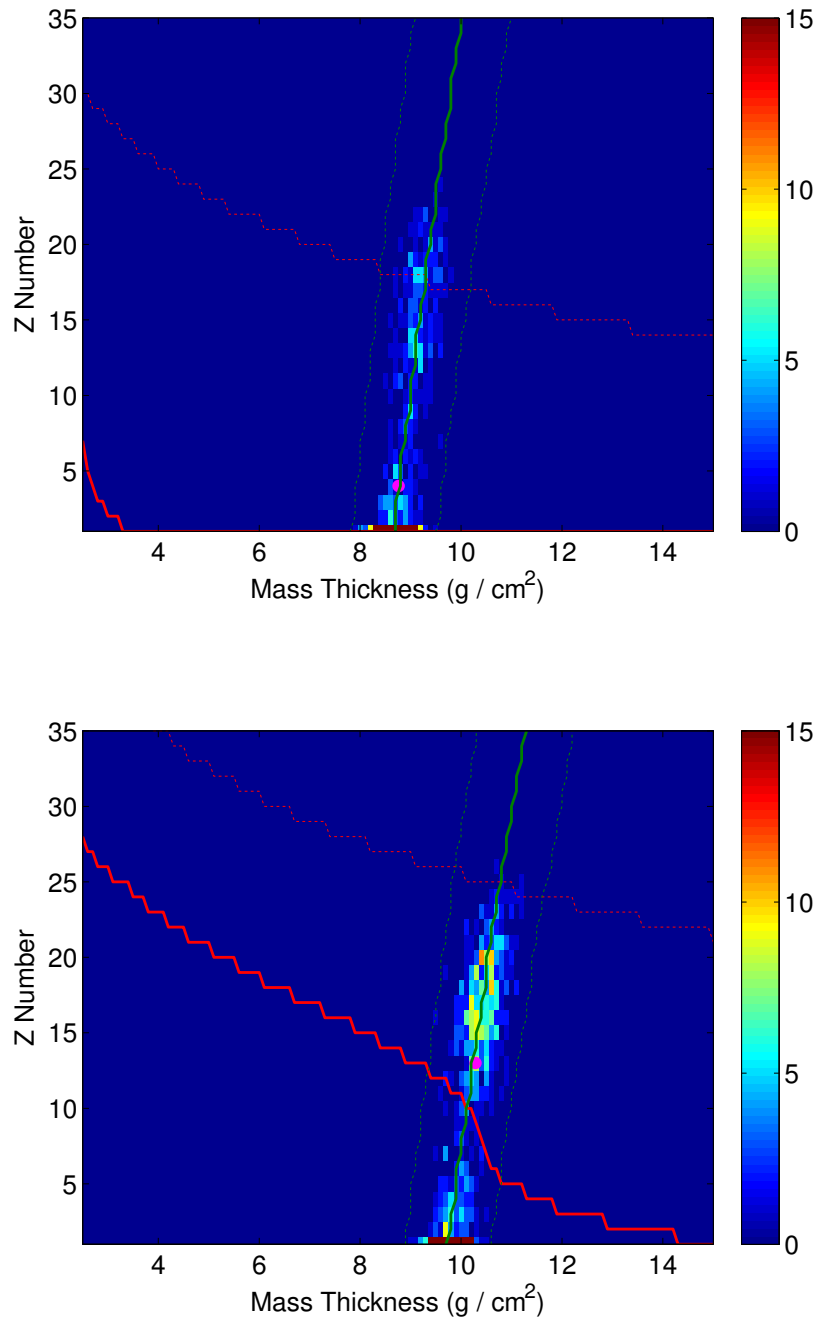
Figure 4.31: Histogram of bootstrap sampled spectra results using the shielding detection method. The binned results are calculated by sampling the PDF created from the recorded data and estimating the shielding parameters from the sampled spectra. Both histograms include 1000 spectra with 200,000 events between 0 and 250 keV. A 7.62 cm thick high density polyethylene slab shielded the source in the top histogram whereas the bottom histogram used a 3.81 cm thick planar aluminum shield. The true mass thickness and effective Z number is shown with the magenta dot. No variation in the β parameter was applied for these histograms.

ratio. Because the calculated ratio is larger than it truly is due to energy measurement uncertainty, the effective Z of the shield will be underestimated. A correction factor for thick shields could be included to correct for this small effect or the energy resolution could be further improved.

The standard deviation of the calculated shielding parameters as a function of iron shield thickness is shown in Fig. 4.30. The standard deviation of mass thickness increases for thicker shields because uncertainty in the ratio between Compton scattered events and unattenuated counts increases. The standard deviation of the effective Z number has a minimum value. Shields made of this thickness will attenuate enough photons for discernible differences in the intensity of the gamma-ray lines, but will not cause so much attenuation that the uncertainty in the calculated net photopeak counts is large. The variance in the calculated mass thickness and effective Z number is reduced with more events in the spectrum. The variance in the mass thickness is very sensitive to the uncertainty in the β parameter used to account for forward-scattering in the detection apparatus or source itself when no shield is present.

As shown in Fig. 4.31, the variance in the calculated effective Z number is quite high for low-Z shields. This is because the attenuation properties do not vary significantly as a function of atomic number for low-Z materials. Therefore, small perturbations in the input spectrum can cause large differences in the calculated Z. However, the estimate of mass thickness is still accurate. As shown in Table 4.3, the standard deviation for the 7.62 cm thick polyethylene sheet was only 0.30 g/cm^2 and the standard deviation for the 3.81 cm thick aluminum sheet was 0.41 g/cm^2. The 1.27 cm thick steel sheet, about the same mass thickness as 3.81 cm of aluminum, has a standard deviation of 0.28 g/cm^2. The mass thickness uncertainty does not change significantly because Compton scattering is only weakly correlated with the effective atomic number as shown in Eq. 4.23 since Z and A are strongly correlated.
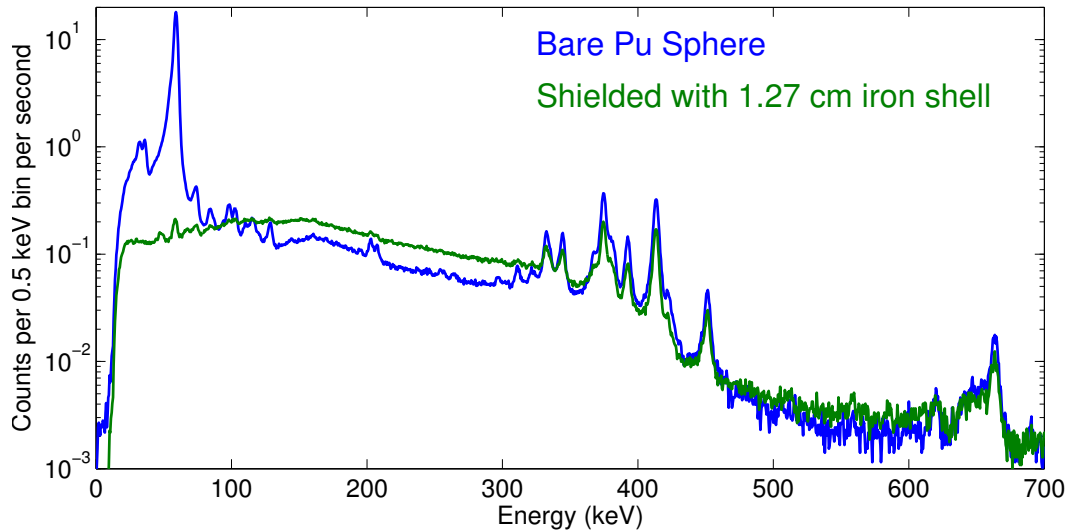
Figure 4.32: Measured gamma-ray energy spectrum from a plutonium sample measured with the prototype digital CdZnTe array system. The plutonium sample was measured bare and shielded with a 1.27 cm thick iron shell.

4.4.5 Application of Shielding Identification Method to Plutonium Measurements

Most plutonium gamma rays are emitted above 300 keV, complicating the use of this algorithm for three reasons. First, the gamma rays will be weakly attenuated by thin shields resulting in more measurement uncertainty. Second, there are more energy bins available for a photon to scatter into, reducing the probability term in Eq. 4.15. This will reduce the signal-to-noise ratio of the small-angle Compton scattering portion of the algorithm. Finally, the higher energy gamma rays lead to more uncertainty in the initial peak ratios as they will vary more with source thickness and source composition.

The 59.5 keV gamma ray from the decay of ^{241}Am is often the strongest emission from aged plutonium sources [51]. However, if this line is used to determine the shielding materials, one must make another estimate of the plutonium age in order to obtain accurate peak ratios. It is useful to identify low-Z shields, however.

At the DAF, spherical plutonium sources were attenuated with shells of shielding
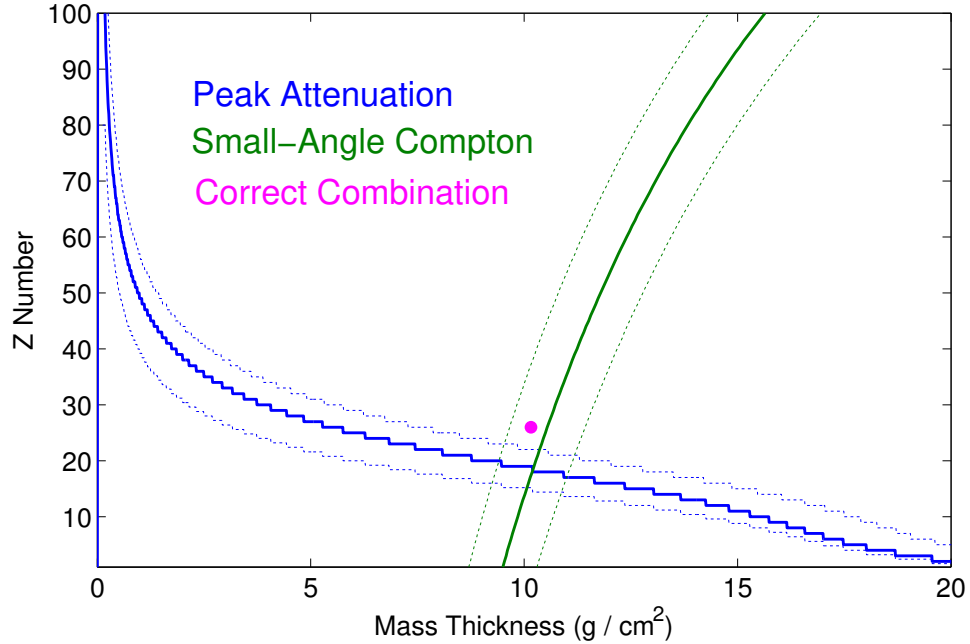
Figure 4.33: Contour plot of photopeak attenuation and small-angle Compton scattering algorithms for a 1.27 cm thick iron shell shielding a spherical plutonium sample measured at the DAF. This measurement does not include the 60 keV gamma-ray line from ^{241}Am. The correct combination of effective Z number and areal density is shown with the magenta dot.

materials. The spectral regions used for the attenuation analysis were photopeaks at 129 keV, 312 keV, 332 keV, 393 keV, 451 keV, and a triplet of lines around 375 keV, all signatures of ^{239}Pu. The statistics in the other peak regions were deemed too poor to use. The gamma-ray energy spectra of the bare source and the source shielded with iron are provided in Fig. 4.32. The region used for small-angle Compton scattering was below the triplet of lines at 375 keV. About 6% of these photons will forward-scatter to between 350 and 360 keV from the Klein-Nishina formula ($\int_{\Omega_i}^{\Omega_f} \frac{d\sigma_c}{d\Omega} d\Omega$ in Eq. 4.21 is 6%). The β factor used in Eq. 4.24 was maintained at 5%. As shown in Fig. 4.33, this method, with bootstrapping to determine uncertainty, predicts the shield is made of a material with Z number of 19 ± 6 and a mass thickness of 10.2 ± 0.30 g/cm^2. The shield had a Z number of 26 and an areal density of 10.16 g/cm^2.
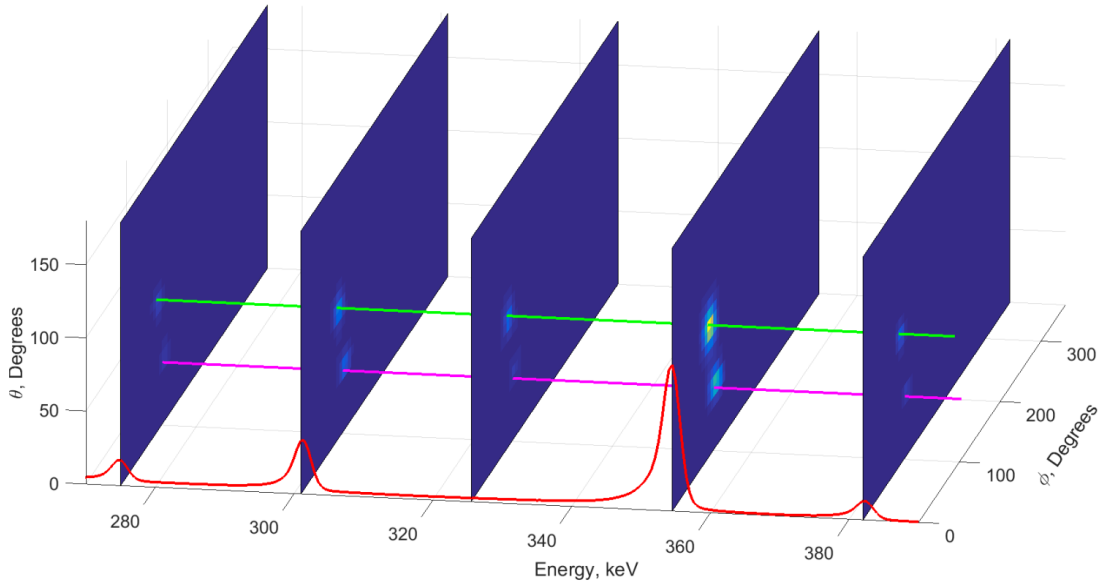
Figure 4.34: MLEM Compton images for various energy windows of a ^{133}Ba measurement. Two sources were in the field of view. The source tracked with the green line through the images was shielded by 3.3 mm of lead while the source tracked with the magenta line was bare. This figure courtesy of David Goodman.

4.4.6 Angular Deconvolution of Shielding Materials for Multiple Sources

One benefit of the described shielding detection and characterization method is that the scattered photons are deflected through small angles, so some directional information is maintained. It is possible to deconvolve the energy spectrum as a function of incident angle through maximum likelihood estimation maximization (MLEM) techniques [71]. If the angularly deconvolved energy spectra can be accurately determined, differences in the spectra can be used to estimate intervening material as a function of incident direction [109].

Fig. 4.34 gives an example of how this is accomplished. Two ^{133}Ba sources were placed in the field of view and Compton imaged. One of the sources was shielded by a 3.3 mm thick planar sheet of lead. The middle image in Fig. 4.34 is the Compton image of forward-scattered 356 keV photons in the lead. The image intensity is greater for the lead shielded source than the bare source. A forthcoming paper by Goodman

thoroughly analyzes this technique [109].

4.5   Conclusions

The improved energy resolution of CdZnTe using digital readout has many important national security applications. Isotopic sources can be detected more quickly and the improved resolution enhances the ability to characterize it. CdZnTe can determine the isotopic composition of uranium and plutonium sources with accuracy approaching HPGe detectors. Furthermore, the high resolution spectroscopy allows a user to ascertain the identity and thickness of intervening materials strictly via spectroscopic information.

CHAPTER V

Fast and Thermal Neutron Detection

5.1 Thermal Neutron Detection

Cadmium, a principle component of CdZnTe, is a well known thermal neutron absorber. ^{113}Cd has a very large thermal neutron capture cross section of 20,600 barns, so 96% of thermal neutrons are absorbed within 1 mm of the surface of a CdZnTe detector. Upon capturing a neutron, the nucleus de-excites by emitting photons or internal conversion electrons based on the nuclear levels of cadmium. The total energy emitted is 9 MeV with a multiplicity of three or four gamma-rays. Brown showed how thermal neutrons can be detected and imaged using CdZnTe detectors with analog ASICs [68]. In Chap. IV of this thesis, a thermal neutron capture characteristic photopeak at 558 keV was demonstrated during a plutonium measurement. A digital ASIC readout system has better energy resolution, especially for multiple-pixel events, than a system employing analog ASICs. Therefore, one expects better signal-to-noise ratio for detecting thermal neutrons from cascade gamma rays with a digital ASIC system.

This was verified experimentally at the Ohio State University Nuclear Research Reactor Facility [110]. The research reactor has a thermal neutron beam port with a flux of 2.5×10^6 neutrons per square centimeter. PolarisSP [27], a portable CdZnTe array system with two separable planes of detectors in 3×3 arrays using the analog
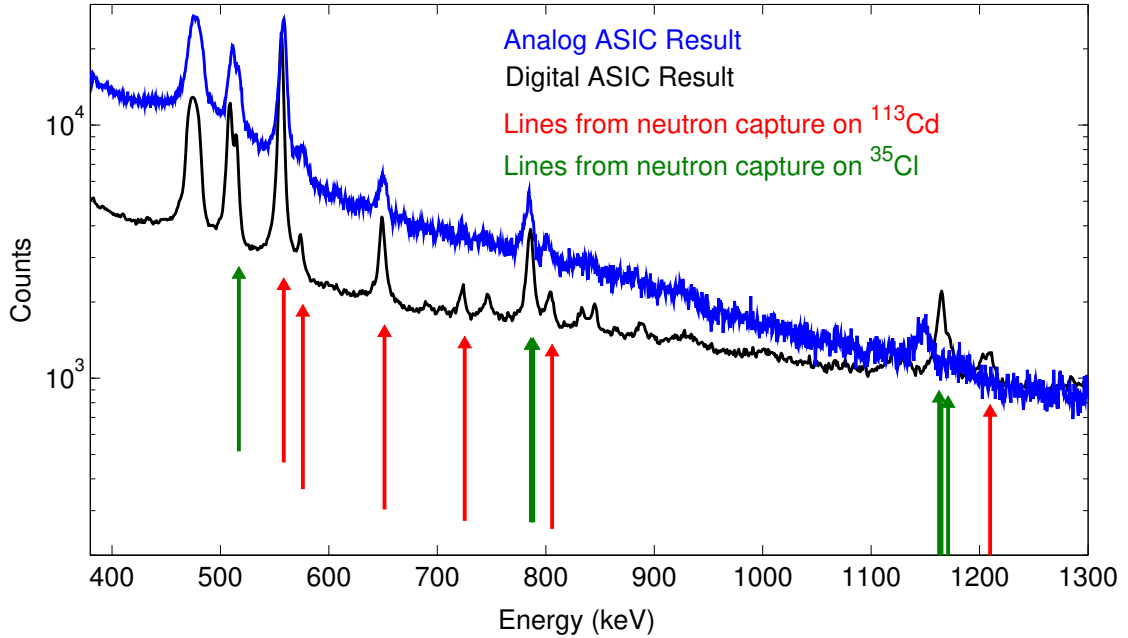
Figure 5.1: Recorded gamma-ray energy spectra comparing the energy resolution performance of an analog ASIC CdZnTe system (single-pixel events only) and a digital system (all events) with both detector systems in the beam with a PVC target to produce additional high-energy (multi-MeV) photons measured for 14 hours.

VAS_UM2.3/TAT4 ASIC, and the portable Orion digital ASIC system were placed in the beam along with a piece of polyvinyl chloride (PVC) to measure the detector response to thermal neutrons and high-energy photons produced from thermal neutron capture on chlorine. As shown in Fig. 5.1, the improved resolution of digitally-sampled CdZnTe allows the user to see the 558 keV peak with a higher signal to noise ratio and discern characteristic gamma-ray lines at higher energies.

While measuring the beryllium reflected plutonium (BeRP) ball [111], a sphere of plutonium kept at the Device Assembly Facility (DAF) at the Nevada Nuclear Security Site (NNSS), the intensity of the 558 keV photopeak changed as different reflector shells were added to the source configuration as shown in Fig. 5.2. When the plutonium sphere was bare, the 558 keV from thermal neutron capture on cadmium was not prominent because the emitted neutrons were at fission energies (average energy of 1 MeV). A small number of neutrons are thermalized in the environment,
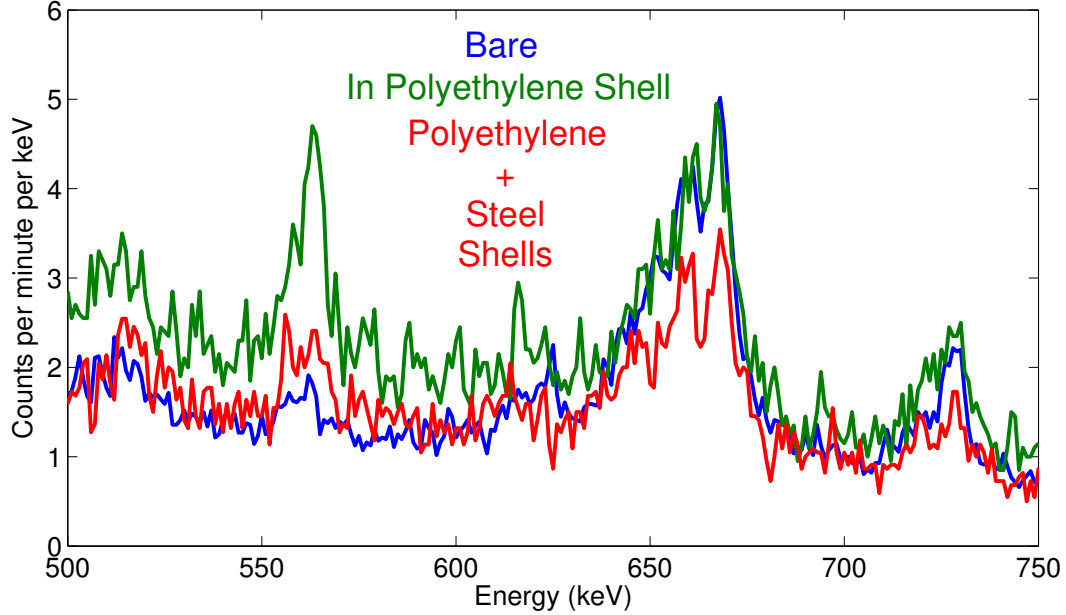
Figure 5.2: Recorded photon energy spectrum from the BeRP ball at DAF with different moderating shells. Each configuration was measured for 15 minutes.

but the geometrical efficiency for detecting these neutrons is low. If a polyethylene shell is added around the BeRP ball, fission neutrons can thermalize in the moderating material, so the 558 keV peak becomes more prominent. Furthermore, these thermal neutrons can escape the configuration even if a steel shell is placed around the polyethylene.

The shielding identification and characterization method proposed in Chap. IV is less sensitive to shields made of low-Z materials. The attenuation and production of thermal neutron signatures may provide more information about the source configuration with low-Z intervening materials present.

5.2   Fast Neutron Detection

At high energies, neutrons primarily interact with CdZnTe target nuclei through inelastic or elastic scattering [3]. Inelastically-scattered neutrons do impart some recoil energy to the target nucleus while producing characteristic gamma rays depending

on the nuclear levels of the target. If these gamma-ray lines can be efficiently detected and separated from background, they indicate fast neutron reactions.

The energy deposited by elastically scattered neutron to the recoil nucleus, E_r, depends on the incident neutron energy, E_n, the scattering angle between the incident and scattered neutron in the center-of-mass frame of reference, θ_c, and the target nucleus mass, A, as shown in Eq. 5.1 [54].

$$E_r = E_n \left(1 - \frac{(1+\alpha) + (1-\alpha)\cos\theta_c}{2}\right) \tag{5.1}$$

$$\alpha \equiv \left(\frac{A-1}{A+1}\right)^2 \tag{5.2}$$

Since the constituent nuclei of CdZnTe detectors are massive relative to the neutron, E_r is small, even for backscattered events (when $\cos\theta_c \approx -1$) because α is close to one. Backscattering on Cd or Te will deposit less than 4% of the incident neutron energy to the recoil nucleus.

The microscopic cross sections for fast neutron interactions in Cd and Te nuclei are shown in Fig. 5.3 [112]. For both elements, the cross section for scattering is a few barns, with elastic collisions being slightly more likely at most energies.

The recorded energy will be reduced further due to quenching. Nuclear recoils will generate fewer electron-hole pairs than the number produced by a photoelectron of the same energy as described via the Lindhard model [113, 114]. The quenching factor for CdZnTe is estimated to be 25% based on previous work with neutron scattering in silicon and germanium, which both exhibit quenching factors of 25% for 50 keV recoil nuclei [115, 116].

Assuming a quenching factor of 25%, simulated neutron energy spectra recorded using CdZnTe are shown in Fig. 5.4. Ten million neutrons are simulated for each neutron source. These spectra do not include the 2 keV Gaussian blur from electronic
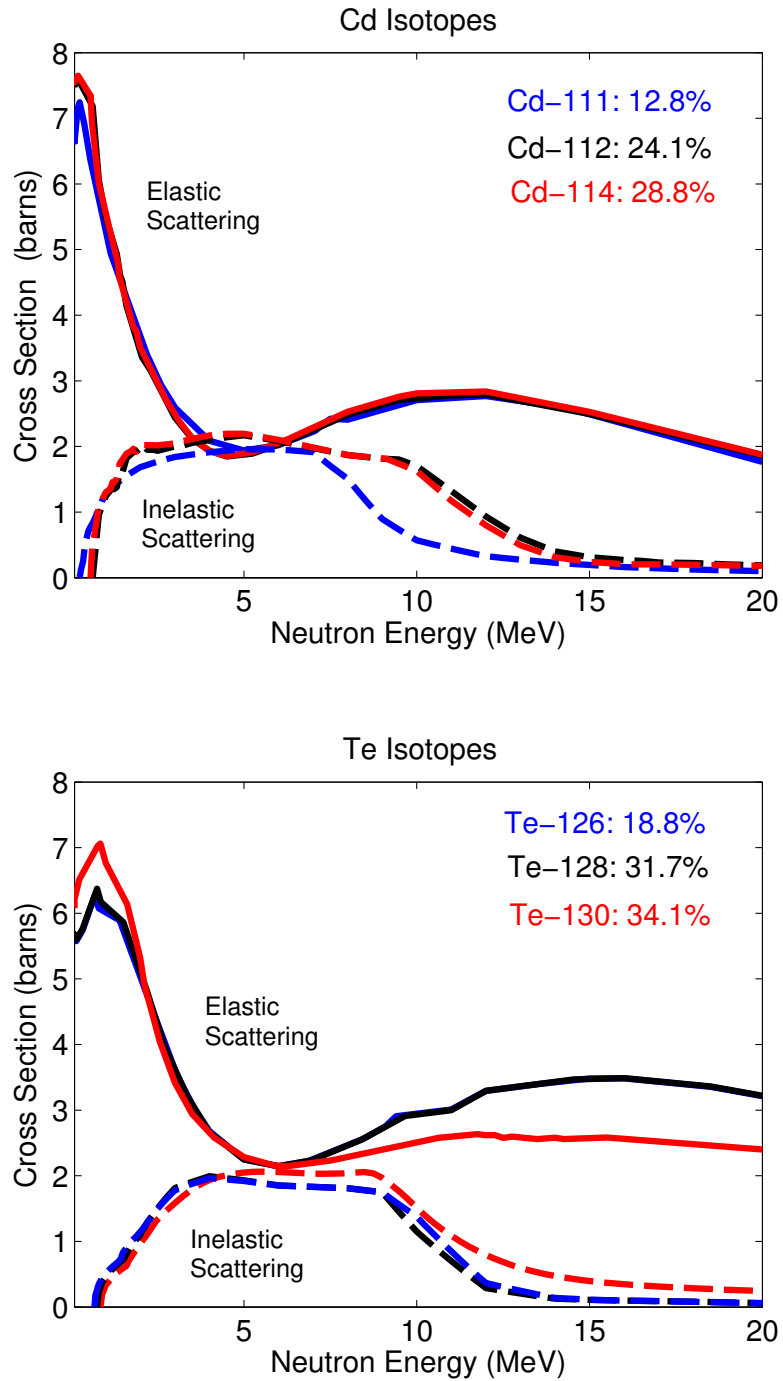
Figure 5.3: Microscopic cross sections for neutron interactions on Cd or Te nuclei. The dashed lines indicate the cross section for inelastic scattering whereas the solid lines indicate the cross section for elastic scattering. The three most abundant isotopes are plotted for each element, but the minor isotopes follow the same trends.
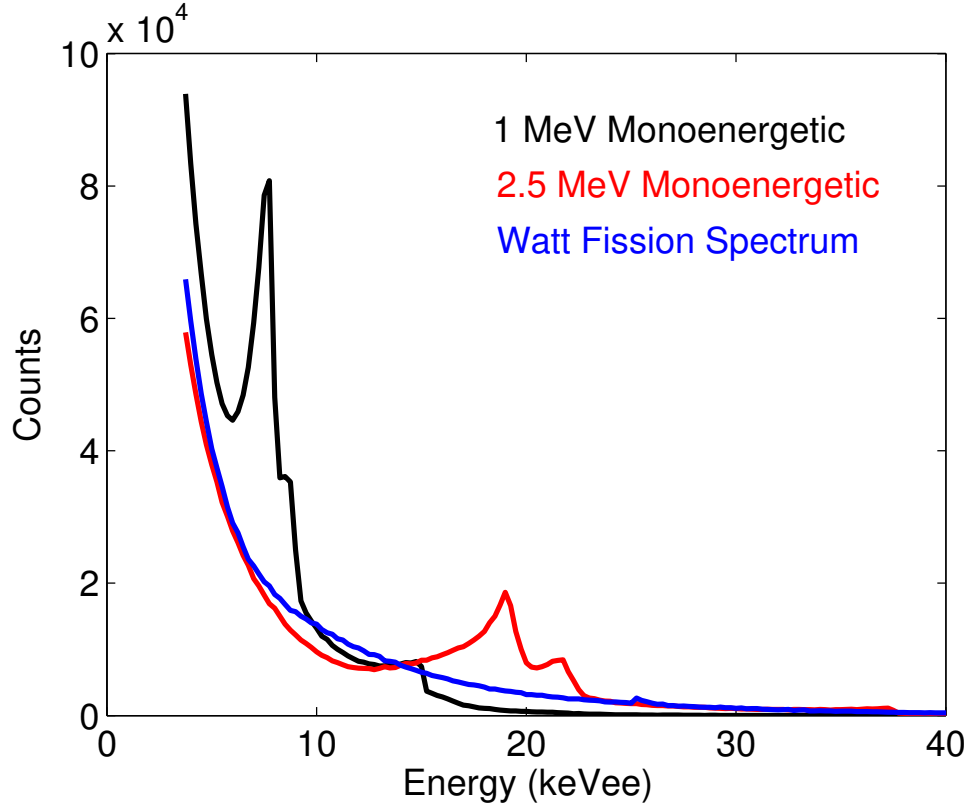
Figure 5.4: Simulated elastic scattering recoil energy spectra from various neutron sources in CdZnTe detectors. These data were simulated assuming a quenching factor of 25%. The spectra are cutoff at 5 keVee. Ten million particles were simulated for each spectrum, so the relative number of counts reflects the detection efficiency.

noise expected from a real system.

To estimate the detection efficiency of CdZnTe for fast neutrons, neutron beams of three different energy distributions were directed at the center of the cathode-side or the center of the side of the detector array as illustrated in Fig. 5.5 in a Geant4 simulation [90]. The detector array was simulated as one large detector for simplicity. The efficiency was calculated as the number of quenched nuclear recoils above the low-energy threshold divided by the simulated number of neutrons in the beam (ten million neutrons). The elastic nuclear recoil theoretical detection efficiency from these simulations is summarized in Table 5.1. Overall, the intrinsic efficiency is on the order of a few percent and is strongly dependent on the low-energy threshold. Since the number of simulated particles was large, the uncertainty in the simulated detection
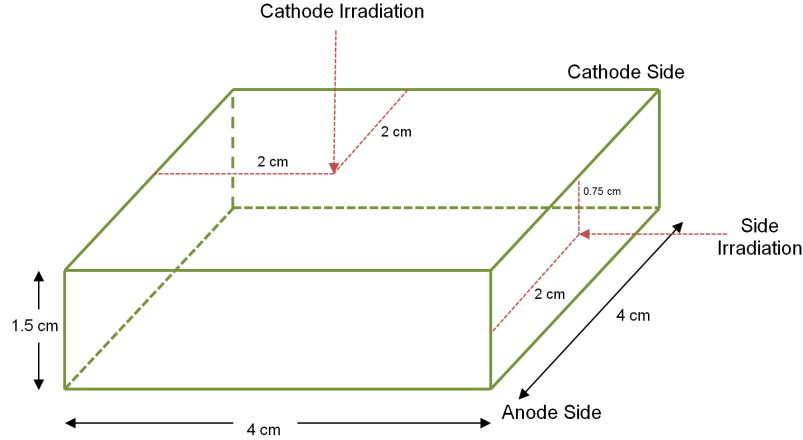
Figure 5.5: Sketch of simulated neutron beams incident on CdZnTe to estimate intrinsic efficiency.

efficiency is less than 0.1% in absolute terms.

5.2.1 Low-Energy Thresholds in Pixelated CdZnTe Detectors

To trigger the VAD_UMv1.2 ASIC, a filtered signal induced on an anode pixel must exceed a user-defined threshold. A CR-$(RC)^4$ filter with a short shaping time is employed by the triggering logic [117]. First, a global threshold is found based on the lowest setting where noise triggering barely saturates the system. Then, each channel is enabled individually to see if that channel contributes significantly to the number of triggers from noise. If the channel does not exhibit a superfluous noise trigger rate, the global threshold is trimmed slightly lower on a channel-by-channel basis until noise triggers become predominant. If the channel does contribute significantly to the number of noise triggers, the threshold is raised slightly higher. Using this procedure, the threshold can be lowered to around 5 keVee with a false trigger rate of less than one count per second. Fig. 5.6 demonstrates what low amplitude signals look like read out by the VAD_UMv1.2 system. The threshold will vary slightly from across channels. Edge pixels tend to have higher energy thresholds (around 10 keVee) due to leakage current from the pixel to the guard ring.

Transient signals induced on pixels neighboring the pixel that collects the charge

Table 5.1: Intrinsic elastic-scattering neutron detection efficiency of the prototype CdZnTe array system read out by ASICs which digitally-sample the pulse waveforms for different beam geometries, low-energy thresholds, and neutron energies, simulated in Geant4.

Neutron Energy	Low-Energy Threshold	Irradiation Direction	Detection Efficiency (%)
1 MeV	5 keVee	Side	11.3
1 MeV	10 keVee	Side	2.2
2.5 MeV	5 keVee	Side	9.0
2.5 MeV	10 keVee	Side	4.9
Watt Spectrum	5 keVee	Side	8.1
Watt Spectrum	10 keVee	Side	3.5
1 MeV	5 keVee	Cathode	4.9
1 MeV	10 keVee	Cathode	0.9
2.5 MeV	5 keVee	Cathode	3.6
2.5 MeV	10 keVee	Cathode	2.0
Watt Spectrum	5 keVee	Cathode	3.3
Watt Spectrum	10 keVee	Cathode	1.4

can also trigger the system using this triggering logic [24, 118]. In order to accurately discriminate transient signals from pixels which collect charge, a software threshold is employed. The mean amplitude of the first fifty digitally-sampled points is subtracted from the mean value of the last fifty sample points to estimate the pulse amplitude. This amplitude should be above a few kilo-electron-volts for collecting pixels. If the amplitude is lower than the software threshold, the trigger is reclassified as a transient signal.

With the low-energy threshold at around 5 keV, the 5.9 keV x-rays from a ^{55}Fe source can be distinguished from noise as shown in Fig. 5.7. The source must be
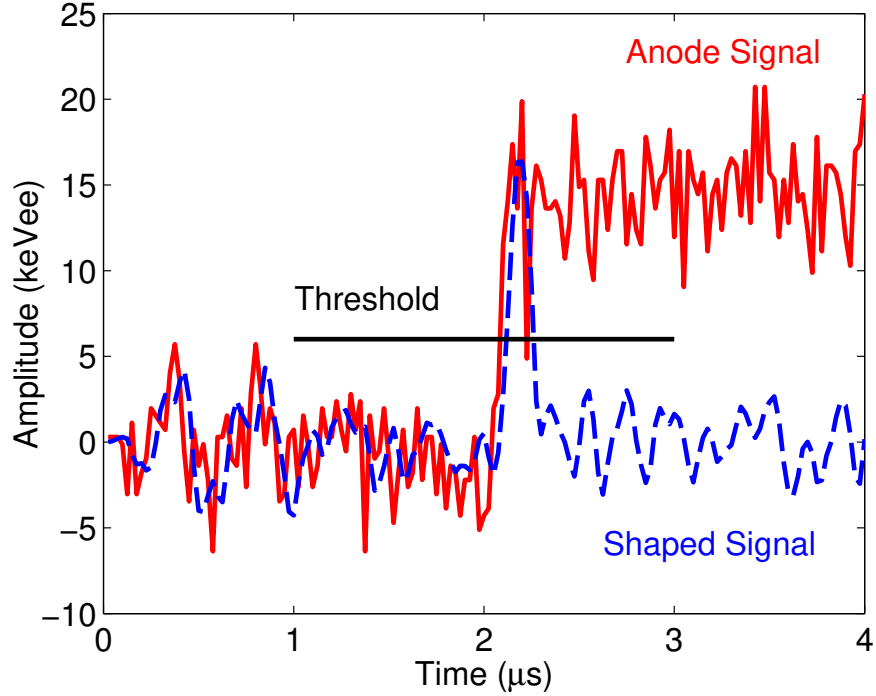
Figure 5.6: Example pulse waveform and filtered signal for a small-energy gamma-ray deposition. The waveform is sampled at 40 MHz.

placed inside the detector housing, as the 2 mm thick aluminum box provides substantial attenuation to low-energy photons. With the source outside the aluminum housing, the continuum to the right of the peak is caused by low-energy background photons that are not attenuated by the aluminum housing or higher-energy background gammas which undergo small-angle Compton scattering in the detector. The peak at very low energies is a convolution of some noise triggering and some 5.9 keV source photons which are not attenuated by the aluminum detector housing. With the source inside the housing, the low-energy peak is primarily from photoelectrically absorbed 5.9 keV photons from the ^{55}Fe source. The electronic noise component is still present, but is weak relative to the source strength.

Because the detector housing attenuates a significant fraction of low-energy photons, an alternative method to measure the low-energy threshold was developed. A ^{133}Ba source was placed outside the aluminum detector housing. The 31 and 35 keV x-rays produced from the source easily reached the cathode surfaces of the CdZnTe
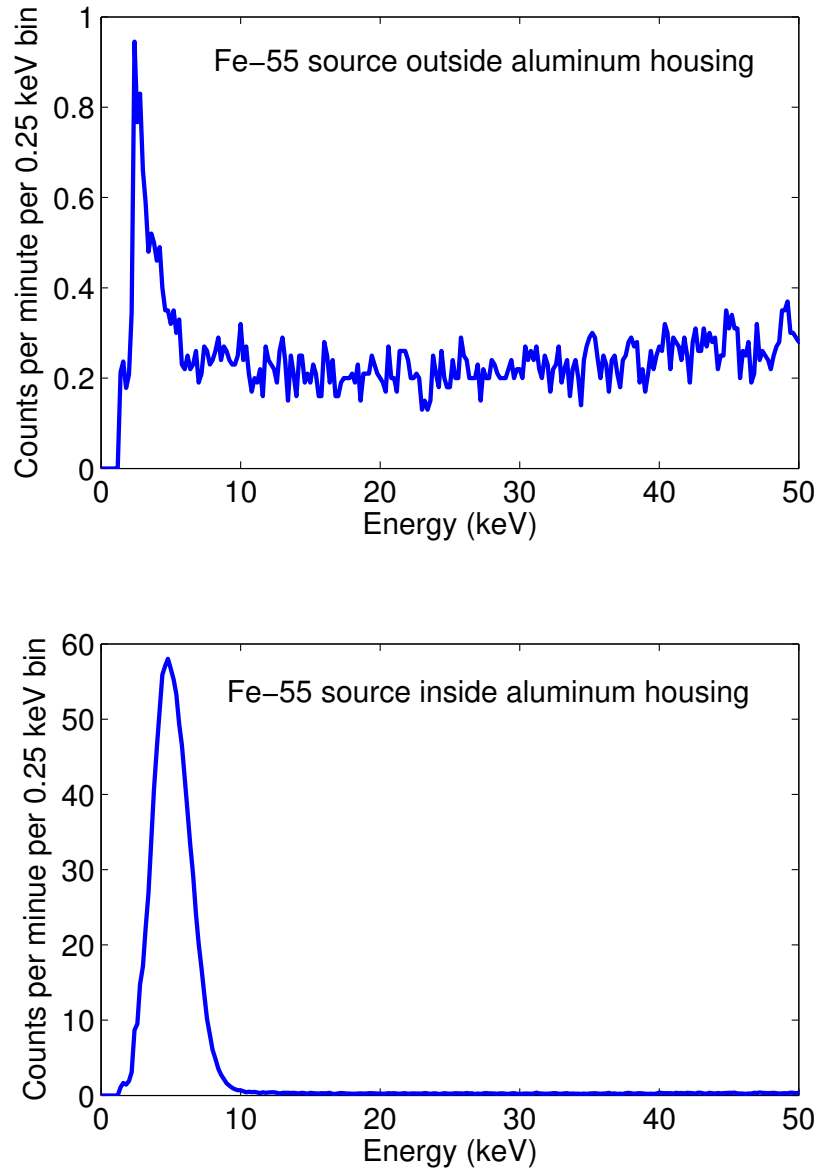
Figure 5.7: Recorded energy spectrum from a 1.5 μCi ^{55}Fe source with the source outside of the detector housing box (top) and inside the housing (bottom). Each measurement lasted one hour.

detectors. Some of these incident x-rays were photoelectrically absorbed and produced a characteristic Cd or Te x-ray which escaped the detection system so that a portion of the deposited energy was not recorded. These events were recorded as escape peaks in the spectrum shown in Fig. 5.8. The ^{133}Ba x-rays were expected to generate peaks at 4, 8, and 12 keV from these interactions. The peaks at 8 and 12 keV were observed with current thresholds.
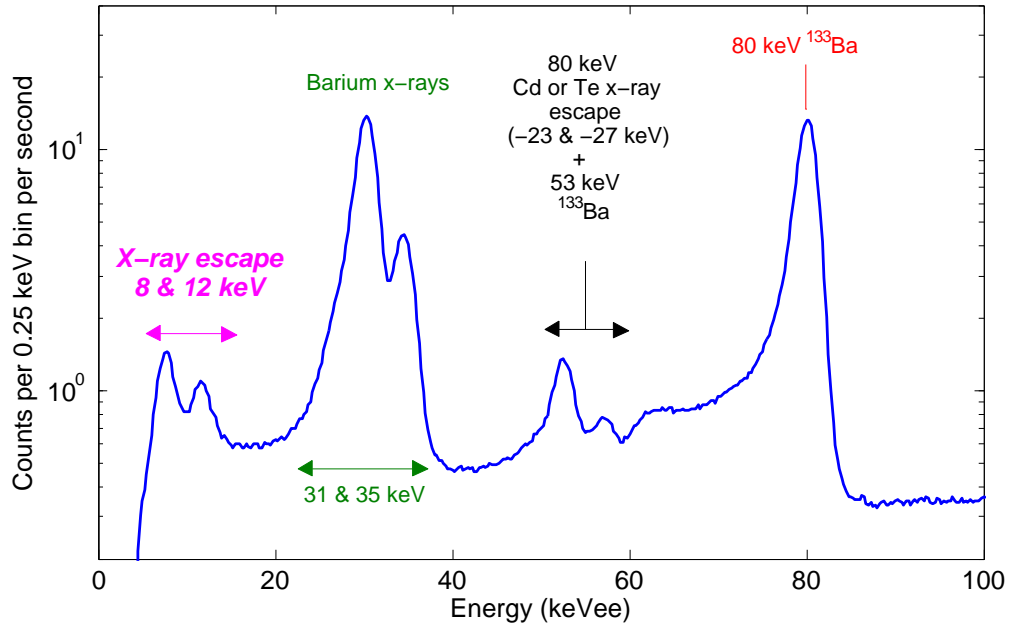
Figure 5.8: Recorded energy spectrum from a ^{133}Ba source. Note that x-ray escape produced characteristic peaks at low energies. The measurement lasted 30 minutes.

5.2.2 Neutron Generator Measurements

As a proof of principle, a Thermo Fisher Scientific MP320 deuterium-deuterium (DD) neutron generator, which produced approximately 10^6 2.5 MeV neutrons per second in 4π, was used to study neutron interactions in CdZnTe detectors. The tube was operated with a potential of 80 kV and a current of 60 μA. The acceleration and deceleration of deuterons produced a significant amount of bremsstrahlung radiation in addition to neutrons. Three millimeters of lead shielding was used to attenuate bremsstrahlung yet preserve neutron signals. The 80 keV emission from a ^{133}Ba source was used to verify that there was ample shielding of bremsstrahlung.

As shown in Fig. 5.9, a high-energy gamma-ray source can slightly increase the low-energy background level through small-angle Compton scattering events which deposit a small amount of energy in the detector. Yet the increase in counts between 0 and 20 keVee when the neutron generator was producing neutrons is clearly higher than the background level or what can be produced from forward-scattered higher-energy photons. Note that the upper end of the low-energy neutron-signature peak

131
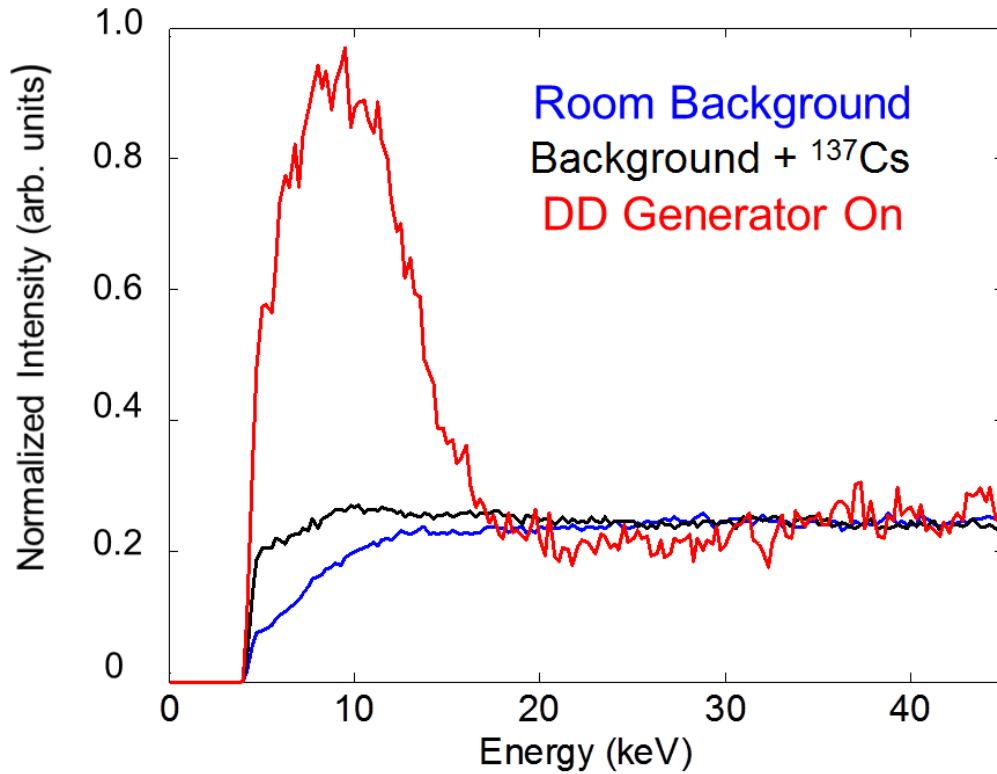
Figure 5.9: Recorded energy spectrum from the DD neutron generator compared to background measurements. The spectra are normalized to the count rate in the 30-40 keV range. These spectra indicate that this neutron detection technique is robust even with a photon source in the background. The ^{137}Cs source was not present during the DD Neutron Generator measurement. It is included in this figure to demonstrate how forward-scattered gamma-rays can minimally affect the low-energy continuum.

begins at around 18 keVee. This indicates a slightly smaller quenching factor, 20% rather than 25%, from the observed to expected (from Fig. 5.4) backscatter peak position ratio.

Another signature of fast neutron interactions are characteristic gamma rays released from inelastic scattering reactions. As shown in Fig. 5.10, the background-subtracted energy spectrum with the neutron generator on shows characteristic peaks related to the constituent isotopes. These signatures may also be used to identify the presence of a neutron source.

To verify that the low-energy signals (5-20 keVee) were from neutrons rather than
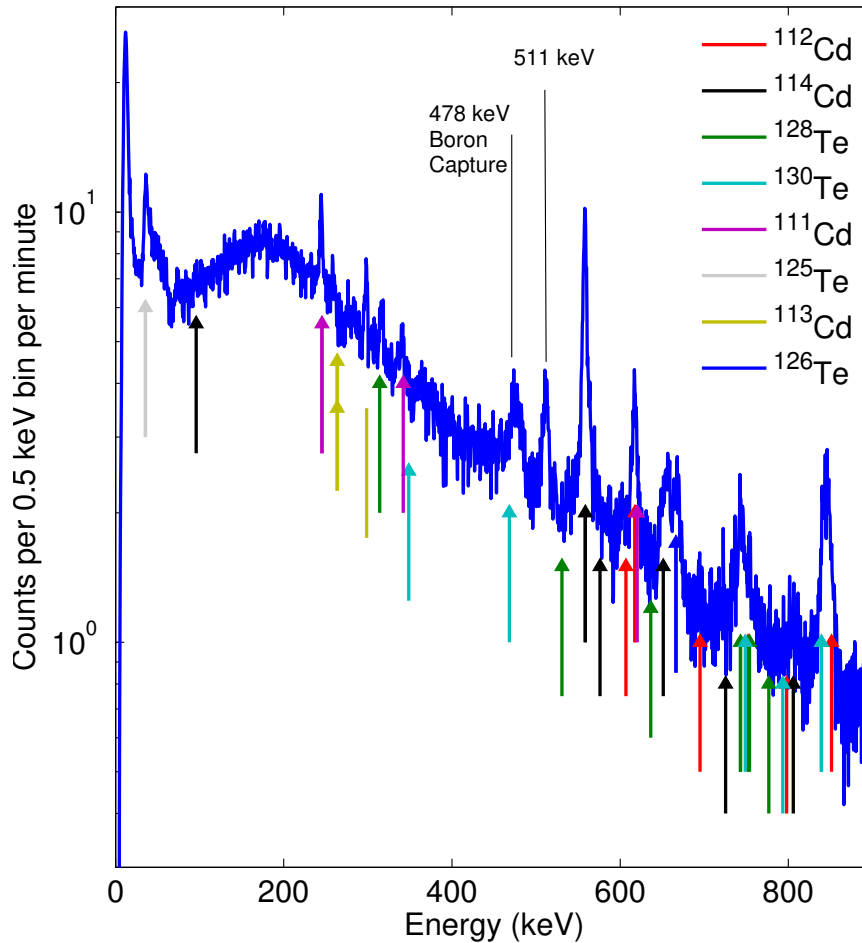
Figure 5.10: Recorded, background-subtracted energy spectrum from the DD neutron generator zoomed to see high-energy characteristic inelastic scattering gamma rays. Vertical lines show the position of expected inelastic gamma rays from the various constituent nuclei. The 511 keV peak is from pair production of other high-energy gamma rays produced from neutron interactions. The boron capture peak comes from boron in the experimental area as well as boron in circuit board components.

photons, several techniques were used to isolate the source of this signal. First, the interaction positions of these energy depositions were noted by mapping the small-energy deposition count rate by the triggered pixel location. Low-energy photons should either be attenuated by the aluminum detector housing or absorbed on the surface of the CdZnTe. However, as shown in the right window of Fig. 5.12, when the neutrons are incident from the side of the detector, a substantial number of low-energy events penetrate deep into the detector. High-energy photons which are
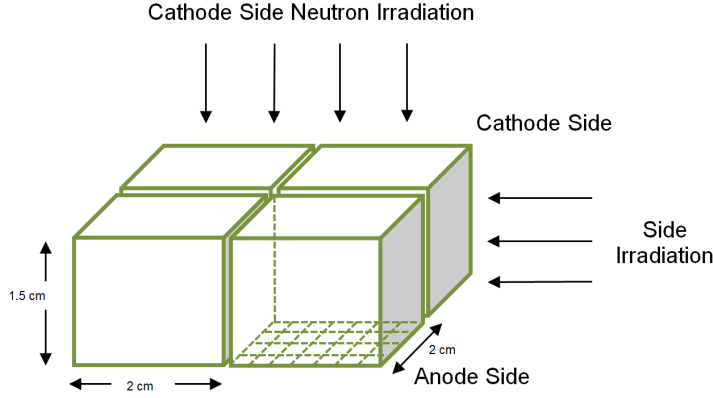
Figure 5.11: Sketh of neutron irradiation directions. The gap between detectors is 2 mm.

Compton scattered through a small angle have a more uniform interaction position distribution than observed in Fig. 5.12. In fact, the attenuation of neutrons from this measurement matches the theoretical attenuation of CdZnTe quite well as shown in Fig. 5.13. The number of counts was calculated by summing the number of counts in each row from Fig. 5.12 and using the center of the pixel as the average interaction position. Similar results were achieved for neutron irradiations from the other sides, as well as intermediate angles as shown in Sect. 5.3.

Borated polyethylene was placed between the detector array and the neutron generator as photographed in Fig. 5.14. The borated polyethylene should reduce the intensity of fast neutron signatures while allowing transport of higher-energy photons. The resulting spectra are shown in Fig. 5.15. Note that the addition of polyethylene significantly reduces the relative height of the low-energy peak indicative of fast neutron elastic scattering interactions. One can model the attenuation of neutrons via an exponential factor as shown in Eq. 5.3, where I is the neutron intensity after passing through a moderator with thickness x.

$$\frac{I}{I_0} = e^{-\Sigma_t x} \tag{5.3}$$

I_0 is the initial neutron intensity, and Σ_t is the measured effective attenuation cross
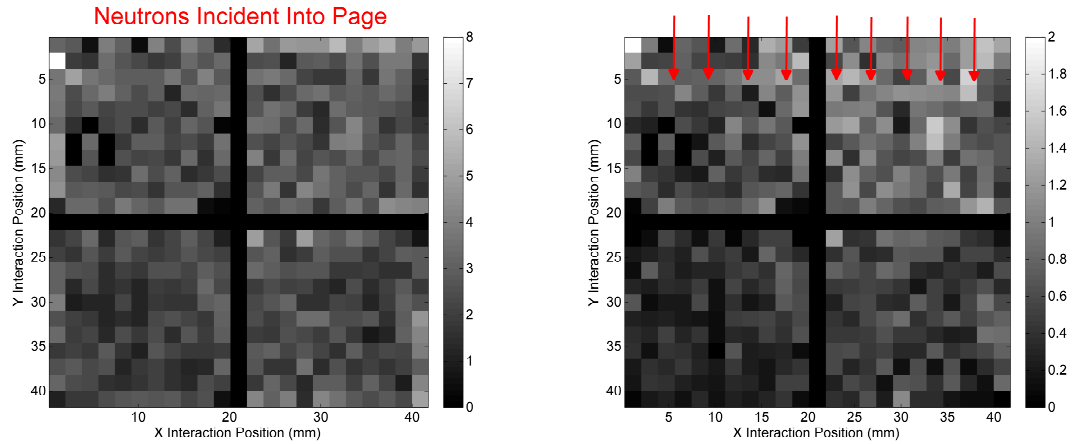
Figure 5.12: Background-subtracted count rate (counts per second) for recorded interactions with energy between 0 and 25 keVee for neutrons incident from the cathode-side (left) and from the side of the detector array (right).
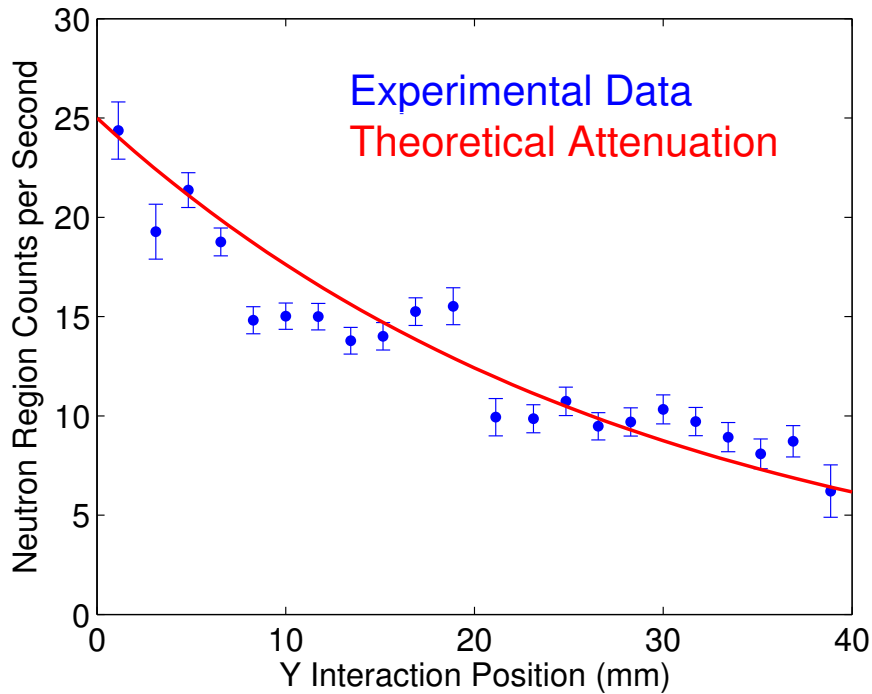
Figure 5.13: Number of recorded background-subtracted small-energy depositions as a function of distance into the CdZnTe detector from the right pane of Fig. 5.12 with the air gap between detectors subtracted. The experimental attenuation matches the theoretical attenuation of neutrons in CdZnTe.

section. Eq. 5.3 assumes that neutrons are removed following a single interaction. Multiple detectable scatters are unlikely, so Eq. 5.3 can be used to estimate the neutron attenuation due to the presence of borated polyethylene.

135
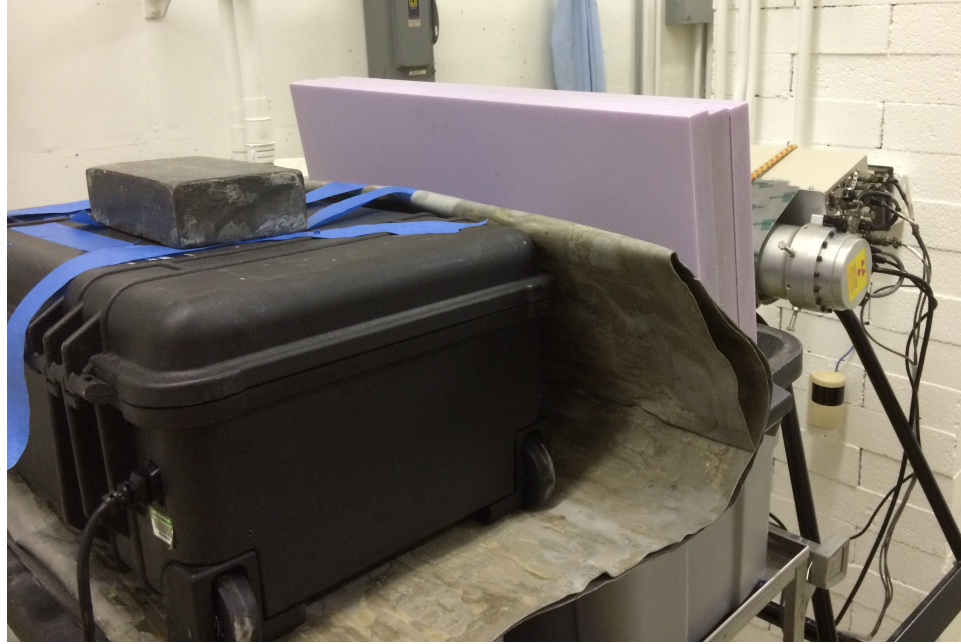
Figure 5.14: Experimental apparatus with the CdZnTe detector array inside the black Pelican® case, lavender sheets of borated polyethylene, and the neutron generator tube behind. The metallic shielding was used to eliminate bremsstrahlung.

Using the net counts (subtracting the mean continuum to the right of the peak) in the neutron signature peak, the measured effective attenuation cross section of the borated polyethylene was calculated to be 0.21 ± 0.05 cm^{-1}. Using MCNPX [119] to simulate the measurement, the effective cross section was calculated to be 0.19 ± 0.01 cm^{-1} using a quenching factor of 25%. Contrastingly, 10 keV photons would be attenuated by 99% by 7.5 cm of polyethylene. High-energy photons do not produce the characteristic peak as shown in Fig. 5.9. Furthermore, only 1% of 100 keV photons would be absorbed by 7.5 cm of polyethylene. Thus, adding polyethylene between the DD generator and detector array modulates the hypothesized neutron signature peak as incident neutrons would, and the spectra cannot be explained by assuming the interactions are from low-energy or high-energy photons. Therefore, these events must be neutron-induced.
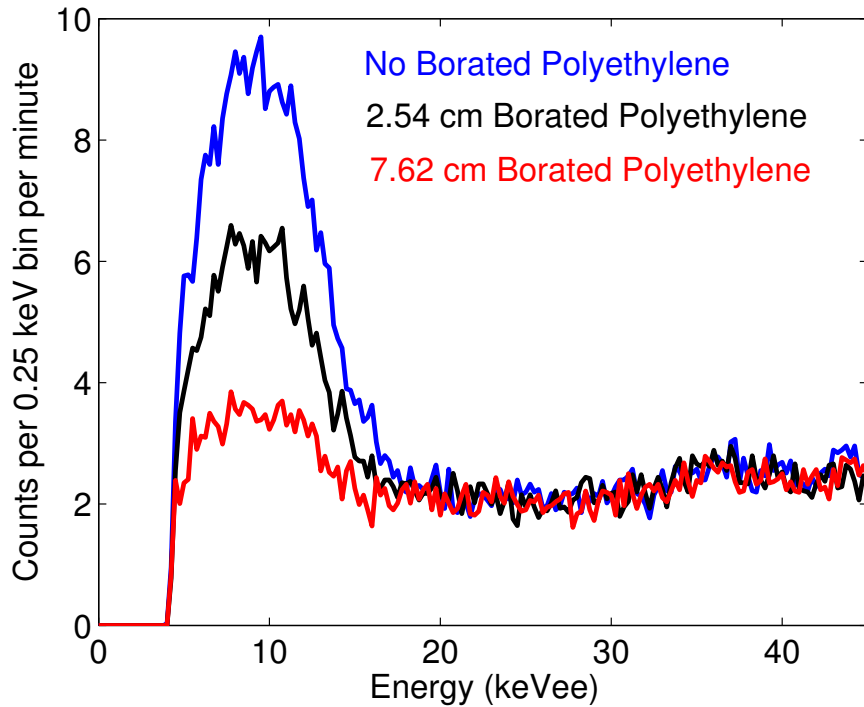
Figure 5.15: Recorded energy spectrum from the DD neutron generator with different thicknesses of borated polyethylene moderator between the detector array and neutron generator. Each measurement lasted 45 minutes.

5.2.3 Measurements of Non-monoenergetic Neutron Sources

Realistic neutron sources encountered in the field are not monoenergetic. Rather, they emit neutrons via fission or (α,n) reactions. An 18 μCi ^{252}Cf spontaneous fission neutron source (generating 80,000 neutrons per second in 4π) was placed 20 cm away from the detector array. Again, some moderating materials were placed between the source and detector array. The recorded energy spectra with different intervening materials are shown in Fig. 5.16. In the cases where the source was bare or shielded with lead, there are considerably more events in the spectra with energy below 25 keVee, indicating the presence of a neutron source. The lead shield attenuates photon signatures of the material, but the neutron detections still indicate the presence of SNM. Practically, if a plutonium source is adequately shielded with lead, the gamma-ray lines around 400 keV may be attenuated while neutrons pass through the shield; in this case, neutrons provide the only available signal for detection.
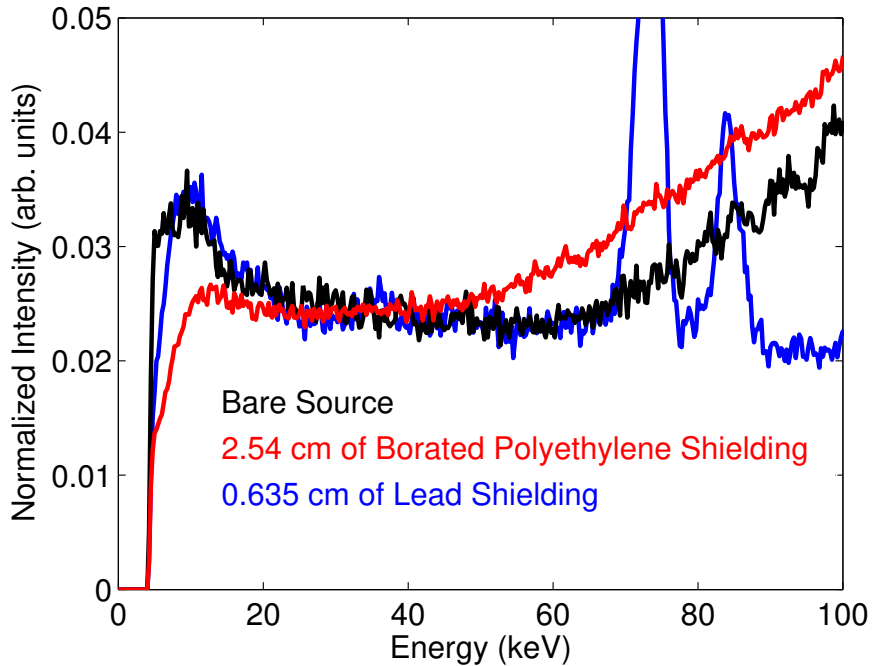
Figure 5.16: Recorded energy spectra from a ^{252}Cf source with different moderators between the detector array and source. The spectra are normalized to the count rate in the 30-40 keV range.

Different neutron sources have different energy spectra. Therefore, one would expect the rising portion of the low-energy neutron-signature peak to vary with the neutron source. As shown in Fig. 5.17, the rising edge of the low-energy peak does change with different neutron sources. The PuBe (α,n) source has the highest neutron energy, so the rising edge begins around 50 keVee. The DD neutron generator is a monoenergetic source, so it has a sharp rising edge, whereas the ^{252}Cf source (with a Watt neutron energy distribution) rises more slowly. This observation matches the physics of elastic fast neutron scattering in CdZnTe. For reference, the neutron energy distributions are given in Fig. 5.18 [120].

5.3 Fast Neutron Source Localization

The attenuation profiles shown in Fig. 5.12 inspired the development of a method to localize a fast neutron source azimuthally [121]. The main idea of the localization
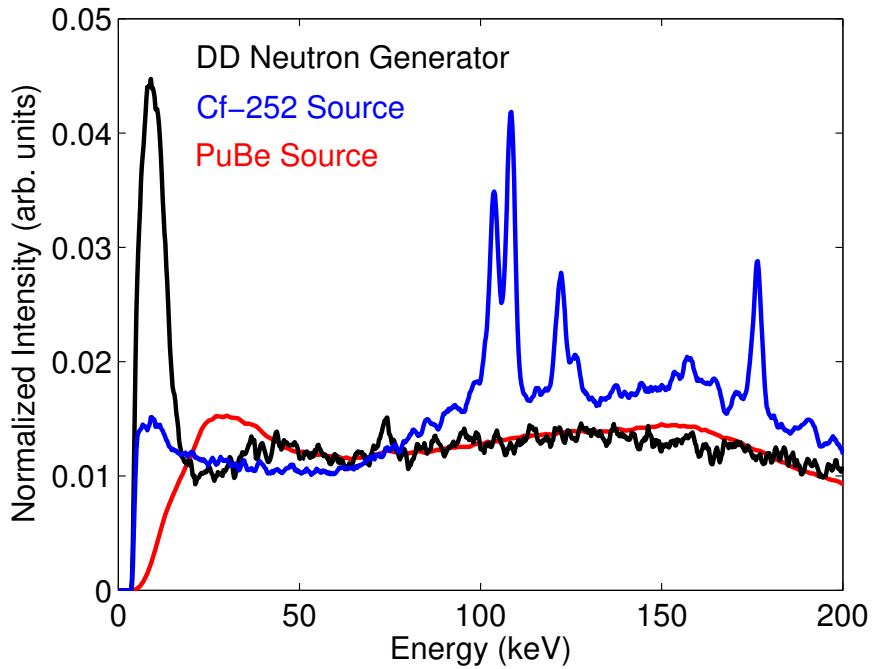
Figure 5.17: Recorded energy spectra from a ^{252}Cf spontaneous fission neutron source, a DD neutron generator, and a PuBe (α,n) source. The spectra are normalized to the count rate in the 65-85 keV range.
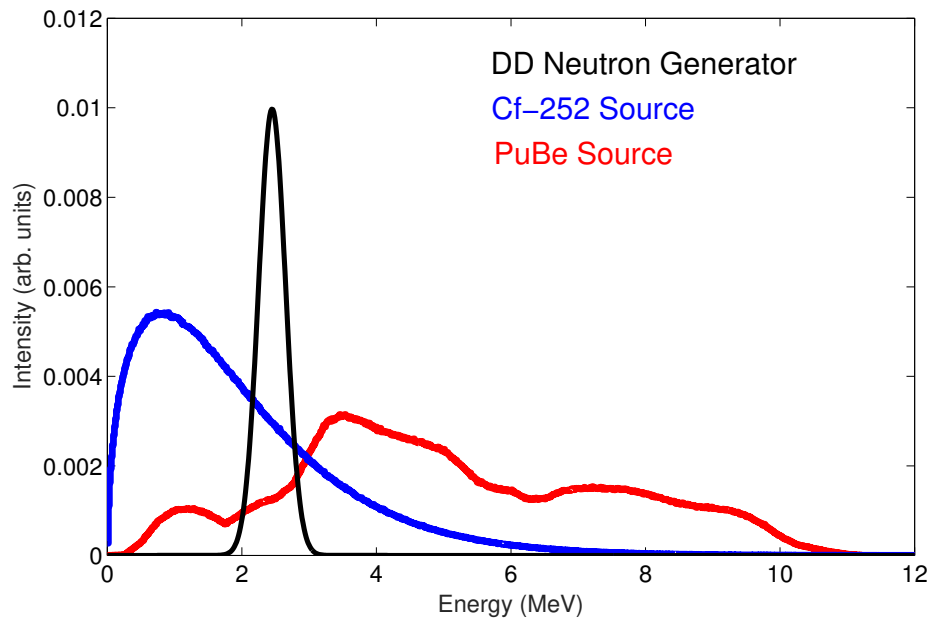
Figure 5.18: Expected neutron energy distributions for the measured neutron sources.
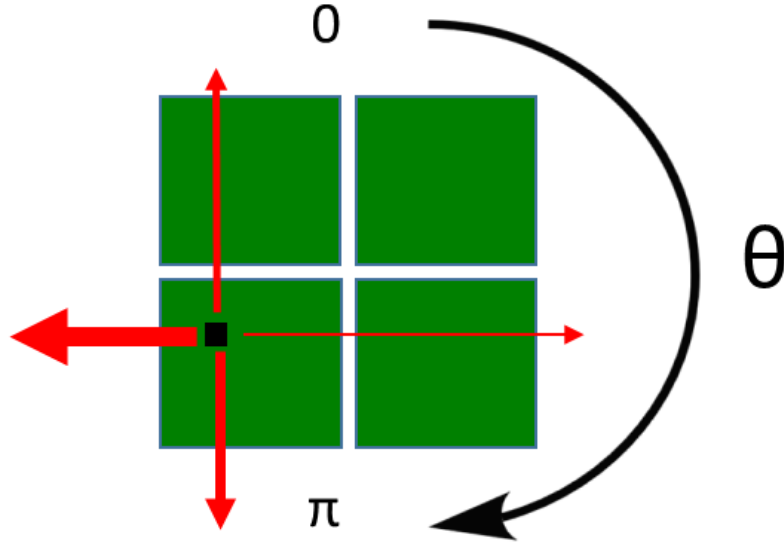
Figure 5.19: Illustration of the reconstruction algorithm principle for fast neutron localization. Directions with less material between the interaction site and the detector's edge are given more weight in the reconstruction. The black curve illustrates the direction of incident angle, θ.

method is illustrated in Fig. 5.19. For each event, the probability that a neutron came from a given azimuthal direction, θ, is proportional to the exponential material attenuation through the CdZnTe from the interaction location to the detector array edge. Each suspected neutron interaction (a small energy deposition) is back-projected through θ and the total linear path length through CdZnTe is calculated. If the path length is large, the attenuation should be large, lowering the back-projected intensity from that direction. Thus, more probable incident directions are closer to the array edge.

To test this algorithm, irradiations from the DD neutron generator were taken from five directions as shown in Fig. 5.20. The localization results are shown in Fig. 5.21. While the angular resolution is poor, the measured results roughly matched what was expected. For instance, irradiation position one and position two are peaked in the opposite direction as expected. Likewise, the peak intensity of position five lies to the right of position one and the peak intensity of position four is to the right of position four's peak intensity. The signal-to-noise ratio is poorest for position three
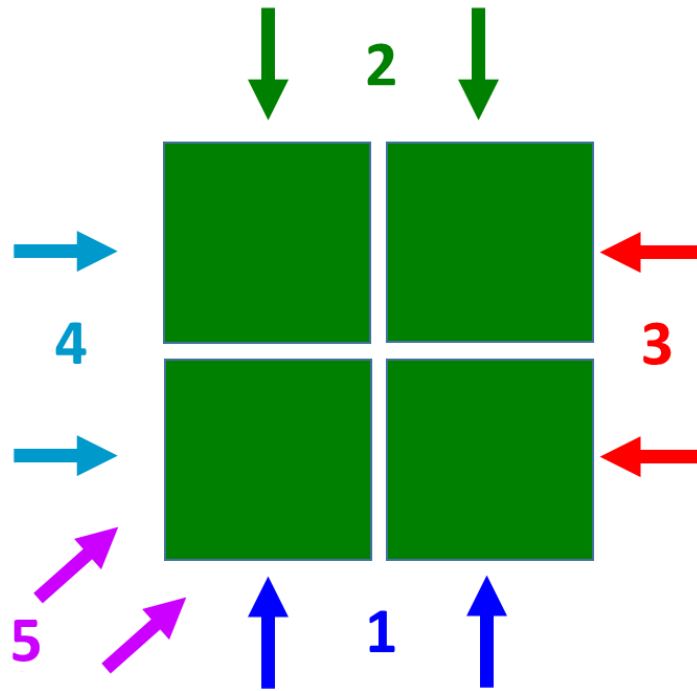
Figure 5.20: Irradiation directions recorded from a DD neutron generator using the prototype digital CdZnTe array.
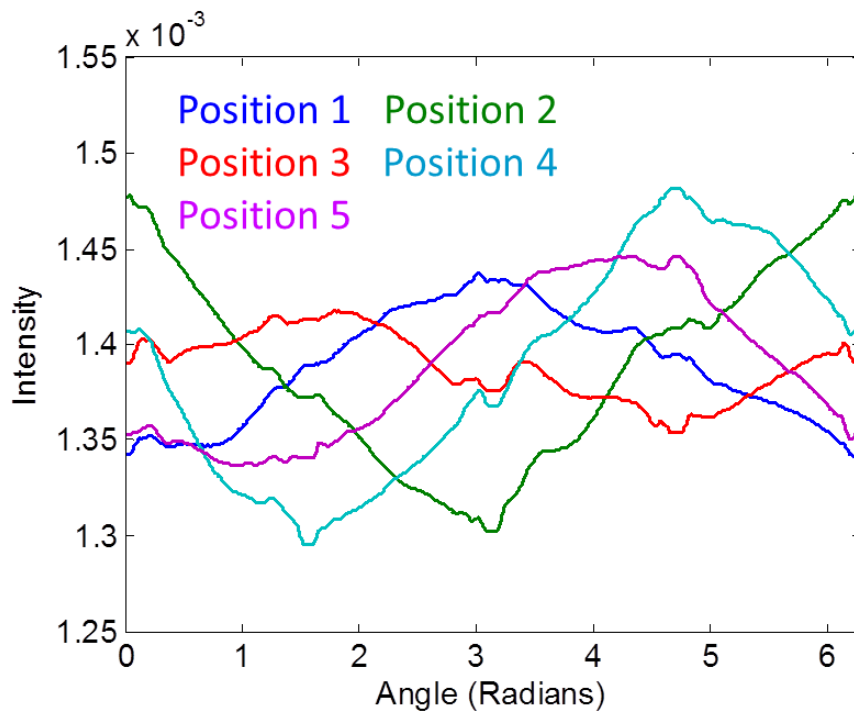
Figure 5.21: Localization reconstruction results from the five irradiation directions shown in Fig. 5.20. This figure courtesy of David Goodman.

because the Peltier heat removal device was between the neutron source and detector for this irradiation orientation. The Peltier device contains a substantial amount of aluminum which scatters the incident neutrons.

5.4   Fast Neutron Damage

Charged particles and neutrons may damage the CdZnTe material in a way that generates trapping sites for charge carriers. HPGe detectors are also susceptible to this form of radiation damage at neutron fluences of 10^{10} neutrons per square centimeter [122]. Previous research has shown the CdZnTe may be damaged by photon doses of 30 kGy [123], proton fluences of 10^8 protons per square centimeter [124], or spontaneous fission neutron fluences of 10^{10} neutrons per square centimeter [125, 126]. Radiation damage has been inferred by reduced mobility-lifetime product of electrons and holes, photopeak position shifts, energy resolution degradation, and altered leakage current. Often, annealing the detector at a slightly raised temperature to drift out damage sites allows the detector performance to recover.

CdZnTe detectors read out by ASICs which digitally sample the pulse waveforms induced on the preamplifier may provide more information about radiation damage due to the higher energy resolution. Perhaps some damage which goes unnoticed on poorer performing systems may be observable using a high performance sensor. During the measurement of the PuBe source, a CdZnTe detector was exposed to a neutron fluence of approximately 2×10^8 n/cm^2.

The energy resolution of the sensor was degraded after irradiation. Before the neutron measurement, the energy resolution was 0.48% FWHM at 662 keV using the 3 MeV dynamic range setting. Immediately after the PuBe irradiation, the energy resolution degraded to 0.58% FHWM at 662 keV. Within two days at bias at room-temperature, the resolution had improved to 0.53% FWHM as shown in Fig. 5.22. Other research has shown CdZnTe energy resolution degradation recovery simply
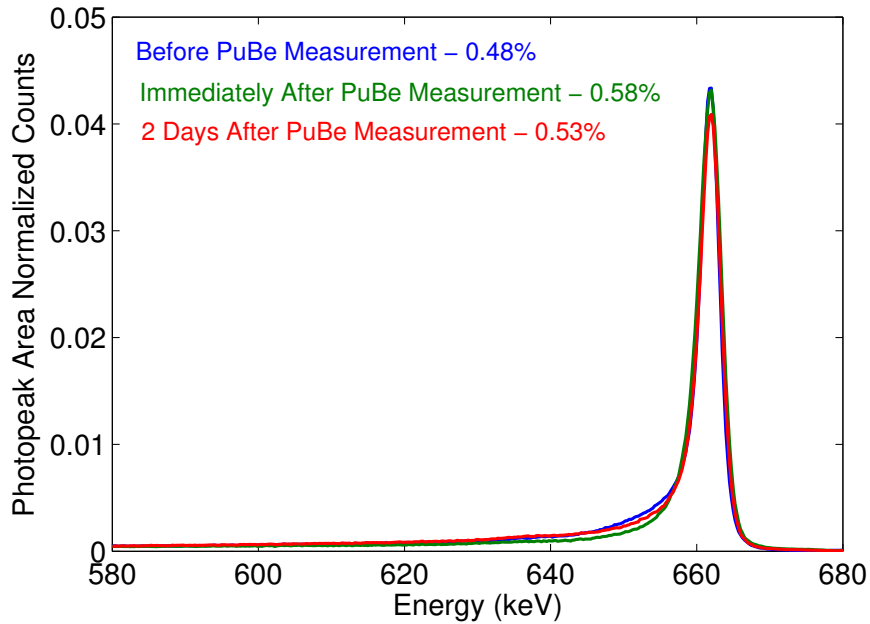
Figure 5.22: Self-corrected ^{137}Cs energy spectra recorded before and after PuBe source measurement for detector 6RID-28 zoomed to photopeak region. The energy resolution has degraded after the neutron irradiation.
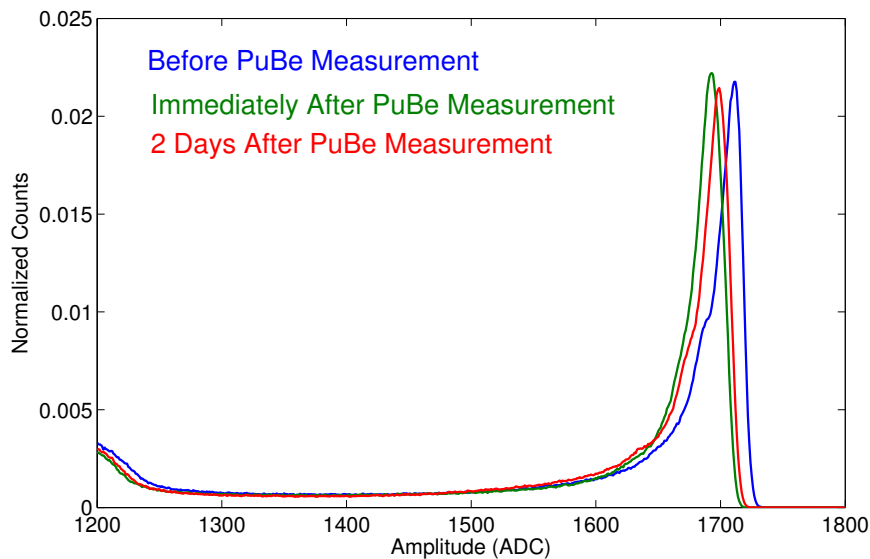
Figure 5.23: Raw photopeak amplitude distribution of ^{137}Cs calibration measurements for 6RID-28 shown in Fig. 5.22. Note that the photopeak centroid position has shifted. Each measurement lasted four hours.

by leaving the detector at bias at room-temperature and not exposing it to further irradiation damage [125].

As shown in Fig. 5.23, the photopeak centroid position has shifted in accordance
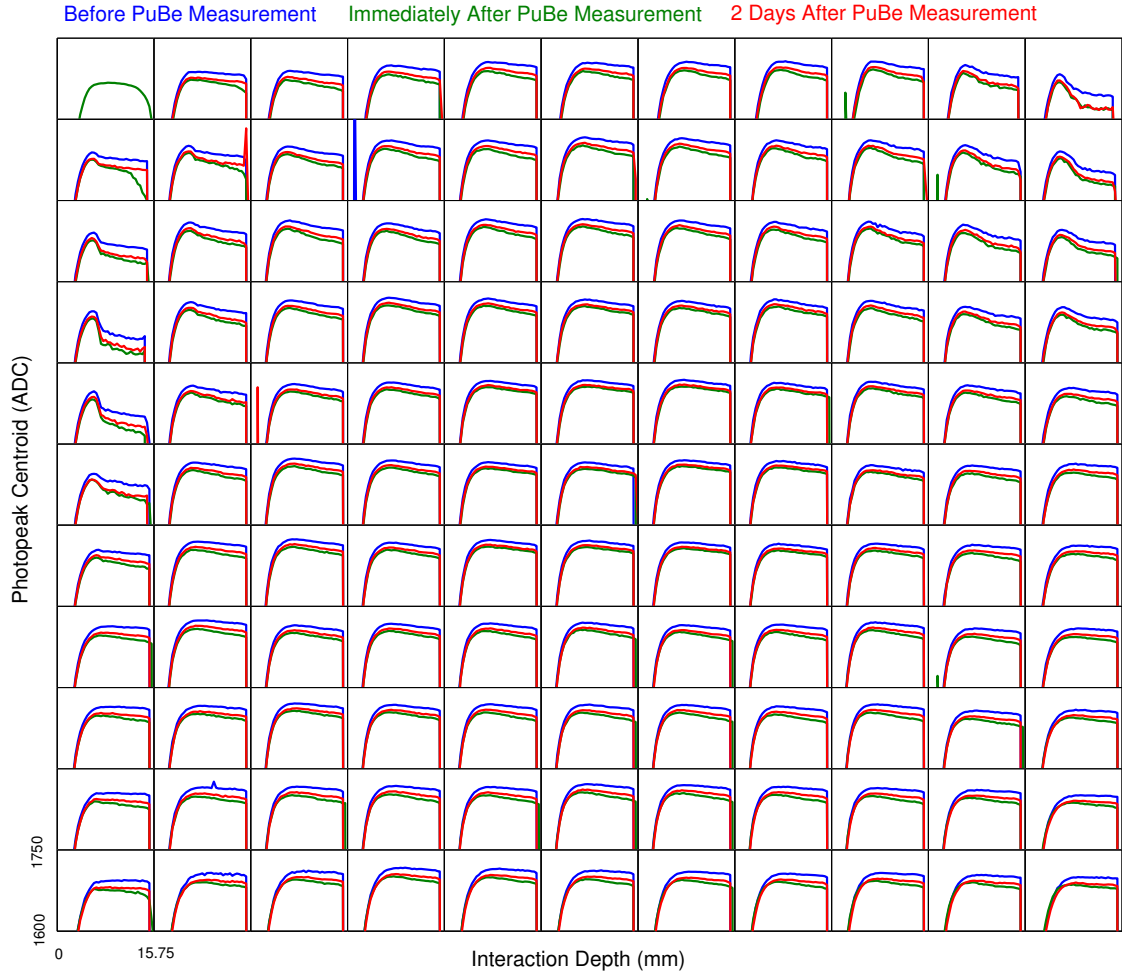
Figure 5.24: Photopeak centroid as a function of depth for each anode pixel in detector 6RID-28 before and after neutron irradiation. The lower left plot shows the scale.

with the energy resolution degradation. The system was tested with another CdZnTe detector which was not irradiated. This detector, 6RID-29, did not show energy resolution degradation or photopeak position shift indicating that the changes are due to damage in the CdZnTe detector from neutron irradiation. However, since direct-attachment detectors (see Sect. 2.5) were used, it is possible that the ASIC was damaged by the neutron irradiation. In the future, modular ASICs should be used to study if neutron damage occurs in the ASIC, detector, or both.

Some evidence indicates that damage is occurring in the CdZnTe material itself. Fig. 5.24 shows the recorded photopeak centroid for single-pixel 662 keV energy de-
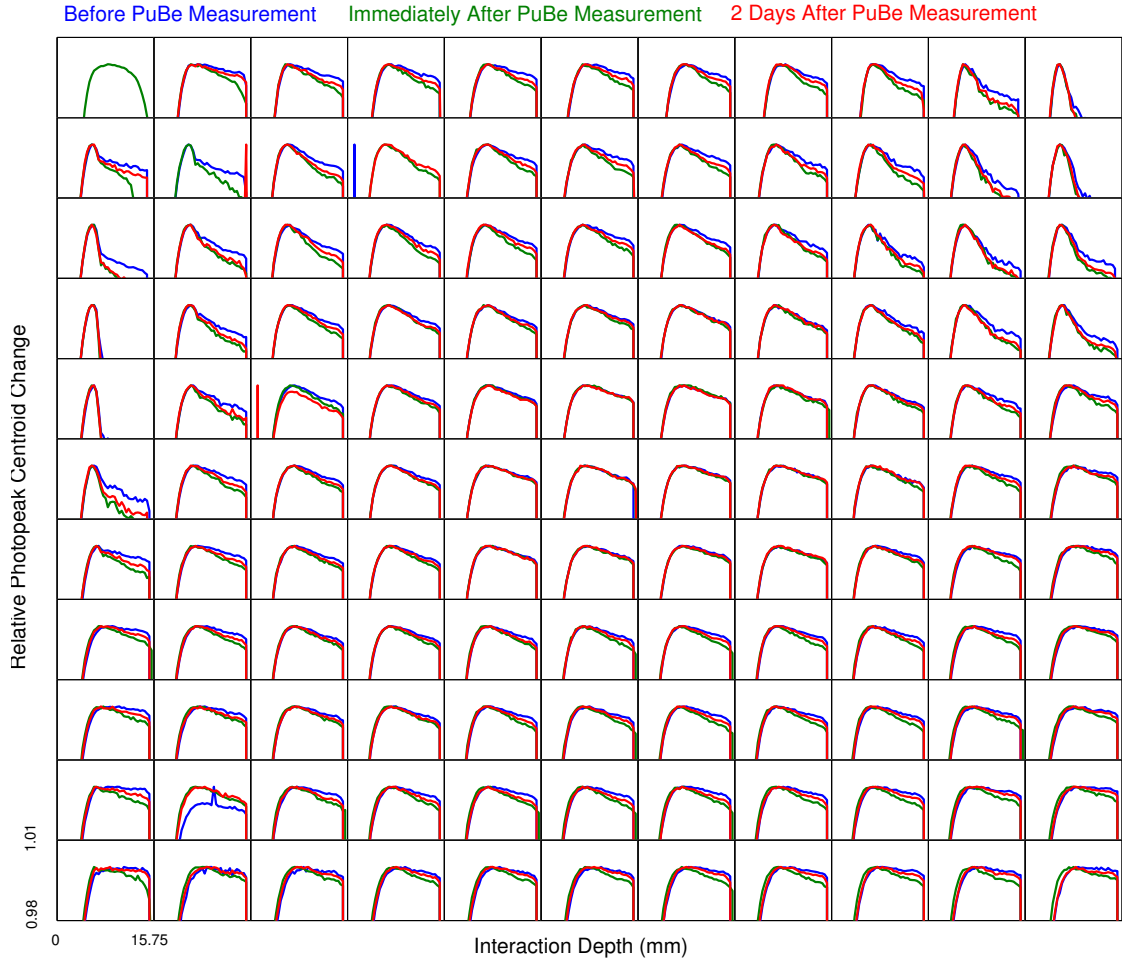
Figure 5.25: Relative photopeak centroid as a function of depth for each anode pixel in detector 6RID-28 before and after neutron irradiation. The maximum value in each pixel is set to one by dividing each photopeak amplitude by the maximum photopeak centroid in each pixel for each measurement. The lower left plot shows the scale.

positions as a function of the interaction depth. While the photopeak centroid is lower following irradiation throughout the bulk, the relative decline is steeper near the cathode-side. Fig. 5.25 normalizes each measurement to the maximum photopeak amplitude in each pixel. From this plot, it is clear that after irradiation, the photopeak centroid is relatively smaller near the cathode after irradiation. This is consistent with neutron damage throughout the bulk which creates charge trapping sites. Photoelectric interactions on the cathode-side will have to drift through more damage centers, reducing the signal amplitude. This is also consistent with a smaller

value for the mobility-lifetime product, $(\mu\tau)_e$, following neutron irradiation.

Again, these effects have likely occurred in other CdZnTe spectrometer systems exposed to neutron irradiation. However, with the advent of digitally-sampled pulse waveforms, the effects neutron damage at lower fluences can be studied.

5.5 Conclusions

Thermal neutron detection using CdZnTe detectors has been known for many years. However, the improved energy resolution and larger volumes achieved from monolithic pixelated detectors read out by digital electronics have improved the signal-to-noise ratio for neutron detection.

Only recently have the low-energy thresholds of CdZnTe detector reached levels where energy depositions from fast neutron nuclear recoils are visible. While neutron interactions cannot be discriminated on an event-by-event basis from photon energy depositions, when a fast neutron source is present, a characteristic low-energy feature is observed in the spectrum. CdZnTe attenuates neutrons and the attenuation pattern can be use to localize the azimuthal direction of the source. Observation of characteristic inelastic scattering gamma rays are also observed when a neutron source is measured with a CdZnTe detector.

Energy resolution degradation was observed in CdZnTe detectors at lower neutron fluences than previously measured. This is likely due to the improved energy resolution of CdZnTe detectors read-out by digitally sampling the preamplifiers which allows the observation of this slight degradation.

146

CHAPTER VI

High-Energy Gamma ray and Cosmic Muon Detection

The detection of high-energy photons (multi-MeV) is critical if CdZnTe is to be deployed for active interrogation. Active scanning systems interrogate a "black-box" with neutrons or high-energy gamma rays and observe secondary emissions. If the interrogated material is fissile, active interrogation will induce high-energy fission gamma-rays and fast neutrons. If these high-energy gammas and neutrons can be efficiently detected, CdZnTe could find use in these systems which currently employ low-resolution gamma-ray spectrometers (mostly NaI) and neutron detectors (scintillators and ^{3}He).

Nuclear resonance fluorescence (NRF) techniques have been studied to characterize incoming cargo for national security [127, 128]. These techniques rely on the accurate and efficient detection of high-energy photons. High-resolution spectroscopy is demanded so HPGe is typically used for NRF. CdZnTe, with improved high-energy gamma-ray energy resolution, could replace HPGe in these scanners due to its advantages including room-temperature operation, higher effective Z number, and additional gamma-ray imaging and neutron detection capabilities.

Furthermore, any time neutrons are present, high-energy photon emissions are possible due to thermal neutron capture. These capture gamma rays provide infor-
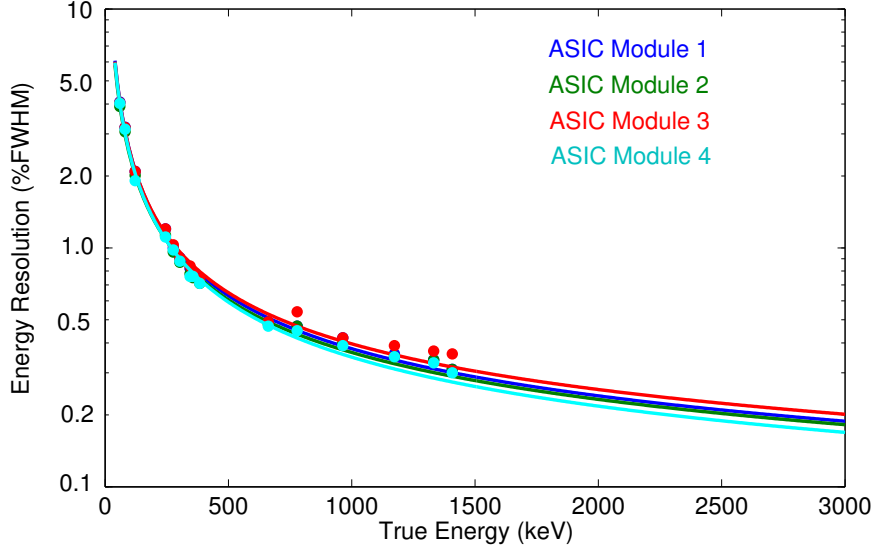
Figure 6.1: Energy resolution as a function of incident photon energy for single-pixel events measured using the prototype digital CdZnTe array. Note the log-scale on the y-axis.

mation about surrounding materials as the photon energy depends on the capturing nucleus. From nuclear weapons, lines from nitrogen, hydrogen, and oxygen are indicative of explosives surrounding a neutron emitting medium. This chapter explores the challenges encountered when using CdZnTe for high-energy photon detection with documentation of several successful high-energy gamma-ray measurements as well.

6.1 Energy Resolution Degradation at High Energies

In theory, energy resolution improves as $E^{-\left(\frac{1}{2}\right)}$ from carrier statistics [3]. In electronic noise limited systems, like the best CdZnTe detectors, resolution should improve considerably at high energies. However, the energy resolution for single-pixel events at 2.6 MeV is worse than expected based on the resolution measured for single-pixel events at 662 keV.

Fig. 6.1 shows how the energy resolution changes as a function of photon energy, E. The data are fit using Eq. 6.1 [3] where R is the energy resolution expressed as a percentage, α describes peak broadening not related to the energy deposited (such
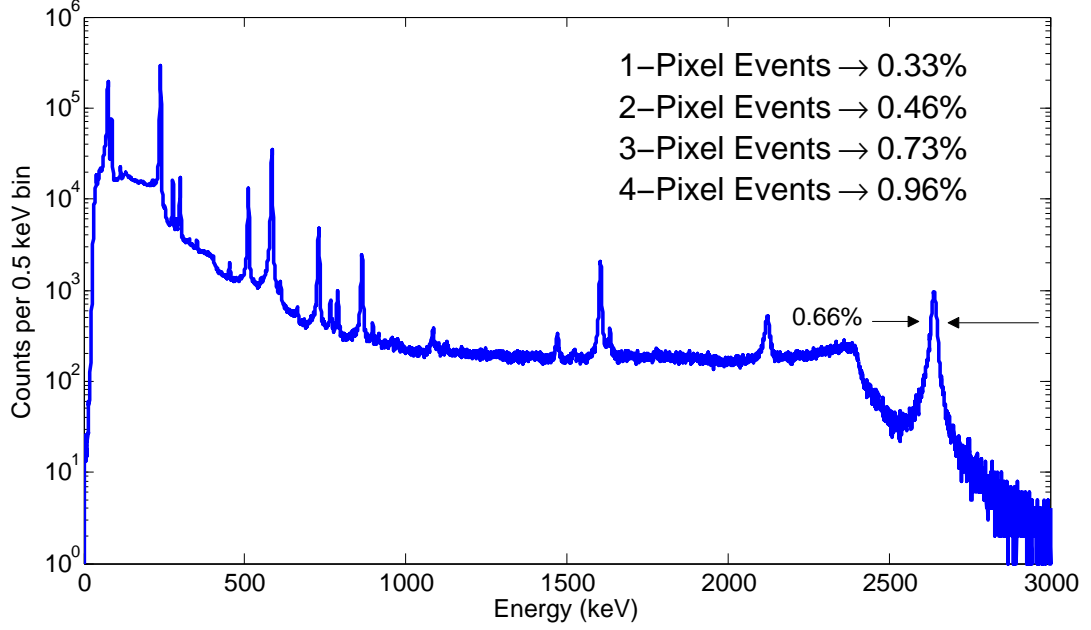
Figure 6.2: All-events gamma-ray energy spectrum from a ^{228}Th source. The all-events energy resolution of the 2.6 MeV photopeak, from the ^{208}Tl daughter, is highlighted. The photopeak energy resolution as a function of the number of pixels triggered is provided in the inset text. The measurement duration was 8 hours.

as electronic noise), and β describes resolution degradation due to larger deposited energy (such as uncertainty from carrier statistics).

$$R = \frac{\sqrt{\alpha + \beta E}}{E} \tag{6.1}$$

Based on the fits in Fig. 6.1, the single-pixel energy resolution at 2.6 MeV should be around 0.2% FWHM. However, as shown in Fig. 6.2, the measured single-pixel energy resolution is 0.33% FWHM at 2.6 MeV. The resolution is poorer than expected even at 1 MeV as illustrated by the markers deviating from the fits at higher energies in Fig. 6.1. Furthermore, the all-events energy resolution of the 2.6 MeV photopeak is worse than the resolution at 662 keV shown in Fig. 2.3. Even the best detectors only achieve 0.27% FWHM at 2.6 MeV. The all-events energy resolution degrades due to a non-linear energy response from the ASIC, larger electron cloud size, and higher probability of multiple-pixel interactions.
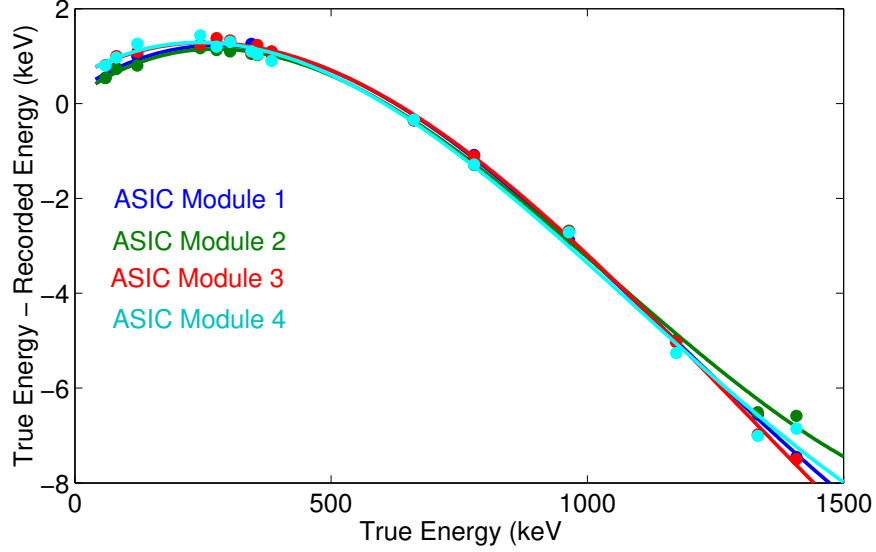
Figure 6.3: Difference between true and reconstructed energy for photons of various energies in the prototype digital CdZnTe array system. The lines are polynomial fits of the energy non-linearity used to correct it.

6.1.1 Non-linear Energy Response

ASICs designed by IDEAS, including the VAD_UMv1.2 and VAD_UMv2.2 ASICs, exhibit a non-linear energy response. Fig 6.3 shows the measured energy non-linearity for each of the four ASIC modules in the prototype digital CdZnTe array system which is more severe at higher photon energies [65]. If uncorrected, this degrades the energy resolution for multiple-pixel events because the reconstructed energy depends on how the photon energy is shared between collecting pixels or scattering interactions.

Non-linearity is corrected with a set of gamma-ray energy measurements at a variety of photon energies. A polynomial fit is to correct the measured energy to the true energy. The size of the improvement from this correction increases as photon energy increases and as the number of triggered pixels increases as shown in Fig. 6.4. For the 2.6 MeV photopeak from ^{228}Th, the non-linearity correction improves the overall energy resolution to 0.59% FWHM.
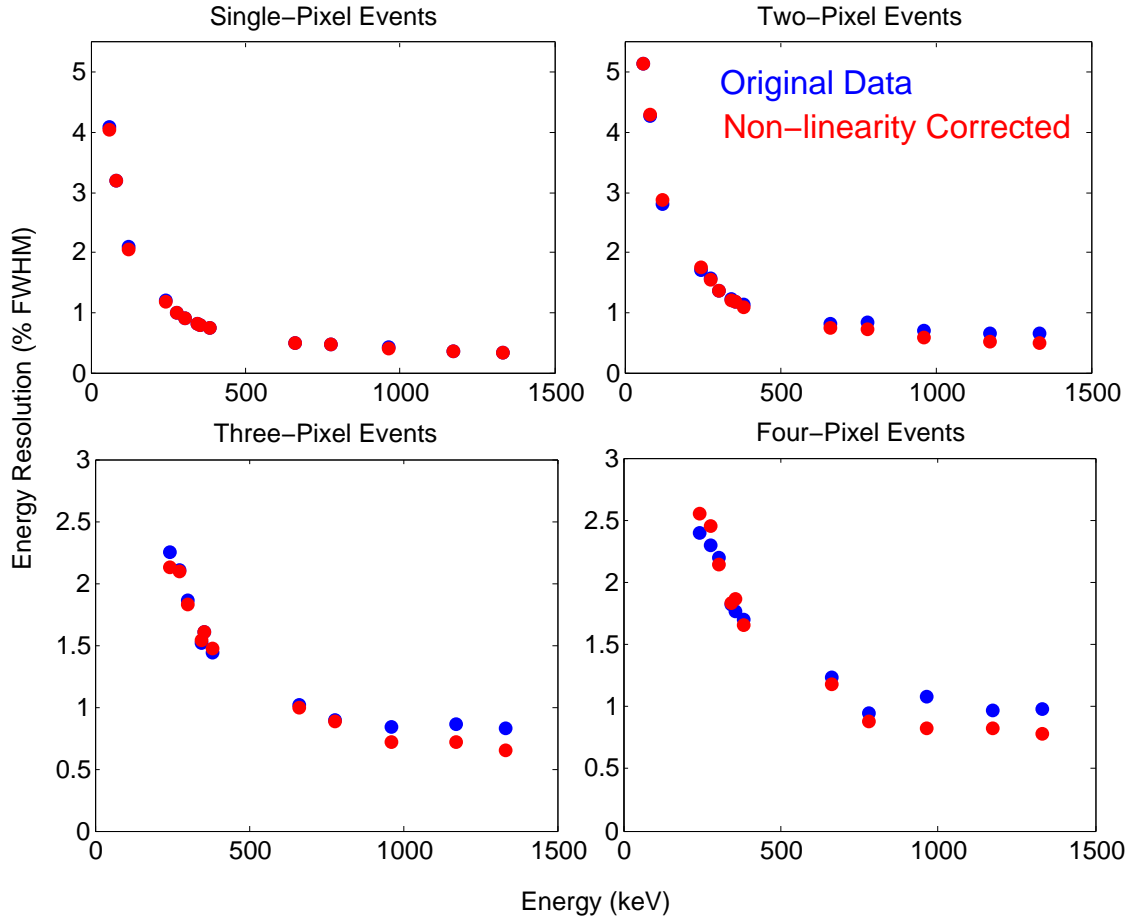
Figure 6.4: Energy resolution as a function of photon energy before and after non-linearity energy correction separated by the number of pixels triggered.

6.1.2 Remaining Energy Resolution Degradation

As the number of triggered pixels, N, increases, the electronic noise contribution to the energy resolution increases by $\sqrt{N}$. This is unavoidable from the addition of N Gaussian noise distributions. As the incident photon energy increases, the expected number of triggers per event increases because Compton scattering becomes more likely (leading to more interaction sites) and the electron cloud size increases [66]. The larger electron cloud leads to more charge-sharing events. Charge-sharing events are difficult to correct due to uncertainty in WPCT, the effect of transient signals, and electron steering in the vicinity of the anode pixel as discussed in Chap. II.

For example, a direct-attachment detector, 6RID-29, exhibits excellent single-pixel

energy resolution of 0.34% FWHM at 662 keV. For two-pixel cathode-side events where both interactions occur in inner 9×9 non-neighboring pixels, the energy resolution degrades to 0.49% FWHM - very close to the $\sqrt{2}$ factor predicted from electronic noise. However, the energy resolution of two-pixel side-neighbor events is 0.89% FWHM using current reconstruction algorithms. This degradation drives the overall two-pixel events energy resolution to 0.74% FWHM at 662 keV.

The energy resolution degradation of single-pixel events at high energies may be caused by charge leak from the collecting pixel to neighbor pixels which is not accurately corrected. Another hypothesized reason for energy resolution degradation involves variation in microscopic electron-trapping sites due to material defects. Theoretically, the depth-of-interaction correction should account for electron trapping. However, microscopic trapping centers encountered by the electron cloud as it drifts toward the anode may cause variation in the measured signal amplitude which degrades the energy resolution. As the electron cloud becomes larger, less dense, and more variable in size for high-energy photon energy depositions, this trapping variability may become more important [66].

To study whether this is the case, one can compare the energy resolution of single-pixel photoelectric absorptions with the energy resolution of double-escape peaks following pair production at roughly the same energy [129]. Pair production events will have smaller electron clouds because the photon energy is shared between a positron and an electron rather than a single photoelectron as in photoelectric absorption. If microscopic defects cause energy resolution degradation at high photon energies for single-pixel events, the smaller electron cloud may be less effected even though the charge density is higher. Anecdotally, the energy resolution of the double-escape peak at 1.6 MeV from Fig. 6.2 has a single-pixel energy resolution of 0.32% FWHM, better than the single-pixel energy resolution at 2.6 MeV which should not be true based on Eq. 6.1. This may be due to trapping variation on the order of the size of the electron

cloud. This effect may also be due to large electron clouds moving through different weighting potentials which are not accurately captured by the centroid depth. The electron trapping for a large electron cloud may not be accurately reconstructed either. More study should be carried out in this area at different photon energies to verify this hypothesis.

6.2   Detection of Photons with Energy Higher than 3 MeV

Boucher performed gamma-ray spectroscopy measurements for neutron activated water using a deuterium-tritium neutron generator to produce 14.1 MeV neutrons [48]. The neutrons undergo (n,p) reactions with ^{16}O in the water and produce 6.1 MeV photons in 69% of decays from ^{16}N or 7.1 MeV photons in 5% of decays. Analog VAS_UM2.3/TAT4 ASICs were used to read out eighteen detectors measuring the secondary gamma rays. However, the energy resolution was 2.45% FWHM at 2.6 MeV, and the 6.1 MeV photopeak could not be resolved using this sytem. Boucher suggested that transient signals were not properly rejected, leading to unresolvable high-energy peaks. Digital array systems have much better energy resolution at higher energies and have software trigger thresholds to limit the effect of transient signals.

To test the energy resolution of digitally-sampled CdZnTe arrays for high-energy photons, the Orion prototype system, using the VAD_UMv1.2 ASIC, was taken to the Ohio State University Research Reactor facility. A beam of thermal neutrons was directed at a piece of PVC to create high energy gamma rays from thermal neutron capture on ^{35}Cl. Kroupa used a similar approach to test the energy resolution at high photon energies for HPGe, LaBr$_3$, and NaI detectors [130]. Using CdZnTe, thermal neutrons were also captured on ^{113}Cd generating other capture gamma rays. The recorded energy spectrum is shown in Fig. 6.5. This measurement did not have an energy non-linearity correction applied.

A small peak is visible around 3 MeV and perhaps another at 5 MeV, close to
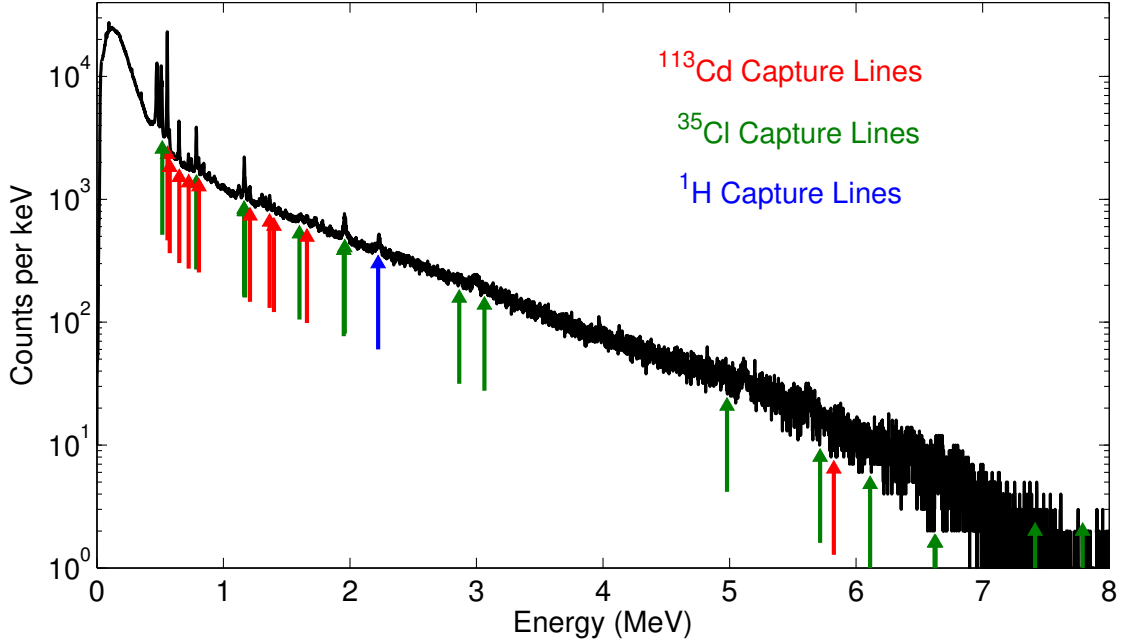
Figure 6.5: Recorded all-events gamma-ray energy spectrum for a thermal neutron beam incident on a PVC target recorded using a 2×2 array of CdZnTe detectors read out using the VAD_UMv1.2 ASIC. The measurement lasted 14 hours.

the energy of capture gamma rays from ^{35}Cl, but high-energy gamma-ray lines were not clearly resolved. However, upon further analysis, it appears that the geometry was not very efficient at generating gamma rays from thermal neutron capture or the detector array was too far away. Only 13,000 net counts were detected in the 788 keV photopeak, one of the most probable emissions following neuron capture on ^{35}Cl [131]. The photopeak efficiency for 3 MeV or higher energy gamma rays is at least an order of magnitude less, so it is not surprising that the photopeaks were not resolved.

Another attempt to measure high-energy gamma rays was made using a ^{239}PuBe (α,n) neutron source. After the ^{9}Be(α,n)^{12}C* nuclear reaction, the carbon nucleus is left in an excited state which de-excites via the emission of a 4.438 MeV gamma-ray [132]. This line has been measured using NaI and HPGe detectors [133]. The line is significantly Doppler-broadened depending on the energy of the alpha particle. The FWHM of the line is expected to be around 150 keV from Doppler broadening based on an alpha particle energy of 5.1 MeV [134].

154
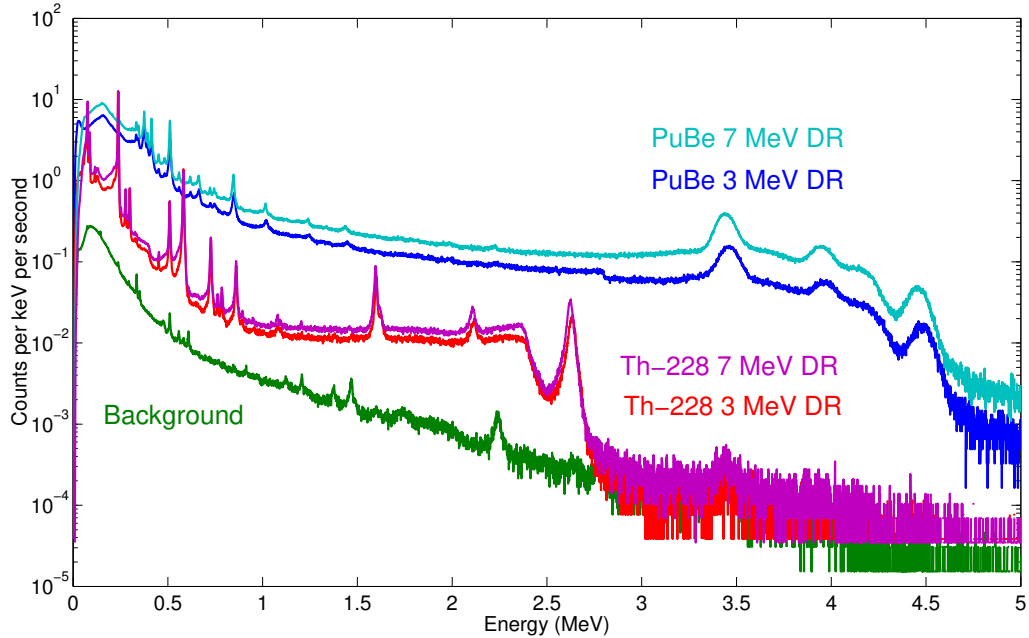
Figure 6.6: Recorded all-events gamma-ray energy spectrum for various sources using the VAD_UMv2.2 array system. The different dynamic range (DR) settings used are indicated. Peaks indicative of the 4.4 MeV gamma ray are visible regardless of the dynamic range setting. Each PuBe source measurements lasted one hour, each ^{228}Th measurement was 4 hours, and background was measured for 12 hours.

Two CdZnTe detectors directly coupled to VAD_UMv2.2 ASICS were placed in the system shown in Fig. 2.4. This system was used to observe if the additional dynamic range settings improved high-energy detection. A non-linearity correction was not applied. Yet, as shown in Fig. 6.6, the full-energy peak, double-escape peak, and single-escape peak of the 4.4 MeV line are all visible in the recorded energy spectrum. The measured FWHM of the full-energy peak is 142 ± 15 keV.

The double-escape peak from the 4.4 MeV photon may be visible during the background and ^{228}Th measurements included in Fig. 6.6 for reference. During these measurements, the PuBe source was placed in a polyethylene-filled barrel one room away. It is possible that 4.4 MeV gamma rays escaped the barrel and were detected during other measurements. Also note in Fig. 6.6 that the shape of the 2.6 MeV photopeak from ^{228}Th is different than the 4.4 MeV associated peaks, demonstrating Doppler broadening.
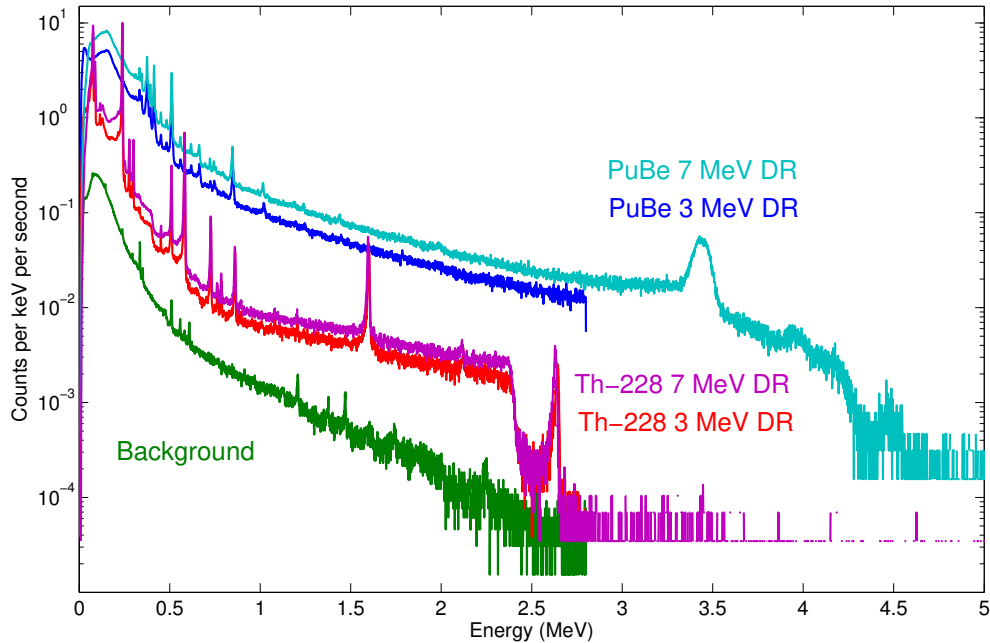
Figure 6.7: Recorded single-pixel events gamma-ray energy spectrum for various sources and dynamic ranges using the VAD_UMv2.2 array system.

The step in the PuBe measurement around 3 MeV using the 3 MeV dynamic range setting comes from events above that energy saturating the charge sensitive preamplifier. Detected saturated waveforms (i.e. exhibiting an abnormal noise distribution in the waveform tail) are rejected, resulting in the step. This indicates that there are some single-pixel interactions with an energy deposited above 3 MeV because the spectrum is discontinuous. Fig. 6.7 demonstrates this even more clearly. Using the 7 MeV dynamic range setting, the double-escape peak, at 3.4 MeV, is resolvable in the single-pixel energy spectrum.

Fig. 6.8 shows the distribution of pixels triggered as a function of the peak energy. In general, the percentage of single-pixel triggers decreases rapidly as photon energy increases. Two-pixel peak events are dominant beginning around 500 keV until around 2 MeV. The relative likelihood of a four-pixel event continues to rise up to 5 MeV. Note that the double-escape peaks do not follow this trend because the electron cloud is smaller, so charge sharing is less likely. Also, a large energy deposition from Compton scattering followed by pair production is energetically unlikely. Photoelec-
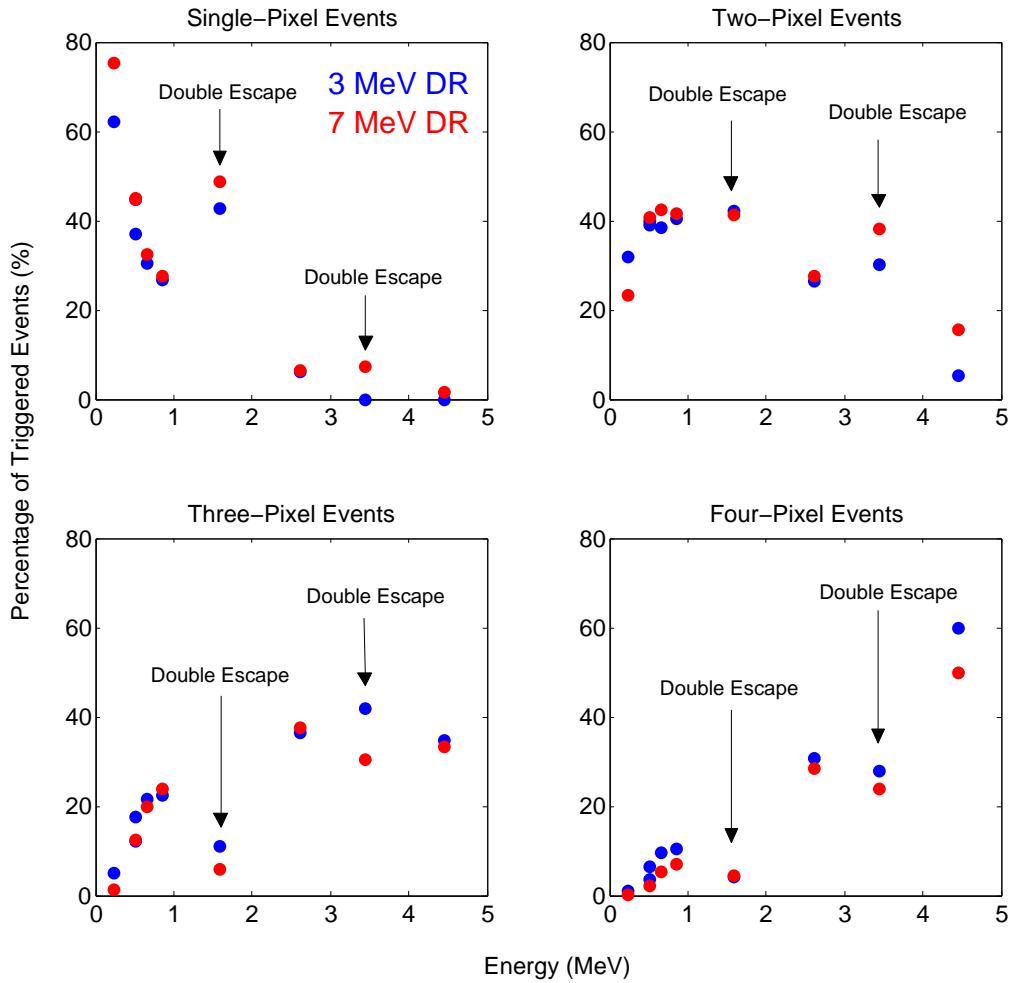
Figure 6.8: Percentage of events with one, two, three, or four triggered pixels as a function of energy for two dynamic range settings. The uncertainty is contained within the markers.

tric absorption following a significant Compton scattering energy deposition is more likely for photons of intermediate energy (between 1 and 3 MeV). As expected, there is little difference between the 3 and 7 MeV dynamic ranges in the number of pixels triggered.

The energy resolution of high-energy photons could not be well characterized because a high-intensity, high-energy, non-Doppler-broadened, monoenergetic source was not available for use. A subsequent investigation is underway to observe the gamma-ray energy spectrum following thermal neutron capture on ^{35}Cl in a higher count rate geometry.

6.3 Detection of Cosmic Muons in CdZnTe

Muons, like electrons, are leptons with elementary charge of -1. The mass of a muon is roughly 207 times greater than an electron. Muons are produced as secondary reaction product of cosmic rays and molecules in the upper atmosphere. The muon flux at sea level is about 1 muon per square centimeter per minute.

Muons at sea level are relativistic particles. In fact, without the time dilation from relativity, muons would decay before reaching Earth's surface. Muons typically have energies of 4 GeV at sea level meaning they are probably created at 6 GeV. Muons interact via Coloumbic interactions with matter as they are charged like electrons. As they move through matter, muons lose energy at a rate of 2 MeV per g/cm^2 [135].

Recently, using the natural muon background has been a popular technique for scanning large vehicles or cargo containers [136, 137]. Tomographic information can be ascertained by calculating the deflection angle through the container [138]. Muon tomography was also famously used to search for locations of hidden chambers in the Great Pyramid at Giza although none were found [139].

CdZnTe detectors have been used to detect muons before since any charged particle will generate electron-hole pairs in the semiconductor. However, the distribution of triggered pixels and energy will differ from gamma-ray interactions. The energy deposited in the detector should be several MeV - much greater than 2.6 MeV, the highest naturally occurring background gamma ray. Muons travel in a straight-line path through the detection medium. If the pixel array is parallel to the muons path, a large number of pixels should trigger co-linearly during a muon interaction. Most muons come from the zenith rather than the horizon, so the detector orientation should be selected accordingly.

Because the muon frees a large number of electron-hole pairs along a straight-line, the electron cloud looks very different than that of a gamma ray. This can be used to study neighbor signal induction for distributed electron clouds.
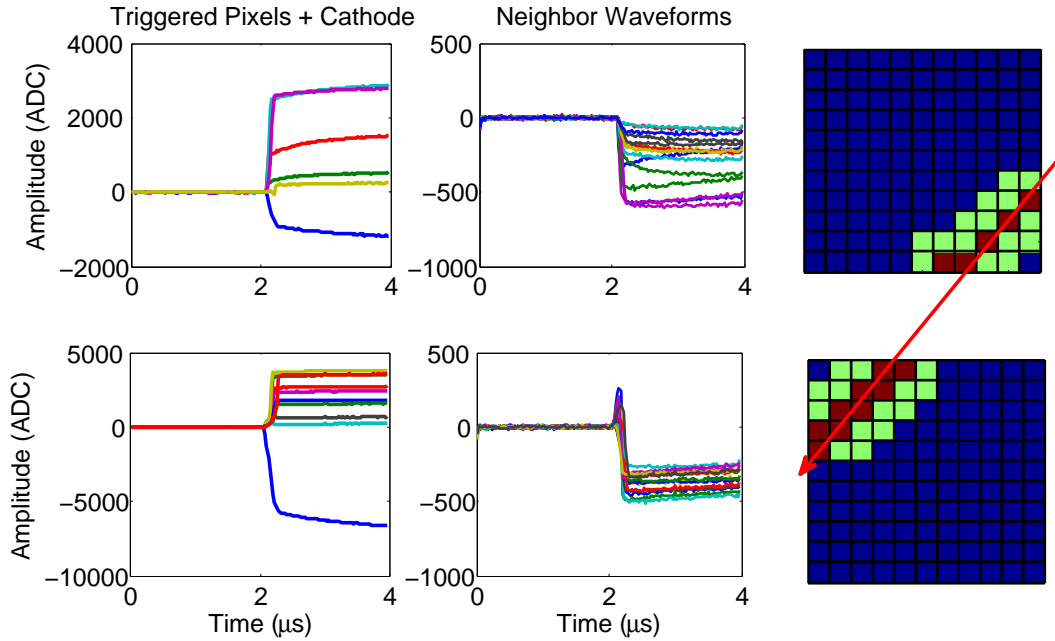
Figure 6.9: Recorded muon interaction using an array of CdZnTe detectors read out using the VAD_UMv1.2 ASIC. Two detectors were triggered during the event. The left column shows the pulse waveforms from the triggered anode pixels and cathode for each of the triggered detectors. The center column shows the pulse waveforms induced on neighbor pixels for both detectors. The right column shows the layout of the triggered pixel locations (filled red squares) and valid neighbor locations (filled in green squares) for both of the detectors. The red line is the proposed path of the muon through the detector array.

Fig. 6.9 shows the recorded pulse waveforms for a clear muon interaction in CdZnTe. In this case the detectors were oriented so that the cathode and anode surfaces were parallel with the zenith. This muon came from an intermediate angle between the horizon and zenith. The muon passed through the detector close to the anode side because the cathode and anode pulse waveforms begin rising almost simultaneously. In total, 3.2 MeV was deposited in the top detector and 8.4 MeV was deposited in the bottom detector. There is not a clear correlation between the amplitude induced and the triggered pixel location, indicating that the muon did not deposit energy uniformly across the detector. This must be from different distances traversed through each pixel as the energy loss as a function of path length is constant for a muon.

One noticeable feature in the pulse waveforms is the slope in the waveform tail. This indicates that hole movement can impact particularly the cathode amplitude but also the anode waveforms for anode-side events when a large amount of energy is deposited.

Muon detection was hindered by some challenges which remain to be solved. The Orion prototype system was configured to run for 26 hours to record the gamma-ray background. The array was oriented as described previously with the cathode and anode pixel array parallel to the zenith. Using a muon flux of 1 cm^{-2} min^{-1} and a surface area of 4×1.5 cm^2, one would expect around nine thousand muons to interact in the device. To declare a muon detection, more than 1 MeV had to be deposited in two side-neighbor detectors with five or more triggered pixels in each detector. Only three thousand events met this criteria meaning that two thirds of muons went undetected.

Fig. 6.10 illustrates some of the issues encountered when detecting muons with the VAD_UMv1.2 ASIC. 6.8 MeV was deposited in the detector during this interaction. First, note that more pixels should be triggered in the pixel map, but the muon path appears to abruptly stop. The ASIC triggering circuitry likely failed so the event was not read out properly. Also, note the unusual noise in the cathode waveform. The cathode preamplifier is saturated for this event and is likely to be saturated for many muon events. However, the event rate with saturated cathode preamplifiers is lower than one would expect. Furthermore, based on the timing difference between the cathode waveform start and the anode waveform beginning, most muon interactions appear to occur near the anode. Events should be evenly distributed in depth so perhaps cathode saturation causes the ASIC to reset and not trigger properly.

Fig. 6.11 is provided next to Fig. 6.10 to compare the induced neighbor waveforms for a possible muon event next to a probable 1.4 MeV gamma-ray induced event. The neighbor waveforms from a muon interaction are much broader due to the diffuse

160
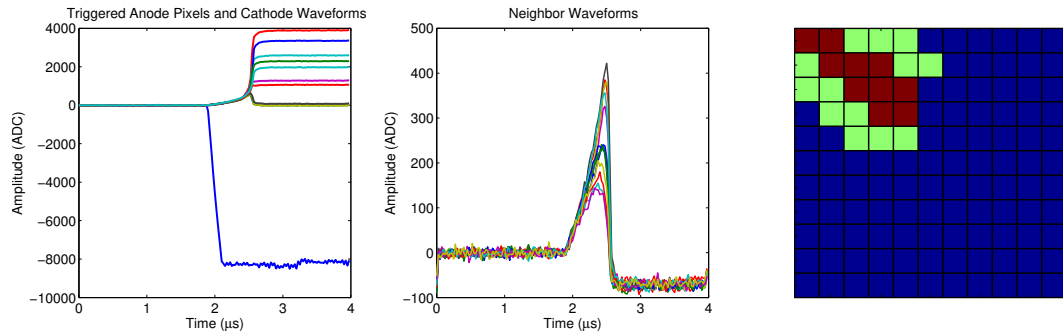
Figure 6.10: Recorded muon interaction with common problems using an array of CdZnTe detectors read out with the VAD_UMv1.2 ASIC. The caption for Fig. 6.9 explains what is shown in each of the three plots.
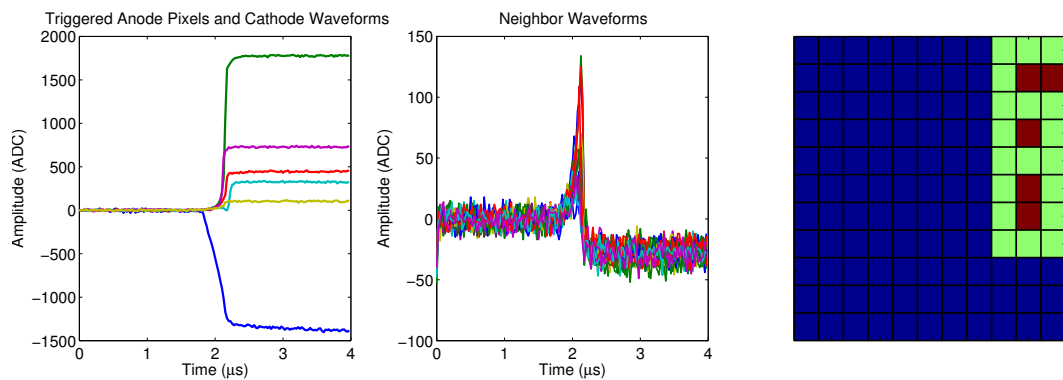
Figure 6.11: Recorded gamma-ray energy deposition in CdZnTe detectors read out with the VAD_UMv1.2 ASIC. The caption for Fig. 6.9 explains what is shown in each of the three panes.

electron cloud whereas the gamma-ray interaction has sharp neighbor waveforms.

CdZnTe detectors are not the best choice for muon tomography applications for national security because wide area, thin, inexpensive detectors are preferred. However, muons provide a useful signal to study how CdZnTe detectors respond when a large number of electron-hole pairs are generated. Although the distribution of the electron cloud is very different than what is expected for high-energy photon energy depositions, one can learn much about hole movement and neighbor signal induction from muon interactions.

CHAPTER VII

Summary and Future Work

7.1 Summary

National security applications for digitally-sampled room-temperature 2×2×1.5 cm^3 CdZnTe detectors were explored in this thesis. Situations where digital readout significantly expands the capabilities of CdZnTe compared to traditional analog systems were investigated as were cases where high-performance CdZnTe can directly compete with high-purity germanium or sodium iodide spectrometers. This thesis also demonstrated the first successful use of CdZnTe to measure plutonium isotopic composition, the first detection of fast neutrons in CdZnTe from elastic scattering, resolution of high-energy photopeaks above 3 MeV, and the first extended use of a portable digital CdZnTe array.

Digitally-sampled pulse waveforms provide better understanding of CdZnTe detector physics. Pulse waveforms illustrate space charge effects and electric field non-uniformity which have implications for sub-pixel position sensing and measurement of the electron mobility-lifetime product. Understanding hole movement and its impact in CdZnTe is simplified by observing the pulse waveforms. As the electronic noise contribution to energy resolution decreases for digital CdZnTe systems, the effects of microscopic trapping and trapping/de-trapping centers can be studied. These material defects may limit the energy resolution for the best CdZnTe detectors and

degrade energy resolution at higher photon energies.

Direct-attachment of CdZnTe detectors to ASICs without interposer boards minimized capacitance and reduced electronic noise. With excellent CdZnTe detectors, energy resolution of less than 0.35% FWHM for single-pixel events at 662 kev was achieved.

Defects in pulse waveforms which degrade energy resolution in high count rate scenarios were studied using digitally-sampled CdZnTe systems. While digital readout require more readout time, limiting the maximum possible reconstructed event rate, good energy resolution can be maintained at high dose rates by correcting waveform flaws. The defects are caused by ASIC reset signals, interference of ASIC trigger signals, and preamplifier decay. Cathode decay can be estimated by measuring the baseline and tail slope and subtracted from the waveform. The decay rate provides an estimate of the dose rate. Anode channel preamplifier decay must be optimized at high count rates by reducing the feedback resistance. Detector polarization due to slow moving holes manifested itself as decreased slope in the electron drift portion of cathode waveforms at high dose rates.

CdZnTe spectrometers were compared with existing detectors used for national security. A 2×2 array of 2×2×1.5 cm^3 CdZnTe detectors detected simple monoenergetic radiation sources faster than commercially available NaI detectors. Although HPGe detectors outperformed the digital CdZnTe array in determining uranium and plutonium isotopic composition, the measurement accuracy and precision were similar.

The energy resolution of digitally-sampled CdZnTe is adequate to observe small spectral differences from forward Compton-scattered photons in shielding. Intervening material between the source and detector may be identified by effective atomic number and areal density by comparing net photopeak counts ratios of different gamma-ray lines and a small-angle Compton scattering region. Shielding charac-

terization was demonstrated for intervening materials made of various thicknesses and compositions. Shielding as a function of angle was estimated from angularly deconvolved spectra for sparse source geometries.

Thermal neutron detection sensitivity is increased using digital rather than analog readout in high background environments due to improved energy resolution. Moderating effects of shielding material around SNM can be estimated by monitoring the thermal neutron capture rate.

Fast neutrons were detected in CdZnTe by detecting characteristic inelastic scattering gamma rays and by reducing the low-energy threshold so that elastic scattering interactions were observed. Several techniques were used to eliminate other possible causes of small energy depositions and ensure that the characteristic low-energy peak observed when the detector is irradiated with fast neutrons is due to elastic scattering interactions. One verification technique based on the interaction location of small energy depositions led to the development of a simple technique to localize fast neutron sources.

Finally, 4.4 MeV photons were detected and resolved using CdZnTe for the first time. By limiting transient signal effects, digitally-sampled CdZnTe should have enhanced detection capabilities over analog systems at high photon energies. Increasing the dynamic range improved high-energy gamma ray detection because pair production results in a smaller electron cloud than a photoelectric absorption so the entire energy may be deposited under a single pixel. Muon interactions were investigated to learn how very large electron clouds drift in CdZnTe.

Overall, CdZnTe can be used for national security to address "black-box" problems illustrated in Fig. 7.1. In these scenarios, a radioactive object is encountered and must be characterized without optical information. High-resolution spectroscopy can determine the radioisotope identity, characterize the isotopic composition of the source, and calculate the identity and thickness of intervening materials. Combined
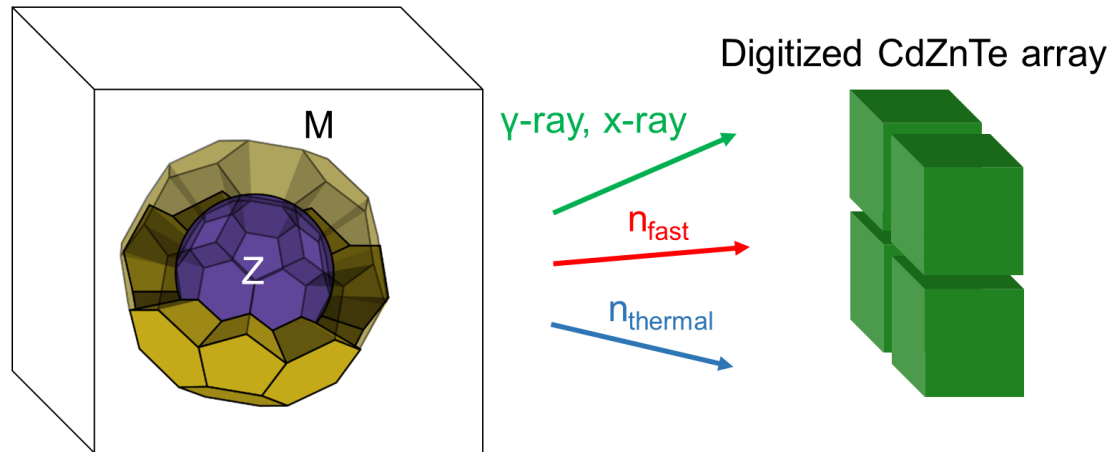
Figure 7.1: A "black-box" imaging scenario demonstrating the particle types emitted by SNM and detectable by CdZnTe. Z is a high-density radioactive material and M is a low-density moderating material.

Compton and coded-aperture imaging can be used to ascertain the physical configuration of the object. If photon signatures are heavily shielded, CdZnTe can determine whether the object is producing neutrons, possibly estimate the neutron generation mechanism, and coarsely localize the neutron source. With sensitivity to high-energy photons, fission gamma rays may be detected from a heavily shielded object while thermal neutron capture lines from low-Z intervening material such as hydrogen, oxygen, or carbon can be resolved and identified.

7.2   Suggestions for Future Work

Although CdZnTe is rapidly becoming a mature technology, there are still many active research areas. To continue improving material properties, collaborations with CdZnTe manufacturers should proceed in order to understand how detector growth and fabrication affect final performance. Neighbor waveform amplitude and steering between pixels to improve multiple-pixel reconstruction will become even more important to optimize during crystal growth and fabrication as the single pixel energy resolution approaches the theoretical limit of 0.2% FWHM at 662 keV. Better un-

derstanding of readout electronics will reduce electronic noise in future systems and improve energy resolution.

Sub-pixel position resolution may be improved for some detectors by better understanding electric field non-uniformities and correcting them or working with detector manufacturers to reduce non-uniformity. Using guard ring signals may improve sub-pixel position resolution for edge and corner pixels. This has been shown in theory, but should be demonstrated experimentally.

Fast and thermal neutron detection in CdZnTe has been demonstrated. However, clear statistical methods to declare detection must still be developed. These algorithms should flag the user if a neutron source is detected and report the associated detection confidence. Energy thresholds should be further reduced to improve fast neutron detection efficiency in CdZnTe. Reduced cathode noise will enable the ability to reconstruct the three-dimensional interaction location of the scattered neutron by improving depth reconstruction. Detecting fast neutrons from real special nuclear material will be valuable to demonstrate this capability's importance. Developing a statistical method to quantify the likelihood a neutron emitting object is a fission or an (α,n) source would also be useful.

The energy resolution of multi-MeV gamma-ray lines is still worse than expected. By using a high-intensity, non-Doppler-broadened gamma-ray source such as thermal neutron capture on ^{35}Cl, the resolution of multi-MeV gamma rays can be more thoroughly studied. Transient signal correction for charge sharing events, charge leak from collecting pixels to neighbor pixels, and weighting potential cross talk may contribute to the poor performance in addition to effects from larger electron clouds. While resolution of 4.4 MeV photons was shown, the root causes of energy resolution degradation is still not well understood and must be studied further.

Building readily-deployable systems is important for the future of CdZnTe. The detector housing should be small and thin while the power consumption must be
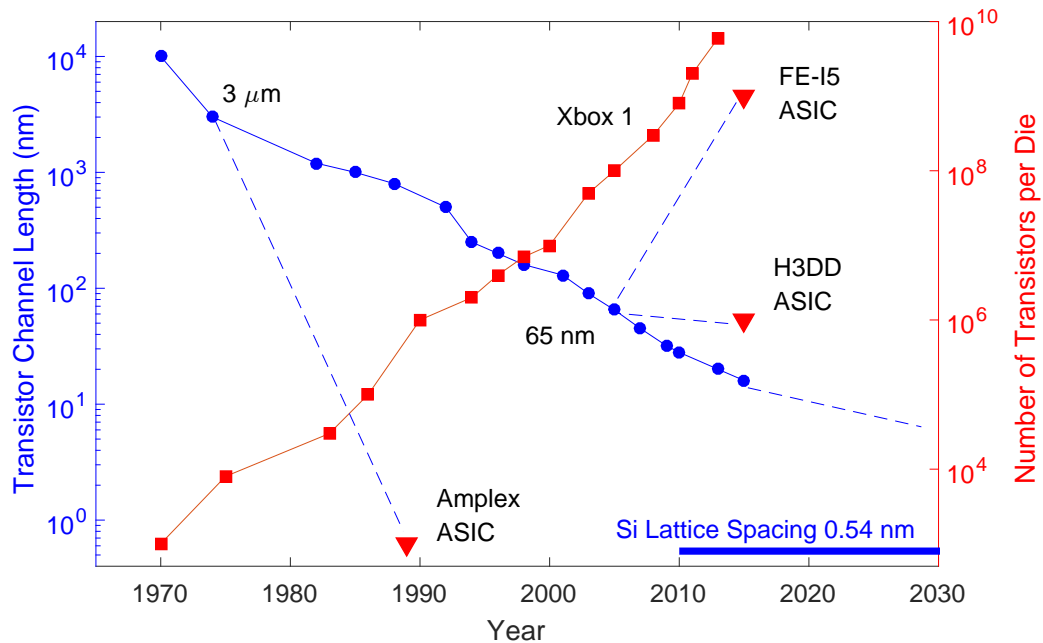
Figure 7.2: Demonstration of Moore's Law which states the number of transistors on a die doubles every eighteen months. The triangles show ASICs developed for radiation detectors. The connecting line from the triangle to the circle shows the transistor channel length used in the radiation detection ASIC.

limited. One of the main power consumers in current systems is the Peltier thermoelectric cooler which maintains an ambient temperature near 20 °C so the system gain does not drift and degrade energy resolution. If temperature effects can be more accurately corrected, allowing the system temperature to vary, the battery life of portable CdZnTe systems will be enhanced.

7.3 Vision for the Future of CdZnTe Imaging Spectrometers

One main advantage of CdZnTe is its modularity. Large, efficient systems can be created by tiling detectors together into large arrays. Contrastingly, small personal dosimeters can be achieved by using an individual detector.

Fig. 7.2 shows how integrated circuitry has improved over time [140]. This is famously known as Moore's law which states that the number of transistors per die

doubles every eighteen months [141]. This pace is driven by the consumer electronics market. Fig. 7.2 also shows the technology used in ASICs for radiation detection. In general, these chips are a decade behind the consumer electronics industry. Substantial improvement is expected as radiation detection ASIC design catches up to consumer electronics state-of-the-art. More functionality will be added to ASICs in the future including signal processing, data buffering, and perhaps data communication. If everything can be accomplished on a single chip, large sensor networks can be created, maximizing the aggregate information. This functionality will improve portability and reduce power consumption while increasing the utility of future digitized CdZnTe systems.

BIBLIOGRAPHY

[1] R. Rhodes, *The Making of the Atomic Bomb.* New York: Simon & Schuster, 1986.

[2] C. Nelson, *The Age of Radiance: The Epic Rise and Dramatic Fall of the Atomic Era.* New York: Simon & Schuster, 2014.

[3] G. F. Knoll, *Radiation Detection and Measurement.* Hoboken: Wiley, 2000.

[4] R. D. Evans, *The Atomic Nucleus.* New York: Krieger, 1982.

[5] R. Hofstadter, "Alkali halide scintillation counters," *Phys. Rev.*, vol. 74, pp. 100–101, 1948.

[6] I. V. Khodyuk *et al.*, "Optimization of scintillation performance via a combinatorial multi-element co-doping strategy: Application to NaI:Tl," *J. of Appl. Phys.*, vol. 118, p. 084901, 2015.

[7] Canberra Industires Inc., "NAIS-2×2 NaI:Tl LED temperature-stabilized scintillation detector," http://www.canberra.com/products/detectors/pdf/NAIS-2x2-SS-C38656.pdf, 2011.

[8] J. B. Birks, *The Theory and Practice of Scintillation Counting.* Oxford: Pergamon Press, 1964.

[9] P. R. Menge, G. Gautier, A. Iltis, C. Rozsa, and V. Solovyev, "Performance of large lanthanum bromide scintillators," *Nucl. Instrum. and Meth. Phys. Res. Sect. A Accel. Spectrometers, Detect. Assoc. Equip.*, vol. 579, no. 1, pp. 6 – 10, 2007.

[10] C. M. Wilson *et al.*, "Strontium iodide scintillators for high energy resolution gamma ray spectroscopy," *Proc. of the International Soc. for Optics and Photonics*, vol. 7079, pp. 17–24, 2008.

[11] E. Siciliano *et al.*, "Comparison of PVT and NaI:Tl scintillators for vehicle portal monitor applications," *Nucl. Instrum. and Meth. Phys. Res. Sect. A Accel. Spectrometers, Detect. Assoc. Equip.*, vol. 550, no. 3, pp. 647 – 674, 2005.

[12] U. Fano, "Ionization yield of radiations: The fluctuations of the number of ions," *Phys. Rev.*, vol. 72, pp. 26–29, 1947.

[13] G. Bertolini and A. Coche, *Semiconductor Detectors.* Amsterdam: Elsevier-North Holland, 1968.

[14] T. Takahashi and S. Watanabe, "Recent progress on CdTe and CdZnTe detectors," *IEEE Trans. on Nucl. Sci.*, vol. 48, pp. 950–959, 2001.

[15] R. O. Bell, G. Entine, and H. B. Serreze, "Time-dependent polarization of CdTe gamma-ray detectors," *Nucl. Instrum. and Meth.*, vol. 117, no. 1, pp. 267 – 271, 1974.

[16] P. Siffert *et al.*, "Polarization in cadmium telluride nuclear radiation detectors," *IEEE Trans. on Nucl. Sci.*, vol. 23, no. 1, pp. 159–170, 1976.

[17] T. B. Mohammed, A. Friant, and J. Mellet, "Structure MIS effects on polarization of HgI_2 crystals used for gamma-ray detection," *IEEE Trans. on Nucl. Sci.*, vol. 32, pp. 383–385, 1985.

[18] J. E. Baciak and Z. He, "Long-term stability of 1-cm thick pixelated HgI_2 gamma-ray spectrometers operating at room temperature," *IEEE Trans. on Nucl. Sci.*, vol. 51, no. 4, pp. 1886–1894, 2004.

[19] W. Koehler *et al.*, "Quantitative investigation of room-temperature breakdown effects in pixelated TlBr detectors," *IEEE Trans. on Nucl. Sci.*, vol. 61, no. 5, pp. 2573–2578, 2014.

[20] B. Donmez *et al.*, "The stability of TlBr detectors at low temperature," *Nucl. Instrum. and Meth. Phys. Res. Sect. A Accel. Spectrometers, Detect. Assoc. Equip.*, vol. 623, pp. 1024–1029, 2010.

[21] Y. Eisen, "Current state-of-the-art industrial and research applications using room-temperature CdTe and CdZnTe solid state detectors," *Nucl. Instrum. and Meth. Phys. Res. Sect. A Accel. Spectrometers, Detect. Assoc. Equip.*, vol. 380, pp. 431–439, 1996.

[22] W. Shockley, "Currents to conductors induced by a moving point charge," *J. of Appl. Phys.*, vol. 9, p. 635, 1938.

[23] S. Ramo, "Currents induced by electron motion," *Proc. of the I.R.E.*, pp. 584–585, 1939.

[24] Z. He, "Review of the Shockley-Ramo theorem and its application in semiconductor gamma-ray detectors," *Nucl. Instrum. and Meth. Phys. Res. Sect. A Accel. Spectrometers, Detect. Assoc. Equip.*, vol. 463, pp. 250–267, 2001.

[25] P. Luke, "Single-polarity charge sensing in ionization detectors using coplanar electrodes," *Appl. Phys. Lett.*, vol. 65, no. 22, pp. 2884–2886, 1994.

[26] M. Fritts *et al.*, "Analytical model for event reconstruction in coplanar grid CdZnTe detectors," *Nucl. Instrum. and Meth. Phys. Res. Sect. A Accel. Spectrometers, Detect. Assoc. Equip.*, vol. 708, pp. 1–6, 2013.

[27] J. D. Mann, "Improving cadmium zinc telluride spectrometer performance and capabilities," Ph.D. dissertation, University of Michigan, 2016.

[28] H. H. Barrett, J. D. Eskin, and H. B. Barber, "Charge transport in arrays of semiconductor gamma-ray detectors," *Phys. Rev. Lett.*, vol. 75, no. 1, pp. 156–159, 1995.

[29] J. Eskin, H. Barrett, H. Barber, and J. Woolfenden, "Effect of pixel geometry on spatial and spectral resolution in a CdZnTe imaging array," in *Nucl. Sci. Symp. and Medical Imaging Conf., (NSS/MIC), 1995 IEEE*, vol. 1. IEEE, 1995, pp. 544–548.

[30] Z. He *et al.*, "1-D position sensitive single carrier semiconductor detectors," *Nucl. Instrum. and Meth. Phys. Res. Sect. A Accel. Spectrometers, Detect. Assoc. Equip.*, vol. 380, no. 1, pp. 228 – 231, 1996.

[31] Z. He, W. Li *et al.*, "3-D position-sensitive CdZnTe gamma-ray spectrometers," *Nucl. Instrum. and Meth. Phys. Res. Sect. A Accel. Spectrometers, Detect. Assoc. Equip.*, vol. 422, pp. 173–178, 1999.

[32] D. McGregor *et al.*, "CdZnTe semiconductor parallel strip Frisch grid radiation detectors," *IEEE Trans. on Nucl. Sci.*, vol. 45, no. 3, pp. 443–449, 1998.

[33] A. E. Bolotnikov *et al.*, "Optimization of virtual Frisch-grid CdZnTe detector designs for imaging and spectroscopy of gamma rays," in *Proc. SPIE*, vol. 6706, 2007, pp. 670 603–670 603–14.

[34] A. E. Bolotnikov, N. M. Abdul-Jabber *et al.*, "Effects of Te inclusions on the performance of CdZnTe radiation detectors," *IEEE Trans. on Nucl. Sci.*, vol. 55, no. 5, pp. 2757–2764, 2008.

[35] G. A. Carini *et al.*, "Effect of Te precipitates on the performance of CdZnTe detectors," *Appl. Phys. Lett.*, vol. 88, pp. 143 515–143 515–3, 2006.

[36] A. E. Bolotnikov *et al.*, "Cumulative effects of te preciepitates in cdznte radiation detectors," *Nucl. Instrum. and Meth. Phys. Res. Sect. A Accel. Spectrometers, Detect. Assoc. Equip.*, vol. 571, pp. 687–698, 2007.

[37] W. Li *et al.*, "A data acquisition and processing system for 3-D position sensitive CdZnTe," *IEEE Trans. on Nucl. Sci.*, vol. 46, no. 3, pp. 1989–1994, 1999.

[38] F. Zhang *et al.*, "Improved resolution for 3-D position sensitive CdZnTe spectrometers," *IEEE Trans. on Nucl. Sci.*, vol. 51, no. 5, pp. 2427–2431, 2004.

[39] F. Zhang and Z. He, "3-D position sensitive CdZnTe gamma-ray spectrometers - improved performance with new ASICs," *Proc. of SPIE.*, vol. 5540, pp. 135–143, 2004.

[40] F. Zhang *et al.*, "3-D position sensitive CdZnTe spectrometer performance using third generation VAS/TAT readout electronics," *IEEE Trans. on Nucl. Sci.*, vol. 52, no. 5, 2005.

[41] F. Zhang, C. Herman, Z. He, G. D. Geronimo, E. Vernon, and J. Fried, "Characterization of the H3D ASIC readout system and 6.0 cm^3 3-D position sensitive CdZnTe detectors," *IEEE Trans. on Nucl. Sci.*, vol. 59, no. 1, pp. 236–242, 2012.

[42] G. D. Geronimo *et al.*, "Readout ASIC for 3-D position-sensitive detectors," *IEEE Trans. on Nucl. Sci.*, vol. 55, no. 3, pp. 1593–1603, 2008.

[43] Y. Zhu and Z. He, "Performance of a 2-kev digitizer ASIC for 3-D position-sensitive pixelated semiconductor detectors," in *Nucl. Sci. Symp. and Medical Imaging Conf. (NSS/MIC), 2012 IEEE*, 2012, pp. 4109–4112.

[44] M. Streicher *et al.*, "A portable 2×2 digital 3-D CZT imaging spectrometer system," in *Nucl. Sci. Symp. and Medical Imaging Conf. (NSS/MIC), 2014 IEEE*, 2014.

[45] F. P. Doty *et al.*, "Properties of CdZnTe crystals grown by a high pressure Bridgman method," *J. Vac. Sci. Technol. B*, vol. 10, pp. 1418–1422, 1992.

[46] H. Chen *et al.*, "Characterization of traveling heater method (THM) grown $Cd_{0.9}zn_{0.1}Te$ crystals," *IEEE Trans. on Nucl. Sci.*, vol. 54, no. 4, pp. 811–816, 2007.

[47] J. Mann, L. Tjayadi, and Z. He, "Performance of 20×20×5 mm^3 pixelated cadmium zinc telluride semiconductor detectors from various anode fabrication techniques," in *Nucl. Sci. Symp. and Medical Imaging Conf.(NSS/MIC), 2013 IEEE*, 2013.

[48] Y. A. Boucher, "Analysis of cadmium zinc telluride detector performance and characteristics for applications in gamma-ray imaging spectrometers," Ph.D. dissertation, University of Michigan, 2013.

[49] ANSYS, "Maxwell: Explore engineering simulation," https://www.ansys.com.

[50] Y. Zhu *et al.*, "Performance comparison of steering-grid and simple-pixel CdZnTe detectors," in *Nucl. Sci. Symp. and Medical Imaging Conf.(NSS/MIC), 2013 IEEE*, 2013.

[51] D. Reilly, N. Ensslin, H. Smith, and S. Kreiner, "Passive nondestructive assay of nuclear materials," Los Alamos National Laboratory, Tech. Rep. NUREG/CR-5550 LA-UR-90-732, 1991.

[52] M. Yamashita, L. D. Stephens, and H. W. Patterson, "Cosmic-ray-produced neutrons at ground level: Neutron production rate and flux distribution," *J. of Geophysical Research*, vol. 71, no. 16, pp. 3817–3827, 1966.

[53] M. Korun, R. Martincic, B. Pucelj, and M. Ravnik, "Measurement of the ambient neutron background with a high-resolution γ-ray spectrometer," in *Symp. on Rad. Protection in Neighboring Countries in Central Europe*, 1995.

[54] J. J. Duderstadt and L. J. Hamilton, *Nuclear Reactor Analysis.* New York: Wiley, 1976.

[55] A. Miyake *et al.*, "Development of a CdTe thermal neutron detector for neutron imaging," *Nucl. Instrum. and Meth. Phys. Res. Sect. A Accel. Spectrometers, Detect. Assoc. Equip.*, vol. 677, pp. 41 – 44, 2012.

[56] D. S. McGregor, J. T. Lindsay, and R. W. Olsen, "Thermal neutron detection with cadmium$_{1-x}$ zinc$_x$ telluride semiconductor detectors," *Nucl. Instrum. and Meth. Phys. Res. Sect. A Accel. Spectrometers, Detect. Assoc. Equip.*, vol. 381, no. 2, pp. 498 – 501, 1996.

[57] S. T. Brown, Y. A. Boucher, J. Mann, Y. Zhu, and Z. He, "Thermal neutron source location using a 3-D position-sensitive CdZnTe detector array," in *Nucl. Science Symposium and Medical Imaging Conference (NSS/MIC), 2013 IEEE*, 2013.

[58] N. Mascarenhas, J. Brennan, K. Krenz, P. Marleau, and S. Mrowka, "Results with the neutron scatter camera," *IEEE Trans. on Nucl. Sci.*, vol. 56, no. 3, pp. 1269–1273, 2009.

[59] F. D. Brooks, "A scintillation counter with neutron and gamma-ray discriminators," *Nucl. Instrum. and Meth.*, vol. 4, no. 3, pp. 151 – 163, 1959.

[60] H. Klein and S. Neumann, "Neutron and photon spectrometry with liquid scintillation detectors in mixed fields," *Nucl. Instrum. and Meth. Phys. Res. Sect. A Accel. Spectrometers, Detect. Assoc. Equip.*, vol. 476, no. 12, pp. 132 – 142, 2002.

[61] J. Ljungvall and J. Nyberg, "A study of fast neutron interactions in high-purity germanium detectors," *Nucl. Instrum. and Meth. Phys. Res. Sect. A Accel. Spectrometers, Detect. Assoc. Equip.*, vol. 546, no. 3, pp. 553 – 573, 2005.

[62] N. Veselinovic *et al.*, "Some peculiarities of digital gamma-ray spectroscopy with germanium detectors performed in presence of neutrons," *Physics Procedia*, vol. 59, pp. 63 – 70, 2014.

[63] F. Zhang, "Events reconstruction in 3-D position sensitive CdZnTe gamma-ray spectrometers," Ph.D. dissertation, University of Michigan, 2005.

[64] W. Kaye, "Energy and position reconstruction in pixelated CdZnTe detectors," Ph.D. dissertation, University of Michigan, 2012.

[65] H. Yang, "Applications of digital ASIC array system for noise analysis, non-linearity correction, event classification and reconstructions," Ph.D. dissertation, University of Michigan, 2013.

[66] Y. Zhu, "Digital signal processing methods for pixelated 3-D position sensitive room-temperature semiconductor detectors," Ph.D. dissertation, University of Michigan, 2012.

[67] Z. He, G. F. Knoll, D. K. Wehe, and J. Miyamoto, "Position-sensitive single carrier cdznte detectors," *Nucl. Instrum. and Meth. Phys. Res. Sect. A Accel. Spectrometers, Detect. Assoc. Equip.*, vol. 388, pp. 180–185, 1997.

[68] S. Brown, "Time-encoded thermal neutron imaging using large-volume pixelated CdZnTe detectors," Ph.D. dissertation, University of Michigan, 2017.

[69] S. Joshi, "Coded aperture imaging applied to pixelated CdZnTe detectors," Ph.D. dissertation, University of Michigan, 2014.

[70] E. E. Fenimore and T. M. Cannon, "Coded aperture imaging with uniformly redundant arrays," *Appl. Opt.*, vol. 17, no. 3, pp. 337–347, 1978.

[71] W. Wang, "Techniques and applications of compton imaging for position-sensitive gamma-ray detectors," Ph.D. dissertation, University of Michigan, 2011.

[72] W. Koehler, "Thallium bromide as an alternative material for room-temperature gamma-ray spectroscopy and imaging," Ph.D. dissertation, University of Michigan, 2016.

[73] W. Koehler, M. Streicher, S. O'Neal, and Z. He, "A correction factor to the two-bias method for determining mobility-lifetime products in pixelated detectors," *IEEE Trans. on Nucl. Sci.*, vol. 63, no. 3, pp. 1832–1838, 2016.

[74] H3D, "Polaris-H imaging spectrometer for nuclear power plants," https://www.h3dgamma.com/nuclearProducts.php.

[75] R. M. Lindstrom and R. F. Fleming, "Dead time, pileup, and accurate gamma-ray spectroscopy," *Radioactivity and Radiochemistry*, vol. 6, no. 2, pp. 20–27, 1995.

[76] Canberra, "A practical guide to high count rate germanium gamma-ray spectroscopy," Areva - Canberra subsidiary, Tech. Rep. Gamma Ref 0013, 2002.

[77] K. E. Nelson, T. B. Gosnell, and D. A. Knapp, "The effect of gamma-ray detector energy resolution on the ability to identify radioactive sources," Lawrence Livermore National Laboratory, Tech. Rep. LLNL-TR-411374, 2009.

[78] B. Efron, "Bootstrap methods: Another look at the jackknife," *Annals of Stat.*, vol. 7, no. 1, pp. 1–26, 1979.

[79] SAIC, "GR-135 the identifier manual," Science Applications International Corporation, Tech. Rep. 87317-1, 2004.

[80] D. T. Vo, "Comparison of portable detectors for uranium enrichment measurements," Los Alamos National Laboratory, Tech. Rep. LA-UR-06 2645, 2006.

[81] A. E. Proctor and K. R. Pohl, "Comparison of several detector technologies for measurement of special nuclear materials," Constellation Technology Corporation, Tech. Rep., 2003.

[82] C. T. Nguyen and J. Zsigrai, "Basic characterization of highly enriched uranium by gamma spectrometry," *Nucl. Instrum. and Meth. Phys. Res. Sect. A Accel. Spectrometers, Detect. Assoc. Equip.*, vol. 246, pp. 417–424, 2006.

[83] R. Berndt, E. Franke, and P. Mortreau, "^{235}U enrichment or UF_6 mass determination on UF_6 cylinders with non-destructive analysis methods," *Nucl. Instrum. and Meth. Phys. Res. Sect. A Accel. Spectrometers, Detect. Assoc. Equip.*, vol. 612, no. 2, pp. 309 – 319, 2010.

[84] J. Cantrell, "Uranium enrichment standards of the Y-12 nuclear detection and sensor testing center," in *Proc. of the 52nd Annual INMM Meeting*, 2012.

[85] K. Ianakiev and et. al, "Advanced technology for enrichment monitoring in UF_6 gas centrifuge enrichment plants," Los Alamos National Laboratory, Tech. Rep. LA-UR 10-06263, 2010.

[86] ASTM, "Standard test method for measurement of ^{235}U fraction using enrichment meter principle," ASTM Committee on Nuclear Fuel Cycle, Tech. Rep. C1514-08, 2008.

[87] L. A. Kull and R. O. Ginaven, "Guidelines for gamma-ray spectroscopy measurements of ^{235}U enrichment," Brookhaven National Laboratory, Tech. Rep. BNL 50414, 1974.

[88] T. Burr, S. Croft, and K. Jarman, "Uncertainty quantification in application of the enrichment meter principle for nondestructive assay of special nuclear material," *J. of Sensors*, 2015.

[89] ORTEC, "Micro-Detective and Micro-Detective-DX portable hand-held radioisotope identifiers," Advanced Measurements Technology, Tech. Rep., 2010. [Online]. Available: www.ortec-online.com/download/Micro-Detective.pdf

[90] S. Agostinelli *et al.*, "Geant4 - a simulation toolkit," *Nucl. Instrum. and Meth. Phys. Res. Sect. A Accel. Spectrometers, Detect. Assoc. Equip.*, vol. 506, pp. 250–303, 2003.

[91] H. Yucel and H. Dikmen, "Uranium enrichment measurements using the intensity ratios of self-fluorescence x-rays to 92* kev gamma ray in U Kα spectral region," *Talanta*, vol. 78, no. 2, pp. 410 – 417, 2009.

175

[92] K. Abbas, J. Morel, M. Etcheverry, and G. Nicolaou, "Use of miniature CdZnTe x / γ detector in nuclear safeguards: characterisation of spent nuclear fuel and uranium enrichment determination," *Nucl. Instrum. and Meth. Phys. Res. Sect. A Accel. Spectrometers, Detect. Assoc. Equip.*, vol. 405, no. 1, pp. 153 – 158, 1998.

[93] R. Gunnink, W. Ruhter, P. Miller, J. Goerten, M. Swinhoe, H. Wagner, J. Verplancke, M. Bickel, and S. Abousahl, "MGAU: A new analysis code for measurement U-235 enrichments in arbitrary samples," Lawrence Livermore National Laboratory, Tech. Rep. UCRL-JC-114713, 1994.

[94] T. E. Sampson *et al.*, "The determination of plutonium isotopic composition by gamma-ray spectroscopy," *Nucl. Instrum. and Meth. Phys. Res. Sect. A Accel. Spectrometers, Detect. Assoc. Equip.*, vol. 193, no. 12, pp. 177 – 183, 1982.

[95] T. Dragnev and K. Scharf, "Non-destructive gamma spectrometry measurement of ^{239}Pu / ^{240}Pu and ^{240}Pu / Pu ratios," *The International J. of Appl. Radiation and Isotopes*, vol. 26, no. 3, pp. 125 – 129, 1975.

[96] M. Streicher *et al.*, "Special nuclear material characterization using digital 3-D position sensitive CdZnTe detectors and high purity germanium spectrometers," *IEEE Trans. on Nucl. Sci.*, vol. 63, no. 5, pp. 2649–2656, 2016.

[97] R. C. Runkle, D. L. Chichester, and S. J. Thompson, "Rattling nucleons: New developments in active interrogation of special nuclear material," *Nucl. Instrum. and Meth. Phys. Res. Sect. A Accel. Spectrometers, Detect. Assoc. Equip.*, vol. 663, no. 1, pp. 75 – 95, 2012.

[98] T. N. Dragnev, "Intrinsic self-calibration of non-destructive gamma spectrometric measurements determination of U, Pu and ^{241}Am isotopic ratios," *J. of Radioanalytical Chemistry*, vol. 36, no. 2, pp. 491–508, 1977.

[99] R. J. S. Harry, J. K. Aaldijk, and J. P. Braak, "Gamma-spectrometric determination of isotopic composition without use of standards," IAEA, Tech. Rep., 1976.

[100] W. Ruhter, T. Wang, and C. Hayden, "Uranium enrichment measurements without calibration using gamma rays above 100 kev," Lawrence Livermore National Laboratory, Tech. Rep. UCRL-JC-142832, 2001.

[101] K. E. Nelson, "Shielding and activity estimator for template-based nuclide identification methods," 2013, US Patent 8,417,467.

[102] S. M. Horne *et al.*, "GADRAS-DRF 18.5 users manual," Sandia National Laboratories, Tech. Rep. SAND2014-20625, 2014.

[103] D. N. Anderson *et al.*, "A probabilistic derivation of gamma-ray attenuation and application: Bayesian mass estimation with a low count spectrum," *Nucl.*

Instrum. and Meth. Phys. Res. Sect. A Accel. Spectrometers, Detect. Assoc. Equip., vol. 569, no. 3, pp. 894 – 899, 2006.

[104] K. P. Ziock *et al.*, "Performance of gamma-ray imager using a 38 x 38 crossed-strip Ge detector," in *Nucl. Sci. Symp. and Medical Imaging Conf. (NSS/MIC), 2003 IEEE*, 2003.

[105] T. Johnson *et al.*, "Material differentiation by dual energy CT: initial experience," *European Radiology*, vol. 17, no. 6, pp. 1510–1517, 2007.

[106] D. J. Mitchell and K. M. Tolk, "Trusted radiation attribute demonstration system," Sandia National Laboratories, Tech. Rep. SAND2000-1481C, 2000.

[107] M. Streicher, S. Brown *et al.*, "A method to estimate the atomic number and mass thickness of intervening materials in uranium and plutonium gamma-ray spectroscopy measurements," *IEEE Trans. on Nucl. Sci.*, vol. 63, no. 5, pp. 2639–2648, 2016.

[108] R. Rothe, "Extrapolated experimental critical parameters of unreflected and steel-reflected massive enriched uranium metal spherical and hemispherical assemblies," Idaho National Engineering Laboratory, Tech. Rep. INEEL/EXT-97-01401, 1997.

[109] D. Goodman, M. Streicher *et al.*, "Identification of intervening materials in gamma-ray spectroscopy measurements using angularly deconvolved spectra with multiple sources in the field of view," 2017, manuscript submitted.

[110] O. S. U. Reactor, https://reactor.osu.edu/research-reactor.

[111] S. Walston *et al.*, "Benchmark measurement of the berp ball in various reflectors," Lawrence Livermore National Laboratory, Tech. Rep. LLNL-TR-661297, 2014.

[112] M. B. Chadwick *et al.*, "ENDF/B-VII.1. Nuclear data for science and technology: Cross sections, covariances, fission product yields, and decay data," *Nuclear Data Sheets*, vol. 112, no. 12, pp. 2887–2996, 2011.

[113] E. L. Haines and A. B. Whitehead, "Pulse height defect and energy dispersion in semiconductor detectors," *Review of Sci. Instrum.*, vol. 37, no. 2, pp. 190–194, 1966.

[114] P. Sorensen, "Atomic limits in the search for galactic dark matter," *Phys. Rev. D*, vol. 91, pp. 083 509–1–8, 2015.

[115] T. Shutt *et al.*, "Measurement of ionization and phonon production by nuclear recoils in a 60 g crystal of germanium at 25 mK," *Phys. Rev. Letters*, vol. 69, no. 24, pp. 3425–3427, 1992.

[116] I. Lazanu and S. Lazanu, "Contribution of the electronphonon interaction to Lindhard energy partition at low energy in Ge and Si detectors for astroparticle physics applications," *Astroparticle Phys.*, vol. 75, pp. 44 – 54, 2016.

[117] M. Streicher *et al.*, "Fast neutron detection using pixelated CdZnTe spectrometers," 2017, manuscript submitted.

[118] Y. Zhu, S. Anderson, and Z. He, "Sub-pixel position sensing for pixelated, 3-D position sensitive, wide band-gap, semiconductor, gamma-ray detectors," *IEEE Trans. on Nucl. Sci.*, vol. 58, no. 3, pp. 1400–1409, 2011.

[119] L. S. Waters, "MCNPX user's manual," Los Alamos National Laboratory, Tech. Rep. LA-UR-02-2607, 2002.

[120] H. R. Vega-Carillo, V. M. Hernandez-Davila, T. Rivera-Montalvo, and A. Sanchez, "Characterization of a ^{239}PuBe isotopic neutron source," in *Proc. of the ISSSD*, 2012.

[121] D. Goodman *et al.*, "1D fast neutron source localization using digital pixelated 3-D position sensitive CdZnTe detectors," 2017, manuscript submitted.

[122] H. W. Kraner, "Fast neutron damage in germanium detectors," *IEEE Trans. on Nucl. Sci.*, vol. NS-27, no. 1, pp. 218–234, 1980.

[123] B. Fraboni, A. Cavallini, and W. Dusi, "Damage induced by ionizing radiation on CdZnTe and CdTe detectors," *IEEE Trans. on Nucl. Sci.*, vol. 51, no. 3, pp. 1209–1215, 2004.

[124] L. A. Franks and R. B. James, "Status of radiation damage measurements in room temperature semiconductor radiation detectors," Sandia National Laboratories, Tech. Rep. SAND98-8237, 1998.

[125] L. M. Bartlett *et al.*, "Radiation damage and activation of CdZnTe by intermediate energy neutrons," in *SPIE Proc.*, 1996.

[126] Y. Eisen and A. Shor, "Fast neutron damage of a pixelated CdZnTe gamma ray spectrometer," *IEEE Trans. on Nucl. Sci.*, vol. 56, no. 4, pp. 1700–1705, 2009.

[127] W. Bertozzi, S. E. Korbly, R. J. Ledoux, and W. Park, "Nuclear resonance fluorescence and effective z determination applied to detection and imaging of special nuclear material, explosives, toxic substances and contraband," *Nucl. Instrum. and Meth. Phys. Res. Sect. B Beam Interactions with Materials and Atoms*, vol. 261, no. 2, pp. 331–336, 2007.

[128] W. Bertozzi and R. J. Ledoux, "Nuclear resonance fluorescence imaging in non-intrusive cargo inspection," *Nucl. Instrum. and Meth. Phys. Res. Sect. B Beam Interactions with Materials and Atoms*, vol. 241, no. 4, pp. 820–825, 2005.

[129] S. E. Anderson, "Event classification for 3-D position sensitive semiconductor detectors," Ph.D. dissertation, University of Michigan, 2011.

[130] M. Kroupa, C. Granja *et al.*, "Wide energy range gamma-ray calibration source," *J. of Instrumentation*, vol. 6, no. T11002, 2011.

[131] NNDC, "Thermal neutron capture gammas (CapGam)," National Nuclear Data Center at Brookhaven National Laboratory http://www.nndc.bnl.gov/capgam.

[132] Z. Janout, S. Pospisil, and M. Vobecky, "Observation of a doppler broadening of the 4438 keV gamma-line of ^{12}C in processes ^{12}C(n,n'γ)^{12}C and ^{9}Be(α,nγ)^{12}C," *J. of Radioanalytical Chem.*, vol. 56, no. 1, pp. 71–81, 1980.

[133] H. R. Vega-Carillo *et al.*, "Neutron and gamma-ray spectra of ^{239}PuBe and ^{241}AmBe," *Appl. Radiation and Isotopes*, vol. 57, pp. 167–170, 2002.

[134] V. G. Kiptily *et al.*, "Doppler broadening of gamma ray lines and fast ion distribution in JET plasmas," *Nucl. Fusion*, vol. 50, pp. 84 001–84 010, 2010.

[135] S. Kliewer *et al.*, "The cosmic connection: The Berkeley lab cosmic ray telescope project," http://cosmic.lbl.gov/.

[136] K. N. Borozdin, G. E. Hogan *et al.*, "Surveillance: Radiographic imaging with cosmic-ray muons," *Nature*, vol. 422, p. 277, 2003.

[137] P. Checchia, "Review of possible applications of cosmic muon tomography," *J. of Instrumentation*, vol. 11, no. C12072, 2016.

[138] C. L. Morris *et al.*, "Obtaining material identification with cosmic ray radiography," *AIP Advances*, vol. 2, no. 042128, 2002.

[139] L. W. Alvarez *et al.*, "Search for hidden chambers in the pyramids," *Science*, vol. 167, no. 3919, pp. 832–839, 1970.

[140] G. DeGeronimo, "Microelectronics for national security and fundamental physics," University of Michigan Colloquium Series, 2017.

[141] G. E. Moore, "Cramming more components onto integrated circuits," *Electronics*, vol. 38, no. 8, pp. 114–117, 1965.